Growth Factor-Induced Cell Migration Using Microfabricated Devices

by

QINGJUN KONG

A dissertation submitted to the Graduate Faculty in Mechanical Engineering in partial fulfillment of the requirements for the degree of Doctor of Philosophy, The City University of New York

2009

© 2009

QINGJUN KONG

All Rights Reserved

This manuscript has been read and accepted for the
Graduate Faculty in Engineering in satisfaction of the
dissertation requirement for the degree of Doctor of Philosophy.

	Maribel Vazquez
Date	Chair of Examining Committee
	Mumtaz K. Kassir
Date	Executive Officer

Professor Mitchell B. Schaffler, Ph. D.

Professor John M. Tarbell, Ph. D.

Professor Peter A. Torzilli, Ph. D.

Professor Maribel Vazquez, Sc. D.

Professor Sheldon Weinbaum, Ph. D.
Supervision Committee

THE CITY UNIVERSITY OF NEW YORK

Abstract

Growth Factor-Induced Cell Migration Using Microfabricated Devices

by

QINGJUN KONG

Adviser: Professor MARIBEL VAZQUEZ

Over a quarter of a million people undergo surgical procedures to repair soft tissue such as ligaments and tendons in the United States each year. Multiple methodologies have been developed to enhance ligament healing in recent decades, as these tissues require years to fully recover mechanical properties. Growth factors have been widely applied to enhance soft tissue healing via cell proliferation and migration, as well as synthesis of extracellular matrix proteins.

Growth factor-induced cell migration is essential to tissue repair, as it is one of the first biological processes to initiate and regulate healing quality. Growth factors stimulate cells via receptor binding and intracellular signal transduction, which initiate multiple functions to achieve cell migration. Despite the volume of research in cell migration, it is still incompletely understood because of the complicated interactions between growth factors and their receptors, signal transduction pathways, and the effects of extracellular environment, including pH and temperature. Published findings have illustrated that growth factor gradients can direct cell migration, while increasing growth

factor concentration primarily increases random cell motility. It has also been demonstrated that the spatial profiles and exposure time of growth factor gradients play important roles in cell migration. However, how these gradients impact cell migration remains incompletely understood.

In the past decade, researchers have developed various bioassays from macro-scale to micro-scale that facilitate the study of growth factor-induced cell migration. The conventional bioassays designed in macro-scale, such as transwell assays, Zigmond chambers and scratch wound assays, lack precise measurements of growth factor concentration and gradient around individual cells over time. Hence, they cannot provide a platform with which to accurately analyze growth factor gradient-driven cell migration. Microfabrication, often integrated with imaging technology and computational modeling, has been widely used in biological studies to provide quantitative methodologies and platforms of single-cell analysis to investigate cell migration.

This work has utilized microfabrication to develop a novel microfluidic device, called the Bridged μLane System, to study cell migration in response to different spatiotemporal gradients of Epidermal Growth Factor (EGF). We have developed an optimal loading method to seed cells within the microenvironment, by examining how shear stress-induced cell-cell interconnections, cell-extracellular matrix interactions, and cell morphology affect cell migration. We observed that cell migration was EGF gradient-dependent, while EGF concentration also played an important role in regulating cell migration. Transient EGF gradients were found to be less effective on cell motility than steady-state gradients. The population of motile cells increased with EGF gradients, but decreased when higher EGF concentrations were used. Further, our experimental

results suggest that EGF concentration and gradient are integrated to regulate cell migration.

Herein, we provide a platform with which to study cell migration with quantitative measurement of imposed growth factor gradients. This work can be applied to benefit a variety of cell migration investigations including tissue healing, immunological response, and cancer metastasis.

TABLE OF CONTENTS

LISTS OF TABLES

LISTS OF FIGURES

CHAPTER 1

Introduction

1.0 Background

Each year in the United States, approximately 8 million people consult orthopedic surgeons with medical problems of bone, cartilage, ligament and tendon. Over half a million grafting procedures of bone [1, 2] and a quarter million surgical procedures of cartilage [3, 4] are performed in the United States each year. Further, it is estimated that more than 2 per 1,000 people in the general US population experience knee ligament ruptures each year, including the anterior cruciate ligament (ACL) injury, medial collateral ligament (MCL) injury, and posterior cruciate ligament (PCL) injury [5, 6].

Ligaments are soft connective tissues that connect bones to stabilize joints, guide motion, and prevent excessive joint motion [2, 7]. The ligament is composed of fibroblast cells, approximately 20% by volume, and extracellular matrix (ECM), 80% by volume [2, 8]. Approximately 70% of ECM is water, while the remaining 30% are solids including collagen, elastin, proteoglycans and glycoproteins [2]. In healthy ligaments, fibroblast cells exhibit spindle-like morphology, and are arranged in a complex three-dimensional network of parallel rows [9]. In vivo, fibroblasts are about 15μm in length and 8μm in diameter [7], and have branched cytoplasm with one or two nucleoli and reduced rough endoplasmic reticulum. During ligament development, fibroblasts proliferate, migrate and also synthesize collagen within ECM [5, 7, 8]. When external mechanical stimulus is applied, fibroblasts convert mechanotransduction signals into biological processes, such as modulation of fibroblast migration [10], synthesis and degradation of ECM proteins

[10], and release of growth factors [11]. Type I collagen is the major component of ECM, and provides strength and allows flexibility and movement of ligaments.

Ligament repair is a complex biological process, and often takes years to fully recover. Over the past decades, various methodologies have been developed to enhance ligament healing. However, healing quality and healing time remain the major concerns in ligament repair. In order to help enhance ligament healing, we must first understand how a ligament is healed and what factors play important roles in the healing process.

1.1 Ligament healing

Wound healing of ligaments is generally processed in four phases: Inflammation, Migration, Initial remolding, and Final remolding [7, 12, 13]. During wound healing, platelets aggregate and cause the release of growth factors to stimulate white blood cells to move into the area of injury and remove contaminating bacteria [14]. Fibroblasts are also triggered to migrate to the wounds, but fibroblast motility is low due to intrinsic problems of avascularity and encapsulation with synovial fluid in ligament healing [2]. Such problems delay the initial remolding of the early scar [7, 12, 13], and therefore the entire process of wound healing.

The growth factors released by platelets assist fibroblast proliferation and ECM synthesis, and trigger fibroblast alignment along the ECM for constrictive force generation, which helps facilitate wound closure [14, 15]. Further, as such growth factor-induced migration plays an important role in tissue repair [8, 15, 16], our work seeks to examine how fibroblasts migrate in response to the exogenous growth factors. Treatment with growth factors has been shown to improve healing quality and accelerate the healing

process. In our work, we investigate how growth factors affect the migratory response of MCL-derived fibroblasts.

1.2 Epidermal growth factor and epidermal growth factor receptor signaling

Ligament injuries result in the release of growth factors that initiate the wound healing process [17, 18]. After injury, accumulated platelets are known to secrete growth factors, including Platelet-Derived Growth Factor (PDGF), Epidermal Growth Factor (EGF), and Transforming Growth Factor-β (TGF- β). Among these growth factors, EGF has been shown to play an important role in the repair processes after injury [15] by promoting cell proliferation and collagen synthesis in acute wounds [5, 8, 15]. EGF has also been demonstrated to attract fibroblasts and inflammatory cells to wounded sites, as well as regulate the migration, proliferation and differentiation of fibroblasts [16, 17, 19-21]. Clinical trials for human chronic wound therapeutics have also illustrated that the addition of topical EGF shortens ligament healing time [15]. Further, both in vitro and in vivo studies have shown that EGF can accelerate and improve wound healing by binding to the EGF receptor (EGFR) and triggering subsequent EGFR signaling.

The EGFR, as a Receptor Tyrosine Kinase (RTK) [22], is a globular protein of 170kDa and 1186 amino acids. RTKs are transmembrane receptors with an extracellular portion on the cell surface for ligand binding, and an intracellular, cytosolic portion used for activation of internal signaling cascades. The cytosolic portion contains tyrosine residues that are targets for the tyrosine kinase portion of the receptor, as seen in **Figure 1.1A**. EGFR is activated when the EGF ligand binds to its extracellular portion, and causes phosphorylation, as illustrated in **Figure 1.1B** and **Figure 1.1C**.

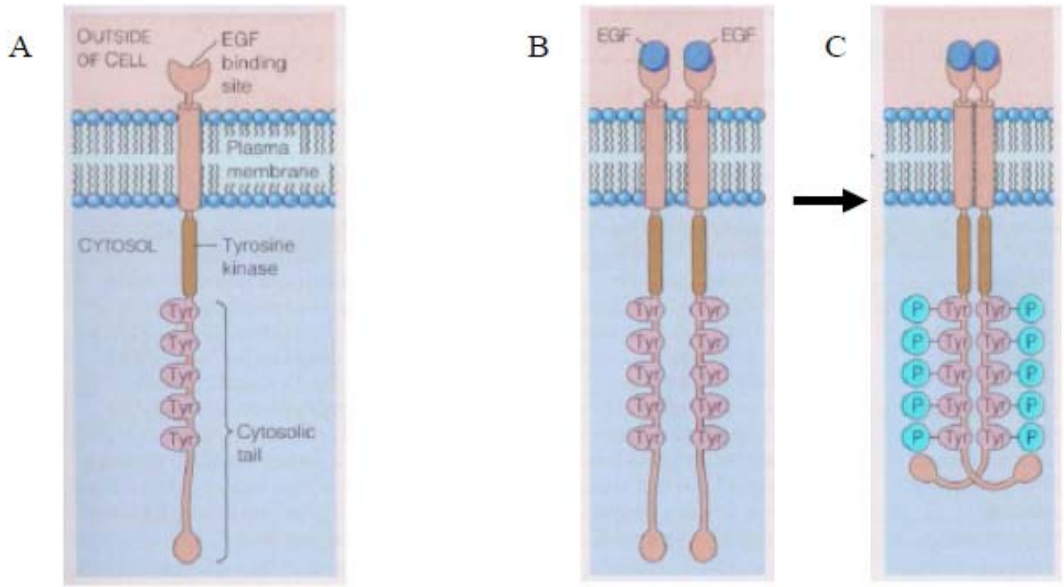

Figure 1.1: The structure and activation of an EGF receptor tyrosine kinase. The EGF receptor is a transmembrane protein, composed of an extracellular part and an intracellular part (A). The extracellular portion of the receptor binds to ligands. Inside the cell, a portion of the receptor has tyrosine kinase activity (B). The remainder of the receptor contains a series of tyrosine residues (Tyr) that are substrate for tyrosine kinase. The activation of receptor tyrosine knases starts with the binding of EGF, causing receptor aggregation and phosphorylated (C). (Borrowed from [22])

Once the EGF ligand binds to its corresponding RTK receptor, i.e. EGFR, signal transduction is initiated. Receptor tyrosine kinases initiate signal transduction cascades via multiple pathways, including the Mitogen-Activated Protein Kinase (MAPK) pathway, Phosphoinositide-3 Kinase (PI3K) pathway and Phospholipase C-γ (PLC-γ) pathway [22-26]. Upon RTK phosphorylation, cytosolic proteins activate a second messenger pathway, such as the well-known Ras pathway, to transduce the extracellular binding signal within the cell. Ras is particularly important for the regulation of growth, proliferation, and migration of ligament fibroblasts [22].

The activation of EGFR affects cytoskeletal organization, integrin-mediated cell/substrate linkages and intracellular force generation, and eventually triggers cell

migration [27]. As a result, EGF is targeted in this work as a means to promote ligament repair via enhanced fibroblast migration to the wounded sites.

1.3 Cell migration

Different cell types exhibit distinct patterns of migration. For example, sperm are known to swim [28], while bacteria swarm and glide [29]. Blood cells are observed to roll [22], while fibroblasts in general crawl [30]. Fibroblast migration is composed of four steps [22, 30]: 1) Extension of a protrusion; 2) Attachment of the protrusion; 3) Translocation; 4) Detachment, as seen in **Figure 1.2**. During this migration, cells first produce two types of protrusion at the leading edge: The thin sheet-like cytoplasm called lamellipodium and the slender cytoplasm called filopodium (**Figure 1.2A**). The cytoplasmic protrusion attaches to a substrate and forms new adhesive sites at the leading edge (**Figure 1.2B**). Afterwards, the cells are pulled forward for translocation via contractile forces (**Figure 1.2C**). Simultaneously, the contraction at the trailing edge releases the cells from attachment at the trailing edge. In some events, this detachment at the trailing edge could cause some part of cells broken from the cell body (**Figure 1.2D**).

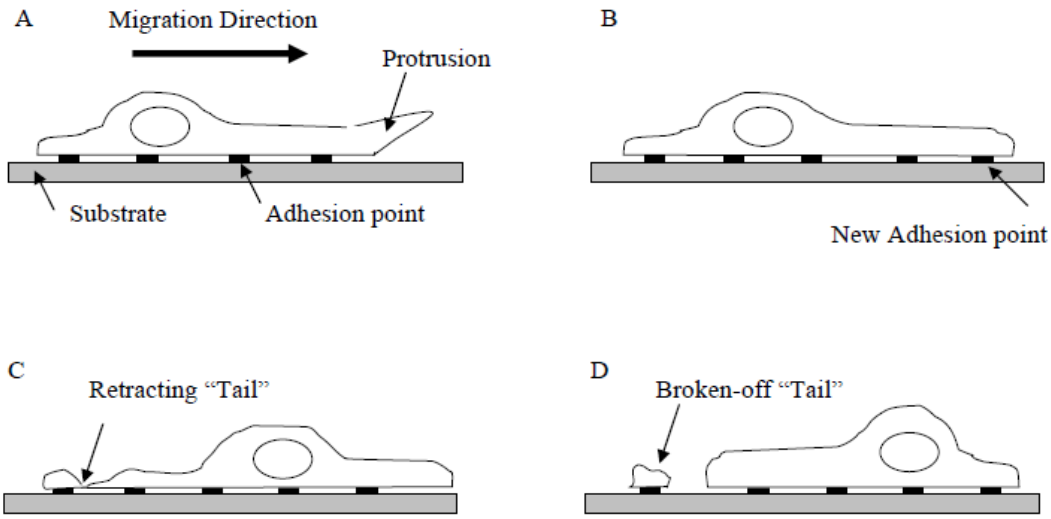

Figure 1.2: Schematics of crawling-like cell migration. When a cell migrates on a substrate, the leading edge of the cell forms protrusion (A). The cytoplasmic protrusion attaches on substrate and form a new adhesion point (B). Cells translocate with detachment at the trailing edge (C). Part of trailing edge is broken from the cell body (D). (Borrowed from [22])

1.4 Effects of exogenous stimuli on cell migration

Cell migration is complex, and largely regulated by intracellular activity and interactions among cells, exogenous stimuli and substrates. Exogenous stimuli such as electrical field [31], mechanical forces [32] and chemical reagents [23] are well known to affect cell migration. Mechanical stress and growth factor are largely studied in clinical applications and laboratory research since they play important roles in enhancing wound healing.

1.4. A Mechanical stress and substrate stiffness

Mechanical stresses can guide cell migration and enhance cell motility via mechanotransduction. The mechanotransduction from ECM to fibroblast cells and fibroblast to fibroblast have been demonstrated to modulate fibroblast migration,

adherence, and synthesis or degradation of ECM [10]. Fibroblasts are able to sense force-induced deformations (strains) in their ECM and respond to mechanotransductions [11]. Additionally, researchers indicated that surface integrins, i.e. transmembrane proteins interconnecting ECM and cells, could also act as 'strain gauges', triggering intracellular signal pathways in response to changes in mechanical stress [11]. When fibroblasts migrated within ECM, integrins regulated attachment and detachment of cells within the ECM [7, 22, 33], which therefore could largely affect cell motility. Stiffness of substrates where cells are attached can also affect cell migration, as researchers have illustrated that high density of collagen ECM can cause low cell motility [34]. The study of mechanical force-induced cell migration may provide clues to help understand ligament healing and methodologies with which to enhance ligament healing.

1.4. B Growth factor gradients

As fibroblasts migrate in response to growth factors, various researches have shown that both growth factor concentration and growth factor concentration gradient can affect cell migration. When growth factor concentration around cells increases, cell motility is enhanced. However, studies have also demonstrated that such cell motility is growth factor concentration-dependent [16], as higher concentration could down regulate receptor binding [24, 35] and inhibit fibroblast migration [5]. Growth factor concentration has been reported to affect distribution of low-affinity EGF receptor and high-affinity EGF receptor [36]. This suggests that a threshold of growth factor concentration may exist to regulate cell migration.

While growth factor concentration was found to increase cell motility, it was also reported to reduce directionality of cell migration [23, 27]. By contrast, growth factor gradient promotes directed cell migration while increasing cell motility [23]. Fibroblasts have been observed to polarize as a way to sense ligand gradient when stimulated during cell migration, as shown in **Figure 1.3A** and **1.3B**. However, other cells, such as neutrophils, are not obviously mobilized to localize signaling molecules and possess specific spatial sensing mechanisms for directional sensing [23]. Fibroblast cells are able to sense steep and shallow ligand gradients with migratory responses. Growth factor gradients were reported to enhance receptor sensitivity at the leading edge, when cells were polarized [37-39]. This could therefore cause higher chemoattractive differences between the leading edge and the trailing edge, which eventually increases cell motility and promote directional cell migration. A small difference of ligand concentration around the cell microenvironment could then be augmented due to the cellular asymmetrical sensitivity and may stimulate cell function for a long period of time. The receptor occupancy plays an important role in regulating cell migration [40]. The receptor occupancy difference of as little as 5% between the front and the back of a cell could cause the cell to generate internal response and may eventually induce persistent cell migration [23, 37].

Ligand gradient profiles have been recently reported to distinctly affect cell migration. Linear ligand gradients enhance cell migration as an asymmetric ligand concentration difference between the leading edge and trailing edge occurs. Non-linear gradients have shown to stimulate cells with higher cell motility than the linear gradients

[41]. Additionally, parabolic and exponential gradients have been generated to investigate how different gradient profiles affected cell migration [42, 43].

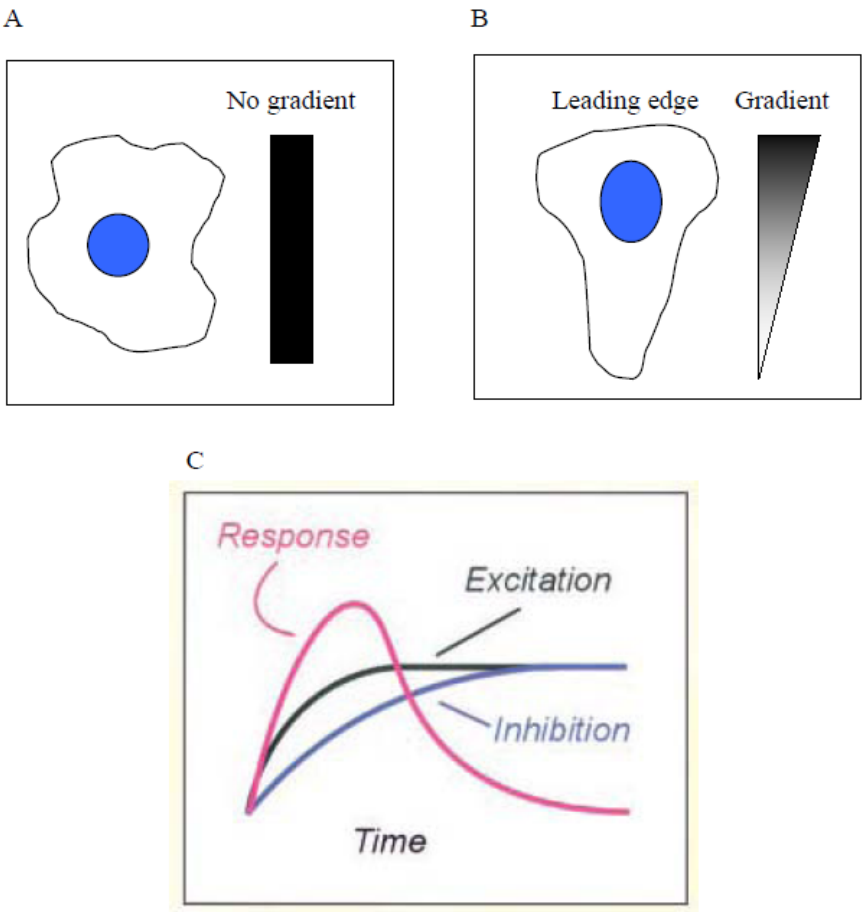

Figure 1.3: Schematics of cell polarization and intracellular activity in response to ligand stimulation. Cells do not exhibit polarized morphology when uniform ligand concentration is used (A). When ligand concentration gradient is formed, cells display polarized morphology with leading edge faced higher ligand concentration (B). Ligand-generated excitation and intracellular inhibition increase over time and reach balanced (C). The net response varies over time. (Borrowed from [23])

The time that ligand gradients are imposed on cells plays an important role in regulating intracellular activity, and therefore affects cell migration. This is because the equilibrium of the binding between ligand and receptor is dynamic, and also time-

dependent [40]. As the time of stimulation via ligand gradients increases, cell response, such as migration, is observed to be less active [23, 37]. The local excitation global inhibition (LEGI) model attempts to explain this phenomenon [37, 44], as illustrated in **Figure 1.3C**. Based on this model, excitation from ligand gradients increases over time, while inhibition from intracellular activity, such as receptor endocytosis, also increases but slowly over time. Therefore, cells are initially stimulated to migrate but exhibit less active as time increases. Cells may finally stop directional migration when excitation and inhibition are balanced. Transient-state ligand gradients were also found to affect cell migration [43, 45, 46]. However, the transient gradients appeared to have fewer effects on cell migration than the steady-state gradients. One of the possible explanations is that the binding between integrin and substrate was weakened [47] when transient ligand gradients existed. By contrast, steady-state gradients provided continuous stimulation on cells, which was observed to enhance cell attachment [39, 48]. However, study of how transient ligand gradients affect cell migration has not yet been widely reported.

1.5 Traditional migration assays

In order to study growth factor-induced migration, various bioassays and methodology have been developed and utilized. Many conventional bioassays examine cell migration by counting the numbers of cells that accomplish a given translocation [16, 49, 50], while others investigate migration using real-time imaging [51, 52]. Some bioassays use structural proteins, such as matrigel and collagen, as an ECM-like medium to deliver ligands and examine cell migration in 3-D ECM [53], while others use liquid-state media to transport ligands and study cell migration on a 2-D substrate [54]. Some

assays focus on the study of ligand gradient-induced cell migration [55], while others only apply uniform ligand concentration upon cells [52].

1.5. A Boyden assay

A large amount of chemotaxis research has been performed using a system called the modified Boyden chamber or transwell assay [16], which was originally developed by Stephen Boyden in 1962 [49]. Here, researchers count the number of cells that migrate though a thin, collagen-coated membrane as induced by the diffusion of chemoattractant molecules normal to the membrane [56, 57], as illustrated in **Figure 1.4A**. Despite the wealth of data obtained using Boyden chambers, results are limited to comparative, time-averaged data in response to ligand concentration gradients that are roughly underestimated as one-dimensional. In fact, how the cells migrated inside the Boyden chamber through the porous membrane can not be observed. Hence, whether, or how, cells changed their morphology and/or produced extracellular matrix proteins can not be answered using the assay.

1.5. B Zigmond assay

Another commonly-used migration assay is the Zigmond assay, which was developed by Sally Zigmond in 1977 [45, 58]. This bioassay enables researchers to visualize cell migration, but is limited to large sample size. The Zigmond assay is composed of two parallel channels that are etched into a glass slide and separated by a ridge, as seen in **Figure 1.4B**. A coverslip where cells are cultured onto is inverted and then placed on the glass slide. Ligand solution and culture media are subsequently input

into the source channel and the sink channel, respectively, to generate ligand concentration gradient. Cells are visualized to migrate on the coverslip from the source region toward the sink region. Gradients vary over time and display a pseudo-steady-state in only 1 hour. This time-dependent ligand distribution along the coverslip further causes difficulties to quantitatively measure ligand concentration and gradient across each cell. Moreover, this assay lacks flexibility to modify the ligand gradients that are already established during experiments. Since the assay is open, evaporation is another inevitable problem to limit its further applications.

1.5. C Dunn chamber

In 1997, the Dunn chamber was designed by Graham Dunn to improve upon the Zigmond assay with minimum solution evaporation [59, 60]. It consists of two concentric, circular wells manufactured from glass and an annular ridge between these two connected circular wells, as shown in **Figure 1.4C**. Although evaporation is largely reduced, it has similar limitations as the Zigmond assay, i.e. it cannot allow quantitative measurement of ligand gradients at different points over time.

1.5. D Micropipette

Another method widely used for generating ligand gradients in vivo and in vitro [37, 61] is to deliver ligand through a micropipette, as shown in **Figure 1.4D**. Here, a ligand-containing micropipette is injected into a tissue or cells that are cultured on a plate, and release the ligand radically. This method is straightforward, but is highly irreproducible and uncontrollable, as the inject flow rate, inject angle and size of the

micropipette tip can largely affect ligand gradient generation. A small environmental variation, such as evaporation or vibration, can cause forced fluid flow, i.e. convection, which distorts the ligand gradients and lead to unpredictable ligand transport.

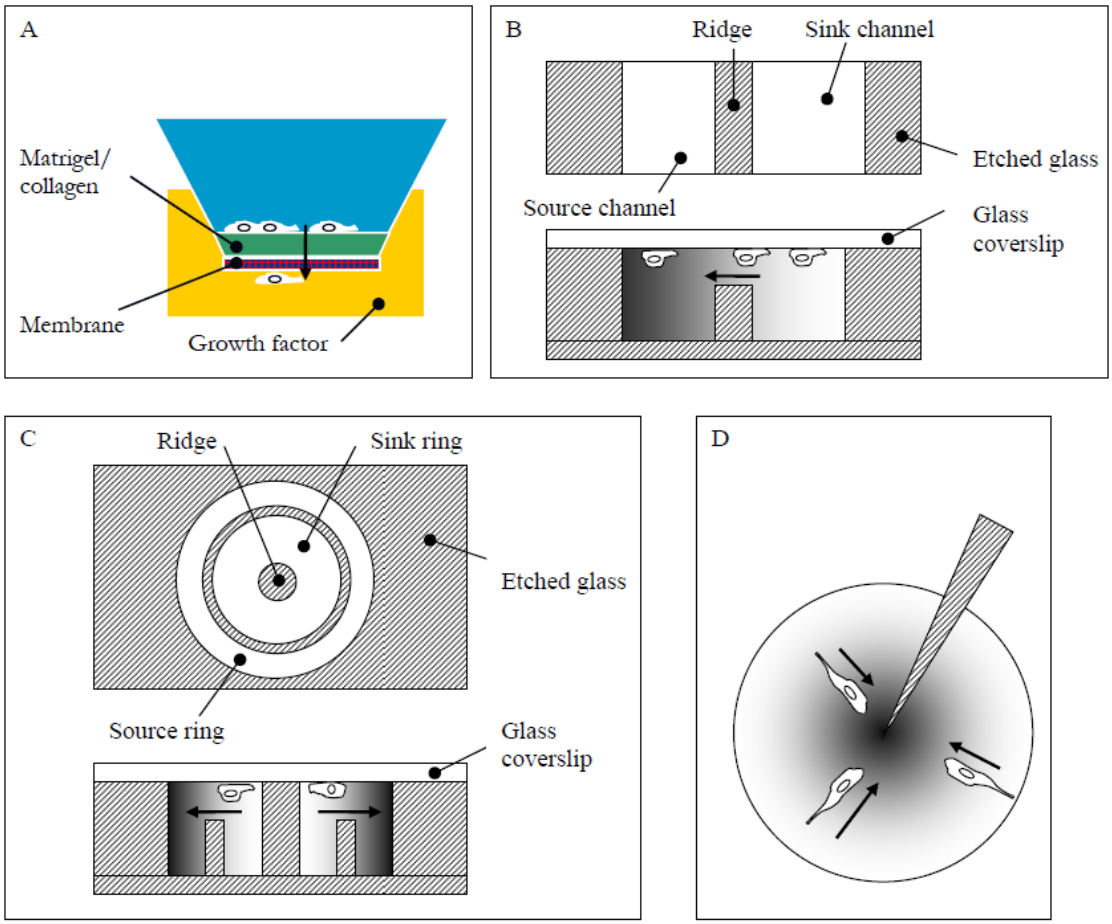

Figure 1.4: Schematics of Boyden assay (A), Ziomond assay (B), Dunn chamber (C) and micropipette-generated gradient assay (D). Arrow points to the direction of cell migration. Schematics are not drawn to scale. (Borrowed by [49, 58, 59, 61])

1.5. E Scratch assay

The conventional scratch wound assay has also been widely used to mimic in vitro wound healing [62, 63]. As seen in **Figure 1.5**, after cells are cultured on a slide or

petri dish, cells are scratched from the center using a pipette tip to simulate a wound site. Culture media with growth factors is usually applied into the assay to stimulate cell migration toward the center of the wound. This method allows real-time observation of cell migration in response to growth factors as a mimic of cell migration in wounded environment. However, precise growth factor gradients are difficult to generate across cells using this method. Therefore, it only examines cell migration in uniform growth factor concentration.

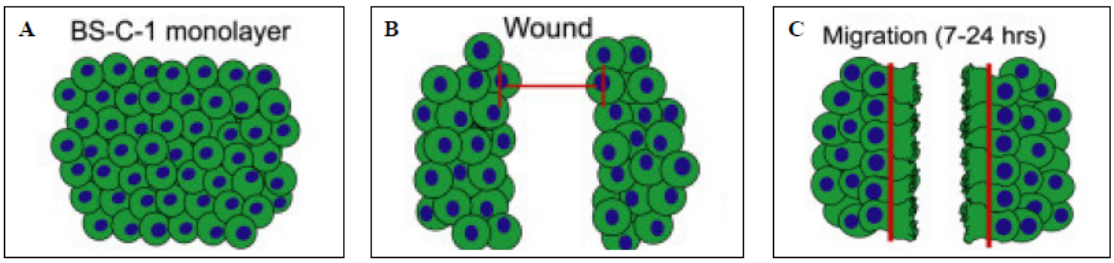

Figure 1.5: Cartoons of BS-C-1 cell migration using scratch wound assay. BS-C-1 cells were cultured on a coverslip (A). A scratched wound was produced at the center of the coverslip (B). Cells migrated toward the center in 7-24 hours (C). Vertical red lines illustrated the reference borders where the scratched wound was initially produeced. (Borrowed from [62])

These traditional migration assays provide straightforward and user-friendly methods with which to examine growth factor-induced cell migration. However, the assays either lack quantitative measurement of ligand concentration and concentration gradient in real time, or fail to establish a stable microenvironment with which to observe cell migration upon long periods of time. Hence, a novel bioassay is needed to provide accurate and quantitative platforms that allow investigation on how different ligand concentration gradients in transient-state and steady-state and ligand gradients of linear and non-linear profiles affect cell migration.

1.6 Microfabricated devices

Microfabrication [64-66], as a technology to fabricate devices in micrometer size, enables bioassay design and development in micro-scale, which greatly benefits the study of cell migration with precise control of ligand gradients. It also provides feasibility to generate distinct ligand gradient patterns to meet various biological research needs. Microfabrication allows real-time single-cell analysis in microenvironment and quantitative measurement of ligand gradients when incorporated with computer and microscopy techniques. Single-cell analysis using microfabricated devices provides a close investigation on how individual cells migrate in response to exogenous stimulation, which provides a platform with which to investigate cell migration in a cellular to molecular level. Using microscopy and numerical computation, spatiotemporal profiles of ligand gradient around single cells can be examined and predicted, which is also greatly beneficial for quantitative cell migration study. Microfluidic devices [65, 67] and micropattern technology [68, 69] have been largely used in establishing ligand gradient for cell migration study. Both methodologies can generate quantitative ligand gradients with advantages of high throughput and low cost, while the traditional cell migration assays cannot.

Micropattern systems use microfabrication technology and elastomeric stamping to print chemicals on micron-sized areas of a substrate surface. By printing ligands with different spacing and size, a non-continuous ligand gradient is generated along a cell length, as seen in **Figure 1.6**. Using micropatterning, both linear ligand gradients and non-linear ligand gradients can be generated on the substrate. Micropatterning is straightforward to fabricate and require minimum equipment to maintain a fluidic

environment. However, the gradients generated using micropattern methods are not continuous and leave areas where cells are not in contact with ligands. Therefore, micropatterning cannot provide precisely quantitative information of ligand gradient along the cells, which heavily affects the study of ligand gradient-induced cell migration. Moreover, the ligands micropatterned on the substrate may not exhibit enough biological function or be denatured when bound on solid substrates [66]. Further, micropatterning does not enable study of cell migration within 3-D ECM.

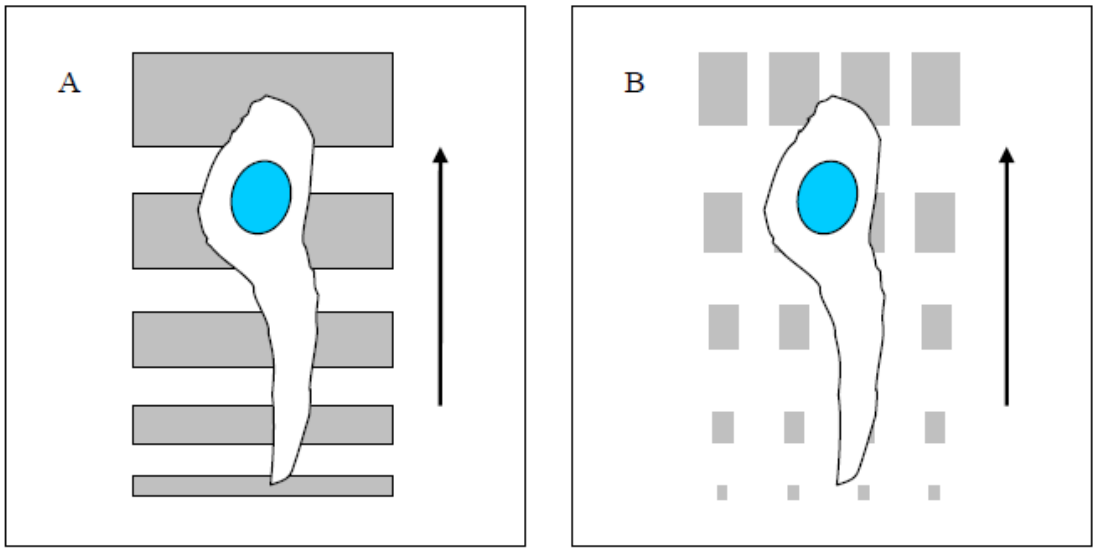

Figure 1.6: Schematics of micropatterned devices used for cell migration study. Large (A) and small (B) printing spacing and size are used to approximate continuous ligand gradient at cellular level. Arrows point to cell migration direction. (Borrowed from [70])

Microfluidic devices utilize micro-scale fluid flow to deliver ligand to cells, which have been increasingly applied in numerous cell migration studies, such as tissue development [71], inflammation [72], wound healing [73] and cancer metastasis [74], due to its flexibility to design distinct ligand gradient patterns. Its advantages of low cost, high throughput, and flexibility to design ligand gradient from simple single

microchannel to complex multi-layer microsystem have motivated researchers to develop different novel microfluidic devices for various biological validation.

The ligand gradients generated by microfluidic devices can be established in short times, at the order of minutes, and last for hours. Due to the relative short time period of stable ligand gradients exposed to cells, these devices are majorly used to examine fast-responding cells, such as neutrophils and bacteria.

Steady-state gradients provide a quantitative platform to study cell migration in response to ligand concentration and ligand gradients in a long period of time. This benefits the studies that require longer-time observation, such as wound healing and cancer metastasis. Moreover, steady-state gradient generation allows examination of different ligand gradient patterns and time imposed upon cell migration. Computational models often accompany with the microsystems to predict the spatiotemporal gradient profiles, which helps to quantitatively measure the microenvironment during cell migration. Fluid streams, hydrogels, membranes, and interconnected microfluidic channels are commonly seen in the microfabrication of these steady-state gradient systems.

1.6. A Nanopore microfluidic devices

A microdevice, called the Nanopore microfluidic device [75], uses porous membranes to minimize loading effects, as illustrated in **Figure 1.7A**. Porous membranes with 200-nm pores are placed in between 3 PDMS layers to eliminate bulk flow when loading solutions in the source chamber and the cell chamber. Since the bulk flow is largely reduced, ligand could be delivered to cells via diffusion. It takes hours to form a

stable ligand gradient via this method, but it cannot last over 24 hours. This microfabricated device enables quantitative measurement of ligand gradient and microscopic observation of cell migration. However, the chamber sizes are not designed large enough to maintain constant ligand concentration during given experimental times, and no extra equipment is used to supply ligands and remove waste solutions. Therefore, any volume unbalance between the source chamber and the sink chamber can cause hydraulic pressure difference within the cell-cultured microchannel, which then generates unpredicted bulk flow. Ligand concentration in the source chamber also depletes, which causes time-dependent gradients exposed to cells.

1.6. B Microvalved microfluidic devices

Elastomeric microvalves [76] are controlled by vacuum pressure, and are designed to manage establishment of ligand gradients, as shown in **Figure 1.7B**. Once the microvalve is pulled to open, ligand solution diffuses from the source chamber into the cell-cultured chamber and then triggers cells to migrate toward the source chamber. This microdevice does not require sophisticated equipment for operation, and provides temporal control over ligand gradient initiation. However, the diffusion from the cell-cultured chamber to the source chamber is a complex unstable 3-D process, and practically difficult to measure and model. Therefore, the microvalved microfluidic device is best suited for short-term experiment without need of quantitative ligand gradient measurement.

1.6. C K-K chamber

The KK-chamber, designed by Shiro Kanegasaki and Yuji Kikuchi [77], is another design that uses connected fluidic chambers to minimize the uncontrolled bulk flow within the micochannel, as shown in **Figure 1.7C**. This device can establish ligand gradients within the entire microchannel for less than 5 minutes, and only maintain relatively stable ligand gradients for 1 hour. After that, ligand concentration in the source region depletes, which then induces transient ligand gradients. Since the ligand supply and waste solution disposal within the device are well controlled by sophisticated equipments, and the aspect ratio of the microchannel is high enough to approximate 1-D transport, the transient ligand transport within the microchannel can be modeled and precisely predicted. Therefore, the KK-chamber provides a platform for quantitative study of transient ligand gradient-induced cell migration.

1.6. D Microfluidic multi-injectors

The microfluidic multi-injector [78], as illustrated in **Figure 1.7D**, is a design to deliver ligands using microfluidic injection. Accompanied with microvalves, this microdevice can control the time to initiate ligand gradients. Ligand gradients are formed radically in the cell-cultured reservoir after ligand solution is ejected from the orifice. However, the ligand gradients generated by multiple orifices can only maintain stead-state for about 3 hours. Therefore, this device is best suitable for cell migration study using transient ligand gradients. Moreover, the overlapped ligand gradient distributions generated from the multiple micro-injectors increase the difficulties to model the transient ligand gradients within the reservoir, and lead to inaccurate prediction.

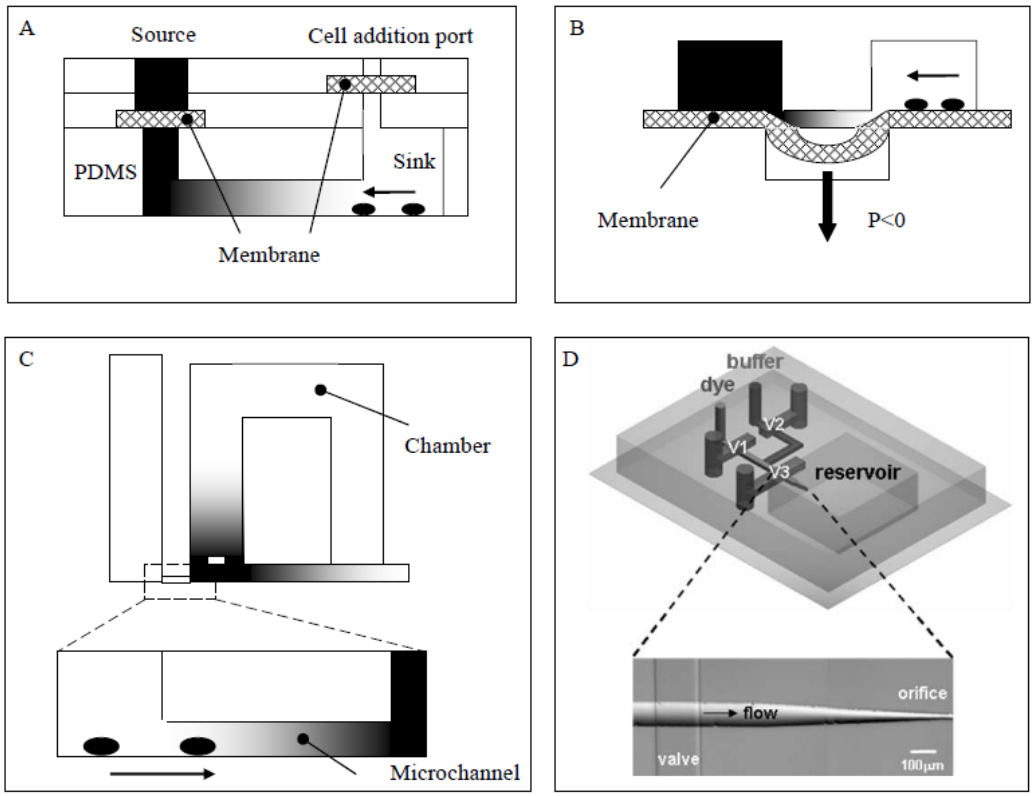

Figure 1.7: Schematics of different microfluidic devices: Nanopore microdevice (A), Microvalved microdevice (B), KK-chamber (C) and Microfluidic multi-injector (D). V1, V2 and V3 represent microvalve. Arrows point to cell migration direction. (Borrowed from [75-78])

1.6. E Parallel-flow microfluidic devices

Researchers have used laminar fluid flow to deliver ligands to cells and hence generate ligand gradients across cells. In the method of parallel-flow, ligand solution and media solution flow parallelly through a channel, while ligand diffusion occurs perpendicular to flow direction. As shown in **Figure 1.8A**, when ligand solution and ligand-free medium were injected into the channel, ligand molecules diffused from the ligand solution to the medium solution at a direction perpendicular to the flow direction. This method enables stable ligand gradient for long periods of time on the condition of continuous solution supply. However, ligand gradients are only formed in a small region

at the interface along the channel and more than half of the channel does not exhibit ligand gradients. Therefore, the distance of cell migration is largely limited by the width of the channel. Meanwhile, cells migrate with flow impact. The shear stress caused by the flows may also induce cell migration, which may overlap the effect of ligand gradient and therefore cause experimental bias. Additionally, in order to maintain steady-state ligand gradients, solutions must be supplied continuously, which requires additional equipment and large amounts of solutions used.

Another microfluidic device using parallel-flow has been developed to provide longer distances for cell migration by premixing ligand solution and medium solution delivered to cells [79]. As seen in **Figure 1.8B**, ligand solutions and medium solution are premixed in the small "z"-shape microchannels before they enter the main channel. The mixed solutions flow into the main channel with multiple streams of different ligand concentrations. Ligands diffuse perpendicular to the flow direction and ligand gradients along the width of the main channel. One of the major advantages using this microfabricated device is that it can generate different ligand gradient pattern, from linear gradient to non-linear gradients, by controlling the initial ligand concentration and flow rates at the inlets. However, it also requires extra equipment and large amount of ligand solution and medium to maintain continuous supply, and the inlet flow rate has to be carefully chosen to minimize shear effects on cell migration. Moreover, this microdevice limits its applications to cell migration study in 2-D, as ligand transport cannot generate 3-D gradients perpendicular to flow direction by means of parallel-flow through ECM.

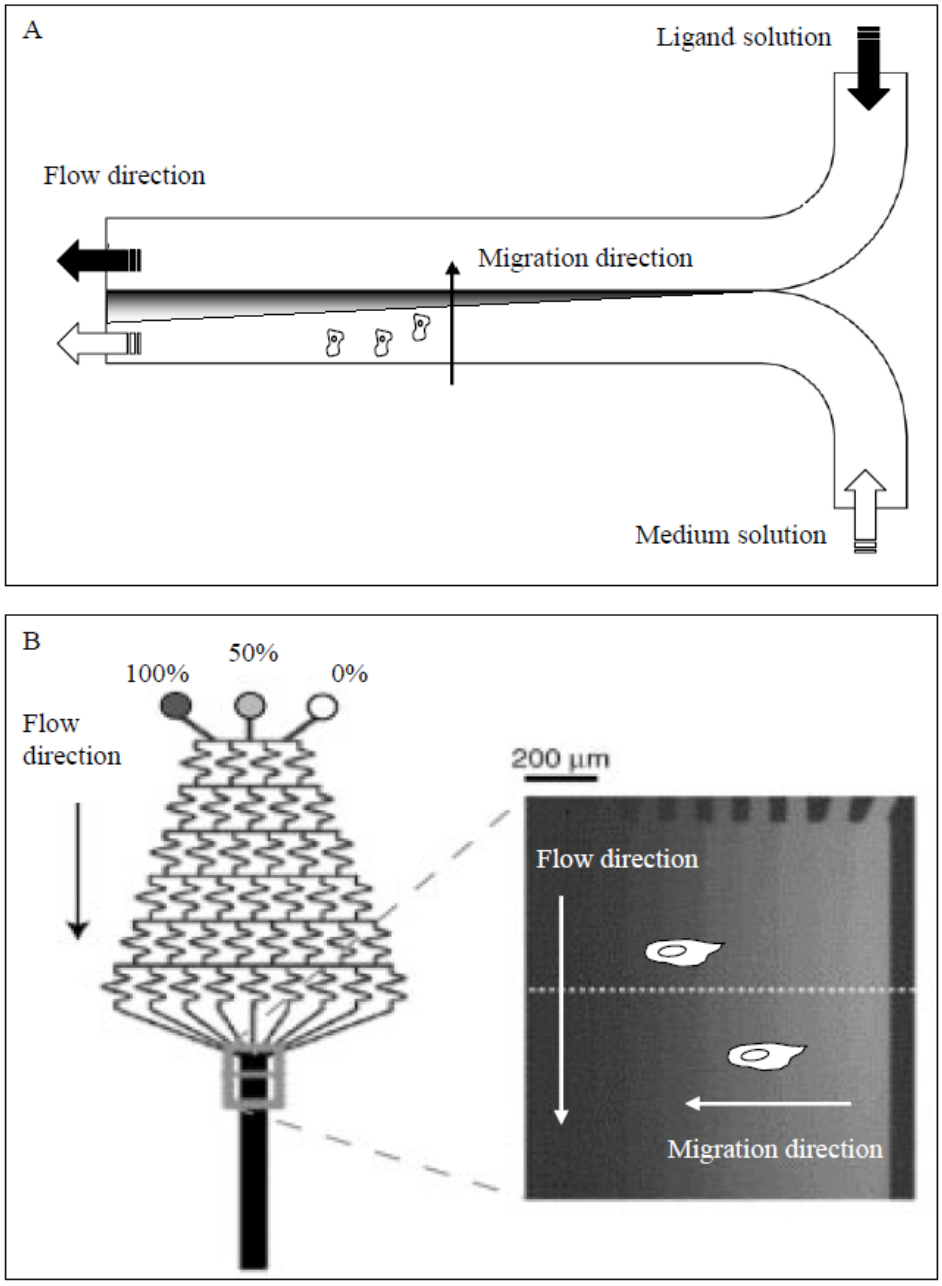

Figure 1.8: Schematics and microscopy image of T channel (A) and premixer gradient generator (B). In the T channel, ligand solution and medium solution were injected into the channel simultaneously. In the premixer gradient generator, solutions containing maximum ligand concentration, denoted as 100%, half of maximum ligand concentration, denoted as 50%, and culture medium (no ligand), denoted as 0%, were injected into the device separately. Arrows point to flow direction and cell migration direction. (Borrowed from [79, 80])

1.6. F Hydrogel microfluidic devices

Porous material, including hydrogel and membrane, is often used to minimize flow convection when loading solutions into microchannels. A common strategy is to place porous material in the stream path between the source chamber and the sink chambers where convection are largely generated. Once the convection is largely reduced, delivery of ligands toward cells could occur with only diffusion. In that case, both experimental examination of ligand transport and computational models are feasible to perform and provide reliable data to validate experiments and predict spatiotemporal ligand delivery. As illustrated in **Figure 1.9**, a hydrogel was placed into the microdevice between the source reservoir and the sink reservoir. Bulk flow, i.e. convection within the microdevice, was largely reduced so that ligand diffused within the hydrogel and formed a linear ligand gradient along the hydrogel. The ligands within the hydrogel also diffused vertically into the microchannel, which eventually reaches a steady-state linear gradient along the microchannel. This straightforward method to generate linear gradients requires no sophisticated equipment to maintain the stable ligand gradient within the microchannel. However, the major limitation of using this microdevice is that it lacks dynamic control over the ligand gradient and feasibility to form a complex ligand gradient, i.e. non-linear gradient, to meet different needs in biological systems. Moreover, using hydrogels may affect imaging resolution, since the hydrogel has relatively low optical transparency compared to glass or PDMS. Additionally, this method requires relatively large amount of reagents, as most of them are distributed within the hydrogel and only a small amount of ligands are delivered to the microchannel and stimulate cells.

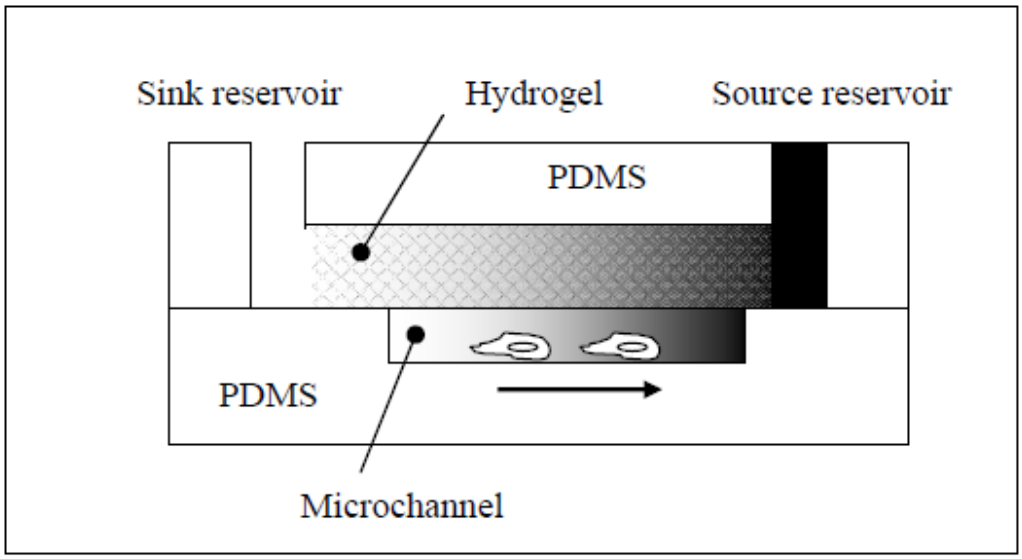

Figure 1.9: Schematics of hydrogel gradient generator. Hydrogel was sandwiched between two PDMS layers. A microchannel was placed under the hydrogel. Arrow points to the cell migration direction. (Borrowed from [81])

1.6. G Microchannel arrays

Instead of using the low optical transparent hydrogel as a media to reduce convective flow, arrays of small microchannels are also used to minimize fluid flow. A small microchannel is characteristic of high shear stress and high surface tension, which can reduce flow with high friction. As shown in **Figure 1.10**, flow through the microjets arrays, measured about of 1.5 µm x 1.5 µm in cross-section for each microchannel, was largely reduced at the entrance of the chamber before it entered the cell cultured chamber [82]. This resulted in a pure diffusion of ligands across the chamber. The linear ligand gradients reached steady-state in 10 minutes and could be maintained stable for long period of time. The open-surface chamber also facilitates cell culture with sufficient gas supply. This device also allows ligand gradient establishment within 3-D ECM. However, the microdevice cannot generate complex ligand gradients, i.e. non-linear ligand

gradients. Therefore, this limits its further biological applications. Additionally, the microdevice requires extra equipment to continuously supply solutions, and particular care when loading solutions, as the microchannel array is easy to clog.

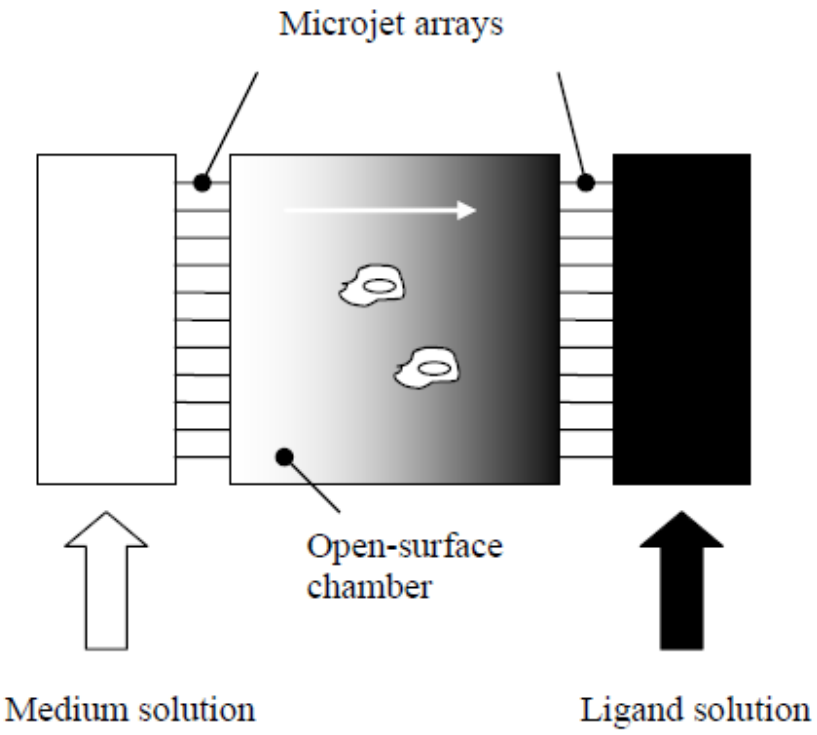

Figure 1.10: Schematics of Microject device. Microjet arrays are connected the region of ligand solution and the region of medium solution. Solutions were injected into the open-surface chamber and generated with gradient within the chamber. White arrow point to the cell migration direction. (Borrowed from [82])

Microfabricated devices have been designed to meet various needs of biological studies. Each successful microfabricated device has its unique advantages and distinguished functions to solve particular problems. Some microdevices have been designed to investigate cell migration in 2-D environment, while some others were developed to help understand cell migration in 3-D ECM. As steady-state gradients have been widely studied, transient gradients are also of keen interest. Ligand gradient profiles

have been recently reported to affect cell migration differently. However, such study has not yet been widely investigated. In our research, we seek to develop a new type of microfluidic device that will enable us to image cell migration in real-time under different ligand gradient profiles and manipulate chemotactic response via 2-D and 3-D microenvironments.

1.7 The bridged μlane system

We have developed a microfabricated system that provides a user-friendly and reliable platform to study cell migration. Its challenges lay in: 1) A suitable size for cell culture and single-cell analysis in microenvironment; 2) Biocompatible property to culture cells and maintain regular cell activity; 3) Feasibility to perform surface coating with different biocompounds; 4) Feasibility to deliver ligand toward cells, generate different ligand gradients across cells and perform cell migration; 5) Possibility to maintain steady-state ligand gradient in a long period of time; and 6) Ability to examine and predict local ligand gradients at any cell position over time.

Our system, called the bridged μLane System, contains two layers of biopolymers. The top layer is composed of bridge channel while the bottom layer consists of a cell-cultured microchannel with a cross-sectional size of 100 μm x 100 μm, as seen in **Figure 1.11**. The size has been tested to ensure cell viability, while minimize shear effects on regular cell activities during solution loading. PDMS is used as a biomaterial for microfabrication due to its known biocompatibility and high permeability of gas and nutrient. We also use glass as a substrate for biocompound coating, as it is low cost and has been largely used to coat surface with different ECM such as collagen and fibronectin.

We deliver ligands toward cells via microfluidics. By controlling the bulk flow within the microchannel, we will be able to design different ligand gradients across cells, which allows observation of single-cell migration in different experimental conditions. In order to maintain stable ligand gradients within the microchannel, large chamber volumes are used to keep ligand source concentration and sink concentration constant. Further, the source chamber and the sink chamber are connected to eliminate hydraulic pressure difference within the microchannel due to chamber volume difference. This largely reduces bulk flow and enables steady-state gradients maintained in long periods of time. The ligand transport within the microchannel is accurately predicted using convective diffusion models. Hence, the spatiotemporal profiles of ligand concentration and gradients for individual cells within the microchannel length are achieved to facilitate cell migration study.

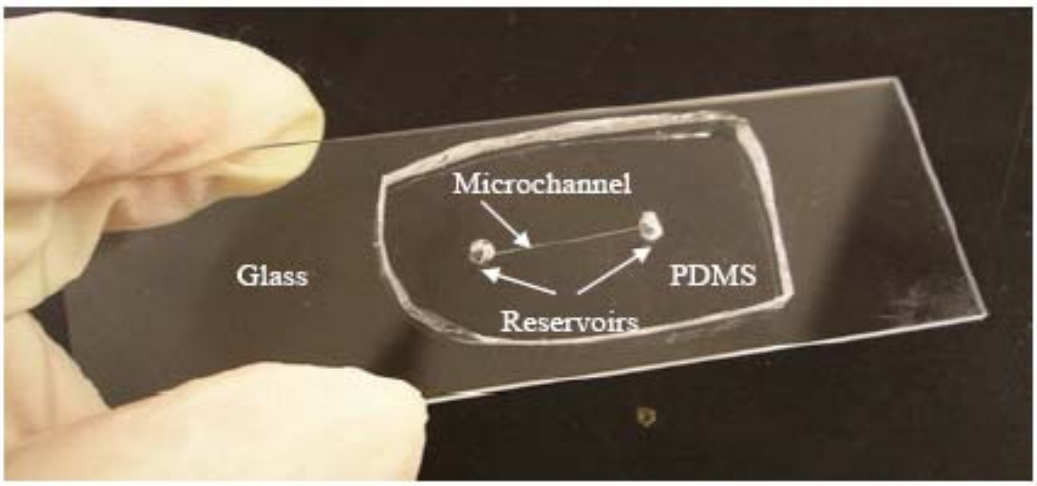

Figure 1.11: Image of microchannel fabricated in PDMS. The PDMS of the microchannel with two reservoirs was bound onto a glass slide.

The bulk flow, caused by inertia during solution loading, is laminar flow with a low Reynolds number of less than 10^{-3}, and a Peclet number between 10 and 50 when

EGF (MW: 6kDa) and Dextran (MW: 10kDa) are used. Ligand transport within the microchannel can be approximated to be 1-D due to its large ratio of the microchannel length to its width. Additionally, our microsystem can also examine cell migration at transient ligand gradients and non-linear steady-state gradients, as well as cell migration within 3-D ECM.

This microsystem does not require sophisticated equipment to maintain gradient status. Moreover, our microsystem might provide a new angle to study cell migration in wound healing, as growth factor gradient may be non-linear and transient during the complex tissue repair [46, 83]. The imaging techniques and computational modeling allow us to quantitatively measure local ligand concentration and gradients, which can greatly benefit cell migration study as the traditional bioassays are not able to detect.

1.8 Overview

In this dissertation, we discuss the development of our microfabricated system based on the effects of microfluidics on cell-cell communication, cell-ECM interaction ad cell morphology. We utilize all of these data in the experimental design and prototype testing of our microdevices. In Chapter 2, we discuss how shear stress affected the MCL-derived fibroblast morphology, the intercontacts between cells, and the interconnection between cell and collagen. We found that shear stress increased cell-cell and cell-ECM interconnections. We used this to influence the design of our microsystems. In Chapter 3, we discuss how different magnitudes and time scales of shear stress were used to affect cell-cell communication, 3-D cell-ECM network, and collagen structure. Results show that shear stress enhanced cell-cell communication via gap junctions and cell-cell

contacts within collagen network, and also suggested that there could be an optimal loading method to seed cells into microenvironments with minimum shear effects. In Chapter 4, the design and microfabrication of a novel microfluidic device, the bridged μlane system, and its usage in generating steady-state Dextran gradients are discussed. The Dextran transport within the entire microsystem was also modeled. The diffusion coefficient of Dextran measured using the mathematical and experimental methodology was in line with published values, which demonsrated the feasibility and realibilty of reagent gradient establishment via our microsystem. In Chapter 5, the bridged μlane system was used to generate steady-state EGF gradients. Cell migratory responses, including cell motility and the number of motile cells, in response to the steady-state EGF gradients are discussed. Here, we found that cell migration was EGF gradient-dependent and that EGF concentration and gradient were both important to regulate cell migration. In Chapter 6, cell migration in response to transient EGF gradients was reported to exhibit lower cell motility than steady-state gradients. Additionally, the transient EGF gradients were observed to have fewer effects on cell morphology change. Lastly, in Chapter 7, we discuss the development of microfabricated systems, present future experiments of our investigation in cell migration, and consider using our microdevice to examine cell migration via intracellular signaling cascades.

1.9 Abbreviated materials and methods

This study has utilized various materials and methods from biological examination to mechanical methodology to investigate cell-cell communication, cell-ECM interaction, cell migration and microfluidic device development. The specific

details of experimental designs and materials are described in each chapter. Below is an outline of the materials and methods used in our experiments.

1.9. A Mechanical apparatus

A syringe pump and capillary tubing of different inner diameters were utilized to impose mechanical stress on cells and collagen. Conventional oven and hot plates were used to evenly heat up substrate samples. A rheomter was used to experimentally detect collagen viscosity as a function of shear rate. A milling machine, lathe and jig saw were largely used to manufacture acrylic molds for polymer casting in microfabrication.

1.9. B Biological reagents and assays

Primary antibodies and secondary antibodies were used to detect cell-cell communication and growth factor receptor activity via immunostaining and In-Cell Western blotting. Cell proliferation was examined using proliferation assays (MTT assay). Cell migration was tested using transwell assays (Boyden assays) and microfluidic devices.

1.9. C Fabrication

Photolithography and elastomeric PDMS stamping were used when making microfluidic devices. Spin processer was utilized to evenly coat chemicals on substrates while UV light was applied to change polymer structures during photolithography. High-frequency generator was used to facilitate PDMS bonding with substrates.

1.9. D Optical detection and imaging equipments

A spectrophotometer was used to detect light intensity of cell samples, while an infrared scanning machine was applied to detect infrared fluorescence of protein samples. Fluorescent microscopes were used to image cell function and detect ligand transport with a motorized stage mounted for position control. Confocal microscopy was also used to detect protein expression while a scanning electron microscope (SEM) was used to study collagen structure.

1.9. E Mathematical modeling and computational methods

The Stokes-Einstein equation was utilized to estimate ligand diffusivity. The Power law was used to theoretically calculate viscosity of polymer solutions, while convective-diffusion equations were applied to model ligand transport within the entire microfluidic devices. The Navior-Stokes equation was applied to analyze bulk flows within the microchannel of the microsystem. Finite element method was also used to solve the convective diffusion equation and generate spatiotemporal profiles of ligand transport.

CHAPTER 2

Internal Fluid Flow Increases Cellular Interconnects between *Medial Collateral* Ligament Fibroblasts and Cellular Extensions within Three-Dimensional Collagen Matrixes

Qingjun Kong

Department of Mechanical Engineering

The City College of The City Universty of New York (CCNY)

140th Street and Convent Ave., T-402

New York, NY 10031

empyreankqj@yahoo.com.cn

Phone: 212.650.6766 Fax: 212.650.6727

and

*Maribel Vazquez, Sc.D.**

New York Center for Biomedical Engineering

Department of Biomedical Engineering

The City College of The City University of New York (CCNY)

140th Street and Convent Ave., T-403D

New York, NY 10031

Vazquez@ccny.cuny.edu

Phone: 212.650.5209 Fax: 212.650.6727

**Corresponding Author*

Running title: Fluid Flow Increases Cellular Interconnects

Kew words: shear stress, interconnects, ligament, fibroblast, collagen, three-dimensional

ABSTRACT

The interconnectivity of fibroblasts within the ligamentous extracellular matrix has been largely overlooked. Studies on the cell-to-cell contacts with their neighbors via gap junctions in ligament fibroblasts, and works on the ability of fibroblasts to generate interconnected networks *in vivo*, suggest inter-fibroblastic interactions play an important role in fundamental biological processes, including homeostasis and wound healing. The current study examines how fluidic shear stresses imposed by internal flow can be used to mediate the formation of three-dimensional, interconnected fibroblast networks within collagen solutions. Several fibroblast-collagen solutions were exposed shear stresses via Poiselle Flow. The consequent changes in cell networking, interconnections, and cell morphology within collagen matrixes exhibited by cells derived from Bovine *Medial Collateral Ligaments* were analyzed. Results illustrate that higher imposed stresses generate cells with more dendritic and/or branched morphologies, which form more visible three-dimensional networks within collagen matrixes than fibroblast-collagen solutions that were unexposed to shear stress.

2.1 INTRODUCTION AND BACKGROUND

The inter-relationship between the widely-spaced cells of connective tissue and their surrounding extracellular matrix (ECM) has generated extensive research into the cell-matrix interactions that enable ligaments, tendons, and bones to bear mechanical loads [1-3], set respective viscoelastic limits for these tissues [4-6], and contribute to fundamental differences in physiological healing capacities [7,8]. The diminished strength of injured and/or healing connective tissue is due in large part to the alignment of collagen fibers, and intercommunication between constituent fibroblasts [9-11]. Investigators have illustrated that collagen alignment parallel to the longitudinal axis provides maximum strength and stiffness for connective tissues [10, 15, 16]. However, researchers have only recently demonstrated that constituent connective tissue fibroblasts are able to explore and respond to changes in the surrounding ECM by forming gap junctions with neighboring cells despite their large *in vivo* spacing [12-14]. As a result, there has been a concerted effort to develop protocols, experimental methods, and biomaterials that promote intracellular networking and biochemical communication between constituent fibroblasts [5, 7, 17], as well as align cells and polymer fibers in preferential orientations [16]. Multiple investigators have demonstrated that both biopolymers and monolayers of various cell types can be aligned in the direction of shear stress imposed by external fluid flow [18]. However, the application of fluid flow to promote intracellular communication between cells positioned within 3D matrixes remains unexplored.

In this work, we investigate the ability to influence 3D cellular networking between ligament-derived fibroblasts within an *in vitro* collagen matrix by applying

fluidic shear stress via internal, capillary flow, known as Poiselle flow [19]. Unlike the application of external fluid flow, which imposes shear stress on only those cells and matrix present on the interfacial surface, internal flow imposes shear stress along cellular perimeters and collagen polymers within the entire capillary. For these experiments, we hypothesize that stress-induced changes of fibroblast-populated collagen solutions affect cell-matrix interactions to generate increased 3D fibroblast networking, indicative of intracellular communication. Experiments will study the effects of fluidic shear stresses on two types of solutions: (i) Buffered solutions of *Medial Collateral* Ligament (MCL)-derived fibroblasts, only (i.e. no surrounding matrix); and (ii) Solutions of MCL-derived fibroblasts seeded within a collagen matrix. Solutions will be displaced, or loaded, through micrometer-sized capillaries in order to expose constituent cells and collagen polymers to fluidic shear stresses, $\boldsymbol{\tau}$, defined by the fluid mechanics relation:

$$\tau = \frac{4Q\eta}{r^3} \qquad (2.1)$$

where $\boldsymbol{Q}$ is volume flow-rate, $\boldsymbol{r}$ is capillary radius, and $\boldsymbol{\eta}$ is solution viscosity [20]. Via ***Equation (2.1)***, greater shear stresses are applied onto solutions when they are displaced through capillary tubing, or loaded, at larger volume flow-rates, $\boldsymbol{Q}$. As per Poiselle flow, the shear stress applied to solutions will vary proportionally from the capillary wall to the capillary centerline. Applied shear stresses will be maximum on the wall, and approach zero towards the capillary centerline. In this study, solutions will be loaded through capillaries at four specified volume flow-rates between 10 μL/min and 30μL/min, collected, and incubated overnight. Afterwards, solutions will be imaged to investigate the fibroblastic networking and interconnections displayed between cells of both types of

solutions (i.e. with and without a surrounding collagen matrix), as well as observe changes in the shear-induced morphology of constituent fibroblasts. Results of this study will be used to develop *in vitro* techniques that facilitate detailed investigations of intracellular communication within pre-stressed, 3D matrixes needed for homeostasis and wound healing research of connective tissue.

2.2 METHODS AND MATERIALS

Cell Culture: Primary cultured fibroblast cells were harvested from young (1-3 years), male bovine *Medial Collateral* Ligament (MCL) explants received from the Soft Tissue laboratory at the Hospital for Special Surgery (New York, NY). These primary passage cells were then washed and cultured with sterile growth media M199, 10% fetal bovine serum (FBS), and 1% antibiotic-antimycotic solution, pH 7.1-7.3 (Mediatech Inc., VA) and plated onto sterile polystyrene tissue culture flasks (BD Biosciences, MA). Cells were maintained in a 5% CO_2 humidified incubator at 37^{o}C. Serial passages were performed when cultures became ~ 90% confluent by detaching cells from flasks via a three-minute treatment with 0.05% tripsin-0.53mN EDTA (Mediatech Inc., VA) at 37^{o}C. The suspension was then diluted with equal volumes of serum-containing growth medium, and cells were collected via centrifuge, suspended in growth medium, and subcultured for no more than five passages to insure maintenance of phenotype.

Preparation of Collagen Gels: Three-dimensional collagen gels were prepared by dissolving type I collagen from Rat Tail (BD Biosciences, MA) in 0.01M hydrochloric acid. Collagen was polymerized at a final concentration of 0.10mg/mL using buffered Medium 199 (M199) (Mediatech Inc., VA). Fibroblasts were harvested in culture (with

FBS), collected, and added as the last component prior to polymerization at a cell density of approximately 10^4 cells per milliliter, as measured per hemocytometer.

System loading and incubation: Collagen-fibroblast solutions were exposed to fluidic shear stresses via loading through a capillary tubing system. Fibroblasts in a 10^4cells per milliliter density were mixed with 0.1mg/mL of collagen in 100μL of media, and placed into a 100μl syringe (BD Biosciences, MA). This low cell density was chosen from a range which other researchers have shown is the lower limit where fibroblasts can form networks within collagen matrixes [14, 21], while low collagen concentration was selected to mimic the lowest extreme of injured collagenous tissue. The syringe was connected to a capillary tubing of 100μm-inner-diameter (Upchurch Scientific Inc., WA) on one side, and a low volume flow-rate syringe pump (Harvard Apparatus, MA) on the other. Solutions were carefully displaced through the tubing using the syringe pump to control the applied volume flow-rate, $\boldsymbol{Q}$, between 10μL/min and 30μL/min. Individual solutions were loaded within new, 5-cm-long capillary tubing in order to generate internal fluidic shearing for all experiments. Solutions exiting the capillary were collected using 35-mm-diameter Petri dishes to gather individual droplets that landed into their centers without splatter upon contact. Droplet position was unchanged during experiments such that accumulation of successive droplets generated 100μl volume solutions that covered the entire surface of the Petri dish, and were incubated overnight ***(Figure 2.1).*** Note that a 500-mL-volume of cold water (10^oC) was used to surround the syringe, Petri dishes, and tubing during all experiments in order to impede temperature-dependent effects upon cells or collagen gelation. Resultant fibroblast-populated collagen

gels exhibited approximate 1-mm-thickness within Petri dishes during a minimum of 4 loading experiments per volume flow-rate.

Microscopy and Digital Imaging: An epi-fluorescence microscope (NIKON TE300, Morrell Instruments, NY) was used to gather images of fibroblast-collagen gels prior to and after capillary loading. The digital pictures within a 0.58-mm by 0.44-mm centerline, cross-sectional area of the gel were acquired using SPOT software (Version 4.1, Diagnostic Instruments, MI) after overnight incubation at the magnitude of 20X using phase contrast, long working distance objectives (20X /NA 0.40 /WD 3.0mm, NIKON) and transmitted light. All images are representative of the cell densities seen within the center sections of Petri dishes after loading experiments were performed.

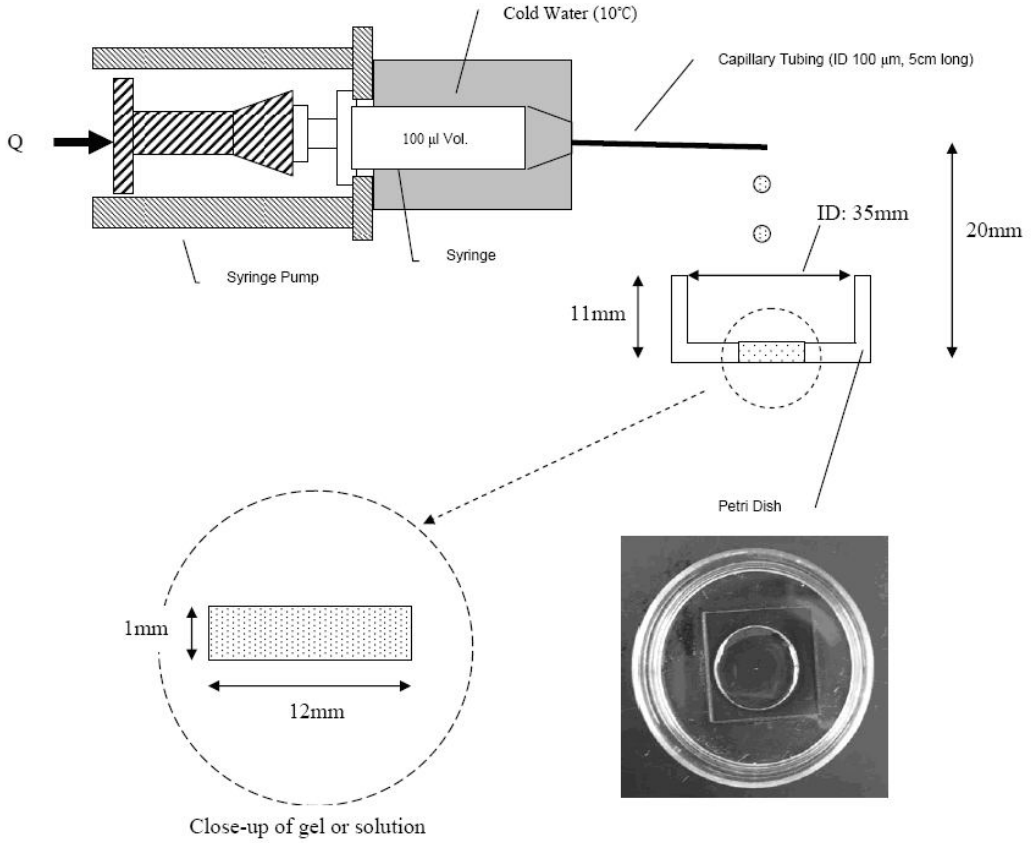

Figure 2.1: A schematic diagram of the experimental system used to impose shear stresses onto MCL-derived fibroblasts suspended in buffered media without collagen matrix or seeded within collagen matrix. All solutions containing fibroblasts with or without collagen matrix were loaded through a 100-µm-ID capillary tubing, 5cm long. A displacement syringe pump was used to admit a constant volume flow-rate, Q, between 10 and 30µl/min. A 500-ml-volume bag of cold water was placed around the syringe to maintain the solutions at approximately 10^{o}C. Solutions were collected in the center of Petri dishes in the diameter of 12mm, and incubated overnight to produce gels of approximate 1-mm thickness. A photo of the whole Petri dish and the center area to collect solutions was shown. Gels were imaged using an inverted transmission microscope.

2.3 RESULTS

The effects of fluidic shearing were assessed by investigating cell and polymer interactions within two individual types of solutions displaced through capillaries at four different volume flow-rates of 10µL/min, 15µL/min, 20µL/min, and 30µL/min: (i)

Solutions of MCL-derived fibroblasts only (i.e. no surrounding matrix); and (ii) Solutions of MCL-derived fibroblast cells seeded within a 3D collagen matrix.

MCL-Derived Fibroblast Solutions: As control experiments, fibroblast solutions were pipetted into Petri dishes, without prior displacement through capillaries, and allowed to adhere overnight for subsequent imaging and analysis. Via use of large diameter pipettes (100μL tips), these experiments imposed zero to minimal shear stress onto fibroblast solutions displaced into Petri dishes, and were, therefore, benchmarked as controls. Images of these control solutions exhibited exclusive 2D adhesion to the inner substrate surface during multiple pipette experiments ***(Figure 2.2.A.i)***. Cells appeared lamellar and flattened, and displayed minimal contact with neighboring fibroblasts. In contrast, images of fibroblast solutions that had been displaced through capillaries at different volume flow-rates prior to overnight incubation exhibited cell populations that had visible interconnections with their neighbors ***(Figure 2.2.A.ii-2.2.A.v)***. Cells of solutions loaded at the lowest volume flow-rate of $\boldsymbol{Q}$=10μL/min exhibited multiple close contacts and extensions between neighboring cells. However, solutions displaced through the capillary at higher volume flow-rates, $\boldsymbol{Q}$>15μL/min, exhibited long, extended tethers between neighboring fibroblasts.

A.i. (Control, Q~0) (MCL-derived fibroblasts within buffered media)	B.i. (Control, Q~0) (MCL-derived fibroblasts Seeded within collagen matrix)	C.i. (Control, Q~0) (Fibroblasts morphology)
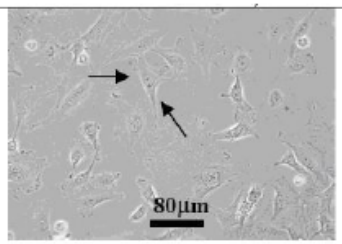	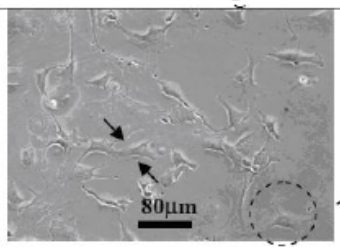	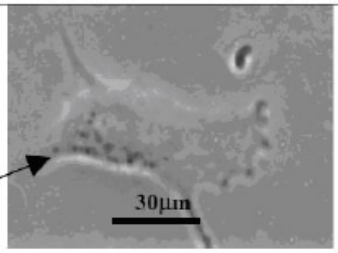
A.ii. Q=10µL/min	B.ii. Q=10µL/min	C.ii. Q=10µL/min
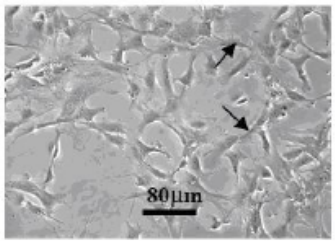	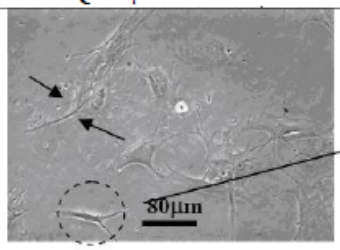	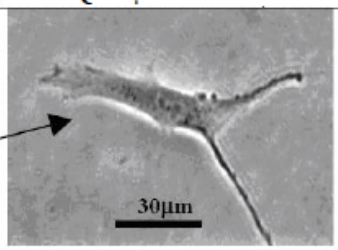
A.iii. Q=15µL/min	B.iii. Q=15µL/min	C.iii. Q=15µL/min
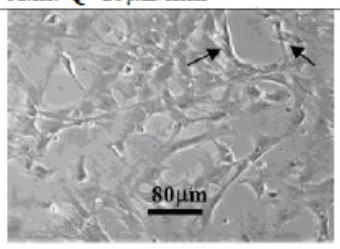	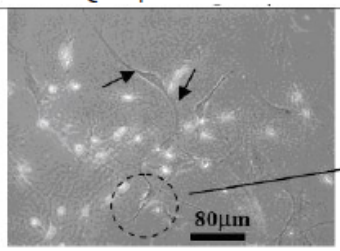	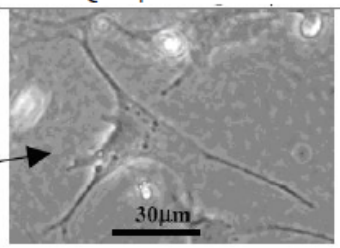
A.iv. Q=20µL/min	B.iv. Q=20µL/min	C.iv. Q=20µL/min
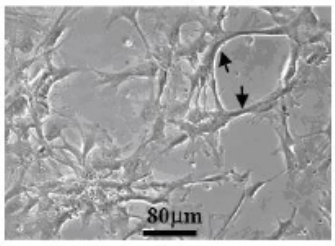	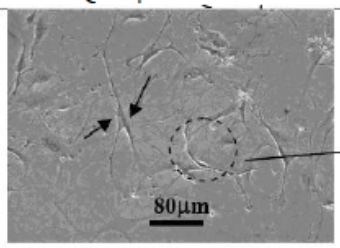	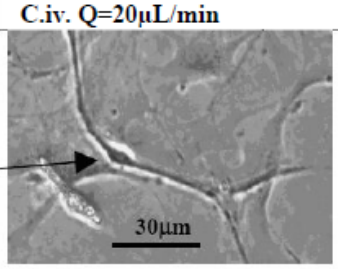
A.v. Q=30µL/min	B.v. Q=30µL/min	C.v. Q=30µL/min
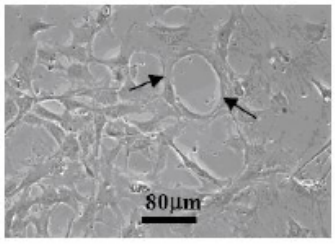	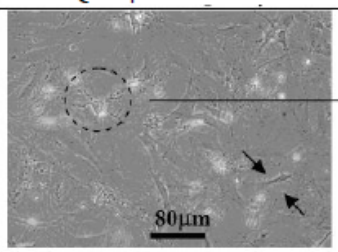	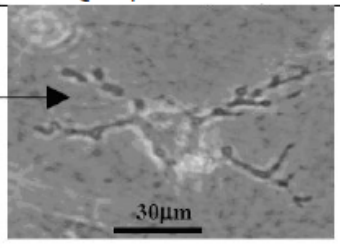

Figure 2.2: Microscope images of MCL-based solutions (MCL fibroblasts only and collagen solutions seeded within MCL fibroblasts) in experiments that applied zero to minimum shear, (A.i, B.i, C.i), and in experiment that loaded solutions through 100-μm-ID capillary tubing at constant volume flow-rates of 10μl/min (A.ii-C.ii), 15μl/min (A.iii-C.iii), 20μl/min (A.iv-C.iv), and 30μl/min (A.v-C.v). The left-hand column illustrates images of solutions containing only fibroblast cells after solutions were loaded into capillary tubing at different volume flow rate, Q, (A.i-A.v). Images shown in the center column illustrate images of collagen gels seeded with fibroblast cells after solutions had been loaded into capillary tubing at different volume flow rate, Q, (B.i-B.v). Bright spots seen in the images represent cells out of the substrate plane of focus, indicating 3D interconnections within the collagen matrix. Images in right-hand column (C.i-C.v) depict enlarged cell morphologies from fibroblast-collagen solutions loaded at different volume flow rate, Q. Arrows in the left-hand column mark cell inter-contact seen when cell solutions were displaced through capillaries at different volume flow rates, while arrows in the center column points to cells that exhibit morphology representative of entire gel.

Additionally, data illustrates that the number of cells per unit area varied between experiments of the no-shear control, and the experiments that imposed shear via displacement of solutions through capillaries at different volume flow-rates. Cells of the control experiment were seen to distribute uniformly over 95% of the Petri dish substrate area, while cells loaded at different volume flow-rates were uniformly distributed within solely the center about 60% of the Petri dish area ***(Figure 2.3)***. The number of connections between neighboring cells illustrates that cell solutions which had been loaded through the capillary system exhibited approximately the same number of cells per unit area upon the inner substrate surface regardless of volume flow-rate used. As seen, the number of cell interconnections between neighbors increased by 30% when shear was applied, but remained relatively independent of the magnitude of volume flow-rate used thereafter ***(Figure 2.4)***.

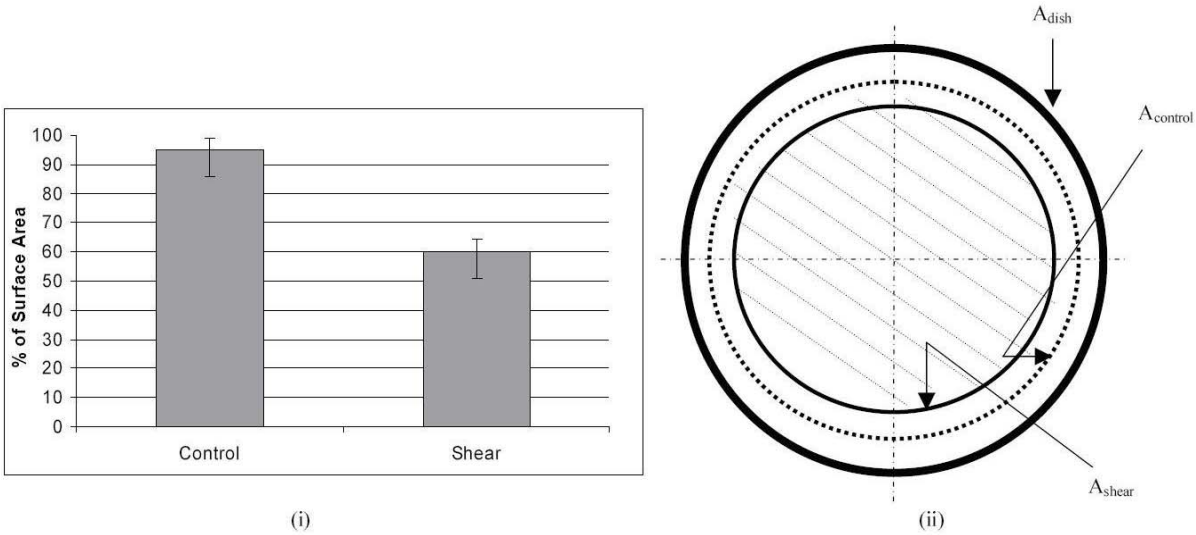

Figure 2.3: Measurement of cell location within Petri dishes after loading and incubation of buffered cell solutions (no matrix). (i) The left-hand-side illustrates that cell solutions exhibited an approximately uniform distribution which covered 95% of the surface area when directly pipetted onto Petri dishes with minimal shear, i.e. control. In contrast, cell solutions loaded at different volume flow-rates exhibited a uniform distribution of cells that was concentrated within the center about 60% of the dish. (ii) The right-hand side of the figure illustrates a schematic top view of a Petri dish to demonstrate the different, concentric distribution of cells after loading. Cells of the control were seen along 95% of the surface areas of the dish, Acontrol, while cells of sheared solutions were uniformly distributed solely throughout the center 60% of the dish, Ashear . The surface area where solutions were cover was represented with Adish.

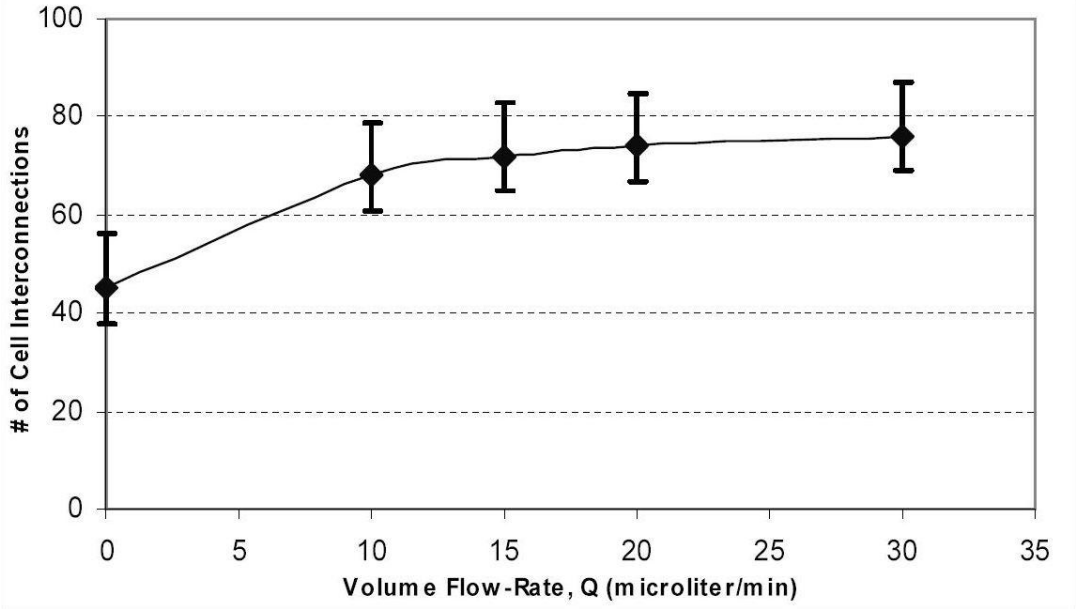

Figure 2.4: The number of cell interconnections between neighboring fibroblasts increased when shear stress was applied to buffered cell solutions (no matrix) via displacement through capillary tubing. The number of cell connections between neighbors was minimum during control experiments (no shear, Q~0), but increased for cell solutions that had been exposed to shear stress via internal flow, by average 45%. The number of cell connections between adjacent cells was approximately constant between solutions that had been displaced through the capillary system at Q≥20µl/min.

Collagen Gels Seeded with MCL-Derived Fibroblasts: As before, control solutions of collagen seeded with MCL-derived cells were identified as those which were directly pipetted into Petri dishes without prior displacement through capillaries (i.e. zero to minimal shear imposed onto solutions). Images of control solutions that had polymerized in overnight displayed cells which were dispersed throughout the thickness of the gel, as well as intermittently interconnected within the collagenous ECM ***(Figure 2.2.B.i).*** Cells were seen elongated and in contact with neighbors at varying distances from the substrate surface. In addition, cells were evident both in and out of the focal plane, indicative of 3D fibroblast location within the collagen matrix. Note, only images captured from the focal plane of the center, the inner substrate surface, are shown.

Additionally, as with previous loading experiments, solutions of cells loaded with collagen matrix exhibited interconnected cells that were distributed throughout the center 60% of the surface area of the Petri dish for all volume flow-rates used, while cells of control samples where distributed throughout the entire Petri dish.

Images of collagen-fibroblast solutions that had been displaced through capillaries at different volume flow-rates depicted varying amounts of cell networking within polymer gels. Solutions loaded through the capillary at the lowest volume flow-rate of $\boldsymbol{Q}$=10μL/min exhibited high-density networks of flattened, spindle-like cells on the substrate surface, only ***(Figure 2.2.B.ii)***. No 3D cell location within the gel or 3D networking between cells was observed for multiple loading experiments at this volume flow-rate, although such networking was evident in images of the control solution. In contrast, solutions displaced through capillaries at higher flow-rates, $\boldsymbol{Q}\geq$15μL/min, displayed 3D interconnected networks of neighboring fibroblasts within the collagen matrix ***(Figure 2.2.B.iii-2.2.B.v)*.** Cells were seen in and out of the focal plane, indicative of 3D positioning, and exhibited clear cytoplasmic extensions between neighbors for multiple loading experiments per volume flow-rate.

Lastly, images of collagen-fibroblast solutions displaced through capillaries generated gels that exhibited marked changes in constituent fibroblast morphology. MCL phenotype within gels loaded at the lowest volume flow-rate ($\boldsymbol{Q}$=10μL/min) appeared lamellar and flattened, as typically seen during 2D substrate adhesion ***(Figure 2.2.C.ii)*.** However, fibroblast morphology within solutions that exhibited 3D interconnections was visibly different between samples. Although a small subset of cells within solutions loaded at a 15μl/min illustrated 2D adhesion to the substrate, a majority of cells appeared

elongated, and displayed an increasing number of cytoplasmic extensions throughout the thickness of the gel ***(Figure 2.2.C.iii).*** Similarly, the majority of fibroblasts displaced through the capillary at 20μL/min exhibited phenotypes that were more visibly spindle-like, and bore an increasing number of cytoplasmic extensions per cell ***(Figure 2.2.C.iv).*** A number of cells within solutions loaded at a 30μL/min flow-rate exhibited a unique, highly branched morphology, supported by dendritic extensions that protruded radially outwards from the cell into the 3D matrix ***(Figure 2.2.C.v).*** In order to describe the differences in observed morphology more quantitatively, the number of cellular extensions of a typical cell within each experimental gel was measured for each loading experiment. Upon counting the number of extensions per cell within over 50 cells per volume flow-rate experiment, the data illustrate that the number of cell pseudopods increased from a minimal value of 2 during zero shear control samples, i.e. Q~0, to a maximum value of 7 within cells loaded at the highest volume flow-rate of Q=30μl/min ***(Table 2.1)***.

Q (μL/min)	# of Cell Extensions
0	2 +/- 1.5
10	4 +/- 2.7
15	6 +/- 2.3
20	6 +/- 3.1
30	7 +/- 2.2

Table 2.1: The average number of cellular extensions measured within cells of fibroblast populated collagen gels that were loaded at different volume flow-rates. Approximately 20 cells of 4 different experiments per each volume flow-rate were measured to obtain a sample size of 80 cells per column entry. As seen, the number of pseudopods increased from an average of 2 extensions during control experiments (i.e. no shear), to an average of 7 when exposed to shear stresses via capillary displacement at a volume flow-rate of 30μl/min.

2.4 DISCUSSION

The ability of cells derived from ligament tissue to generate three-dimensional, interconnected networks under various types of mechanical loading is of critical importance to connective tissue researchers. In this work, we performed experiments which tested the ability of MCL-derived fibroblasts to generate networks within surrounding 3D collagen solutions under shear stresses imposed by fluidic loading through capillary tubing.

Minimal Shear (Controls*):* We note two important findings about designated control experiments (zero to minimal shear). First, the ability of MCL-derived fibroblasts to form 3D networks within collagen gels without imposed shear (i.e. controls) was largely influenced by the addition of Fetal Bovine Serum (FBS), rather than by the buffer or media used. Multiple experiments were performed using either Media 199 or Dulbecco's Modified Eagle's Medium (DMEM) as control buffers, with and without FBS (data not shown). Our results demonstrated no visible differences between gels constituted with either media, but rather, illustrated that the addition of FBS to either media generated gels that exhibited 3D networks of elongated fibroblasts. This result corroborates the work of others who have illustrated that growth factors are able to promote fibroblastic extensions within collagen matrixes [14]. This is also of practical interest, as multiple buffers have been used in the literature for gel seeding experiments, and we report little notable differences induced solely by the two most commonly used medias.

Additionally, the visualization of cellular networking between MCL-derived cells with a low seeding density (~10^4cells/mL) is unexpected. Using a simplified geometric argument that models cells as uniformly distributed spheres of 10-μm-diameter, a cell density of 10^4 per millilieter within a collagenous matrix indicates that, without such external influences such as temperature gradients or shear, the cells would be separated from their neighbors by approximately 465μm. Such a remarkable spacing of more than 47 times the cell diameter suggests that the cells are unlikely able to form interconnects readily. However, data presented here illustrates interconnections between low cell density collagen gels, suggesting that fibroblast-populated collagen gels can exhibit a large degree of fibroblast networking between connective tissue cells when exposed to shear stresses, and should be further investigated.

Imposed Fluidic Shear: Images of MCL solutions gathered after capillary loading illustrated that while cells were unable to form three-dimensional networks (presumably because they lacked a matrix onto which to adhere), fibroblasts were nonetheless able to form visible interconnects with their neighbors at all volume flow-rates used. This behavior suggests that, first, cells were physiologically unharmed by the shear stress imposed during these loading experiments, and that, second, cells retained the ability to reach out to surrounding cells after imposed shear. Using the values of volume flow-rate selected for these experiments, the Poiselle flow relation of ***Equation (2.1)*** indicates that the internal flow used imposed a maximum wall shear stress of less than 10Pa (100 dynes/cm²) in magnitude onto cell solutions. While the use of connective tissue fibroblasts during fluidic shear experiments via internal flow has been unreported, typical values of shear stress imposed from external fluid flow experiments onto ligament

fibroblasts are on the order of 25 dynes/cm² [17]. Further, the shear stress required to detach fibroblasts from glass or polystyrene surfaces is at least two order magnitudes higher, at approximately 420Pa (4200 dynes/cm²) [22]. Hence, the shear stresses applied in our internal flow experiments will not exert significant damage on cells. The interconnection patterns were distinct with volume flow-rate used, as they ranged from minimal close contacts between neighboring cells at low volume flow-rate, to what appears to be extended, intercellular tethers at higher volume flow-rates. Given the lack of a collagen matrix in these experiments, the results suggest that MCL-derived cells are extremely sensitive to minimal values of shear stress, and that their interactions with one another can be influenced by internal fluid flow.

The capillary loading of collagen solutions bearing fibroblasts demonstrated that the application of shear stress via internal flow affected cell ability to form interconnects with neighbors. While cells exhibited 2D cell tethering in the absence of an ECM under a given shear stress in previous experiments, they responded to the same magnitude of shear stress by forming 3D interconnected networks that exhibited dramatic changes in 3D phenotype in the presence of a collagen ECM. While it is recognized that cells adherent to substrates with or without collagen are expected to exhibit different cell morphologies because of the noted differences in integrin and non integrin-mediated binding [23], our data documents marked differences in specific cell morphology between cells of MCL-collagen solutions during shearing experiments. Cells became increasingly spindle-like when increased shear stress was applied via higher volume flow-rate, and ultimately exhibited small populations with a unusual branched morphology at the highest flow-rate used. The observed differences in shear-induced

phenotype are novel, and potentially provide support for evolving theories regarding the relationship between fibroblast morphology and mechanotransduction. For instance, the shear-induced phenotype observed in this study could indicate that cells were changing morphology in efforts to interconnect with neighbors as a means to mechanotransduce the externally applied shear stress. Alternatively, the morphology could suggest that cells had altered phenotype in order to adhere more effectively to the surrounding ECM and better contract the surrounding gel, such as needed during wound healing. Such observations at low collagen concentration are surprising, and point to a potential new avenue of research in connective tissue repair. However, in order to determine whether cells are indeed in a resting or active state, detailed biochemical testing is needed to identify the viability of gap junctions and other cell-to-cell contacts formed between 3D networked cells as a result of imposed stresses.

The experiments additionally exhibited marked differences in the distribution of cells between control and shear experiments, with or without matrix. Data of experimental loading of cell solutions (no matrix) illustrate that cell solutions without shear, i.e. controls, were uniformly distributed throughout the Petri dish used, while cells loaded through capillaries were concentrated towards the dish center. Similar results were seen from experiments that loaded solutions containing both cells and collagen. While cell contraction in the ECM is expected to position cells towards the gel center, such concentric cell distribution should not similarly be seen for cell solutions lacking a collagen ECM. The observation of similar results between solutions with and without matrix suggests that internal flow may affect cell connectivity via more physical interactions. That is, the close proximity of cells stimulated via capillary loading may

have induced cellular interconnections that were long lasting. Further investigation of such properties will significantly impact those research areas seeking to build matrixes with interconnected cells to better mimic connective tissue.

Lastly, it is noted that capillary loading may act directly upon collagen polymers to promote chain fracture and/or scission under high magnitudes of shear stress. Such shearing can create an extracellular matrix comprised of shorter polymer chains, and/or polymer strands that are spaced further apart, which can directly influence fibroblast-polymer interactions. However, experiments avoided such difficulties by applying minimal shear stresses unlikely to fracture polymer chains of pre-crosslinked solutions having low collagen concentration [19]. In addition, temperature was tightly controlled to 10°C during experiments in order to impede collagen polymerization during capillary loading, which could also directly affect cell-collagen interactions. Time-dependent polymerization was similarly minimized via usage of short loading times less than 10 minutes in duration during testing. However, because partial collagen polymerization is difficult to detect under conditions of flow, and with the addition of live, embedded cells, a complementary rheological study is recommended to more completely understand the potential, complex polymer-cell interactions that may be present during portions of capillary loading.

In conclusion, the results of this study suggest that shear stress applied via internal fluid flow can be used to influence fibroblast-matrix interactions as well as cell phenotype. Successful development of experimental techniques that promote cell networking *in vitro* will aid in the biological research directed towards identifying and understanding complex biochemical cues that promote fibroblastic interconnections of

connective tissue, as well as assist the large research efforts currently undertaken to develop novel biomaterials for use in tissue repair and engineering.

Acknowledgements

This research was supported by the National Science Foundation (BES 0428573), the National Institutes of Health (1R21 GM071703), and the PSC-CUNY Foundation (64683-00-01).

References

1. Hull ML, Berns GS, Varma H, Patterson HA, *Strain in the medial collateral ligament of the human knee under single and combined loads.* J Biomech, 1996. **29**(2): p. 199-206.

2. Kanamori A, Woo SL, Ma CB, Zeminski J, Rudy TW, Li G, Livesay GA, *The forces in the anterior cruciate ligament and knee kinematics during a simulated pivot shift test: A human cadaveric study using robotic technology.* Arthroscopy, 2000. **16**(6): p. 633-9.

3. Woo SL, Debski RE, Withrow JD, Janaushek MA, *Biomechanics of knee ligaments.* Am J Sports Med, 1999. **27**(4): p. 533-43.

4. Bonifasi-Lista C, Lake SP, Small MS, Weiss JA, *Viscoelastic properties of the human medial collateral ligament under longitudinal, transverse and shear loading.* J Orthop Res, 2005. **23**(1): p. 67-76.

5. Hingorani RV, Provenzano PP, Lakes RS, Escarcega A, Vanderby R Jr, *Nonlinear viscoelasticity in rabbit medial collateral ligament.* Ann Biomed Eng, 2004. **32**(2): p. 306-12.

6. Weiss JA, Gardiner JC, and Bonifasi-Lista C, *Ligament material behavior is nonlinear, viscoelastic and rate-independent under shear loading.* J Biomech, 2002. **35**(7): p. 943-50.

7. Abramowitch SD, Papageorgiou CD, Debski RE, Clineff TD, Woo SL, *A biomechanical and histological evaluation of the structure and function of the healing medial collateral ligament in a goat model.* Knee Surg Sports Traumatol Arthrosc, 2003. **11**(3): p. 155-62.

8. Woo SL, Niyibizi C, Matyas J, Kavalkovich K, Weaver-Green C, Fox RJ, *Medial collateral knee ligament healing. Combined medial collateral and anterior cruciate ligament injuries studied in rabbits.* Acta Orthop Scand, 1997. **68**(2): p. 142-8.

9. Langevin, H.M., C.J. Cornbrooks, and D.J. Taatjes, *Fibroblasts form a body-wide cellular network.* Histochem Cell Biol, 2004. **122**(1): p. 7-15.

10. Lo IK, Ou Y, Rattner JP, Hart DA, Marchuk LL, Frank CB, Rattner JB, *The cellular networks of normal ovine medial collateral and anterior cruciate ligaments are not accurately recapitulated in scar tissue.* J Anat, 2002. **200**(Pt 3): p. 283-96.

11. McNeilly CM, Banes AJ, Benjamin M, Ralphs JR, *Tendon cells in vivo form a three dimensional network of cell processes linked by gap junctions.* J Anat, 1996. **189 (Pt 3)**: p. 593-600.

12. Banes, A.J., P. Weinhold, X. Yang, M. Tsuzaki, D. Bynum, M. Bottlang, and T. Brown, *Gap junctions regulate responses of tendon cells ex vivo to mechanical loading.* Clin Orthop Relat Res, 1999 367 Suppl: p. S356-70.

13. Ko K, Arora P, Lee W, McCulloch C, *Biochemical and functional characterization of intercellular adhesion and gap junctions in fibroblasts.* Am J Physiol Cell Physiol, 2000. **279**(1): p. C147-57.

14. Grinnell F, Ho CH, Tamariz E, Lee DJ, Skuta G, *Dendritic fibroblasts in three-dimensional collagen matrices.* Mol Biol Cell, 2003. **14**(2): p. 384-95.

15. Pedowitz RA, O'Connor JJ, Akeson WH, *Daniel's knee injuries: Ligament and cartilage structure, function, injury, and repair*. Lippincott Williams & Wilkins, Philadelphia, PA, 2003 2nd edition: p. 12, 33

16. Lee CH, Shin HJ, Cho IH, Kang YM, Kim IA, Park KD, Shin JW, *Nanofiber alignment and direction of mechanical strain affect the ECM production of human ACL fibroblast*. Biomaterials, 2005, 26: p. 1261-70

17. Hung, C.T., Allen, F.D., Pollack, S.R., Attia, E.T., Hannafin, J.A., Torzilli, P.A., *Intracellular calcium response of ACL and MCL ligament fibroblasts to fluid-induced shear stress*. Cell Signal, 1997, Vol. 9, No. 8: p. 587-94

18. Thi MM, Kojima T, Cowin SC, Weinbaum S, Spray DC, *Fluid shear stress remodels expression and function of junctional proteins in cultured bone cells*. Am J Physiol Cell Physiol., 2003, 284: p. C389-C403

19. Bird RB, Armstrong RC, Hassager O, *Dynamics of polymeric liquids: volume 1, fluid mechanics*. John Wiley & Sons, Inc., New York, NY, 1987

20. Smits AJ, *A physical introduction to fluid mechanics*. John Wiley & Sons, Inc., New York, NY, 1999

21. Pizzo AM, Kokini K, Vaughn LC, Waisner BZ, Voytik-Harbin SL, *Extracellular matrix (ECM) microstructural composition regulates local cell-ECM biomechanics and fundamental fibroblast behavior: a multidimensional perspective*. J. Appl. Physiol., 2005, May, 98(5): p. 1909-21

22. Yamamoto A, Mishima S, Maruyama N, Sumita M, *Quantitative evaluation of cell attachment to glass, polystyrene, and fibronectin- or collagen-coated polystyrene by measurement of cell adhesive shear force and cell detachment energy*. J. Biomed. Mater. Res., 2000, May; 50 (2): 114-24

23. Cukierman E, Pankov R, Yamada KM, *Cell interactions with three-dimensional matrices*, Current Opinion in Cell Biology, 2002, 14: 633-9

CHAPTER 3

Flow-induced shear stresses increase the number of cell-cell contacts within extracellular matrix

Qingjun Kong

Department of Mechanical Engineering

The City College of The City Universty of New York (CCNY)

140th Street and Convent Ave., T-402

New York, NY 10031

empyreankqj@yahoo.com.cn

Phone: 212.650.6766 Fax: 212.650.6727

and

*Maribel Vazquez, Sc.D.**

New York Center for Biomedical Engineering

Department of Biomedical Engineering

The City College of The City University of New York (CCNY)

140th Street and Convent Ave., T-403D

New York, NY 10031

Vazquez@ccny.cuny.edu

Phone: 212.650.5209 Fax: 212.650.6727

**Corresponding Author*

Running title: Flow-induced shear stresses increase the number of cell-cell contacts

Kew words: shear flow, cell-cell contacts, extracellular matrix, pre-stressed gel, Connexin 43

Abstract: The formation of cell–cell contacts within extracellular matrix (ECM) is essential to maintain tissue homeostasis and metabolism, as well as critical toward the cell–ECM mechanotransduction that can affect intracellular organization and intercellular communication to enable cell response to external stimuli. This work illustrates the effects of shear stresses on cell–cell contacts within pre-stressed collagen ECM that were loaded in two separate conditions of constant flow (CF) and constant elution time (CET). The numbers of cell–cell contacts and cytoplasmic processes in both media and 3D ECM gels were analyzed in order to examine the shear effects of different magnitudes and time periods on 3D cell–ECM formation. The sheared collagen ECM microstructures were imaged and studied via scanning electron microscopy (SEM) to illustrate greater distances between constituent cells when larger shear stresses were applied. And the gap junction Connexin 43 expressed between networked cells that were sheared in short time period using CF loading exhibited more than those using CET loading. Notably, the number of cell–cell contacts increased when larger shear stresses were applied, suggesting these stresses may be used to increase intercellular communication within 3D matrixes.

3.1 INTRODUCTION

Cell-cell contacts within tissue are critical for the intercellular communication and transduction of external stimuli needed to maintain tissue organization and integrity, as well as facilitate tissue repair [1-3]. Yet, as layers of cells within tissue are often separated by extensive, 3-D extracellular matrix (ECM), the formation of these important cell-cell contacts is largely dependent upon cell adhesion to the ECM. Cells adhere to the ECM and to one another through specific types of transmembrane adhesion receptors that enable bi-directional communication between the inside and outside of the cell [2, 4]. The cell response to mechanical forces is then coupled to the internal organization of the cytoskeleton as well as to its adhesion to surrounding cells and ECM. Structural cues from the ECM, such as anisotropy or topology of constituent proteins, as well as the location of cell-cell contacts within ECM, can cause a cell to re-orient its body, shape, or functional state [4, 5], and consequently alter how cells adhere to their surroundings [5-7]. It has been recently proposed that the material characteristics of 3-D ECM may affect the mechanism of cell adhesion within the matrix via cell-matrix entanglements, thereby altering the formation of subsequent cell-cell contacts [2, 8, 9]. Such a model would greatly affect the engineering and material communities, as cell anchorage and communication within 3-D matrixes have been stimulated using 3-D dynamic forces in vitro, such as shear stress, pulsate flow, and compression, to stimulate explants of connective tissues, induce alignment for blood vessels, as well as develop engineered tissues with improved structural and functional properties [10, 11].

In this work, we investigate the effects of shear stress on the formation of cell-cell contacts within ECM by imposing changes to the 3-D structure of the surrounding matrix. Shear stress was selected for this study because it is well-known to influence the 3-D architecture of matrix solutions by deforming the length and distribution of polymer chains as well as altering the spacing and size of matrix pores [12, 13]. Furthermore, shear stress has also been reported to alter the distribution of gap junction proteins between cells, i.e. communication channels characteristic of cell-cell contacts, as a consequence of mechanotransduction [14-16].

This study utilized closed-channel fluid flow to apply shear stress to polymerizable solutions of collagen ECM, seeded with cultured fibroblast cells. In this manner, experiments generated so-called pre-stressed gels, by imposing mechanical queues to both the cells and ECM, simultaneously. Further, as the viscoelastic properties of extracellular collagen are known to depend upon both the magnitude and duration of imposed shear stress [17, 18], solutions were extruded through microcapillaries at different volume flow-rates using two separate conditions of constant flow (CF) and constant elution time (CET), and the resulting polymer structure was imaged via Scanning Electron Microscopy (SEM). In addition, immunostaining of Connexin 43 (Cx43), a gap junction protein notable for its role in connective tissue mechanotransducition [14] and altering cell function during tissue wound healing [19],was also preformed to examine the effects of CET and CF-generated shear stresses on Cx43 distribution between networked cells. It was observed that cells supported within pre-stressed gels exhibited a larger number of cell-cell contacts when larger magnitudes of shear stress were applied. Further, cells exposed to high values of shear

stress for subsecond time periods displayed 3-D cell-cell contacts within pre-stressed gels, while cells exposed to the same shear stresses for longer time periods did not. Lastly, immunostaining experiments illustrated significant changes in Cx43 distribution along cell-cell interfaces between samples loaded using CF and CET conditions.

3.2 MATERIALS AND METHODS

Cell culture: Primary fibroblast cells were harvested from bovine Medial Collateral Ligament (MCL) explants received from the Soft Tissue laboratory of Dr. Peter Torzilli at the Hospital for Special Surgery (New York, NY) [20, 21]. Primary cells were washed and cultured with sterile growth media M199, 10% fetal bovine serum (FBS), and 1% antibiotic-antimycotic solution (penicillin, streptomycin, amphotericin B) (Mediatech Inc., VA) with pH 7.1-7.4 and plated onto sterile polystyrene tissue culture flasks (Becton Dickinson Labware, NJ). Cells were then maintained at 37^{o}C in a 5% CO_2 humidified incubator. Serial passages were performed when cultures became ~ 90% confluent by detaching cells from flasks via a three-minute treatment with 0.05% trypsin-0.53mM EDTA (Mediatech Inc., VA) at 37^{o}C. The suspension was then diluted with equal volumes of serum-containing growth medium, and cells were collected via centrifuge, suspended in growth medium, and subcultured for less than 5 passages prior to experimental use.

Preparation of collagen solution: Specimens of collagen ECM were prepared by dissolving a stock solution of type I rat tail collagen (BD Biosciences, Bedford, MA) in phosphate buffered saline (1 X PBS, Mediatech Inc., Herndon, VA) to reach final dilute concentrations of 0.10mg/mL. The pH of all samples was adjusted to 7.4 using sodium

hydroxide (NaOH) as needed to insure polymerization [22]. To generate specimens of cell seeded collagen ECM, collagen was first diluted from the stock solution into sterile growth media M199 with FBS to a final concentration of 0.10mg/mL, and afterwards cultured fibroblasts were collected and added to the solutions prior to collagen polymerization. Solutions of sheared collagen with and without embedded fibroblasts were incubated overnight (~12 hours) for experimental observation the following day. We note that experiments of this study utilized a low cell density (10^4 fibroblasts per milliliter) as well as a low collagen concentration (0.10mg/mL) in order to examine the formation of 3-D cell-cell contacts within minimal environments, as clinical investigators have illustrated that both collagen concentration and cell density can be significantly reduced for physiological conditions, such as trauma, or injury [3, 23].

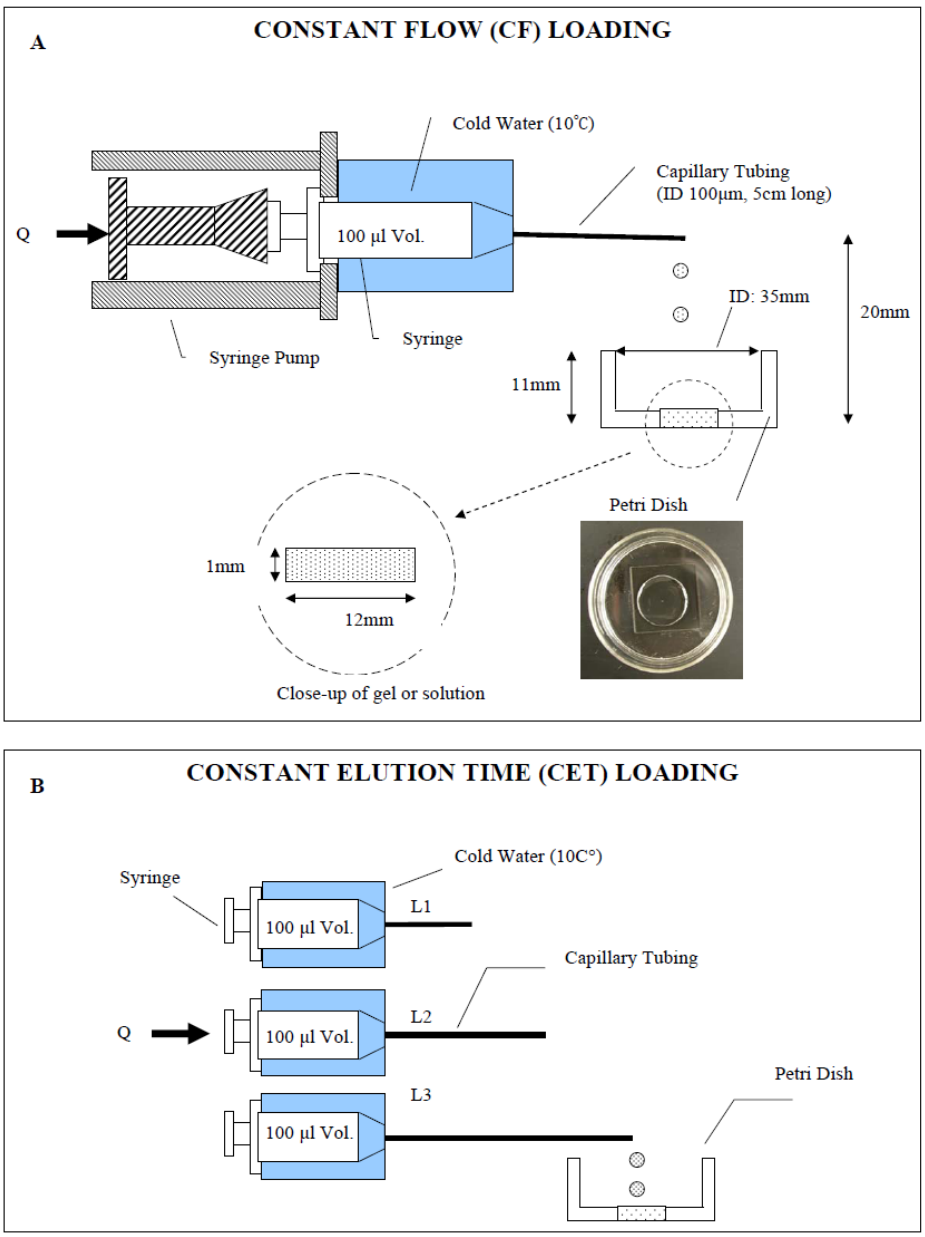

Figure 3.1: A schematic diagram of the Constant Flow (CF) and Constant Elution Time (CET) loading conditions used to impose shear stresses onto solutions. Using CF loading conditions shown in (A) solutions were pressure-driven through microcapillaries of fixed 5-cm-length and 100-µm-inner-diameter using a displacement syringe pump at a volume flow-rate, Q, between 15 and 30µl/min. Using CET loading conditions shown in (B) solutions were pressure-driven through varying lengths of microcapillary tubing having 100-µm-inner-diameters. A 500-ml-volume bag of cold water was positioned around the syringe during each test to maintain the solution at approximately 10^{o}C. Solutions were collected in the center of Petri dishes, and incubated overnight to produce so-called pre-stressed collagen gels with approximate 1-mm thickness.

System loading and incubation: Solutions were exposed to shear stresses via displacement through 100-μm-inner-diameter capillaries (Upchurch, MA) using a syringe pump (Harvard Apparatus, MA) operated at different volume flow-rates as shown in **Figure 3.1**. Solutions were placed into a 100μl syringe (Hamilton, CA) and displaced through adjoining capillary tubings at volume flow-rates, Q, between 15 μL/min and 30 μL/min. Sheared solutions were then collected in Petri dishes (MatTek Corp., MA) located directly below the exit of the capillary tubing, such that individual droplets exited the tubing and landed into the center of the dish without splatter upon contact. Droplet position was unchanged during experiments**.** Further, a 500-mL-volume of ice water (10^{o}C) was used to surround the syringe during experiments in order to impede temperature-dependent collagen gelation. Sheared solutions were collected and incubated overnight (~12 hours) to generate pre-stressed gels with approximate 1-mm-thickness. Lastly, control experiments used large diameter pipettes to displace solutions onto Petri dishes, directly, in order to mimic zero shear conditions. Similarly, the control solutions were also incubated overnight (~12 hours). Note that all of the cell solutions, including the sheared and control solutions, were tested to confirm cell viability using Calcein AM (Cat. # C3099, Molecular Probes, Eugene, OR) after overnight incubation (data not shown).

Experiments in this study applied shear stresses using flows that can be modeled as non-Newtonian Poiseuelle Flow, i.e. fully developed, laminar flow within circular channels [24]. Here, the shear stress imposed by fluid flow varied gradually from a maximum at the channel wall (i.e. microcapillary inner radius) to a minimum at the

channel centerline, such that shear stress imposed, τ, is defined by the fluid mechanics relation:

$$\tau = \eta(\dot{\gamma}) \cdot \dot{\gamma} \tag{3.1}$$

where η is solution viscosity and $\dot{\gamma}$ is shear-rate. Further, the shear-rate imposed during fluid flow is defined as:

$$\dot{\gamma} = dV_z / dr \tag{3.2}$$

where v_z is the fluid velocity in the axial direction (z-direction). For non-Newtonian fluids such as collagen, viscosity is a function of shear rate, and is commonly studied using the power law fluid model [24]:

$$\eta = m(\dot{\gamma})^{n-1} \tag{3.3}$$

where m is a consistency index between 2/3 and 1, and (n-1) is a value between -0.1 and -0.6 that represents the slope of the curve on a log-log plot [25]. Using this model, the volume flow-rate, Q, is derived as:

$$Q = \frac{\pi R^3}{3 + 1/n} \cdot \frac{\tau_R^{1/n}}{m^{1/n}} \tag{3.4}$$

where R is the channel radius and τ_R is the shear stress on the wall (i.e. when radius equals R). In addition, as the power law fluid models viscoelasticity, two different experimental configurations of constant elution time (CET) and constant flow (CF) were used. Using the CF conditions shown in **Figure 3.1A**, solutions were displaced through microcapillaries of fixed cross-section and fixed 5-cm-length using volume flow-rates between 15 and 30 μL/min. As a result, shear stresses were imposed onto extruded solutions for different time periods per volume flow-rate used, ranging between 0.8 and

1.6 seconds, as shown in **Table 3.1.** Using the CET conditions shown in **Figure 3.1B**, solutions were similarly loaded through microcapillaries of fixed cross-section using volume flow-rates between 15 and 30 μL/min. However, microcapillaries of lengths between 30 cm and 90 cm were used as listed in order to insure that CET conditions imposed shear stresses onto solutions for the same 14-second time period in each experiment.

Rheometer testing: A parallel-plate rheometer (ARES-LS, TA Instruments, DE) was used to impose shear stress onto collagen solutions at shear-rates between $1x10^{-3}$ 1/s and $5x10^{3}$ 1/s, i.e., 6 orders of magnitude. The plates of this instrument were separated by 0.8 mm, and torque was exerted on the bottom plate by the rotating top plate from a minimum value of 0.1 μNm. The separation between the parallel plates was filled with 1.6 mL of collagen sample, so that the solution viscosity could be recorded as a function of shear-rate. The instrument was used to measure the viscosity of collagen solutions as a function of shear-rate in three identified regions: A zero-shear rate plateau, a shear-thinning region, and a high shear-rate plateau.

Immunostaining: Fibroblasts at a concentration of 10^{4} cells/ml within M199 solution were sheared during the CF and CET loading, collected in chambered coverglasses (Nalge Nunc International, Rochester, NY), and incubated overnight. Cells were then fixed with 3.7% parafamalderhyde (Sigma-Aldrich Co., St. Louise, MO) and permeablized with 0.4% Triton X-100 (Sigma-Aldrich Co., St. Louise, MO). Cells were treated with rabbit anti-connexin 43 (Cat. # 710700, Zymed, San Francisco, CA) diluted in solution of PBS (Mediatech Inc., Herndon, VA), 0.4% Triton X-100 and 10% goat serum at 1:1000 for 2 hours, and then stained with Alexafluora 488 goat anti-rabbit IgG

(Cat. # A11008, Molecular Probes, Eugene, OR) diluted in PBS and 0.4% Triton X-100 at 1:3000 for 1 hour. Cells were washed with PBS and 0.4% Triton X-100 and preserved in mounting medium with DAPI (Cat. # H-1200, Vector Lab Inc., Burlingame CA), a fluorescent marker commonly used to label the cell nucleus.

Microscopy and digital imaging: A transmitted-light optical microscope (NIKON TE300, Morrell Instruments, NY) was used to gather images of pre-stressed collagen gels (with cells) after microcapillary loading. The digital pictures within a 0.58mm by 0.44mm cross-sectional area were acquired using SPOT software (Version 4.1, Diagnostic Instruments, MI) before and after overnight incubation. All images shown are representative of cell densities seen within the center section of Petri dishes following loading experiments. Pre-stressed gels were imaged from the bottom of substrate surfaces to the top free surface of collagen gels using long working distance 20X objectives that enabled observation of collagen and cells between ECM layers 80-100 μm thick. Cells with projections that were visibly in contact with one another between these layers of collagen were then measured to produce the cell-cell data presented and discussed in this study.

Immunostaining experiments of the gap junction protein Cx43 utilized a transmitted-light epi-fluorescent microscope (NIKON TE2000, Morrell Instruments, NY) to image labeled fibroblasts using MetaVue software (Version 6.2r4, Universal Imaging Corp., PA). An objective of 20X was used to observe images.

Scanning Electron Microscopy (SEM): Collagen from a stock solution was dissolved in de-ionized water to reach a final concentration of 0.10mg/mL. Collagen solutions collected after CET and CF loading, as well as control solutions (i.e. no shear

applied) were placed on silicon wafers and then dehydrated through a series of ethanol solutions (35%, 50%, 75%, 95% and 99.5% for 10 minutes, respectively) and air dried in desiccators. Note that the collagen solutions dissolved in de-ionized water were not polymerized prior to or after shear stress was applied, as the measured pH of ~7.0 was below the value required to stimulate collagen polymerization [22]. The samples were examined using a scanning electron microscope (Carl Zeiss EVO 40, Boston, MA) with a maximum resolution of 50nm.

Statistical analysis: All experiments were repeated approximately 10 times per volume flow-rate, for each condition of constant flow (CF) and constant elution time (CET). A minimum of 5 micrographs per volume flow-rate were analyzed by selecting between 18 and 24 cells per micrograph to generate a sample size of at least 90 cells per experiment. Analysis of variance was performed for comparison of individual means. Significance of differences presented here exhibited values of $P < 0.005$ as shown specifically in the text where discussed.

3.3 RESULTS

This narrative describes the results obtained from three major experiments performed in this study. First, the viscosity of ECM solutions was altered by the shear stress imposed during microcapillary loading and SEM images demonstrated a notable difference between the collagen orientation of ECM samples following CET and CF loading. Second, the average number of cytoplasmic extensions per cell, n^{E}, increased with increased values of shear stress imposed during both CET and CF loading. Further, an increased number of 3-D cell-cell contacts within extracellular collagen, $n^{C\text{-}C}{}_{ECM}$, were

observed when shear stresses were imposed for sub second time durations using CF loading. And third, immunostaining of Cx43 illustrated an altered distribution of the gap junction protein between networked fibroblast cells after shear stresses were imposed via CET and CF loading.

Imposed Shear Stress Induced Changes in ECM Viscoelasticity

This study measured the changes in solution viscosity, η, as a function of shear-rate, $\dot{\gamma}$, in order to verify non-Newtonian, shear-thinning viscosity profiles for the dilute collagen solutions used as ECM. First, a rheometer was used to identify the time required for ECM solutions (without cells) to fully polymerize. As depicted in **Figure 3.2A**, the viscosity of an ungelled ECM solution increased from a minimum of $\eta = 0.06$ Pa-s at time t=0, to a steady-state value of $\eta = 0.25$ Pa-s after t = 550 seconds, or approximately 9 minutes as indicated by the dashed line in the figure. After this time, the solution was presumed gelled. This time parameter was then used to obtain the viscosity profiles of both gelled and ungelled solutions as a function of shear-rate via rheometer. The viscosity profiles of gelled collagen in **Figure 3.2B** were obtained using solutions that had polymerized for 9 minutes prior to testing, while the viscosity of ungelled solutions was recorded using samples immediately after preparation (less than one minute). **Figure 3.2B** illustrates that the shear-rate-dependent viscosity of both gelled and ungelled solutions were approximately constant and had minimum values of $\eta = 1.0$ Pa-s, and $\eta = 0.4$ Pa-s, respectively, at low shear-rates near $\dot{\gamma} = 3\text{x}10^{-3}$ 1/s. At intermediate shear-rates between $\dot{\gamma} = 4\text{x}10^{-2}$ 1/s and $\dot{\gamma} = 10^{2}$ 1/s, the viscosity of both gelled and ungelled

collagen solutions exhibited linearly decreasing values on a log-log scale. Lastly, viscosity values of both solutions remained constant, and at the same lowest value of η = 0.0035 Pa-s, for shear-rates in excess of $\dot{\gamma}$ = 4x10^2 1/s. Using this data, the values of shear stress at the wall, τ_R, imposed by the microcapillary flow of these ECM solutions at different volume flow-rates, Q, was then calculated in accordance with the fluid mechanics relations described in Equations (3.1) through (3.4), as listed in **Table 3.1**. Note that the shear stress imposed during microcapillary loading ranged between maximum values of τ_R = 15.1 and 19.1 Pa at the channel wall, but decreased towards a value of τ_R = 0 at the channel centerline in each experiment as per Poiseuelle flow [26, 27].

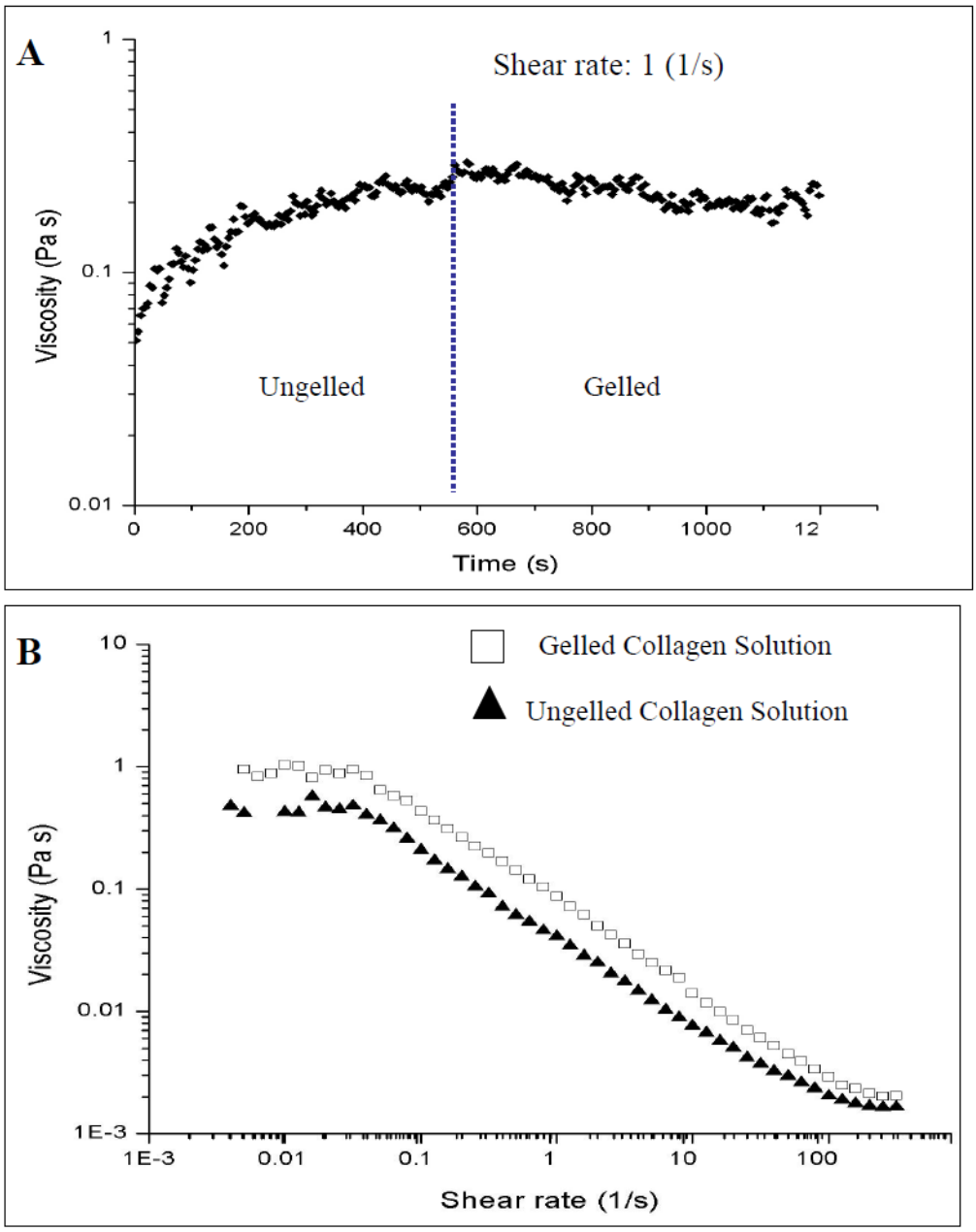

FIGURE 3.2: Rheological data of collagen solutions used as extracellular matrixes (ECM) for fibroblast adhesion and interaction. The graph in (A) illustrates the viscosity of collagen solutions, η, as a function of time, t, at a fixed shear-rate of 1 1/s. The polymer gelation time was estimated as 550 seconds, as denoted by the dashed vertical line. The plot in (B) displays the viscosity of gelled and ungelled collagen solutions as a function of shear-rate, $\dot{\gamma}$. Collagen viscosity is a maximum at low shear-rate ($\dot{\gamma}$ ~10^{-3} 1/s) and a minimum at high shear-rate ($\dot{\gamma}$ ~10^{4} 1/s).

Q (μL/min) [a]	t^{CET} (s) [b]	t^{CF} (s) [c]	τ_R (Pa) [d]
Control (~0)	0	0	0
15.0	14.0	1.6	15.1
20.0	14.0	1.2	16.8
30.0	14.0	0.8	19.1

TABLE 3.1: Conditions used to extrude 100-μl-volume of solution through 100-μm-ID capillary tubings via syringe pump using conditions of constant elution time (CET) and constant flow (CF). Q represents the volume flow-rate used during experiments in units of μL per minute; t^{CET} denotes the solution exposure time to shear stress within microcapillaries using CET loading conditions; t^{CF} depicts the solution exposure time to shear stress within microcapillaries using CF loading conditions; τ_R represents the maximum shear stress present at the channel wall (radius = R), as calculated using the power law fluid model.

Scanning Electron Microscopy (SEM) Illustrates Changes in Collagen Orientation

SEM was used in order to investigate the effects of the shear stresses by the different loading conditions on the collagen microstructure. Three solutions were imaged: (i) Collagen samples of control specimens (minimum shear applied); (ii) Collagen samples following CF loading at 30μl/min through 5-cm capillary tubing, and (iii) Collagen samples after CET loading at 30μl/min through 90-cm capillary tubing. As seen in **Figure 3.3A**, the collagen in the control sample exhibited an ordered alignment, with parallel collagen fibers observed along one preferential angle. Collagen solutions imaged after CET loading, shown in **Figure 3.3B**, appeared significantly disordered and misaligned, as large spacing between the fibers was evident. The collagen samples imaged after CF loading, seen in **Figure 3.3C**, illustrated a similar pattern to the control, but appeared slightly disordered as evidenced by the regions of intersecting collagen fibers.

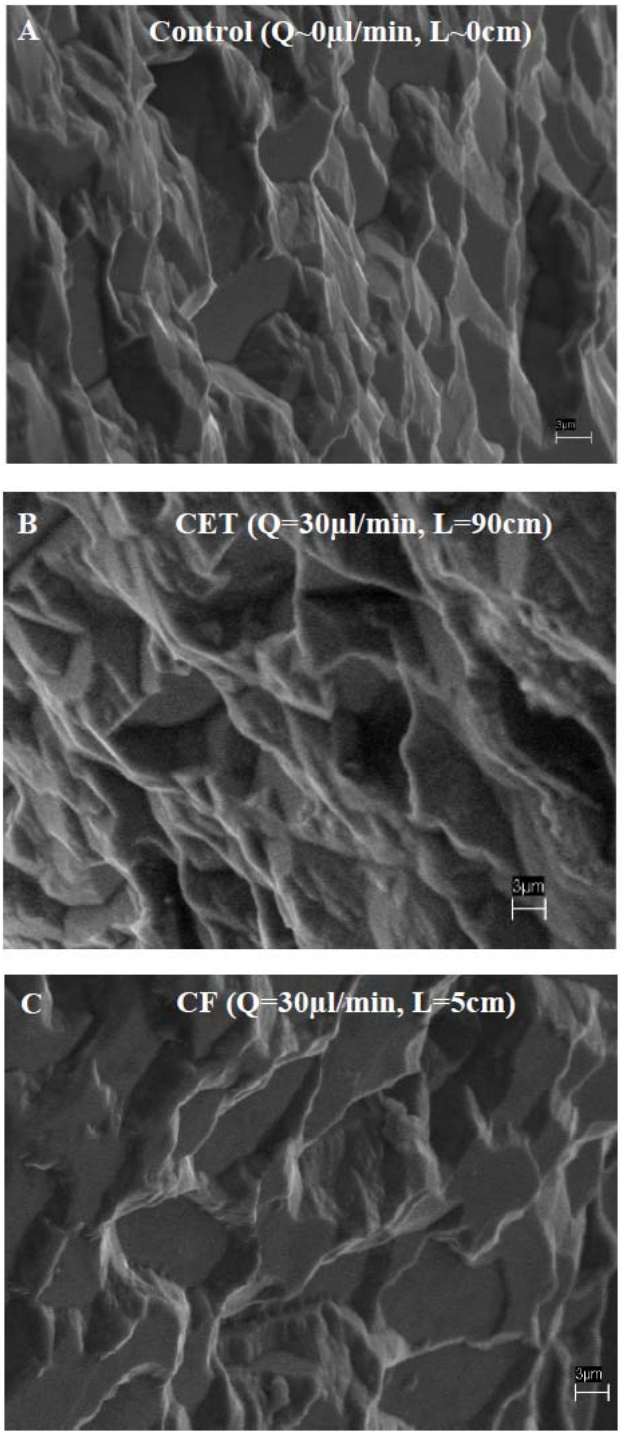

FIGURE 3.3: Scanning electron microscope (SEM) images of collagen samples after shear stress is applied. Control sample (i.e. minimal shear) is shown (A). Collagen samples displaced through 90-cm-long microcapillaries at 30µl/min via Constant Elution Time (CET) loading (B). Collagen samples displaced through 5-cm of microcapillary at 30µl/min via Constant Flow (CF) loading (C). Scale bar: 3µm.

Higher Shear Stress Increased Average Number of Extensions Per Cell

Experiments combined ungelled solutions of extracellular collagen with live populations of cultured fibroblast cells and displaced the solutions through microcapillaries at different volume flow-rates using conditions of Constant Elution Time (CET) and Constant Flow (CF). In addition, populations of cultured fibroblast cells within buffered media solutions (no collagen matrix) were similarly displaced through the microcapillary system using CET and CF conditions as control experiments.

Solutions of buffered fibroblasts pipetted onto dishes as no-shear controls (Q~0) displayed conventional 2-D cellular adhesion to the substrate surface in the absence of matrix (**Figure 3.4A-1**). Solutions of buffered fibroblasts displaced through microcapillaries using CET conditions exhibited cells whose morphologies became more elongated with increased shear stress applied, as cells seen in **Figure 3.4A-2** through **Figure 3.4A-4** illustrate increasingly bipolar morphologies. The average number of primary cytoplasmic extensions was then measured per cell for each experimental condition shown. For example, the cell shown in the control image of **Figure 3.4A-1** displays 3 primary extensions, as highlighted by the surrounding arrows, while the cell seen in **Figure 3.4A-4** exhibits only 2 extensions after CET loading at 30μL/min. The average number of extensions per cell, n^{EXT}, decreased from a value of n^{EXT}= 3.6+/-0.1 in control experiments, to n^{EXT}= 2.4 +/-0.1 (P=0.001) when the maximum volume flow-rate of 30 μL/min was used, as shown in **Table 3.2**. In addition, the average number of cell-cell contacts, n^{C-C}, observed between cells in solution was also tabulated. Here, cell-cell contacts were defined as points where the cytoplasmic extensions of two or more cells

were in physical contact with one another. For the case of CET loading, all cells exhibited 2-D adhesion, and thus, n^{C-C} values represent 2-D contacts only. As shown**,** the average number of cell-cell contacts in CET control experiments was n^{C-C} = 1.5 +/- 0.1, and increased to n^{C-C} = 2.6 +/- 0.1 (P=0.004) between cells loaded at 15 μL/min. However, the difference in the number of cell-cell contacts observed between cells of buffered solutions that were loaded at different volume flow-rates was observed to be minimal, as seen in **Table 3.2**.

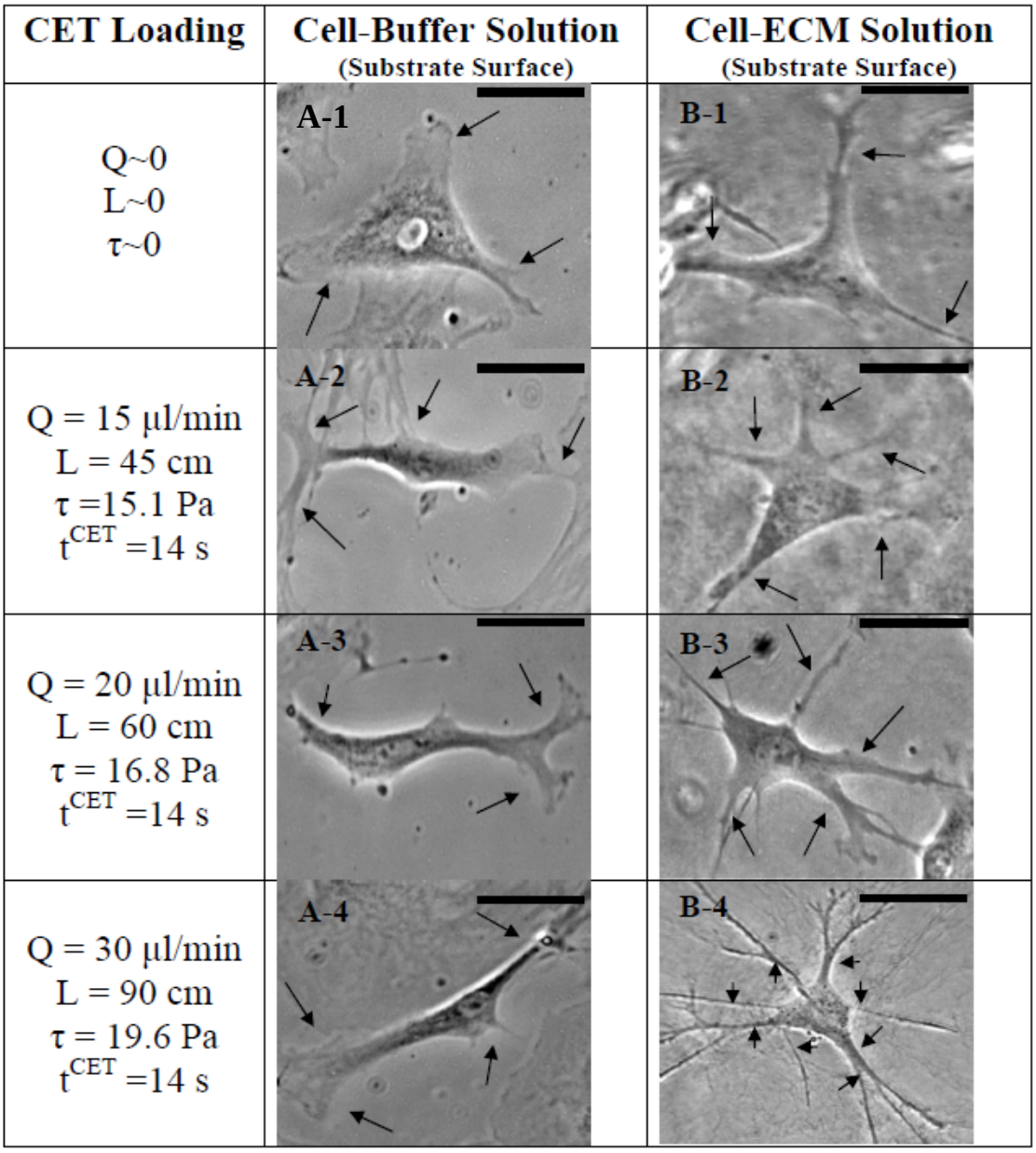

FIGURE 3.4: Images of solutions following microcapillary loading using constant elution time (CET). The CET conditions used during loading are shown, including volume flow-rate, Q, length of capillary tubing, L, shear stress, τ, and loading time within the capillary tubing, t^{CET}. The left-hand column (A-1through A-4) illustrates that cells loaded within PBS solutions (i.e. without extracellular collagen) adhered exclusively onto the inner substrate surface of Petri dishes, with a small numbers of extensions as denoted by arrows. The right-hand column (B-1 through B-4) illustrates that solutions of cells surrounded by extracellular collagen also adhered exclusively to substrate after capillary loading, but displayed a larger number of extensions with increasing volume flow-rate, as denoted by arrows. Scale bar represents a length of 50µm.

Populations of cultured fibroblast cells were next combined with solutions of extracellular collagen matrix and similarly loaded through the microcapillary system using CET conditions. Solutions pipetted onto dishes as no-shear controls (Q~0) displayed gels that supported 3-D cell-cell contacts distributed throughout the collagen ECM. However, solutions of cells within collagen loaded at different volume flow-rates using CET conditions did not support fibroblasts within the 3-D structure of extracellular collagen as seen in **Figure 3.4B:** Cells of all experiments seen in **Figure 3.4B-2** through **Figure 3.4B-4** were observed to adhere exclusively onto the substrate surface, but with an increasing number of cytoplasmic extensions. For example, cells of control **Figure 3.4B-1** illustrate 3 primary extensions per cell, while the cell shown loaded at 30μL/min in **Figure 3.4B-4** illustrates 7 primary extensions, as denoted by arrows. The average number of cell extensions per cell within ECM, n^{EXT}_{ECM}, within control solutions was n^{EXT}_{ECM} = 2.5 +/- 0.2 and increased significantly to n^{EXT}_{ECM} = 7.2 +/- 0.1($P<0.001$) when CET loaded at 30 μL/min. In addition, the average number of cell-cell contacts within ECM, $n^{C\text{-}C}_{ECM,}$ between neighboring cells within control solutions was $n^{C\text{-}C}_{ECM}$ = 0.88 +/- 0.1 and increased significantly to $n^{C\text{-}C}_{ECM}$ = 3.3+/-0.1 ($P=0.002$) when CET loaded at 15 μL/min. However, the average number of cell-cell contacts within ECM displayed little variation with increasing volume flow-rate as seen in **Table 3.2**. Further, the cell-cell contacts were exclusively observed during 2-D cell adhesion to the substrate for all volume flow rates used.

Q (μL/min) [a]	n^{EXT} [b]	n^{EXT}_{ECM}	n^{C-C} [d]	n^{C-C}_{ECM} [e]	τ_R (Pa) [f]
Control (~0)	3.6 +/- 0.1	2.5 +/- 0.2	1.5 +/- 0.1	0.88 +/- 0.2	0.0
15.0 CET	3.4 +/- 0.1	4.4 +/- 0.1	2.6 +/- 0.1	3.3 +/- 0.1	15.1
20.0 CET	3.8 +/- 0.1	6.4 +/- 0.2	2.4 +/- 0.1	3.4 +/- 0.1	16.8
30.0 CET	2.4 +/- 0.1	7.2 +/- 0.1	2.6 +/- 0.1	3.2 +/- 0.2	19.1
Control (~0)	3.6 +/- 0.1	2.5 +/- 0.2	1.5 +/- 0.1	0.88 +/- 0.2	0.0
15.0 CF	4.7 +/- 0.1	3.8 +/- 0.1	1.6 +/- 0.2	0.6 +/- 0.2	15.1
20.0 CF	4.7 +/- 0.1	4.4 +/- 0.1	2.2 +/- 0.1	1.8 +/- 0.2	16.8
30.0 CF	5.5 +/- 0.2	5.3 +/- 0.1	3.4 +/- 0.1	2.3 +/- 0.2	19.6

TABLE 3.2: Data representing the average number of cytoplasmic extensions and cell-to-cell contacts per volume-flow-rate observed following microcapillary loading using conditions of constant elution time (CET) and Constant Flow (CF). Q represents the volume flow-rate used during experiments in units of μL per minute; n^{EXT} denotes the average number of cytoplasmic extensions per cell when loaded within buffered solutions without ECM; n^{EXT}_{ECM} denotes the average number of cytoplasmic extensions per cell when loaded within ECM solutions; n^{C-C} represents the average number of cell-to cell contacts observed between cells loaded within buffered solutions without ECM; n^{C-C}_{ECM} denotes the average number of cell-cell contacts observed between cells loaded within ECM solutions.

Shear Stress Imposed for Short Time Periods Increased Number of 3-D Cell-Cell Contacts within ECM

Experiments were next repeated using conditions of Constant Flow (CF), where solutions were exposed to the same magnitudes of shear stress as in the previous CET experiments, but for shorter time periods. As before, solutions of fibroblasts within buffered media, and solutions of fibroblasts within extracellular collagen were loaded through the microcapillary system. **Figure 3.5A-1** through **Figure 3.5A-4** illustrate that cells of buffered solutions (i.e. no matrix) loaded through the microcapillary system became more elongated with increasing volume flow-rate, and exhibited a small increase in the average number of primary cytoplasmic extensions. The average number of

extensions per cell increased from n^{EXT} = 3.6 +/- 0.1 in the control (Q~0), to n^{EXT} = 5.5 +/- 0.2 (P<0.001) for cells within solutions loaded at 30μL/min as seen in **Table 3.2**. In addition, the average number of cell-cell contacts increased from $n^{C\text{-}C}$ = 1.5 +/- 0.1 in control experiments to $n^{C\text{-}C}$ = 3.4 +/- 0.1 (P=0.001) at 30μL/min. Note that cell-cell contacts remained 2-D in these experiments in the absence of matrix.

The final set of experiments displaced solutions of fibroblasts within extracellular collagen matrix through microcapillaries using conditions of CF. Results of these experiments illustrated that CF loading conditions stimulated the formation of 3-D cell-cell contacts within the collagen ECM. Cells in **Figure 3.5B-1/3.5C-1** through **Figure 3.5B-4/3.5C-4** illustrate cell-cell contacts in one depth of focus within the gel (labeled as the lower level on figure) as well as cell-cell contacts between these same cells and neighbors on a different depth of focus approximately 80-100 μm away (labeled as the upper level in figure). Solutions displaced through capillaries at volume flow-rates of 15, 20, and 30 μl/min illustrated a 3-D cellular distribution within collagen, observed by the focusing of different cells in contact with one another on different representative layers. For example, in **Figure 3.5B-1** cells that were observed out of focus in the lower collagen layer are encircled by a dashed line and imaged in focus in the upper collagen layer shown in **Figure 3.5C-1**. Arrows in both images highlight the 3-D cell-cell contacts evident between cells within the ECM. As illustrated in **Table 3.2**, the average number of extensions per cell within ECM increased from n^{EXT}_{ECM} = 2.5 +/- 0.2 in controls, to n^{EXT}_{ECM} = 5.3 +/- 0.1 (P<0.001) after microcapillary CF loading was performed at 30 μL/min. Further, the average number of cell-cell contacts within ECM increased from $n^{C\text{-}C}_{ECM}$ = 0.88 +/- 0.2 in controls to $n^{C\text{-}C}_{ECM}$ = 2.3 +/- 0.2 (P=0.005) after loading through the

microcapillary system at the highest volume flow-rate of 30 μL/min. Note that these numbers, n^{EXT}_{ECM} and $n^{C\text{-}C}_{ECM}$, were measured only within layers where cells were clearly observed in focus within the ECM. Importantly, these cell-cell contacts were the only 3-D contacts observed within the pre-stressed gels of these experiments.

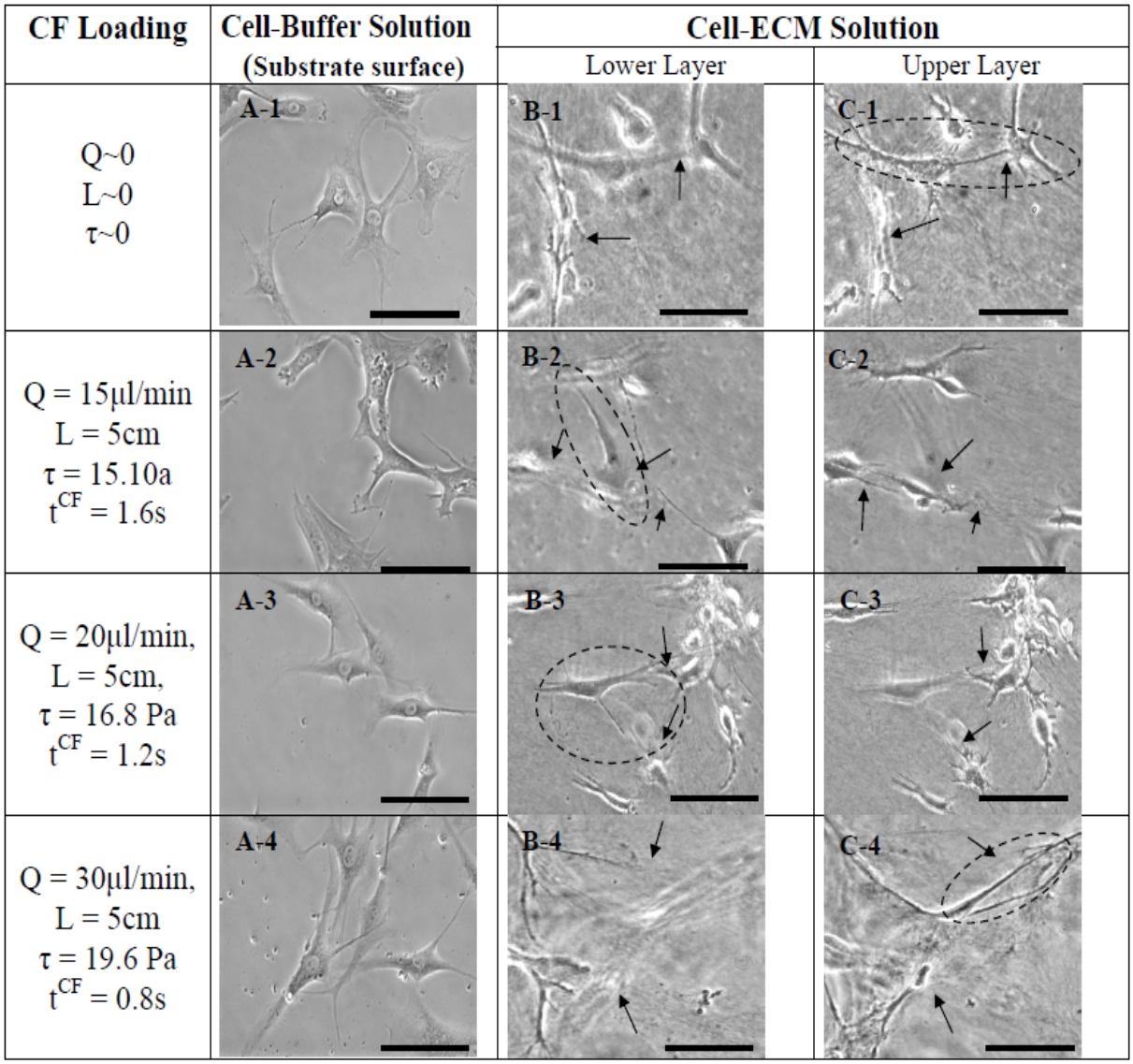

FIGURE 3.5: Images of solutions following loading experiments performed using constant flow (CF) conditions. The conditions of CF loading shown include volume flow-rate, Q, fixed length of capillary tubing, *L*, shear stress, τ, and loading time within the capillary tubing, t^{CF}. Images in the left-hand column (A-1 through A-4) illustrate that cells within PBS solutions loaded through microcapillaries adhered exclusively onto substrate surfaces. Images in the adjoining columns (B-1 through B-4 and C-1 through C-4) illustrate that cells loaded through microcapillaries within extracellular collagen were observed throughout the polymerized gel. Dotted circles within images of the columns (B-1 through B-4 and C-1 through C-4) highlight cells positioned on a lower 3-D plane of extracellular collagen (B-2 and B-3) or a higher 3-D plane (C-1 and C-4) which exhibit contacts with neighboring cells positioned at a higher 3-D plane (C-2 and C-3) or a lower 3-D plane (C-1 and C-4), respectively. Scale bar: 100µm.

Shear Stress Altered Distribution of Gap Junctions between Cells

In order to illustrate how cell-cell communication channels were affected during the different loading conditions used, immunostaining of Cx43 was performed for three different solutions: (i) Solutions of fibroblasts that were not sheared through microcapillaries (i.e. control); (ii) Fibroblasts in solutions that were sheared via CET loading at a volume flow-rate of 30 µl/min through a 90-cm-long microcapillary; and (iii) Fibroblasts in solutions that were sheared via CF loading through a 5-cm-length of microcapillary at a volume flow-rate of 30 µl/min. In control experiments, Cx43 (green) is observed on cell-cell interfaces in a very sparse and scattered pattern as seen in **Figure 3.6A**. Cx43 staining after CET loading is similarly observed along cell-cell interfaces in a disorganized pattern as shown in **Figure 3.6B**. In contrast, fibroblasts exposed to CF loading illustrated a visible, continuous line along cell-cell interfaces as illustrated in **Figure 3.6C**. Cells in control experiments expressed an average of 2.61+/- 0.80 (n=62) Cx43 regions per cell, while cells that were CET loaded expressed approximately 2.3+/- 0.8 (n=74) Cx43 regions per cell, significantly less than that in control ($P<0.0005$). However, cells that were loaded through microcapillaries using CF loading illustrated a larger average of 3.54 +/-1.25 (n=36) Cx43 regions per cell ($P=0.016$) than that in control.

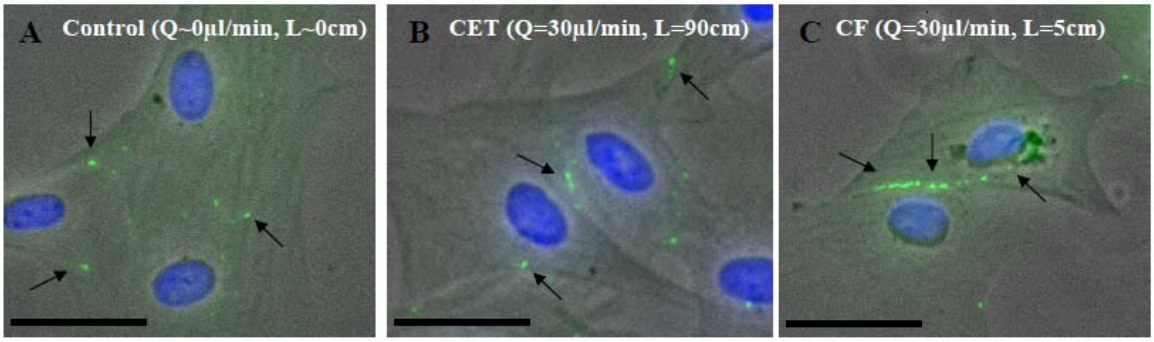

FIGURE 3.6: Immunostained images of the gap junction protein Connexin 43 (Cx43) expressed in fibroblast cells. Cx43 (Green) and cell nuclei (Blue) observed within control solutions (i.e. minimum shear stress) (A) Cx43 and nuclei of cells seen within solutions loaded through 90-cm-long microcapillaries using Constant Elution Time (CET) conditions at a volume flow-rate of 30µl/min (B). Cx43 and cell nuclei within solutions sheared at 30µl/min within a 5-cm-long capillary via Constant Flow (CF) loading, Arrows point to Cx43. Scale bar: 40µm.

3.4 DISCUSSION

The ability to influence the formation of 3-D interconnected networks of cells within extracellular matrix is significant to the study of cell-cell interactions within natural and synthetic biopolymers, as well as critical to the development of novel biomaterials that mimic in vivo tissue response. This study demonstrated an increase in the average number of 3-D cell-cell contacts within ECM when solutions were exposed to fluidic shear stresses for different time periods. Dilute solutions of ECM were used for this study in order to illustrate how small values of shear stress imposed on polymers with widely-spaced 3-D structures have large impacts on cell-cell interactions within a supporting matrix. [28]

Fundamental rheological experiments of the dilute collagen ECM solutions used confirmed a classical, shear thinning viscosity profile that exhibited a decrease in viscosity under the influence of increased values of shear-rate (**Figure 3.2**). Further, all solutions were loaded through microcapillaries for time periods less than the gelation

time of 9 minutes, which eliminated polymerization factors as potential effectors of observed changes in the cell-cell contacts within each capillary-loaded matrix. SEM imaging was utilized to examine how the polymer microstructure of the collagen ECM used was altered by the shear stresses imposed via CET and CF loading. SEM images of control samples of ECM (no shear stress) illustrated an organized alignment of collagen fibers that was only slightly disrupted after loading using CF conditions, but significantly altered after the longer loading times imposed via CET conditions (**Figure 3.3**). As seen, the ECM exhibited an increased spacing between fibers after CET loading, indicative of altered pore size and/or pore distribution within the ECM. As it has been recently suggested that 3-D cell-cell interactions depend largely upon the structure of the surrounding ECM [29-31], subsequent experiments seeded collagen solutions with cultured fibroblast cells in order to examine how shear-induced changes in the ECM polymer structure affected cell-cell networking within the collagen.

Cells within buffered solutions (as a control) displaced through microcapillaries using CET conditions adhered exclusively to the substrate surface (presumably due to lack of matrix) and exhibited small changes in cell morphology as a function of increasing flow-rate, i.e. larger imposed shear stress (**Figure 3.4A**). However, while the average number of cell extensions per cell decreased slightly with increasing flow-rate, the average number of cell-cell contacts upon the substrate surface increased after shear stress was imposed (**Table 3.2**). This pattern suggests that shear flow enabled better contact between neighboring cells, but could not stimulate 3-D cell-cell networking without a surrounding ECM. The same CET experiments performed using cells within ECM exhibited very different results. Cells within ECM that were exposed to minimal

shear stress via pipette were observed to be distributed within the 3-D structure of the matrix, while solutions of cells within ECM loaded through microcapillaries at any volume flow rate resulted in 2-D adhesion to the substrate independent of the volume flow-rate used (**Figure 3.4B**). Cells within CET loaded collagen solutions displayed an increasing number of extensions with increased volume flow rate, as well as an increase in the average number of visible cell-cell contacts (2-D) on the substrate surface (**Table 3.2**). As previously suggested in the literature, the number of extensions per cell can be interpreted to represent the ability of cells to transduce mechanical stimuli onto their surroundings [8, 32, 33]. The behavior observed here suggests that the imposed shear stress increased the ability of cells to transduce stimuli not only to the matrix onto which they were adhered, but also to neighboring cells in order to stimulate communication and perhaps induce concerted cell response.

Solutions of cells loaded through the microcapillary system using CF conditions, with and without surrounding ECM, displayed measurable differences in cell connectivity, distribution, and morphology (**Figure 3.5**). Solutions of cells loaded without ECM as a control displayed a slightly increased average number of extensions with increasing shear stress, while cells loaded within collagen displayed nearly twice as many extensions as the control experiment (**Table 3.2**). However, the most significant difference observed between solutions of cells imposed to shear stresses within ECM and without ECM was the 3-D cellular interconnectivity observed between cells surrounded by extracellular collagen (**Figure 3.5**): Only shear stresses imposed upon cells CF loaded within ECM resulted in 3-D interconnected network**s**. These results illustrate that the shear stress applied using CF conditions generated 3-D networking within ECM, while

the same magnitudes of shear stress applied via CET loading did not. This observed difference can be attributed to the previously-discussed shear-induced changes in the structure of the surrounding matrix imposed by CET and CF conditions (**Figure 3.3**).

CET conditions imposed shear stress onto ECM solutions for the same period of time regardless of the flow-rate used, meaning cells within the matrix were displaced through longer lengths of capillary per increasing flow-rate. The longer loading time and displacement distance imposed via CET likely prevented 3-D cell-cell contact by generating larger amounts of chain stretching and disentanglement within the ECM polymeric structure as seen via SEM. However, several polymer studies have also illustrated that flexible polymers and macromolecules in pressure-driven microchannel flows migrate away from the channel walls and towards the centerline [34, 35]. This phenomenon, known as cross-streamline migration, is enhanced in flows within channels of large length to diameter ratios, leading to accumulation of molecules within the channel centerline. In the case of CET loading, a cross-streamline migration of cells towards the capillary axis may have led to a condition where cells were in close contact with one another, but had little interaction with polymer chains stretched and/or disentangled near the channel walls. This close contact may have caused mechanical stimulation that led to an increase in the average number of extensions per cell observed, but could not initiate 3-D cell-cell contacts within the surrounding sheared polymer chains. In contrast, CF conditions displaced solutions through a shorter, fixed-length microcapillary regardless of the flow-rate used, thereby significantly reducing, or eliminating, cross-streamline migration. Here, the shear stress imposed via microcapillary loading seemed to increase the average number of cell-cell contacts observed with short

exposure to increased shear stress, and perhaps enhance the cell-matrix adhesion needed to support 3-D cell-cell contacts within the surrounding matrix (**Table 3.2**).

Lastly immunostaining of Cx43 illustrated an increased number of cell-cell contacts along fibroblast interfaces when shear stresses were applied during short time CF loadings. Cx43 is seen continuously along the cell interfaces after CF loading, compared to the scattered distribution seen within the control and CET loading experiments (Figure 6). These results were consistent with independent statistical analysis that illustrated cell-cell contacts were significantly increased after exposure to shear stresses via CF loading (Table 2). Hence, we propose that shear stresses imposed for short-time periods may play an important role in generating 3-D cell networks within ECM.

3.5 CONCLUSION

Results of this work illustrate that both the duration and magnitude of imposed fluidic shear stresses contribute to 3-D cell-cell contacts supported within ECM. Such results imply there exists an optimal shear stress and exposure time for a given cell-ECM pair that can promote cell adhesion, contact, and ultimately communication and response. Such findings open possibilities to employ fluid flows to influence cell adhesion to desired bio-matrixes, as well as to promote cell-cell contacts and communication between cells within natural and synthetic ECM. Such avenues of research will enable development of materials that promote contacts between cells of different tissues and/or different points in cell lineage, as well as stimulate communication between cells at

various stages of repair for improved interfacial biomaterials, desired cell differentiation, and understanding of Human health and disease.

ACKNOWLEDGEMENTS:

This study was supported by NIH GM071702-01 and PSC-CUNY. The authors thank Mr. Amar B. Pawar and Dr. Yongwoo Inn from the Chemical Engineering Department of The City College of New York for kind assistance in Scanning Electron Microscopy and rheological measurements, respectively.

.

REFERENCES

1. Gumbiner, B.M. and K.M. Yamada, Cell-to-cell contact and extracellular matrix. Curr Opin Cell Biol, 1995. **7**(5): p. 615-8.
2. Chen, C.S.T., J. Tien, J. , Mechanotransduction at cell-matrix and cell-cell contacts. Annu Rev Biomed Eng, 2004. **6**: p. 275-302.
3. Woo, S.L.J., F. Zou, L. Gabriel, M. T., Functional tissue engineering for ligament healing: potential of antisense gene therapy. Ann Biomed Eng, 2004. **32**(3): p. 342-51.
4. Cukierman E., P.R., Yamada KM,, Cell interactions with three-dimensional matrices. Current Opinion in Cell Biology, 2002. **14**: p. 633-639.
5. DeMali KA, W.K., Burridge K, , Integrin signaling to the actin cytoskeleton Current Opinion in Cell Biology, 2003. **15**(5): p. 572-582.
6. Hynes RO, Cell adhesion: old and new questions. Trends Cell Biol, 1999. **9**: p. M33-M77.
7. DeMali, K.A., K. Wennerberg, and K. Burridge, Integrin signaling to the actin cytoskeleton. Curr Opin Cell Biol, 2003. **15**(5): p. 572-82.
8. Jiang, H. and F. Grinnell, Cell-matrix entanglement and mechanical anchorage of fibroblasts in three-dimensional collagen matrices. Mol Biol Cell, 2005. **16**(11): p. 5070-6.
9. Robert, L., Matrix biology: past, present and future. Pathol Biol (Paris), 2001. **49**(4): p. 279-83.
10. Zavan, B.B., P. Vindigni, V. Amadori, A. Habeler, W. Pontisso, P. Montemurro, D. Abatangelo, G.Cortivo, R., Extracellular matrix-enriched polymeric scaffolds as a substrate for hepatocyte cultures: in vitro and in vivo studies. Biomaterials, 2005. **26**(34): p. 7038-45.
11. Garvin, J.Q., J. Maloney, M. Banes, A. J., Novel system for engineering bioartificial tendons and application of mechanical load. Tissue Eng, 2003. **9**(5): p. 967-79.
12. O'Brien, F.J.H., B. A. Waller, M. A. Yannas, I. V. Gibson, L. J. Prendergast, P. J., The effect of pore size on permeability and cell attachment in collagen scaffolds for tissue engineering. Technol Health Care, 2007. **15**(1): p. 3-17.
13. Ng, C.P. and M.A. Swartz, Mechanisms of interstitial flow-induced remodeling of fibroblast-collagen cultures. Ann Biomed Eng, 2006. **34**(3): p. 446-54.
14. Thi, M., Kojima, T, Cowin SC, Weinbaum, S, Spray, DC,, Fluid shear stress remodels expression and function of junctional proteins in cultured bone cells. Am J Physiol Cell Physiol, 2002. **284**: p. 389-403.
15. Cheng, B., et al., Expression of functional gap junctions and regulation by fluid flow in osteocyte-like MLO-Y4 cells. J Bone Miner Res, 2001. **16**(2): p. 249-59.
16. DePaola, N., et al., Spatial and temporal regulation of gap junction connexin43 in vascular endothelial cells exposed to controlled disturbed flows in vitro. Proc Natl Acad Sci U S A, 1999. **96**(6): p. 3154-9.
17. Forgacs, G.N., S. A. Hinner, B. Maier, C. W. Sackmann, E., Assembly of collagen matrices as a phase transition revealed by structural and rheologic studies. Biophys J, 2003. **84**(2 Pt 1): p. 1272-80.

18. Newman, S.C., M. Allain, C. Forgacs, G. Beysens, D., Viscosity and elasticity during collagen assembly in vitro: relevance to matrix-driven translocation. Biopolymers, 1997. **41**(3): p. 337-47.
19. Ehrlich, H.P. and T. Diez, Role for gap junctional intercellular communications in wound repair. Wound Repair Regen, 2003. **11**(6): p. 481-9.
20. Callaway, G.H.F., L. D. Deng, X. H. Torzilli, P. A. O'Brien, S. J. Altchek, D. W. Warren, R. F., Biomechanical evaluation of the medial collateral ligament of the elbow. J Bone Joint Surg Am, 1997. **79**(8): p. 1223-31.
21. Hung, C.T.A., F. D. Pollack, S. R. Attia, E. T. Hannafin, J. A. Torzilli, P. A. , Intracellular calcium response of ACL and MCL ligament fibroblasts to fluid-induced shear stress. Cell Signal, 1997. **9**(8): p. 587-94.
22. Saltzman, W.M.P., M. R. Parsons-Wingerter, P. Zhu, W. H.,, Three-dimensional cell cultures mimic tissues. Ann N Y Acad Sci, 1992. **665**: p. 259-73.
23. Wright, R.W.A., T. El-Zawawy, H. B. Brodt, M. D. Silva, M. J. Gill, C. S. Sandell, L. J., Medial collateral ligament healing in macrophage metalloelastase (MMP-12)-deficient mice. J Orthop Res, 2006. **24**(11): p. 2106-13.
24. R. Byron Bird, C.F.C., Robert C. Armstrong, Ole Hassager Dynamics of Polymeric Liquids Volume II. 2nd ed. 1989, New York, NY: Wiley Brothers.
25. Wu, C.C.D., S. J. Wang, Y. H. Tang, M. J. Chang, H. C., Mechanical properties of collagen gels derived from rats of different ages. J Biomater Sci Polym Ed, 2005. **16**(10): p. 1261-75.
26. Lazouskaya, V., Y. Jin, and D. Or, Interfacial interactions and colloid retention under steady flows in a capillary channel. J Colloid Interface Sci, 2006. **303**(1): p. 171-84.
27. Kong, Q. and M. Vazquez, Internal fluid flow increases cellular interconnects between Medial Collateral Ligament fibroblasts and cellular extensions within three-dimensional collagen matrixes. Cell Commun Adhes, 2006. **13**(3): p. 139-49.
28. Vazquez, M., D. Matsudaira, P. Ehrlich, D. McKinley, G., Shear-induced degradation of linear polyacrylamide solutions during pre-electrophoretic loading. Anal Chem, 2001. **73**(13): p. 3035-44.
29. Lo IK, O.Y., Rattner JP, Hart DA, Marchuk LL, Frank CB, Rattner JB,, The cellular networks of normal ovine medial collateral and anterior cruciate ligaments are not accurately recapitulated in scar tissue. J Anat., 2002. **200**(Pt 3): p. 283-96.
30. Pizzo AM, K.K., Vaughn LC, Waisner BZ, Voytik-Harbin SL, Extracellular matrix (ECM) microstructural composition regulates local cell-ECM biomechanics and fundamental fibroblast behavior: a multidimensional perspective. J. Appl Physiol, 2005. **98**(5): p. 1909-21.
31. Tamariz, E. and F. Grinnell, Modulation of fibroblast morphology and adhesion during collagen matrix remodeling. Mol Biol Cell, 2002. **13**(11): p. 3915-29.
32. Martin-Bermudo, M.D. and N.H. Brown, The localized assembly of extracellular matrix integrin ligands requires cell-cell contact. J Cell Sci, 2000. **113 Pt 21**: p. 3715-23.
33. Mogilner, A., On the edge: modeling protrusion. Curr Opin Cell Biol, 2006. **18**(1): p. 32-9.

34. Kang, K., L.J. Lee, and K. Koelling, High Shear Microfluidics and its application in rheological measurement. Experiments in Fluids, 2005. **38**: p. 222-232.
35. Saintillan, D.S., ES Darve, E, Effect of flexibility on the shear-induced migration of short-chain polymers in parabolic channel flow. J. Fluid Mech., 2006. **557**: p. 297-306.

CHAPTER 4

A Microfluidic Device to Establish Non-Linear Concentration Gradients using Natural Convection-Driven Forces

Qingjun Kong

Department of Mechanical Engineering

The City College of The City University of New York (CCNY)

160 Convent Ave., ST-481

New York, NY 10031

Qkong@gc.cuny.edu

Phone: 212.650.6766 Fax: 212.650.6727

and

*Maribel Vazquez, Sc.D.**

Department of Biomedical Engineering

The City College of The City University of New York (CCNY)

160 Convent Ave., Steinman Hall Room 403D

New York, NY 10031

Vazquez@ccny.cuny.edu

Phone: 212.650.5209 Fax: 212.650.6727

**Corresponding Author*

Keywords: microfluidic device, microfabrication, concentration gradient, Dextran

Abstract:

Microfabrication has been largely utilized to establish chemical concentration gradients and control microenvironments. However, additional facilities are mostly required to facilitate microfluidic flow, which is often associated with excessive reagent consumption and extra equipment cost. Using microfabrication, a two-layer poly-dimethylsiloxane (PDMS) micro-device, named the bridged μlane system, was fabricated in our laboratory to generate chemical concentration gradients. Fluorescently labeled Dextran (MW: 10 kDa) was used to test feasibility of the microsystem. The Dextran transport within the microsystem was imaged and predicted via numerical simulation. Results illustrated that the diffusion coefficient of Dextran measured using our methodology was in line with the published values, indicative of the feasibility and reliability of our microsystem to generate chemical concentration gradients.

4.0 Introduction

Microfabrication techniques have been widely adapted to develop systems that generate specific spatial chemical concentrations and concentration gradient profiles in real time [13-16]. Various groups have developed microfluidic devices that generate linear [9, 10, 24] and non-linear concentration gradients [25, 26] via forced fluid flow induced by pumps, micromagnetics [27] and acoustic manipulation [28]. The majority of such systems, however, requires costly facilities and equipment for device fabrication and/or sample handling/operation, including 3-D photolithographic layering [31], piezoelectric microactuators [33], and external power supplies [24, 25, 34]. The current study has developed a microfluidic device called the bridged μLane system to generate linear and non-linear concentration gradients using natural convection-driven forces. In brief, it consists of two layers of biocompatible material. The top layer serves to maintain consistent experimental conditions. The bottom layer has a single microchannel, where samples are loaded and examined. The microsystem has been tested using fluorescently-labeled Dextran to ensure feasibility and reliability of chemical gradient generation. Our system can sustain steady-state with ultra-low bulk velocity over several days and can be used for various applications including chemotaxis, cancer cell metastasis, and salinity gradients. Our system can also be used to generate transient chemical gradients and examine their time-evolving effects on samples, such as transient cell migration and particle movement. Further, this stand-alone system can be fabricated in a conventional laboratory without costly computerized apparatus, external power supplies, or clean room facilities.

In this work, the design and fabrication of the bridged μlane system is presented, alongside experimental and numerical validation to generate concentration gradients that were mathematically predicted via convective Fickian diffusion.

4.1 Materials and Methods

4.1.1 Design: The bridged μlane system consists of two layers of poly-dimethylsiloxane (PDMS) with a closed microchannel and two fluidic reservoirs on the first layer, and two fluidic chambers and an open bridge channel on the second, as shown in **Figure 4.1**. The first layer contains two, 3.0-μL-volume reservoirs, the source reservoir (SRR) and sink reservoir (SKR), connected by a single, closed microchannel, or μLane, of 13,000μm length and 94.8μm hydraulic diameter, using $D_h=4A/P$ [44] where *A* is the cross-sectional area and *P* is the perimeter. The ratio of the μLane length to its hydraulic diameter (approximately 137) was kept large in the design in order to facilitate stable, one-dimensional transport within the microchannel. The volume ratio of each reservoir to the μLane was also kept large (approximately 27) in order to maintain stable transport between each reservoir and the microchannel.

The system's 2nd layer of PDMS consists of two cylindrical chambers, defined as the source chamber (SRC) and sink chamber (SKC), and a semi-circular, open channel, known as the bridge (**Figure 4.1B**). The SRC and SKC chambers are of 6-mm-diameter and 6-mm-height each (170uL), and are vertically and fluidically connected with the SRR and SKR reservoirs in the 1st layer of the system, respectively. In addition, the SRC and SKC are connected to each other via the bridge, which is an open channel of 9-mm-length and 2-mm-depth. The bridge is used to balance the solution volume within the

SRC and SKC chambers, in order to eliminate pressure differences between them that would generate pressure gradients within the μlane to thereby affect transport during loading and/or experiments. The volume of each chamber (170 μl) was designed to be 20 times larger than the reservoir and 1450 times larger than that of the μLane, in order to facilitate gradual transport into the microchannel with minimal entrance effects. Further, large ratio of chamber volume to μLane volume facilitated modeling of constant reagent concentration in the chambers during transport experiments.

4.1.2. Microfabrication of bridged μLane system: System fabrication was performed via three different processes: i) Fabrication of microchannel-patterned mold using contact photolithography; ii) Fabrication of the 1st layer PDMS using elastomeric molding and bonding; and iii) Fabrication of the 2nd layer PDMS using elastomeric molding.

i) Photolithography: A pre-cleaned glass substrate was coated with an adhesion promoter, Surpass 3000, (DisChem Inc., Ridgway, PA) and an 100-μm-thick layer of negative photoresist, SU-8 2075, (MicroChem Inc., Newton, MA) using a spin coating apparatus (Laurell Tech. Corp., North Wales, PA). The substrate was baked on a hot plate and irradiated with UV light using a laboratory-fabricated photomask containing desired microchannel patterns (intensity: 21700-8900 μW/cm^2 at 2-10 inches, Model B-100AP, UVP Inc., Upland, CA). Substrates were then re-baked, allowed to cool at room temperature (25°C), and immersed in SU-8 developer (MicroChem Inc., Newton, MA) until photoresist patterns were visible. The patterned substrate exhibited dimensions of 13.0±0.1-mm-length (mean ± SD) by 100±5-μm-width by 90±1-μm-hight as measured

via surface profilometer (Model SJ-301, Mitutoyo America Corp., Middlesex, NJ) and optical microscope (Nikon TE2000, Morrell Instrument Company Inc., Melville, NY).

ii) Fabrication of the 1st layer PDMS: Liquid-state poly-dimethylsiloxane (PDMS) mixed with silicone elastomer curing agent (Dow Corning Corp., Midland, MI) was degassed and poured onto the photoresist-patterned substrate described above. After polymerization, the PDMS elastomer was peeled from the patterned substrates resulting in open microchannels of 13.0±0.1-mm-length by 100±5-μm-width and 90±1-μm-depth. Subsequently, it was punctured with 2-mm-diameter pipette tips (Model 9-inch Pasteur Pipette, Fisher Scientific Co., Agawam, MA) on both ends in order to generate two reservoirs with approximately 9 μl volume each, defined as the source (SRR) and sink reservoirs (SKR). The PDMS elastomer was bonded onto a pre-cleaned glass substrate (unpatterned) by applying ozone generated via a high-frequency generator (Electro-Technic Products, Inc., Chicago, IL) onto both the PDMS and glass surfaces for 30 seconds each. The 1st layer PDMS was then generated as shown in **Figure 4.1A**. Cross-section uniformity of the closed microchannel itself within this 1st layer was verified using an optical microscope (Nikon TE2000). Since large machines, such as deep reactive-ion etching (DRIE) apparatus, were not used in the microfabrication, the cross-section was semi-hemispherical [40-43], as examined via profilometer and optical microscope. We note that such shape was observed to minimize PDMS bulging effects when solutions were loaded into the system [45].

iii) Fabrication of the 2nd layer PDMS: For the second layer of PDMS, a laboratory-made acrylic mold was manufactured via milling machine, to match the dimensions of the SRC, SKC and bridge. After the acrylic mold was aligned on top of the

1st layer PDMS, the mixed solution of liquid-state PDMS and curing agent were poured around the acrylic mold to form a 6-mm-thick 2nd layer PDMS. After the PDMS was polymerized, the acrylic mold was removed. The 2nd layer PDMS consisted of two cylindrical chambers, and a semi-circular, open channel, or so-called bridge channel (**Figure 4.1B**). The two chambers, of 6-mm-diameter and 6-mm-height each, were defined as the source chamber (SRC) and sink chamber (SKC). The SRC and SKC chambers were vertically and fluidically connected with the SRR and SKR reservoirs, respectively, in the 1st layer (**Figure 4.1C**).

The complete bridged μLane system is thus composed of an open bridge channel that connects the SRC and SKC chambers, as well as a closed microchannel that connects the SRR and SKR reservoirs.

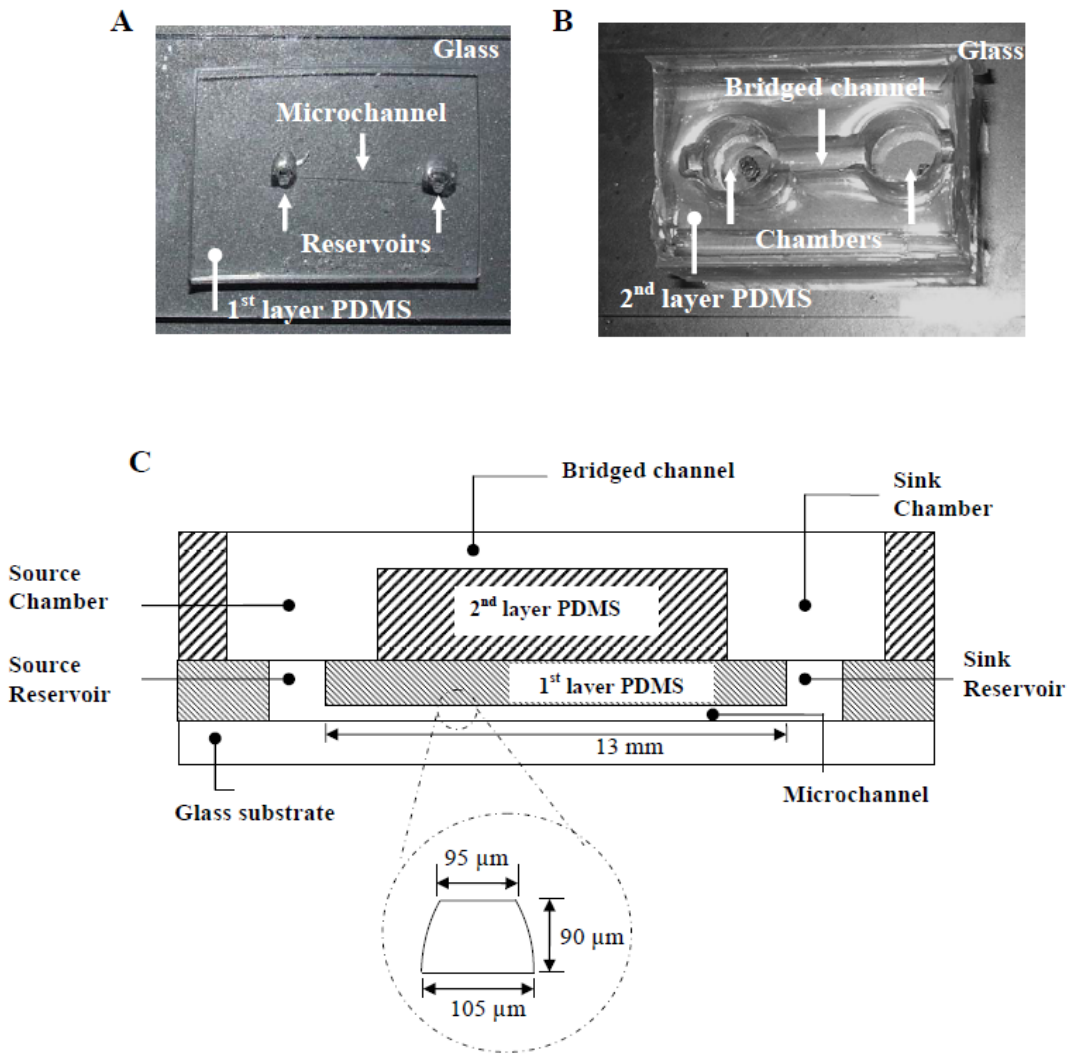

Figure 4.1: Images and schematic of the bridged µLane system. After photolithography and elastomeric molding, a microchannel with two reservoirs was fabricated in polymerized PDMS, defined as the 1st layer PDMS of the bridged µLane system. This PDMS layer was then bonded onto an ultrasonically-cleaned microscope glass slide (A). A second layer of PDMS, consisting of a bridge channel and two chambers, was molded on top of the 1st layer PDMS (B). This layer of PDMS was defined as the 2nd layer PDMS of the system. The chambers in the 2nd layer PDMS were fluidically connected with the reservoirs in the 1st layer PDMS, as shown in the bridged µLane system schematic (C) (not to scale). The microchannel approximately measures 13 mm in length, 90 µm in depth and 100 µm in width (averaged with the upper side of 95 µm and the lower side of 105 µm), as its semi-hemispherical cross-section was shown in inset.

4.1.3. Mathematical modeling of molecule transport: Two-dimensional numerical simulations were performed to describe the transport within the microchannel, both the SRR and SKR reservoirs in the 1st layer PDMS, the bridge channel, and both the SRC and SKC chambers in the 2nd layer PDMS as shown in **Figure 4.3A**. Mathematical modeling of transport within the bridged μLane system was separated into four regions: (i) Transport between the source chamber (SRC) on the 2nd layer and the source reservoir (SRR) on the 1st layer; (ii) Transport within the microchannel in the 1st layer; (iii) Transport between the sink reservoir (SKR) on the 1st layer and the sink chamber (SKC) on the 2nd layer; and (iv) Transport along the bridge channel in the 2nd layer. The transport within the entire microsystem was modeled using a two-dimensional mass transport equation [47]:

$$\frac{\partial C}{\partial t} + V_x \frac{\partial C}{\partial x} + V_y \frac{\partial C}{\partial y} = D\left(\frac{\partial^2 C}{\partial x^2} + \frac{\partial^2 C}{\partial y^2}\right) \qquad (4.1)$$

where C (kg/m^3) is the concentration, V_x (m/s) is bulk flow velocity at the x axis, V_y (m/s) is bulk flow velocity at the y axis and D (m^2/s) is the diffusion coefficient of the reagent molecule. The origin of the coordinate was set at the lower corner of the interface between the SRR reservoir and the microchannel, i.e. the entrance of the microchannel, as shown in **Figure 4.2A**. All physical boundaries of the microsystem were regarded as insulated boundaries of mass transfer because sample solutions do not permeate through PDMS wall boundaries.

i) Diffusion within the SRR reservoir: Reagent molecules transported vertically from the SRC chamber to the SRR reservoir. However, at the low region near the bottom of the SRR reservoir, reagent molecules transported horizontally toward the microchannel, as illustrated in **Figure 4.2A**. Therefore, the entire diffusion within the

SRR reservoir was 2-D. Additionally, diffusion was dominated within the reservoir due to the lack of bulk flow, i.e. convection, examined using 1μm-diameter fluorescent beads (Cat. # T7282, Molecular Probes, Eugene, OR). Note that the effects of gravity on reagent molecule migration within the reservoir were neglected. Hence, the governing diffusion equation (1) was then simplified to be:

$$\frac{\partial C}{\partial t} = D(\frac{\partial^2 C}{\partial x^2} + \frac{\partial^2 C}{\partial y^2}) \qquad (4.2)$$

The initial reagent concentration within the SRR reservoir was set 0 μg/ml because no reagent was added into the reservoir. The initial molecule concentration within the SRC chamber was set to C_H=40 μg/ml and held constant during the simulation, as the chamber volume was so large as to maintain approximately constant sample concentration during the reagent transport experiments. The molecule concentration at the interface between the SRC chamber and the SRR reservoir was constantly set C=40 μg/ml. The reagent concentration at the interface between the reservoir and the entrance of the microchannel within the SRR reservoir ($C_{x=0-}$) was assumed equal to the reagent concentration at the interface within the microchannel ($C_{x=0+}$), i.e. $C_{x=0-}$= $C_{x=0+}$, indicative of continuous boundary.

ii) Transport within the microchannel: The transport within the microchannel from the SRR reservoir to the SKR reservoir was modeled as one-dimensional because of the large ratio of microchannel length to its hydraulic diameter (137: 1), as shown in **Figure 4.2B**. The governing equation (1) was then simplified to be:

$$\frac{\partial C}{\partial t} + V\frac{\partial C}{\partial x} = D\frac{\partial^2 C}{\partial x^2} \qquad (4.3)$$

The initial concentration of reagent within the entire microchannel was set to C=0 μg/ml, as no reagent was filled during reagent transport experiments. The boundary at the entrance of the microchannel was set as continuous boundary ($C_{x=0-}$= $C_{x=0+}$) as mentioned above. Meanwhile, the boundary at the exit of the microchannel (x=0.013 m) was also set as a continuous boundary, i.e. $C_{x=0.013-}$= $C_{x=0.013+}$, as the concentration within the SKR reservoir at the interface between the microchannel and the reservoir ($C_{x=0.013-}$) was regarded to be equal to the concentration within the SKR reservoir at the interface ($C_{x=0.013+}$). Experiments using the beads were performed to measure the bulk velocity within the microchannel, which will be discussed later.

iii) Diffusion within the SKR reservoir: Reagent transport from the SKR reservoir to the SKC chamber also exhibited pure diffusion as a result of no bulk flow found within the reservoir. The reagent horizontally transported into the bottom of the SKR reservoir from the microchannel while the reagent was also found to vertically diffuse into the SKC chamber, as shown in the **Figure 4.2C**. The effects of gravity on reagent diffusion were neglected due to the lack of bulk flow within the reservoir. The diffusion within the entire SKR reservoir was 2-D. The governing equation simplified from Equation (1) then became:

$$\frac{\partial C}{\partial t} = D\left(\frac{\partial^2 C}{\partial x^2} + \frac{\partial^2 C}{\partial y^2}\right) \qquad (4.4)$$

The initial reagent concentration within the SKR reservoir was also set to C=0 μg/ml, as no reagent was added into the reservoir during diffusion experiments. The initial reagent concentration within the SKC chamber in our model was set C_L=0 μg/ml as the chamber was large enough to maintain constant zero concentration and no reagent was added during the entire experiements. The concentration at the boundary between the SKC

chamber and the SKR reservoir was set to C=0 μg/ml. The boundary between the SKR reservoir and the microchannel (x=0.013 m) was regarded as continuous boundary, i.e. $C_{x=0.013-}= C_{x=0.013+}$, as mentioned above.

iv) Diffusion within the bridge channel: Reagent transport within the bridge channel from the SRC chamber to the SKC chamber was modeled as 1-D diffusion because no bulk flow was observed during experiments using fluorescent beads, as displayed in **Figure 4.2D**. Therefore, the governing equation derived from the Equation (1) was then simplified to be:

$$\frac{\partial C}{\partial t} = D\frac{\partial^2 C}{\partial x^2} \qquad (4.5)$$

The initial concentrations of the SRC chamber and the SKC chamber were set to C_H=40 μg/ml and C_L=0 μg/ml, respectively, and maintained constant during simulations.. The initial reagent concentration within the bridge channel was C=0 μg/ml, as no reagent was added initially. The concentrations at the boundaries of the interface between the SRC chamber and the bridge channel, and the interface between the SKC chamber and the bridge channel were constantly set C=40 μg/ml and C=0 μg/ml, respectively, during simulations.

Finite-element-analysis (FEA) software FEMLab Version 3.2 (Comsol Inc., Burlington, MA) was used to solve these four interconnected equations, as shown in **Figure 4.2E**. A fine mesh of 1504 elements was used to generate the distance between nodes to be less than 8 μm. Note that simulation results were approximately the same (<1%) when finer meshes were used.

4.1.4. Mathematical modeling of fluid flow within the microchannel: Solution flow within the microchannel was approximately modeled as Poiseuille flow due to the large ratio of microchannel length to its hydraulic diameter, as mentioned above. The origin of the cylindrical coordinate was set at the central streamline of the microchannel. The radius, r, was used to approximately characterize the cross-sectional dimension of the microchannel. The governing equation of Poiseuille flow using cylindrical coordinates is described in Equation (6) [ref]:

$$\frac{1}{r}\frac{\partial}{\partial r}\left(r\frac{\partial U_x}{\partial r}\right)=\frac{1}{\mu}\frac{\partial p}{\partial x} \qquad (4.6)$$

where μ is solution viscosity (Pa.s), p is pressure (Pa), x is the axis along the length of the microchannel (m) and r is radius (m). The pressure is assumed to be a linear function of axial coordinate x only, i.e. $-\frac{\partial p}{\partial x}=\frac{\Delta p}{L}$, where L (m) is the total length of the microchannel. The solution of Equation (5) is [ref]:

$$U_x=\frac{1}{4\mu}\frac{\Delta p}{L}\left(R^2-r^2\right) \qquad (4.7)$$

where R is half of the hydraulic diameter of the microchannel (m). The average bulk flow velocity is then defined as [ref]:

$$U_{avg}=\frac{1}{\pi R^2}\int_0^R U_x\cdot 2\pi r dr \qquad (4.8)$$

Substituting equation (7) into equation (8), the average bulk flow velocity as a function of pressure is attained as shown:

$$U_{avg}=\frac{D^2}{32\mu}\frac{\Delta p}{L} \qquad (4.9)$$

where D is hydraulic diameter of the microchannel (m).

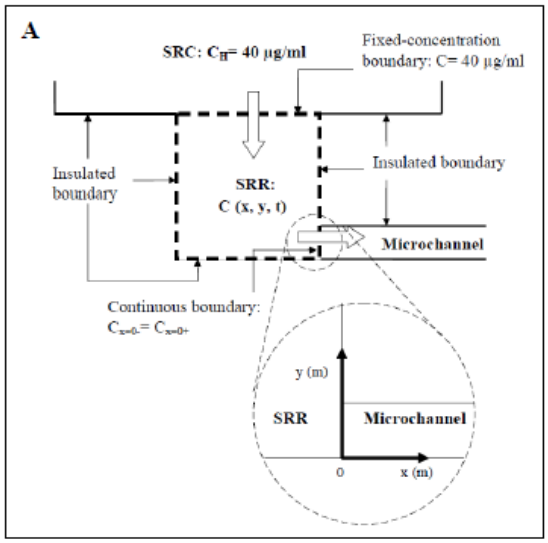
A
SRC: C_H= 40 µg/ml
Fixed-concentration boundary: C= 40 µg/ml
Insulated boundary
SRR: C (x, y, t)
Insulated boundary
Microchannel
Continuous boundary: $C_{x=0-}$= $C_{x=0+}$
y (m)
SRR
Microchannel
0
x (m)

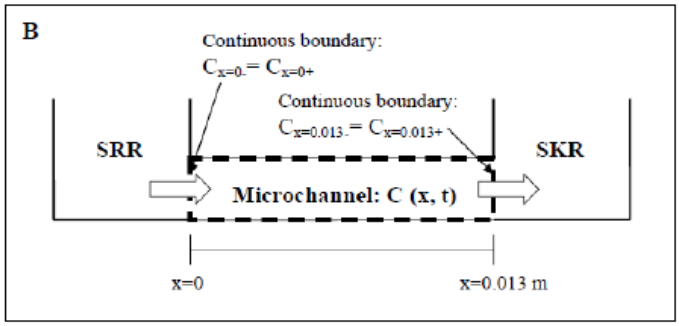
B
Continuous boundary: $C_{x=0-}$= $C_{x=0+}$
Continuous boundary: $C_{x=0.013-}$= $C_{x=0.013+}$
SRR
SKR
Microchannel: C (x, t)
x=0
x=0.013 m

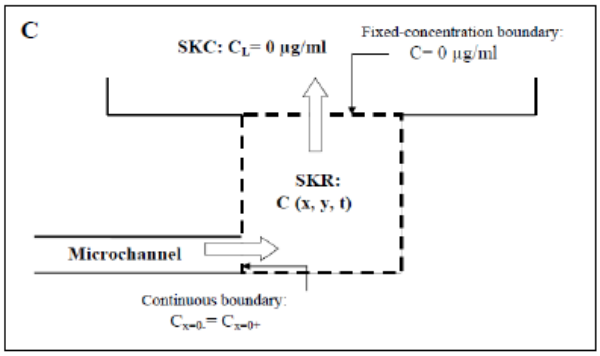
C
SKC: C_L= 0 µg/ml
Fixed-concentration boundary: C= 0 µg/ml
SKR: C (x, y, t)
Microchannel
Continuous boundary: $C_{x=0-}$= $C_{x=0+}$

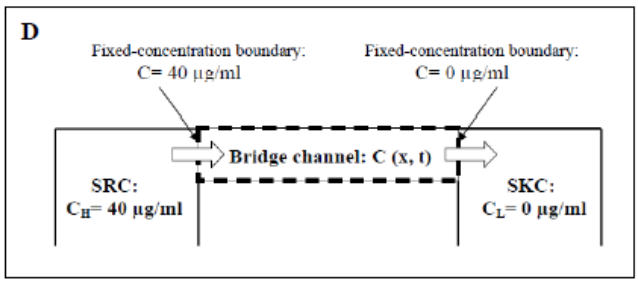
D
Fixed-concentration boundary: C= 40 µg/ml
Fixed-concentration boundary: C= 0 µg/ml
Bridge channel: C (x, t)
SRC: C_H= 40 µg/ml
SKC: C_L= 0 µg/ml

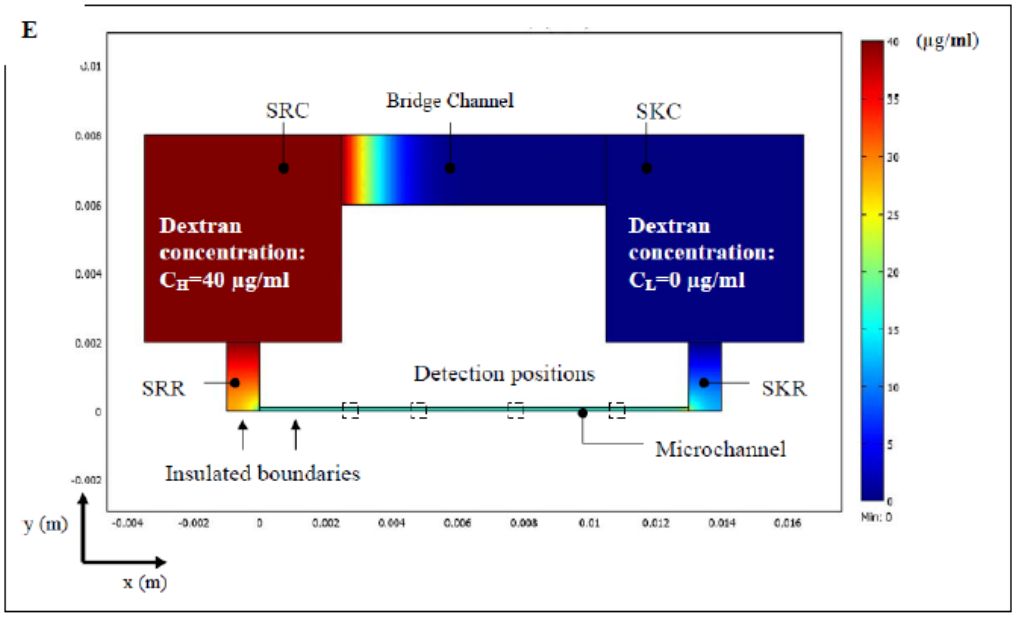
E
(µg/ml)
SRC
Bridge Channel
SKC
Dextran concentration: C_H=40 µg/ml
Dextran concentration: C_L=0 µg/ml
SRR
Detection positions
SKR
Microchannel
Insulated boundaries
y (m)
x (m)
Min: 0

Figure 4.2: Schematics, boundary conditions and simulation of reagent transport modeling within the bridged μlane system. Reagent transported within the SRR reservoir from the SRC chamber toward the microchannel (A). White arrows point to the transport direction. The origin of a two-dimensional coordinates in the mathematical modeling was set at the lower corner of the entrance of the microchannel, as shown in the inset. The reagent concentration within the SRC chamber was set to C_H=40 μg/ml constantly. The reagent concentration at the interface between the SRC chamber and the SRR reservoir was set to C= 40 μg/ml, while the concentration at the interface between the SRR reservoir and the microchannel (x=0) close to the reservoir ($C_{x=0-}$) was set to be equal to the concentration at the interface close to the microchannel ($C_{x=0+}$), i.e. $C_{x=0-}$= $C_{x=0+}$. All the other physical boundaries were regarded as insulated boundaries. Reagent transported within the microchannel between the SRR reservoir and the SKR reservoir as white arrows point to the transport direction (B). The reagent concentration within the microchannel ($C_{x=0.013-}$) at the interface between the microchannel and the SKR reservoir (x=0.013 m) was also set equal to the concentration within the SKR reservoir ($C_{x=0.013+}$) at the interface, i.e. $C_{x=0.013-}$= $C_{x=0.013+}$. Reagent transported through the SKR reservoir from the microchannel to the SKC chamber (C). The reagent concentration at the SKC chamber was set to C_L= 0 μg/ml while the concentration at the boundary between the SKC chamber and the SKR reservoir was also set to C= 0 μg/ml. As the reagent was modeled to transport through the bridge channel from the SRC chamber to the SKC chamber (D), the concentrations at the boundary between the SRC chamber and the bridge channel and boundary between the bridge channel and SKC chamber were set to C=40 μg/ml and C=0 μg/ml, respectively. The transport within the entire bridge μlane system was simulated and shown (E).

4.1.5. Bulk flow and generation of concentration gradients: Fluorescently-labeled Dextran solution (Cat. # D22910, 10 kDa, Molecular Probes, Eugene, OR) and 1.0-μm-diameter fluorescent beads were added into the system in order to explicitly measure Dextran transport within the bridged μlane system. First, phosphate buffer saline (PBS) solution (Mediatech Inc., Herndon, VA) containing the 1.0-μm-diameter fluorescent beads with concentration of 10^4 beads/ml was injected into the microchannel using a 1-ml syringe (Becton, Dickinson and Company, Franklin Lakes, NJ). These beads were used to optically measure bulk flow velocity within the microchannel. PBS solution was then pipetted into the SKC chamber and the bridge, respectively. Note that the PBS solution was added into the bridge and the SKC chamber slowly so that no solution drained into

the SRC chamber to dilute the fluorescent source that was added later. Second, solutions of Dextran at a concentration of 40 μg/ml were added into the SRC chamber only until it contacted the PBS solution present in the bridge. After the contact was made, fluorescent beads and Dextran were observed to migrate slowly within the microchannel from the SRR reservoir to the SKR reservoir. The systems were then placed in a fluorescent microscope for fluorescent intensity measurement.

4.1.6. Microscope Imaging and Fluorescent Measurement: An inverted epi-microscope (Nikon TE2000) with a 20X microscope objective (Nikon Plant 20X, Morrell Instrument Company Inc., Melville, NY) was used to image the μlane systems via a cooled CCD camera (CoolSNAP EZ, Photometrics, Tucson, AZ) with Nikon software (Nikon Instrument Element 2.30 with 6D module, Morrell Instrument Company Inc., Melville, NY). A shutter (HF204, Prior Scientific Inc., Rockland, MA) mounted in the Nikon TE2000 was used to control the exposure time.

An excitation light of wavelength of 488 nm was applied onto the channel during Dextran transport so that emitted fluorescence was collected via microscope objective. The intensity values of fluorescence collected at detection positions 5mm, 8mm and 11mm away from the SRR reservoir were plotted over time. Meanwhile, movement of fluorescent beads within the microchannel was recorded in order to measure the mean bulk flow velocity. Experiments were repeated four times. In each repeated experiment, a new bridged μlane system was used to measure the fluorescent intensity and bulk flow velocity at different detection positions over time. The results were processed using Student's T test and presented in the format of average ± standard deviation.

4.1.7 Data processing and plotting: The experimental data of fluorescent intensity as a function of time, and the simulation data as a function of time were normalized, and plotted in the same diagram using software (Origin 7.5, Origin Lab Corp., Northampton, MA). Note that some dimensionless normalized experimental data slightly exceeded 1 because of experimental noise. The normalized experimental data were fitted into a curve ($R^2 \geq 99.8\%$), using the Hill function, a category of Sigmoidal functions provided by the software, in order to better compare with the simulated data. The Hill function is given as:

$$y = V_{\max} \cdot \frac{x^n}{k^n + x^n} \qquad (4.10)$$

where the V_{max} is the asymptotic value of the experimental data, k and n are empirical constants given by the software, and x and y are axis coordinates. The residual difference, defined as the absolute difference between each individual data point from the Hill-function fit curve and each individual data point from the simulation curves at the same corresponding time point, was analyzed using the Student's t-test in order to identify the simulation curve that was closest to the Hill-function fit curve of the experimental data. The simulation curve with the least standard deviation of residual difference (<2%) and the least average residual difference at all the data points (<10%) was considered to be characteristic of the diffusion coefficients in free solution.

4.3 Results

4.3.1. Transport within the bridged μlane system

Fluorescently-labeled Dextran {Loan CE, 2000 #30} was used to verify the generation of concentration gradients within the bridged μlane system. After Dextran solutions were applied, emitted fluorescent signal was optically observed to displace along the SRR reservoir, bridge channel, SKR reservoir and microchannel. Such transport was also modeled and simulated to predict spatiotemporal Dextran transport within the bridged μlane system using different simplified versions of Equation (1).

4.3.1.(i) Diffusion within the SRR reservoir: Dextran was observed to displace along the SRR reservoir toward the entrance of the microchannel (x=0), as shown in **Figure 4.2A**. No significant change of fluorescent intensity was observed within the SKC chamber, indicative of constant concentrations during experiments, i.e. CH=40 μg/ml. Fluorescent intensity of Dextran was observed to increase within the SRR reservoir with increasing time. No significant bulk flow was seen within the SRR reservoir in horizontal direction, i.e. x axis, and vertical direction, i.e. y axis, indicative of minimal gravity effects on Dextran migration. However, at a small region (approximately 100 μm by 100 μm) close to the entrance of the microchannel, fluorescent beads exhibited slow migration toward the microchannel.

Since the bulk flow, i.e. convection, only occurred at a tiny region around the interface between the reservoir and the microchannel, the transport within the entire SRR reservoir was modeled using a two-dimensional non-convective diffusion Equation (2). Numerical simulation was performed to predict the transport. As seen in **Figure 4.2E**,

Dextran vertically diffused into the SRR reservoir in approximately 1-D direction. As Dextran diffused further down within the reservoir, the diffusion became 2-D, as Dextran concentration varied at vertical direction and horizontal direction. However, when Dextran horizontally entered the microchannel at the entrance, the transport became approximately 1-D along the microchannel.

4.3.1.(ii) Transport within the microchannel: Both Dextran and the fluorescent beads were observed to displace along the microchannel from the SRR reservoir (x=0) to the SKR reservoir (x=13 mm). Dextran transport within the microchannel was imaged and shown in **Figure 4.3**. Dextran concentration increased with increasing time as fluorescent images became brighter. Most of the fluorescent beads (~95%) were seen to flow through the microchannel, while a small portion of them (~5%) were observed to either roll over the substrate surface or stop moving. The average migration velocity of the fluorescent beads along the microchannel was measured to be 0.37±0.01 μm/s, which was then used to represent bulk flow velocity of V=0.37±0.01 μm/s within the microchannel.

Reynolds number (Re) and Peclet number (Pe) were also calculated in order to analyze the fluidic properties of the bulk flow within the microchannel. The Reynolds number (Re) is a dimensionless number that measures the ratio of inertial forces to viscous forces. It is defined as {Bird RB, 2002 #34}:

$$\mathrm{Re} = \rho V d / \mu \qquad (4.11)$$

where ρ is fluid density (kg/m^3), V is flow velocity (m/s), d is characteristic length (m) and μ is fluid viscosity (Pa.s). This value was calculated to be less than 10^{-3}, indicative of viscous, laminar flow within the microchannel. The Peclet number (Pe) is also a

dimensional number which gives a measure of ratio of convection to diffusion. It is defined as {Bird RB, 2002 #34}:

$$Pe = VL / D \qquad (4.12)$$

where V is fluid velocity (m/s), L is the length of channel (m) and D is the diffusion coefficient (m/s^2). The diffusion coefficient of Dextran was reported to range from $0.8x10^{-6}$ cm/s^2 to $0.84x10^{-6}$ cm/s^2 [ref]. The Pe was then calculated to be between 57 and 60, illustrating that bulk flow within the microchannel was large enough to dominate the Dextran transport.

Because of the large ratio of the length of the microchannel to the hydraulic diameter of cross-section, Dextran transport within the microchannel was modeled as 1-D convective mass transfer. Therefore, Equation (3) was used to numerically predict Dextran concentration change along the microchannel at any given time. This model was also utilized to compute spatiotemporal Dextran concentration gradient along the microchannel. The predicted time-evolved Dextran concentrations at different detection positions of the microchannel were then compared with the experimental concentration at the corresponding positions to examine the feasibility of the mathematical modeling and the reliability of reagent concentration gradient establishment.

4.3.1.(iii) Diffusion within the SKR reservoir: Dextran was observed to displace horizontally into the SKR reservoir from the microchannel (along x axis) and diffuse vertically toward the SKC chamber (along y axis), as shown in **Figure 4.2C**. Dextran concentration within the reservoir increased with increasing time, while the PBS concentration within the SKC chamber barely changed due to the large volume of the

chamber to maintain constant concentration during experiments, i.e. C_L=0 μg/ml. After the fluorescent beads migrated past the exit of the microchanne (x=L) and entered the SKR reservoir, they stopped in a small area within the SKR reservoir (100 μm by 100 μm). However, beads were not observed to migrate within the rest of the reservoir. Therefore, the minimal bulk flow at the tiny region within the reservoir was neglected and the gravity effects on bulk flow within the reservoir were considered minimal to zero.

The entire transport of Dextran within the SKR reservoir was then regarded as pure diffusion due to the lack of significant bulk flow. Therefore, the simplified 2-D non-convective diffusion Equation (4) was used to model the diffusion. As indicated in the simulation of **Figure 4.2E**, Dextran horizontally transported into the SKR reservoir, then diffused within the reservoir horizontally and vertically. When Dextran diffused near the SKC chamber, the diffusion became approximately 1-D.

4.3.1.(iv) Diffusion within the bridge channel: Dextran also transported through the bridge channel from the SRC chamber to the SKC chamber, as shown in **Figure 4.2D**. Both of the two chambers were designed large to maintain constant reagent concentrations. Dextran concentration within the bridge channel was seen to increase over increasing time. No significant bulk flow was observed within the bridge channel when beads were used. Therefore, the transport within the bridge channel was modeled as pure diffusion. The simplified 1-D non-convective diffusion Equation (5) was used to predict the Dextran transport within the bridge channel. As shown in **Figure 4.2E**, Dextran within the bridge channel diffused much slower than the Dextran within the microchannel, due to the lack of bulk flow within the bridge channel. Moreover, the SKC

chamber was large to maintain approximately constant concentration during experiments. Hence, the Dextran diffused from the bridge channel did not significantly affect the transport of Dextran within the microchannel.

4.3.2. Estimated Diffusivity: In order to predict Dextran transport within our bridged μlane system, the appropriate diffusion coefficient of Dextran used in our methodology must be measured. We compared the Dextran transport measured at different detection positions within the microchannel with the numerical simulation at the corresponding positions to find out the diffusion coefficient that was mostly characteristic of the Dextran transport in our experiments. Whether the diffusion coefficient measured using our methodology was in line with the published values was also considered a criterion to examine our model and experimental methods to detect Dextran transport. Fluorescent intensity of Dextran measured at specific detection positions within the microchannel were normalized and shown in **Figure 4.4.** As seen in the figure, Dextran concentration at the position of x=3 mm increased with increasing time and reached steady-state in ~9 hours. Note that the time to reach steady-state varied at different detection positions, but the profiles of Dextran concentration as a function of time exhibited similar patterns. In addition, normalized predictions of Dextran concentration at the corresponding detection positions within the microchannel were computed and plotted alongside experimental data in this figure. In the simulation, numerical predictions utilized Dextran diffusivity values between 1.0 x $10^{-6}$$cm^2$/s and in Equation (3) as well as the measured bulk velocity of 0.37 μm/s for a wide range of examination. The experimental data lay in between the curves generated using the diffusivity of 0.8 x 10^{-6} cm^2/s and the diffusivity of 0.9 x 10^{-6}

cm^2/s. To further measure the Dextran diffusivity, we narrowed down the diffusivity range of simulation to be between 0.80 x 10^{-6} cm^2/s and 0.90 x 10^{-6} cm^2/s. Based upon the model data that were within 6% of each experimentally measured intensity, we illustrate that Dextran transport within the bridged μLane system occurs with a diffusivity of 0.82±0.01 x 10^{-6} cm^2/s. This value is in line with the measured diffusivity of Dextran in vitro and in vivo reported to be between 0.80 x 10^{-6} cm^2/s and 0.84 x 10^{-6} cm^2/s [42].

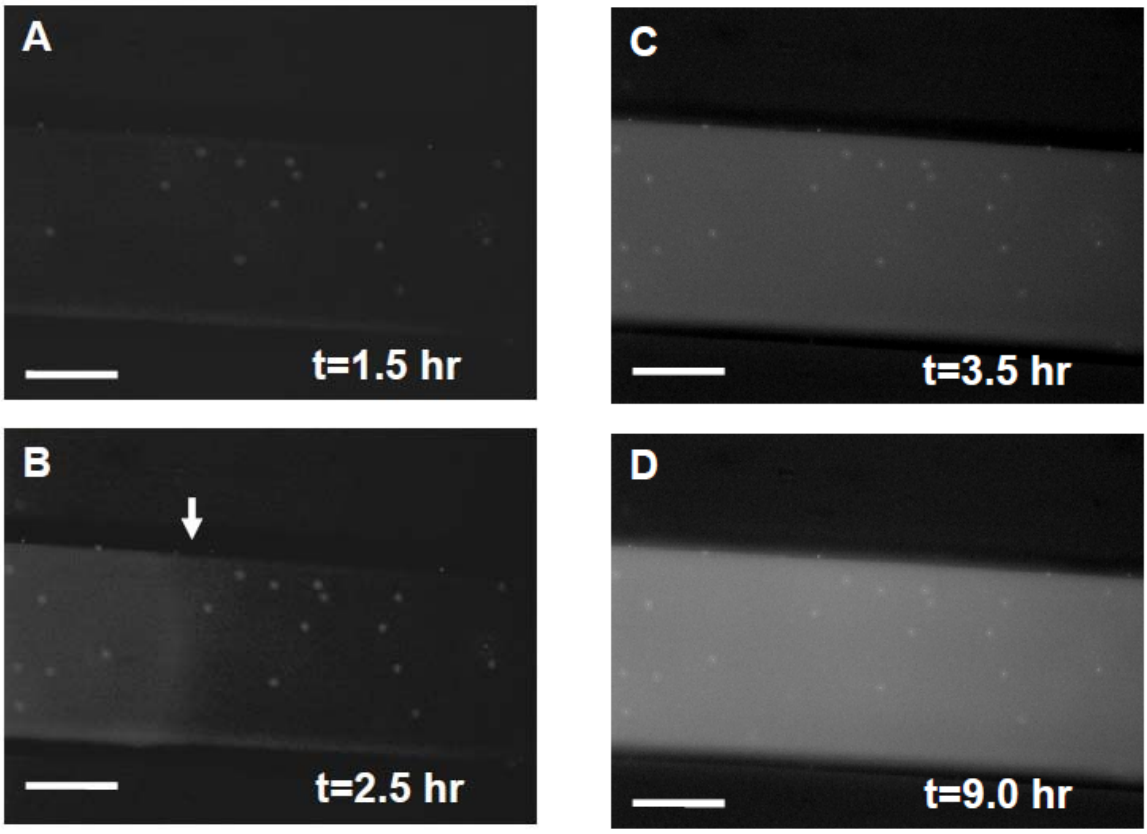

Figure 4.3: Images of Dextran transport within the microchannel over time. Arrow points to the leading edge of Dextran transport visibly observed in the microchannel after 2.5 hours (B). EGF fluorescence was initially observed throughout the microchannel in 3.5 hours (C), with increasingly strong fluorescence after 9 hours (D), until reaching steady-state in 18 hours. The white dots seen in images represent fluorescent beads used inside of the bridged μLane system to measure bulk velocity (if present) during experiments. Scale bar: 50μm.

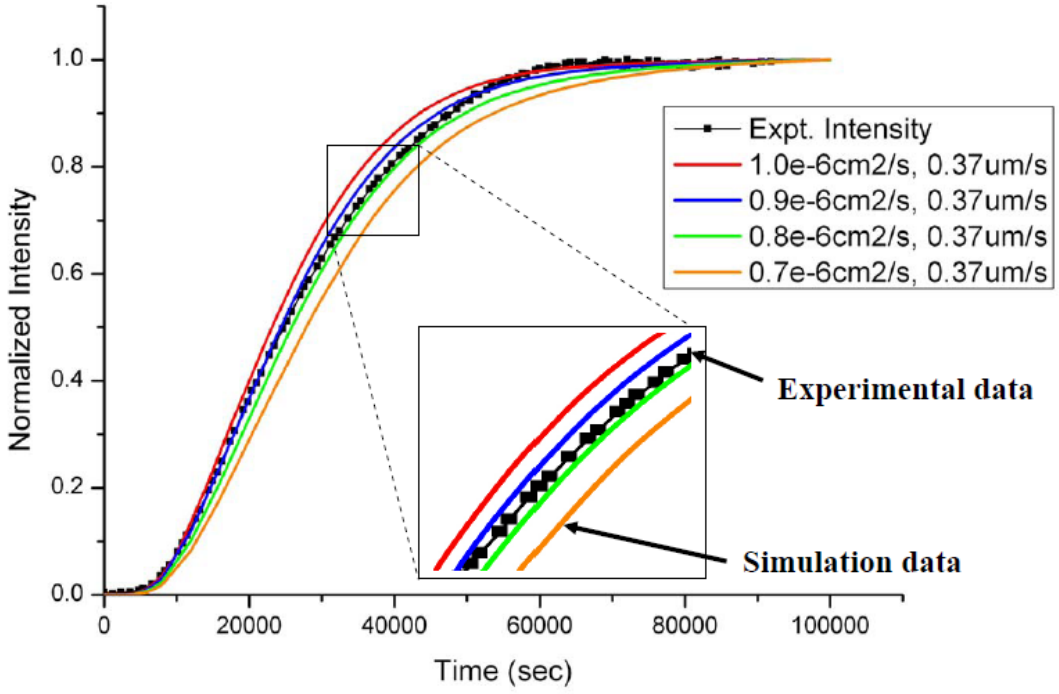

Figure 4.4: Graph of normalized experimental data obtained from Dextran transport experiments at a detection position (x=3 mm) within the bridged μLane system, compared against normalized simulation data generated from the 1-D convective diffusion equation. These normalized data were plotted as a function of time. A range of Dextran diffusion coefficients between 0.7 x 10^{-6} and 1.0 x 10^{-6} cm^2/s, and the experimentally measured mean bulk velocity for Dextran of V=0.37μm/s, were used in the numerical simulation to generate the Dextran concentration profiles shown at different detection positions over time.

4.3.3 Concentration Gradients: Lastly, our mathematical model and numerical simulation were used to graphically illustrate the spatiotemporal profiles of different concentration gradients distributed along the bridged μLane system. Because the microchannel was specifically designed as an observation platform to study reagent transport and concentration gradient establishment, the reagent concentration change along the microchannel was focused and predicted. Two reagents, Dextran and EGF, were used in experiments to respectively measure the bulk flow velocity within the

microchannel. Subsequently, concentration profiles for each of these reagents were generated using our mathematical models and finite-element-method simulation in order to analyze how different reagents generated distinct concentration gradients via our microsystem. Note that the molecular weight for these reagents were similar as molecular weight of Dextran was 10 kDa and 6 kDa for EGF. However, the diffusion coefficient is different. As measured in our experiment, the Dextran diffusivity was 0.82 x 10^{-6} cm^2/s. The EGF diffusivity was attained by averaging the published values [12, 54-57], as a result of 2.0 x 10^{-6} cm^2/s. Here, the reagent concentration applied in the SRC chamber is denoted as C_0, while the concentration within the microchannel is C(x, t). The ratio of $C(x, t)/C_0$ is then defined as dimensionless concentration. The bulk flow velocity within the microchannel for Dextran was measured to be 0.37 μm/s while the bulk flow velocity for EGF was also measured to be 0.37 μm/s using the fluorescent beads. The Re number for EGF was calculated to be less than 10^{-3}, indicative of laminar flow. The Pe number for EGF was calculated to be 50, indicative of convection domination. The reagent diffusivity and bulk flow velocity were then substitute into Equation (3) to predict the reagent concentration and gradients distributed along the microchannel. The gradients were categorized into 5 ranges: $0<G_1<10^{-3}$ ng/(ml.mm), $10^{-3}<G_2<10^{-2}$ ng/(ml.mm), $10^{-2}<G_3<10^{-1}$ ng/(ml.mm), $10^{-1}<G_4<10^{0}$ ng/(ml.mm), and $10^{0}<G_5<10^{1}$ ng/(ml.mm).

As shown in **Figure 4.5A**, our computational model illustrates that the local Dextran concentration and gradient, defined as $\partial C/\partial x$, reached steady-state within the entire microchannel in 33 hours. Dextran concentration and gradient were non-linearly distributed along the microchannel. Dextran concentrations within the microchannel ranged from 52% to 52.5% of the concentration in the SRC chamber, i.e. C_0. The

gradients ranged for 2 orders of magnitude from G_2 to G_3, as gradient G_2 occupied distance of 7 mm and G_3 of 4.5 mm from x=7 mm to x=11.5 mm. The area near the exit of the microchannel (x=13 mm) exhibited fluctuation of concentration, which was not shown in the figure.

EGF also displaced along the microchannel, as seen in **Figure 4.5B**. The simulation illustrated that the time to reach steady-state was 18 hours. As seen, EGF concentration distribution was highly non-linear and so were the gradients. The range of EGF concentration within the microchannel was between 35% and 65% of C_0. The gradient exhibited 5 orders of magnitude. G_1 occupied distance of 6 mm, while G_2 possessed approximately 2 mm, G_3 for approximately 1.5 mm, G_4 and G_5 each for approximately 1 mm.

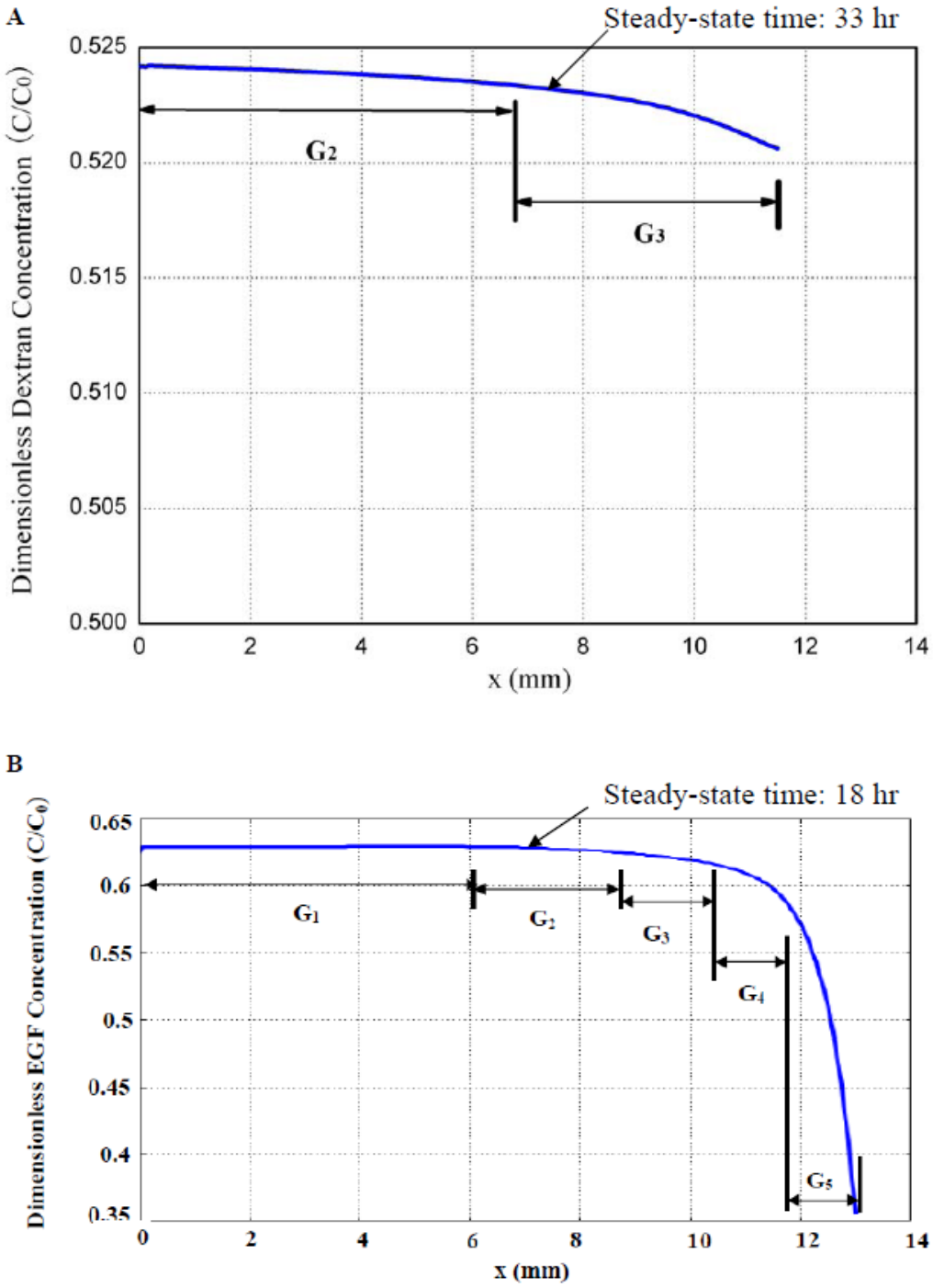

Figure 4.5: Graph of steady-state reagent concentration gradients distributed along the microchannel. Gradients were categorized into 5 ranges: $0<G_1<10^{-3}$ ng/(ml.mm), $10^{-3}<G_2<10^{-2}$ ng/(ml.mm), $10^{-2}<G_3<10^{-1}$ ng/(ml.mm), $10^{-1}<G_4<10^{0}$ ng/(ml.mm), and $10^{0}<G_5<10^{1}$ ng/(ml.mm). Dextran gradients exhibited two orders of magnitudes from G_2 to G_3, while EGF displayed gradients of 5 orders from G_1 to G_5. These gradients were unevenly distributed at different positions along the length of the microchannel.

4.4 Discussion

The capability to produce specific chemical concentrations and concentration gradients in microdevices over time, and mathematically validate these values, was essential for the study of micro/nano-scale mass transport such as salinity and nutrition transport in biological systems. By using a straightforward design, our system delivered reagents via mathematically-validated transport models and enabled measurement of primary diffusion parameters, such as diffusion coefficient and bulk flow velocity. Our microsystem is similar to some existing microdevices {Kanegasaki S, 2003 #433; Abhyankar, 2006 #65}, but is distinct in its efficient, convenient manufacturing, and user-friendly manipulation. While others have used machined parts and complex 3-D assembly, the μlane system accomplishes microfluidic transport using inexpensive PDMS layering. Further, the reagent transport within the microchannel can be held steady-state for up to 48 hours without peripheral accessories such as external pump and power supplies to maintain solution circulation.

In the bridged μLane system, two volumetric reservoirs are used to gradually deliver reagent into the microchannel with minimal entrance effects, which facilitates stable reagent gradient formation within the entire system. Although the reagent transport with the microsystem was 2-D, the transport within the microchannel was treated 1-D due to the large ratio of microchannel length to its hydraulic diameter. The 1-D approximation was demonstrated to be reasonable and reliable as the mathematical modeling results were shown to closely match the experimental results (**Figure 4.4**). Moreover, the Dextran diffusivity measured using our methodology was in line with the

published values, suggesting that our modeling and the experimental methodology are feasible and reliable.

A 2nd device layer contains two additional large volumetric chambers to maintain constant reagent concentrations during experiments. We note that minimal reagent transport in the bridge channel from the SRC chamber to the SKC chamber was present during the experiments (**Figure 4.3**). However, such transport in the bridge channel did not affect the reagent transport in the microchannel in this work, due to the facts that the reagent diffused slowly in the bridge channel without significant bulk flow and reagent concentration within the SKC chamber remained zero during the entire experiments (measured up to 96 hours). The extremely low bulk flow within the reservoirs can be calculated using mass conservation: $V_1 \cdot A_1 = V_2 \cdot A_2$, where V_1 and V_2 are the bulk velocity in a reservoir and the microchannel (μm/s), respectively, and A_1 and A_2 are the cross-sectional area of a reservoir and the microchannel ($\mu m^2/s$), respectively. Substituting the known information of the bulk flow velocity in the microchannel and the geometrical dimension of the reservoirs and the microchannel, the bulk flow velocity within the reservoirs are calculated to be less than 10^{-3} μm/s, which is two orders lower than the velocity in the microchannel. Therefore, it can be neglected in our modeling. Since the velocity approached to zero, the gravity effects on reagent transport within the reservoirs were also minimal.

The 2nd layer is also designed to contain an open, so-called bridge channel that largely eliminates potential hydrostatic pressure differences in the chambers that can cause large pressure-driven flow in the microchannel during experimental loading. Without the bridge channel to balance the volume of two chambers, our experiments have

shown that a tiny volume difference between the chambers, 1 μl for example, can lead to high bulk flow within the microchannel, which measured to have the order of 100 μm/s and lasted for 2 days. Surprisingly, when the chambers were connected using the designed bridge channel, the bulk flow velocity within the microchannel was at the order of 0.1 μm/s.

Although the gravity effects on reagent transport within each individual reservoir were minimal, the hydrostatic pressure difference induced by the density difference between the reagent and PBS solutions within the chambers was the driving forces to cause bulk flow within the microchannel. The hydrostatic pressure that caused reagent transport within the microchannel can be calculated using the hydrostatic pressure equation: $\Delta P = \Delta\rho \cdot g \cdot h$, where ΔP is the pressure difference (Pa), Δρ is the density deference between solutions (kg/m^3), and h is the liquid height (m), i.e. the accumulative thickness of the 1st and 2nd PDMS layer of the microsystem. The density difference between reagent and PBS solution was 40 μg/ml. Note that the liquid height, h, maintained the same for the source side and the sink side. The convective flow within the microchannel was regarded as Poiseuille flow [44], due to its laminar flow characteristics. The bulk flow velocity calculated from the above pressure difference (ΔP) and equation (9), i.e. $U_{avg} = \frac{D^2}{32\mu}\frac{\Delta p}{L}$, was 0.11 μm/s, which exhibited the same order of magnitude of the bulk flow velocity measured within our microsystem, i.e. 0.37 μm/s. However, the inertial flow induced when adding sample solutions and solution evaporation during experiments may be the reasons to cause the difference between the theoretical calculation and the experimental measurement.

As clearly shown in the experiments using fluorescent Dextran and micro-beads, the bridged μLane system relies upon convective transport, i.e. bulk flow, rather than molecular diffusion alone to generate reagent gradients during the desired experimental time. This study utilized the bulk flow as an advantage, as convective transport within the microchannel rapidly decreased the time required for reagent concentration to reach steady-state within the entire microchannel. As an example, Dextran transport via diffusion alone (using the average of cited Dextran diffusivities, 8.2 $x10^{-7}cm^2/s$) would require over 470 hours to reach a linear, steady-state gradient within our 13-mm-long microchannel. However, as a consequence of convection, the bridged μLane system generated steady-state Dextran concentration profiles within approximately 33 hours (**Figure 4.5**). Additionally, EGF reached steady-state in 230 hours without convection while the presence of bulk flow facilitated the transport with steady-state time of 18 hours.

Further, association of convection and molecular diffusion can be combined to change the chemical gradient profile from linear to highly non-linear along the microchannel length, as well as extend reagent gradients to different orders of magnitude (**Figure 4.5**). When high diffusivity was used, the transport was less convection-dominated. Therefore, by changing different ratio of convection to diffusion, our methodology provides a platform to generate different gradient profiles for versatile studies of chemical gradients, such as live biological systems.

In summary, we have designed the bridged μLane system to investigate chemical transport. The bridged μLane can be utilized to deliver a variety of reagent, generate reagent concentration gradients, and observe consequent reagent transport known to play important roles in a multitude of physical and biomedical-related studies [73, 75, 76]. The

bridged μLane system is, therefore, a novel platform with which to generate different chemical gradients and study reagent transport in a quantitative microenvironment.

Acknowledgements:

This work was supported by the National Institutes of Health (GM071702-02), the National Science Foundation (CBET0428573) and PSC-CUNY.

References:

1. Devreotes P and Janetopoulos C, *Eukaryotic Chemotaxis: Distinctions between Directional Sensing and Polarization.* J. Biological Chemistry, 2003. **278**(23): p. 20445-8.
2. Sahai E, *Mechanisms of Cancer Cell Invasion.* Current Opinion in Genetics and Development, 2005. **15**: p. 87-96.
3. Van Haastert, P. and Devreotes PN, *Chemotaxis: Signalling the Way Forward.* Nature, 2004. **5**: p. 626-34.
4. Ware MF, Wells A, and Lauffenburger DA, *Epidermal Growth Factor Alters Fibroblast Migration Speed and Directional Persistence Reciprocally and in a Matrix-Dependent Manner.* J. Cell Science, 1998. **111**: p. 2423-32.
5. McKean JM, Hsieh AH, and Sung KL, *Epidermal growth factor differentially affects integrin-mediated adhesion and proliferation of ACL and MCL.* Biorheology, 2004. **41**(2): p. 139-52.
6. Kayali A. G., Stotland A., Gunst K. V., Kritzik M., Liu G., Dabernat S., Zhang Y. Q., Wu W., and Sarvetnick N., *Growth factor-induced signaling of the pancreatic epithelium.* J Endocrinol, 2005. **185**(1): p. 45-56.
7. Nicholson C and Tao L, *Hindered Diffusion of High Molecular Weight Compounds in Brain Extracellular Microenvironment Measured with Integrative Optical Imaging.* Biophysical J., 1993. **65**: p. 2277-90.
8. Raghavan S., Nelson C. M., Sniadecki N. J., Lim E. A., and Chen C. S., *Engineered microenvironments to investigate cellular behavior.* Conf Proc IEEE Eng Med Biol Soc, 2006. **1**: p. 2357.
9. Saadi W, Rhee SW, Lin F, Vahidi B, Chung BG, and Jeon NL, *Generation of stable concentration gradients in 2D and 3D environments using a microfluidic ladder chamber.* Biomed Microdevices, 2007. **9**(5): p. 627-35.
10. Walker, G.M., J. Sai, A. Richmond, M. Stremler, C.Y. Chung, and J.P. Wikswo, *Effects of flow and diffusion on chemotaxis studies in a microfabricated gradient generator.* Lab Chip, 2005. **5**(6): p. 611-8.
11. Saadi, W., S.J. Wang, F. Lin, and N.L. Jeon, *A parallel-gradient microfluidic chamber for quantitative analysis of breast cancer cell chemotaxis.* Biomed Microdevices, 2006. **8**(2): p. 109-18.
12. Thorne RG, Hrabetova S, and Nicholson C, *Diffusion of Epidermal Growth Factor in Rat Brain Extracellular Space Measured by Integrative Optical Imaging.* J. Neurophysiol, 2004. **92**: p. 3471-81.
13. Whitesides GM, *The origins and the future of microfluidics.* Nature, 2006. **442**(7101): p. 368-73.
14. Folch A, *BioMEMS and cellular biology: perspectives and applications.* J Vis Exp, 2007(8): p. 300.
15. Keenan, T.M. and A. Folch, *Biomolecular gradients in cell culture systems.* Lab Chip, 2008. **8**(1): p. 34-57.
16. Paguirigan, A.L. and D.J. Beebe, *Microfluidics meet cell biology: bridging the gap by validation and application of microscale techniques for cell biological assays.* Bioessays, 2008. **30**(9): p. 811-21.

17. Weibel DB, Garstecki P, and Whitesides GM, *Combining microscience and neurobiology* Curr Opin Neurobiol. , 2005. **15**(5): p. 560-7.
18. Kane RS, Takayama S, Ostuni E, Ingber DE, and Whitesides GM, *Patterning proteins and cells using soft lithography.* Biomaterials, 1999. **20**(23-24): p. 2363-76.
19. Li N., Sip C., and Folch A., *Microfluidic chips controlled with elastomeric microvalve arrays.* J Vis Exp, 2007(8): p. 296.
20. Wu X and Dewey TG, *From microarray to biological networks: Analysis of gene expression profiles.* Methods Mol Biol., 2006. **316**: p. 35-48.
21. Folch, A. and M. Toner, *Microengineering of cellular interactions.* Annu Rev Biomed Eng, 2000. **2**: p. 227-56.
22. Dufva M, *Microchips for cell-based assays.* Methods Mol Biol., 2009. **509**: p. 135-44.
23. Di Carlo, D., Wu LY, and Lee LP, *Dynamic single cell culture array.* Lab Chip, 2006. **6**(11): p. 1445-9.
24. Kanegasaki S, Nomura Y, Nitta N, Akiyama S, Tamatani T, Goshoh Y, Yoshida T, Sato T, and Kikuchi Y, *A novel optical assay system for the quantitative measurement of chemotaxis.* J Immunol Methods., 2003. **282**(1-2): p. 1-11.
25. Lin, F., W. Saadi, S.W. Rhee, S.J. Wang, S. Mittal, and N.L. Jeon, *Generation of dynamic temporal and spatial concentration gradients using microfluidic devices.* Lab Chip, 2004. **4**(3): p. 164-7.
26. Motoo K, Toda N, Arai F, Fukuda T, Sekiyama K, and Nakajima M, *Generation of concentration gradient from a wave-like pattern by high frequency vibration of liquid-liquid interface.* Biomed Microdevices, 2008. **10**(3): p. 329-35.
27. Xia N, Hunt TP, Mayers BT, Alsberg E, Whitesides GM, Westervelt RM, and Ingber DE, *Combined microfluidic-micromagnetic separation of living cells in continuous flow.* biomed Microdevices, 2006. **8**(4): p. 299-308.
28. Oberti S, Neild A, Möller D, and Dual J, *Towards the automation of micron-sized particle handling by use of acoustic manipulation assisted by microfluidics.* Ultrasonics, 2008. **48**(6-7): p. 529-36.
29. Mosadegh B, Huang C, Park JW, Shin HS, Chung BG, Hwang SK, Lee KH, Kim HJ, Brody J, and Jeon NL, *Generation of stable complex gradients across two-dimensional surfaces and three-dimensional gels.* Langmuir, 2007. **23**(22): p. 10910-2.
30. Lin, F., C.M. Nguyen, S.J. Wang, W. Saadi, S.P. Gross, and N.L. Jeon, *Effective neutrophil chemotaxis is strongly influenced by mean IL-8 concentration.* Biochem Biophys Res Commun, 2004. **319**(2): p. 576-81.
31. Yang J, Yang J, Yin ZQ, Svir I, Xu J, Luo HY, Wang M, Cao Y, Hu N, Liao YJ, and Zheng XL, *Microfluidic pool structure for cell docking and rapid mixing.* Anal Chim Acta., 2009. **634**(1): p. 61-7.
32. Li, N., C.H. Hsu, and A. Folch, *Parallel mixing of photolithographically defined nanoliter volumes using elastomeric microvalve arrays.* Electrophoresis, 2005. **26**(19): p. 3758-64.
33. Tanaka Y, Morishima K, Shimizu T, Kikuchi A, Yamato M, Okano T, and Kitamori T, *Demonstration of a PDMS-based bio-microactuator using cultured cardiomyocytes to drive polymer micropillars.* Lab Chip, 2006. **6**(2): p. 230-5.

34. Balagaddé FK, You L, Hansen CL, Arnold FH, and Q. SR, *Long-term monitoring of bacteria undergoing programmed population control in a microchemostat.* Science, 2005. **309**(5731): p. 137-40.
35. Friedl P and Wolf K, *Tumour-Cell Invasion and Migration: Diversity and Escape Mechanisms.* Nature, 2003. **3**: p. 362-74.
36. Hung CT, Allen FD, Pollack SR, Attia ET, Hannafin JA, and Torzilli PA, *Intracellular calcium response of ACL and MCL ligament fibroblasts to fluid-induced shear stress.* Cell Signal, 1997. **9**(8): p. 587-94.
37. Iwabu A, Smith K, Allen FD, Lauffenburger DA, and Wells A, *Epidermal Growth Factor Induces Fibroblast Contractility and Motility via a Protein Kinase C Delta-Dependent Pathway.* J. Biological Chemistry, 2004. **279**(14551-60).
38. Wang SJ, Saadi W, Lin F, Nguyen CM, and Jeon NL, *Differential Effects of EGF Gradient Profiles on MDA-MB-231 Breast Cancer Cell Chemotaxis.* Experimental Cell Research, 2004. **300**: p. 180-9.
39. Arai H, Tsou CL, and Charo IF, *Chemotaxis in a lymphocyte cell line transfected with C-C chemokine receptor 2B: evidence that directed migration is mediated by betagamma dimers released by activation of Galphai-coupled receptors.* Proc. Natl. Acad. Sci., 1997. **94**(26): p. 14495-9.
40. Imshik Lee, Kwong-Yu Chan, and David Lee Phillips, *Growth of electrodeposited platinum nanocrystals studied by atomic force microscopy* Applied Surface Science, 1998. **136**(4): p. 321-30.
41. Timothy E. McKnight, A.V.M., Derek W. Austin, Tyler Sims, Michael A. Guillorn, and Michael L. Simpson, *Microarrays of Vertically-Aligned Carbon Nanofiber Electrodes in an Open Fluidic Channel.* J. Phys. Chem. B, 2004. **108**(22): p. 7115–7125.
42. Vazquez, M., Schmalzing D., D. Ehrlich, P. Matsudaira, and G. McKinley, *Shear Induced Degradation of Linear Polyacrylamide Solutions during Pre-electrophoretic Loading.* Anal Chem, 2001. **73**: p. 3035-44.
43. Vazquez, M., G. McKinley, L. Mitnik, S. Desmarais, P. Matsudaira, and Ehrlich D., *Electrophoretic Injection within Microdevices.* Anal Chem, 2002. **93**: p. 3088-98.
44. Crowe CT, Elger DF, and Roberson JA, *Engineering Fluid Mechanics*. 7th ed: John Wiley & Sons, Inc.
45. Holden MA, Kumar S, Beskok A, and Cremer PS, *Microfluidic diffusion diluter: bulging of PDMS microchannels under pressure-driven flow.* J. Micromech. Microeng., 2003. **13** p. 412-8.
46. Kong Q and Vazquez M, *Flow-induced shear stresses increase the number of cell-cell contacts within extracellular matrix.* Journal of Biomedical Materials Research Part A, 2008. **[In production, Epub ahead of print]**.
47. Bird RB, Stewart WE, and Lightfoot EN, *Transport Phenomena*. 2nd ed. 2002, New York: John Wiley & Sons, Inc.
48. Gennerich A and Schild D, *Anisotropic Diffusion in Mitral Cell Dendrites Revealed by Fluorescence Correction Spectroscopy.* Biophysical J., 2002. **83**: p. 510-22.

49. Das, M., T. Miyakawa, C.F. Fox, R.M. Pruss, A. Aharonov, and H.R. Herschman, *Specific radiolabeling of a cell surface receptor for epidermal growth factor.* Proc Natl Acad Sci U S A, 1977. **74**(7): p. 2790-4.
50. Haller MF and Saltzman WM, *Localized Delivery of Proteins in the Brain: Can Transport Be Customized? .* Pharmaceutical Research, 1998. **15**(3): p. 377-85.
51. Hiemenz PC and Rajagopalan R, *Principles of Colloid and Surface Chemistry* 3rd ed. 1997, New York: Marcel Dekker. 650.
52. Saltzman WM, Radomsky ML, Whaley KJ, and Cone RA, *Antibody Diffusion in Human Cervical Mucus.* Biophys J, 1994. **66**: p. 508-15.
53. Chen, H., J. Kovar, S. Sissons, K. Cox, B. Matter, F. Chadwell, P. Luan, C.J. Vlahos, A. Schutz-Geschwender, and D.M. Olive, *A Cell Based Immunocytochemical Assay for Monitoring Kinase Signaling Pathways and Drug Efficacy.* Anal. Biochem., 2005. **338**: p. 136-42.
54. Loan CE, Aberle T, and Burchard W, *Structure Properties of Dextran. 2. Dilute Solution.* Macromolecules, 2000. **33**(15): p. 5730 -5739.
55. Carpenter G and Cohen S, *Epidermal Growth Factor.* J. BIOLOGICAL CHEMISTRY, 1990. **265**(14): p. 7709-7712.
56. Haugh, J.M., *Deterministic model of dermal wound invasion incorporating receptor-mediated signal transduction and spatial gradient sensing.* Biophys J, 2006. **90**(7): p. 2297-308.
57. Sanabria, H., Y. Kubota, and M.N. Waxham, *Multiple diffusion mechanisms due to nanostructuring in crowded environments.* Biophys J, 2007. **92**(1): p. 313-22.
58. Abhyankar, V.V., M.A. Lokuta, A. Huttenlocher, and D.J. Beebe, *Characterization of a membrane-based gradient generator for use in cell-signaling studies.* Lab Chip, 2006. **6**(3): p. 389-93.
59. Kong Q and Vazquez M, *Flow-induced shear stresses increase the number of cell-cell contacts within extracellular matrix.* Journal of Biomedical Materials Research Part A, 2009. **89**(4): p. 968-79.
60. Kong, Q. and M. Vazquez, *Internal fluid flow increases cellular interconnects between Medial Collateral Ligament fibroblasts and cellular extensions within three-dimensional collagen matrixes.* Cell Commun Adhes, 2006. **13**(3): p. 139-49.
61. Abhyankar V. V., Toepke M. W., Cortesio C. L., Lokuta M. A., Huttenlocher A., and Beebe D. J., *A platform for assessing chemotactic migration within a spatiotemporally defined 3D microenvironment.* Lab Chip, 2008. **8**(9): p. 1507-15.
62. Naoki H, Sakumura Y, and Ishii S, *Stochastic control of spontaneous signal generation for gradient sensing in chemotaxis.* J Theor Biol., 2008. **255**(2): p. 259-66.
63. Wang, S.J., W. Saadi, F. Lin, C. Minh-Canh Nguyen, and N. Li Jeon, *Differential effects of EGF gradient profiles on MDA-MB-231 breast cancer cell chemotaxis.* Exp Cell Res, 2004. **300**(1): p. 180-9.
64. Vicente-Manzanares M, W.D., Horwitz AR, *Cell Migration at A Glance.* J. Cell Science, 2005. **118**: p. 4917-9.
65. Parent CA and Devreotes P, *A Cell's Sense of Direction.* Science, 1999. **284**: p. 765-70.

66. Saadi W, W.S., Lin F, Jeon NL, *A Parallel-Gradient Microfluidic Chamber for Quantitative Analysis of Breast Cancer Cell Chemotaxis.* Biomed. Microdevices, 2006. **8**: p. 109-18.
67. Rees AR, Gregoriou M, Johnson P, and Garland PB, *High Affinity Epidermal Growth Factor Receptors on the Surface of A431 Cells Have Restricted Lateral Diffusion.* EMBO Journal, 1984. **3**(8): p. 1843-7.
68. Bellot F, M.W., Kris R, Mirakhur B, Verlaan I, Ullrich A, Schlessinger J, Felder S,, *High-Affinity Epidermal Growth Factor Binding Is Specifically Reduced by a Monoclonal Antibody, and Appears Necessary for Early Responses.* J, Cell Biology, 1990. **110**: p. 491-502.
69. Woo SL, Debski RE, Zeminski J, Abramowitch SD, Saw SS, and Fenwick JA, *Injury and repair of ligaments and tendons.* Annu. Rev. Biomed. Eng., 2000. **02**(83-118).
70. Lauffenburger DA, H.A., *Cell Migration: A Physically Integrated Molecular Process.* Cell, 1996. **84**: p. 359-69.
71. Sogabe Y, Abe M, Yokoyama Y, and Ishikawa O, *Basic fibroblast growth factor stimulates human keratinocyte motility by Rac activation.* Wound Repair Regen, 2006. **14**(4): p. 457-62.
72. Kurten, R.C., P. Chowdhury, R.C. Sanders, Jr., L.M. Pittman, L.W. Sessions, T.C. Chambers, C.S. Lyle, B.J. Schnackenberg, and S.M. Jones, *Coordinating epidermal growth factor-induced motility promotes efficient wound closure.* Am J Physiol Cell Physiol, 2005. **288**(1): p. C109-21.
73. Pedowitz RA, O'connor JJ, and Akeson WH, *Daniel's Knee Injuries: Ligament and Cartilage Structure, Function, Injury, and Repair*. 2nd ed. 2003, Philadelphia: Lippincott Williams & Wilkins.
74. Boehm, M. and E.G. Nabel, *Cell cycle and cell migration: new pieces to the puzzle.* Circulation, 2001. **103**(24): p. 2879-81.
75. Corcoran, A. and R.F. Del Maestro, *Testing the "Go or Grow" hypothesis in human medulloblastoma cell lines in two and three dimensions.* Neurosurgery, 2003. **53**(1): p. 174-84; discussion 184-5.
76. Maheshwari G, Wiley HS, and Lauffenburger DA, *Autocrine epidermal growth factor signaling stimulates directionally persistent mammary epithelial cell migration.* J. Cell Biology, 2001. **155**(7): p. 1123-8.
77. Liu, Y., R. Sun, W. Wan, J. Wang, J.J. Oppenheim, L. Chen, and N. Zhang, *The involvement of lipid rafts in epidermal growth factor-induced chemotaxis of breast cancer cells.* Mol Membr Biol, 2007. **24**(2): p. 91-101.

CHAPTER 5

Effects of EGF Gradients on Cell Chemotaxis within a Microfabricated Device

Qingjun Kong

Department of Mechanical Engineering

The City College of The City University of New York (CCNY)

140th Street and Convent Ave., T-402

New York, NY 10031

Qkong@gc.cuny.edu

Phone: 212.650.6766 Fax: 212.650.6727

and

*Maribel Vazquez, Sc.D.**

New York Center for Biomedical Engineering

Department of Biomedical Engineering

The City College of The City University of New York (CCNY)

140th Street and Convent Ave., T-403D

New York, NY 10031

Vazquez@ccny.cuny.edu

Phone: 212.650.5209 Fax: 212.650.6727

**Corresponding Author*

Keywords: microfluidic device, microfabrication, concentration gradient, fibroblast, EGF

Abstract: Cell migration in response to ligand stimulation is essential to numerous BME studies. The ligand concentration gradient generated in the cell microenvironment by short- and long-range diffusion is well-known to affect cell function and direct cell motility. Using microfabrication, a two-layer poly-dimethylsiloxane (PDMS) micro-device, named the bridged μlane system, was fabricated to generate ligand concentration gradients within the system. Unlabeled EGF (MW: 6 kDa) at concentrations between 40 ng/ml and 400 ng/ml were applied into the system to generate different EGF gradient profiles to stimulate cell migration. Application of 40-ng/ml EGF concentration was observed to stimulate cells with highest cell motility, while 80-ng/ml EGF concentration triggered the highest number of cells to migrate. Increasing EGF gradients enhanced cell motility. Both EGF concentration and gradients were found to significantly regulate cell migration.

5.1 Introduction

Cells accomplish a variety of physiological processes via migratory responses to signaling from extracellular ligand concentration [1-3]. For many cell types, exposure to increased ligand concentration yields increased cell motility [4], proliferation [5], and/or protein secretion [6]. However, little research has been performed to examine the effects of ligand gradients, rather than extracellular concentration, on cell migration. The effects of ligand gradients across cell populations is expected to be significant, as small changes in the cell microenvironment are known to affect cell function and response [7-9]. Further, numerous biological studies have illustrated measurable changes in cell behavior in response to different ligand gradients [10-12]. Ligand gradient is often difficult to measure, as the majority of published studies utilize assays that primarily tabulate the numbers of cells that migrate in response to ligand concentrations over fixed time periods, e.g. transwell assays. Usage of such technologies prevents the researcher from imposing specific ligand gradients across cell populations, or from measuring the value of those gradients for individual cells. The community is, therefore, in need of novel microtechnologies that enable cell migration studies to correlate measured motility data with stimuli imposed upon the cell microenvironment.

Microfabrication techniques have been adapted in many recent biomedical studies to develop systems that visualize cell response to specific ligand concentrations and different ligand gradient profiles in real time [13-16]. Microarrays, microvalved microsystems and cell pattern microsystems have been largely used to investigate cell function at different threshold ligand concentrations [17-19], gene expression in cell cycles [20] and cell-protein interaction in stable biological environments [21-23]. Many

groups have fabricated novel microfluidic devices to generate linear ligand concentration gradients [9, 10, 24] and non-linear ligand concentration gradients [25, 26] via fluid flow to examine cell migration, Others have used other methods, such as micromagnetics [27] and acoustic manipulation [28] to induce fluid flow and deliver biocompounds. Using such devices, researchers have examined cell response to steady-state ligand gradients [29] and found that cell motility was ligand gradient-dependent [30]. However, some of these microfabricated systems may lack quantitative measurement of spatiotemporal profiles of ligands around individual cells.

Unfortunately, the majority of microdevices recently reported in the literature require costly facilities and equipment for device fabrication and/or sample handling/operation. For example, 3-D photolithographic layering [31], utilization of microvalves [32] and microactuators [33], as well as external pumps and power supplies [24, 25, 34] are often required for microdevice manufacture and operation. In addition, many systems continue to require large populations of cells (10^2 cells per channel) for testing before ligand gradients can be generated [10, 24]. The current study has developed a conveniently-manipulated microfabricated system, called the bridged μLane system, which is able to experimentally generate linear and non-linear ligand concentration gradients that are mathematically validated using well-established convective transport models. Further, the system can be fabricated in a conventional biomedical engineering laboratory without the need for costly computerized apparatus, external power supplies, or clean room facilities. In brief, the PDMS system consists of two volumetric reservoirs connected by a single microchannel, within which bulk ligand transport is well-established and mathematically predictable. Our system is adaptable to

work with both large and small cell populations (as low as 10 cells per channel) in dosage-dependent microenvironments, known to induce chemotaxis, apoptosis, proliferation, and/or cell-cell communication [35-39].

Fluorescently-labeled Dextran was used to experimentally verify the ability of the bridged μLane system to generate steady-state non-linear ligand gradients that were mathematically predicted by convective Fickian diffusion. Cell responses to both low ligand concentration gradients and high ligand concentration gradients as a function of position within the microchannel over time were optically observed and quantitatively analyzed. The experimental data illustrated that steady-state gradients of the model cytokine, Epidermal Growth Factor (EGF), directed cell migration and stimulated cell motility. Additionally, flat and steep EGF gradient profiles were seen to affect cell migration. Moreover, EGF concentrations were found to largely regulate cell migration with significant effects on cell motility and the number of motile cells when integrated with EGF gradients.

5.2 Materials and Methods

Microfabrication of bridged μLane system: The μlane system was designed to deliver ligands toward cells, and facilitate observation of cell responses to stimuli. It consisted of two layers of PDMS with a closed microchannel and two reservoirs on the first layer, as well as two chambers and an open bridged channel on the second. The fabrication of the bridged μLane system consisted of three steps: i) contact photolithography, ii) elastomeric molding of poly-dimethylsiloxane (PDMS) and bonding of 1st layer PDMS, and iii) casting of 2nd layer PDMS.

i) Photolithography: A pre-cleaned glass substrate was coated with an adhesion promoter, Surpass 3000, (DisChem Inc., Ridgway, PA) and an 80-μm-thick layer of negative photoresist, SU-8 2075, (MicroChem Inc., Newton, MA) using a spin coating apparatus (Laurell Tech. Corp., North Wales, PA). The substrate was baked on a hot plate and irradiated with UV light using a laboratory-fabricated photomask containing desired microchannel patterns (intensity: 21700-8900 μW/cm^2 at 2-10 inches, Model B-100AP, UVP Inc., Upland, CA). Substrates were then re-baked, allowed to cool at room temperature (25°C), and immersed in SU-8 developer (MicroChem Inc., Newton, MA) until photoresist patterns were visible. The patterned substrate exhibited dimensions of 13.0±0.1-mm-length (mean ± SD) by 100±5-μm-width by 90±1-μm-depth as measured via surface profilometer (Model SJ-301, Mitutoyo America Corp., Middlesex, NJ) and optical microscope (Nikon TE2000, Morrell Instrument Company Inc., Melville, NY).

ii) Elastomeric molding and bonding of 1st layer PDMS: Liquid-state poly-dimethylsiloxane (PDMS) mixed with silicone elastomer curing agent (Dow Corning Corp., Midland, MI) was degassed and poured onto the photoresist-patterned substrate

described above. After polymerization, the PDMS elastomer was peeled from the patterned substrates resulting in open microchannels of 13.0±0.1-mm-length by 100±5-μm-width and 90±1-μm-depth. Subsequently, it was punctured with 2-mm-diameter pipette tips (Model 9-inch Pasteur Pipette, Fisher Scientific Co., Agawam, MA) on both ends in order to generate two reservoirs with approximately 3 μl volume each (**Figure 5.1A**). These reservoirs were defined as the source reservoir (SRR) and the sink reservoir (SKR), to be used for application of ligand and buffer solutions, respectively. The PDMS elastomer was then bonded onto a pre-cleaned glass substrate (unpatterned) by applying ozone generated via a high-frequency generator (Electro-Technic Products, Inc., Chicago, IL) onto both the PDMS and glass surfaces for 30 seconds each. These components were then defined as the 1st layer PDMS for the bridged μLane system (**Figure 5.1A**). Cross-section uniformity of the closed microchannel itself within this 1st layer was verified using an optical microscope (Nikon TE2000). Since large machines, such as deep reactive-ion etching (DRIE) apparatus, were not used in the microfabrication, the cross-section exhibited approximately rectangular or semi-hemispherical [40-43], as examined via profilometer and optical microscope.

The hydraulic diameter, D_h, of the closed channel was calculated to be 94.8 μm, using $D_h=4A/P$ [44] where *A* is the cross-sectional area and *P* is the perimeter. The semi-hemispherical cross-sectional shape of the microchannel was observed to minimize PDMS bulging effects when solutions were loaded into the system [45]. The ratio of the microchannel length to its hydraulic diameter (approximately 137) was kept large in the design in order to facilitate ligand transport within the microchannel as one-dimensional.

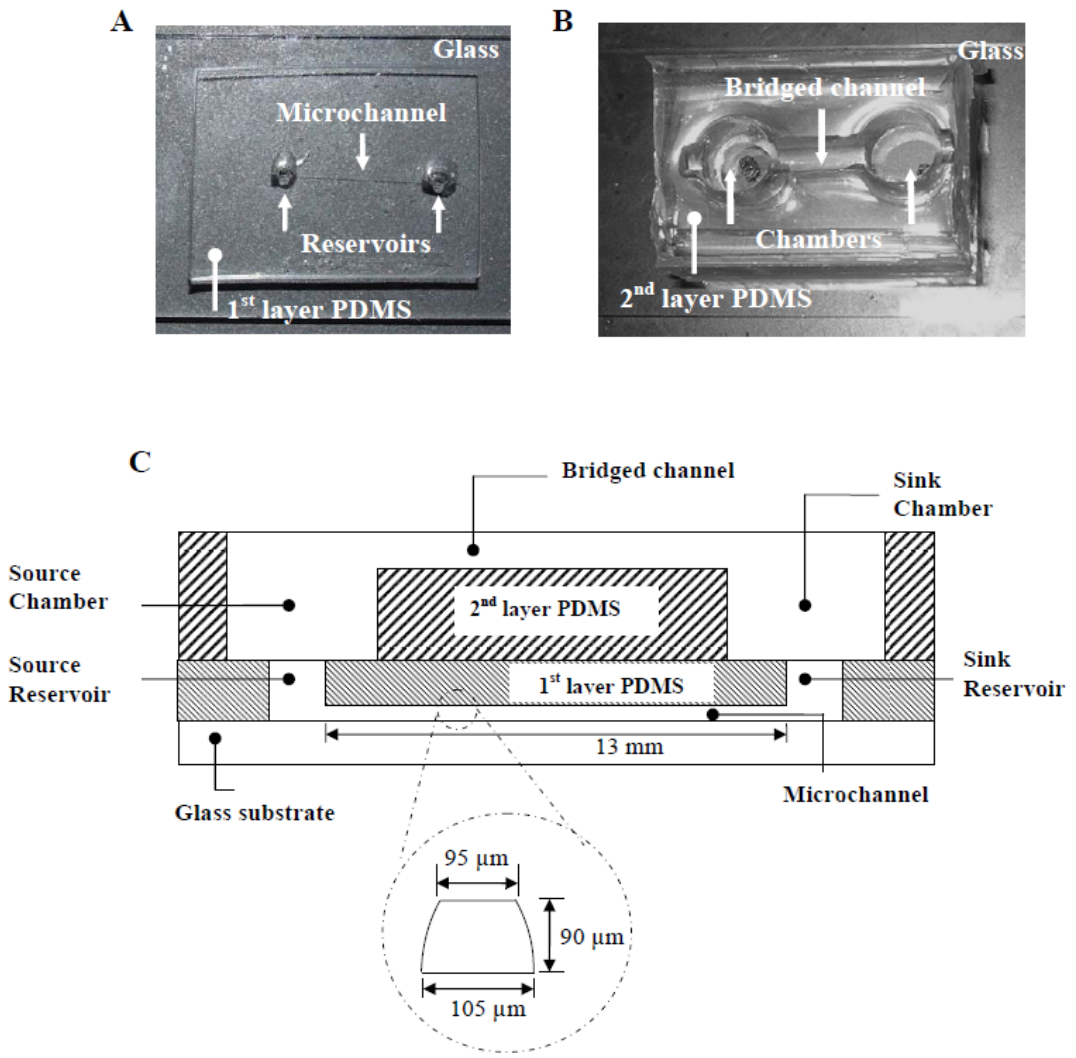

Figure 5.1: Images and schematic of the bridged µLane system. After photolithography and elastomeric molding, a microchannel with two reservoirs was fabricated in polymerized PDMS, defined as the 1st layer PDMS of the bridged µLane system. This PDMS layer was then bonded onto an ultrasonically-cleaned microscope glass slide (A). A second layer of PDMS, consisting of a bridge channel and two chambers, was molded on top of the 1st layer PDMS (B). This layer of PDMS was defined as the 2nd layer PDMS of the system. The chambers in the 2nd layer PDMS were fluidically connected with the reservoirs in the 1st layer PDMS, as shown in the bridged µLane system schematic (C) (not to scale). The microchannel approximately measures 13 mm in length, 90 µm in depth and 100 µm in width (averaged with the upper side of 95 µm and the lower side of 105 µm), as its semi-hemispherical cross-section was shown in inset.

iii) Casting of 2nd layer PDMS: A laboratory-made acrylic mold was then placed atop the 1st layer PDMS described above. Liquid-state PDMS and curing agent were mixed and poured around the acrylic mold. After the PDMS was polymerized and formed the 2nd layer, the acrylic mold was removed. The 2nd layer PDMS consisted of two cylindrical chambers, and a semi-circular, open channel, or so-called bridged channel (**Figure 5.1B**). The two chambers, of 6-mm-diameter and 6-mm-height each, were defined as the source chamber (SRC) and sink chamber (SKC). The SRC and SKC chambers were vertically and fluidically connected with the SRR and SKR reservoirs, respectively, in the 1st layer. Lastly, the bridged channel, of 9-mm-length and 2-mm-depth, connected the SRC and SKC chambers and was used to balance the solution volume within the chambers, which then eliminated pressure differences in the microchannel during solution loading and/or experiment operation, as shown in **Figure 5.1C**. The complete bridged μLane system is thus composed of an open bridged channel that connects the SRC and SKC chambers, as well as a closed microchannel that connects the SRR and SKR reservoirs (**Figure 5.1C**).

The volume ratio of each reservoir to the microchannel was also kept large (approximately 27) in order to maintain stable EGF transport between each reservoir and the microchannel. The volume of each chamber (170 μl) was designed to be 55 times larger than the reservoir and 1450 times larger than the microchannel, in order to gradually transport EGF into the microchannel with minimum entrance effects. The EGF concentrations in the SRC chamber and the SKC chamber remained constant during the EGF transport within the μlane system.

Generation of Dextran gradients within the bridged μlane system and fluorescent intensity measurement: Fluorescently-labeled Dextran solution (Cat. # D22910, 10 kDa, Molecular Probes, Eugene, OR) was added into the system in order to explicitly measure its transport and examine its gradient generation within the μlane system. Initially, Phosphate buffer saline (PBS) solution (Mediatech Inc., Herndon, VA) containing 1.0-μm-diameter fluorescent beads (Cat. # T7282, Molecular Probes, Eugene, OR) with concentration of 10^4 beads/ml was injected into the microchannel using a 1-ml syringe (Becton, Dickinson and Company, Franklin Lakes, NJ). These beads were used to optically measure bulk flow velocity within the microchannel. PBS solution was then pipetted into the SKC chamber and the bridged channel, respectively. Note that the PBS solution was added into the bridged channel and the SKC chamber slowly so that no solution drained into the SRC chamber to dilute the fluorescent source that was added later. Secondly, solutions of Dextran at a concentration of 40 μg/ml were only added into the SRC chamber until it contacted the PBS solution present in the bridged channel. After the contact was made, fluorescent beads were observed to migrate slowly within the microchannel from the SRR reservoir to the SKR reservoir. The systems were then placed in a fluorescent microscope for fluorescent intensity measurement.

While fluorescent Dextran displaced past three different specified detection positions in the microchannel, 5mm, 8mm and 11mm away from the SRR reservoir, where excitation light of wavelength of 488 nm was applied, fluorescence was emitted and collected via a microscope objective. The intensity values at these specific detection regions over time were plotted. Meanwhile, movement of fluorescent beads caused by inertial flow within the microchannel was recorded in order to measure the mean bulk

flow velocity. In these experiments, four different μlane systems were used to measure fluorescent intensity and bulk flow velocity at different detection positions over time.

Cell culture: Primary fibroblast cells were harvested from bovine Medial Collateral Ligament (MCL) explants received from the Soft Tissue laboratory of Dr. Peter Torzilli at the Hospital for Special Surgery (New York, NY) as described previously by our laboratory [46]. Primary cells were washed and cultured with sterile complete Essential Modified Eagle's Medium (EMEM), 10% fetal bovine serum (FBS), 2% L-Glutamine and 1% antibiotic-antimycotic solution (penicillin, streptomycin, amphotericin B) (Mediatech Inc., VA) with pH 7.1-7.4 and plated onto sterile polystyrene tissue culture flasks (Becton Dickinson Labware, NJ). Cells were then maintained at 37^{o}C in a 5% CO_2 humidified incubator. Serial passages were performed when cultures became ~ 90% confluent by detaching cells from flasks via a five-minute treatment with 0.05% trypsin-0.53mM EDTA (Mediatech Inc., VA) at 37^{o}C. The cells were collected via centrifuge, suspended in growth medium, and subcultured for less than 5 passages prior to experimental use.

Cell proliferation assays: To monitor cell proliferation stimulated by EGF within 96 hours, four 96-well culture plates (Corning Inc., Corning, NY) were used. In the control experiments, a 100 μl of fibroblast solution at a density of $5x10^4$ cells/ml in EMEM complete media was added into 8 wells of the culture plates. Fibroblast solutions mixed with EGF concentrations of 0.1 ng/ml, 1 ng/ml, 10 ng/ml, 40 ng/ml, 80 ng/ml and 400 ng/ml, respectively, were added into 8 additional wells for each concentration. Note that each well contained minimum of 5000 cells, as required by the manufacture of

proliferation assays. The plates were then incubated at 37^{o}C. To measure cell proliferation, each well was then treated 15 µl of cell proliferation Dye Solution (Part # G4002, Promega Corp., Madison, WI), followed with a 2-hour incubation. Subsequently, 100 µl of cell proliferation Stop Solution (Part # G4001, Promega Corp., Madison, WI) was pipetted into each well and the plate was incubated for another 1 hour. To measure cell proliferation, a 96-well plate reader (Synergy HT, BioTek Instruments Inc., Winooski, VT) was used to record the absorbance of the plate at a wavelength of 570 nm. The proliferation rates in cells were calculated based on the initial number of cells that were placed into plates on the first day. The cell proliferation experiments were repeated 4 times to ensure data reliability.

Cell and EGF loading in the bridged µlane system: The µlane system was first coated with fibronectin (Sigma-Aldrich Co., St. Louis, MO) at a concentration of 10 ng/ml overnight before cells were inserted. After coating, solutions of fibroblasts with density of 3 x 10^5/ml were injected into the microchannel of the system from the SRC chamber using a 1-ml syringe. The SRC chamber, the SKC chamber and the bridged channel were subsequently filled with solutions of growth media. The bridged µlane systems were then incubated overnight (~14 hours) to allow cells to fully adhere and visibly spread inside of the system prior to next experiments.

In the experiments where uniform EGF (Invitrogen Corp., Eugene, OR) concentration was applied, solution of 40-ng/ml, 80-ng/ml and 400-ng/ml EGF were individually used. First, the growth media in the µlane system was carefully aspirated to avoid cell detachment in the microchannel. Next, EGF solution was injected into the

microchannel using a syringe and then filled into the SRC chamber, the SKC chambers and the bridge channel. Lastly, the system was placed in a micro-incubator (Warner Instruments LLC, Hamden, CT) that was mounted on a motorized stage of the inverted microscope (Nikon TE2000) for observation. The temperature in the micro-incubator was maintained at 37ºC.

For the experiments where EGF gradients were used, the procedure for establishing concentration gradient in the μlane system is described below. After cells were cultured in the microsystem overnight, the growth media was aspirated out. Fresh growth medica was only injected into the microchannel, and pipetted into the SKC chamber and the bridge channel. Next, EGF solution was added into the SRC chamber until came into contact with the growth media present in the bridge channel. The systems were then placed in the micro-incubator and imaged via the microscope. Transport of EGF from the SRC chamber to the SKC chamber through the microchannel was then modeled as described below.

Microscopy and cell images: An inverted epi-microscope (Nikon TE2000) with a 20X microscope objective (Nikon Plant 20X, Morrell Instrument Company Inc., Melville, NY) was used to image cells that adhered in the culture plates and the μlane systems via a cooled CCD camera (CoolSNAP EZ, Photometrics, Tucson, AZ) with Nikon software (Nikon Instrument Element 2.30 with 6D module, Morrell Instrument Company Inc., Melville, NY). All images were in dimensions of 0.38-mm-length by 0.46-mm-width, and displayed the specific cell positions within the culture plates and the

microchannels. A shutter (HF204, Prior Scientific Inc., Rockland, MA) mounted in the Nikon TE2000 was used to control the exposure time.

Simulation of 1-D diffusion: Numerical simulations were performed to estimate the transport of ligand from the SRR reservoir to SKR reservoir. The transport within the microchannel was modeled as one-dimensional because of the large ratio of microchannel length to its hydraulic diameter (137: 1). The one-dimensional convective-diffusion equation was used to model ligand transport within the microchannel and defined as [47]:

$$\frac{\partial C}{\partial t} + V\frac{\partial C}{\partial x} = D\frac{\partial^2 C}{\partial x^2} \qquad (5.1)$$

where C (mg/ml) is the concentration, V (m/s) is the mean bulk velocity in the microchannel, and D (m^2/s) is the diffusion coefficient of the fluorescent molecule. Finite-element-analysis (FEA) software FEMLab Version 3.2 (Comsol Inc., Burlington, MA) was used to solve this equation. A fine mesh of 1504 elements was used in the simulation such that ligand gradients across small populations of cells can be predicted. Note that simulation results were not significantly increased (<1%) when larger meshes were used. The microchannel, both the SRR and SKR reservoirs in the 1st layer PDMS, bridged channel, and both the SRC and SKC chambers in the 2nd layer PDMS were modeled as shown in **Figure 5.3A**. First, the initial concentrations of ligand at the SRC chamber in the diffusion model were set to the values used in experiments, while the ligand concentration within the SKC chamber was set to 0 ng/ml. The ligand concentrations in both SRC and SKC chambers remained constant during the simulation. Second, the mean bulk velocity in the microchannel, V, was experimentally measured using the fluorescent beads, as described before. The mean bulk flow velocity within the

microchannel was measured as 0.37 ± 0.01 μm/s (n=10) when Dextran was applied. The mean bulk flow velocity was 0.60 ± 0.01 μm/s (n=10) when EGF was used. Third, we estimated the diffusion coefficients of ligands by averaging different values published in the literature. For Dextran diffusion, the published diffusivity values have been reported between 0.80×10^{-6} cm^2/s and 0.84×10^{-6} cm^2/s [48]. However, a wider range between 0.7×10^{-6} cm^2/s and 1.0×10^{-6} cm^2/s was used and substituted into the equation (4.1) in the simulation in order to fully examine the Dextran diffusivity from our experiments. As reported in **Table 5.1**, published EGF diffusivity ranged from 0.5×10^{-6} cm^2/s measured via in vivo rodent experiments to 2.3×10^{-6} cm^2/s computed from numerical solutions of the Stokes-Einstein Equation [12, 49-52]. These multiple diffusivities were averaged to obtain a value of 2.0×10^{-6} cm^2/s as EGF diffusivity in our experiments, which was then used in the simulation of EGF transport to generate EGF concentration profiles as a function of time and position. **Figure 5.3B** illustrates the graphical solution to the convective-diffusion equation using the conditions discussed.

Experiment	EGF Diffusivity (10^{-6} cm^2/s)	Reference
In vivo (rat cortex)	0.50-0.53	12, 55
In vitro (dilute agarose)	1.2-1.7	12, 55, 57
Computational models	2.1-2.3	54, 56
Simulation	2.0	Present study

Table 5.1: Published EGF diffusivities measured using different experimental and computational methods. EGF diffusivity measured within the in vivo rat cortex was reported to be $0.50\text{-}0.53 \times 10^{-6}$ cm^2/s, while the in vitro measure of EGF diffusivity using dilute agarose gel yielded $1.2\text{-}1.7 \times 10^{-6}$ cm^2/s. The computation of EGF diffusivity using the Stokes-Einstein Equation was also reported in the literature with a value of $2.1\text{-}2.3 \times 10^{-6}$ cm^2/s. The EGF diffusivity used in the present simulation was chosen to be 2.0×10^{-6} cm^2/s, i.e. the average of published EGF diffusivities in free solution.

Data processing and plotting: The experimental data of fluorescent intensity as a function of time, and the simulation data as a function of time were normalized, and plotted in the same diagram using software (Origin 7.5, Origin Lab Corp., Northampton, MA). Note that some dimensionless normalized experimental data slightly exceeded 1 because of experimental noise. The normalized experimental data were fitted into a curve ($R^2 \geq 99.8\%$), using the Hill function, a category of Sigmoidal functions provided by the software, in order to better compare with the simulated data. The Hill function is given as:

$$y = V_{\max} \cdot \frac{x^n}{k^n + x^n} \qquad (5.2)$$

where the V_{max} is the asymptotic value of the experimental data, k and n are empirical constants given by the software, and x and y are axis coordinates. The residual difference, defined as the absolute difference between each individual data point from the Hill-function fit curve and each individual data point from the simulation curves at the same corresponding time point, was analyzed using the Student's t-test in order to identify the simulation curve that was closest to the Hill-function fit curve of the experimental data. The simulation curve with the least standard deviation of residual difference (<2%) and the least average residual difference at all the data points (<10%) was considered to be characteristic of the diffusion coefficients in free solution.

In-cell western blotting: This technique has been used in the detection of growth factor receptor phosphorylation, as described in the literature [53]. Fibroblasts with growth media (10% FBS and 2% L-Glutamine in EMEM) were seeded into a 48-well plate (Corning Inc., Corning, NY) and incubated at 37^{o}C for 3 days until cells reached confluence with a density of 10^6 cells/well. Cells were then starved by replacing the

growth media with serum-free EMEM, and incubated at 37^{o}C for 4 hours. Cells were treated with EGF at different concentrations, 0.1 ng/ml, 1 ng/ml, 10 ng/m, 40 ng/ml, 80 ng/ml and 400 ng/ml, for 1 hour. Afterwards, cells were fixed with 3.7% paraformaldehyde (Sigma-Aldrich Inc., St. Louis, MO), permeated with 0.1% Triton X-100 (Sigma-Aldrich Inc., St. Louis, MO), washed with 0.1% Tween-20 (Across Organics, Morris Plains, NJ), treated with blocking buffer (Li-Cor, Inc., Lincoln, NE) at room temperature (25^{o}C) and incubated with rabbit polyclonal anti-EGFR primary antibody (Abcam Incl, Cambridge, MA, part #: ab2430) and mouse monoclonal anti-phosphorylated EGFR primary antibody (Biodesign International, Saco, ME, part #: K67902M) at 4^{o}C for overnight (~14 hours). The cells were then washed and incubated with goat-against-rabbit secondary antibody (Li-Cor, Inc., Lincoln, NE, part #: 926-32211) and goat-against-mouse secondary antibody (Li-Cor, Inc., Lincoln, NE, part #: 926-32220) at room temperature for 1 hour. Subsequently, an infrared imaging system, Odyssey (Li-Cor, Inc., Lincoln, NE), was used to record the infrared intensity from EGFR and the phosphorylated EGFR within the cells.

5.3 Results

Ligand transport within the μlane system

The first set of experiments measured fibroblast migration in response to EGF gradients within the bridged μlane system. In order to examine the feasibility of ligand gradient generation within the microsystem, the widely-studied fluorescent labeled Dextran was first tested [54].

After the Dextran solution was applied into the microsystem, fluorescent signal from the Dextran was optically observed to displace along the microchannel, as seen in **Figure 5.2**. The bulk flow velocity of Dextran transport within the microchannel measured to be 0.37±0.01 μm/s. The Dextran transport within the microsystem was also modeled and simulated using finite element analysis, as illustrated in **Figure 5.3**. Note that Dextran was also observed to transport through the bridged channel toward the SKC chamber. However, the transport was neglected because no flow was observed within the bridge channel and the Dextran diffusion in the bridged channel was therefore much slower than the Dextran diffusion within the microchannel, as seen in the **Figure 5.3A**. Moreover, the Dextran concentration in the SKC chamber remained zero during experiments for up to 96 hours. Fluorescent intensity measured at specific detection positions from Dextran transport experiments and the mathematical prediction of 1-D simulation of Dextran transport within the microchannel, were normalized and plotted as a function of time, shown in **Figure 5.4**. As seen, Dextran concentration within the microchannel increased over time and reached steady-state at the entire microchannel in approximately 18 hours. The explicit gathered intensity data were compared against mathematical data obtained via simulation using a range of Dextran that included these diffusivities found in the literature. As seen, the Dextran diffusivity in our experiment was measured to be 0.82±0.01 x 10^{-6} cm^2/s, which was in line with the reported values between 0.80 x 10^{-6} cm^2/s and 0.84 x 10^{-6} cm^2/s [48].

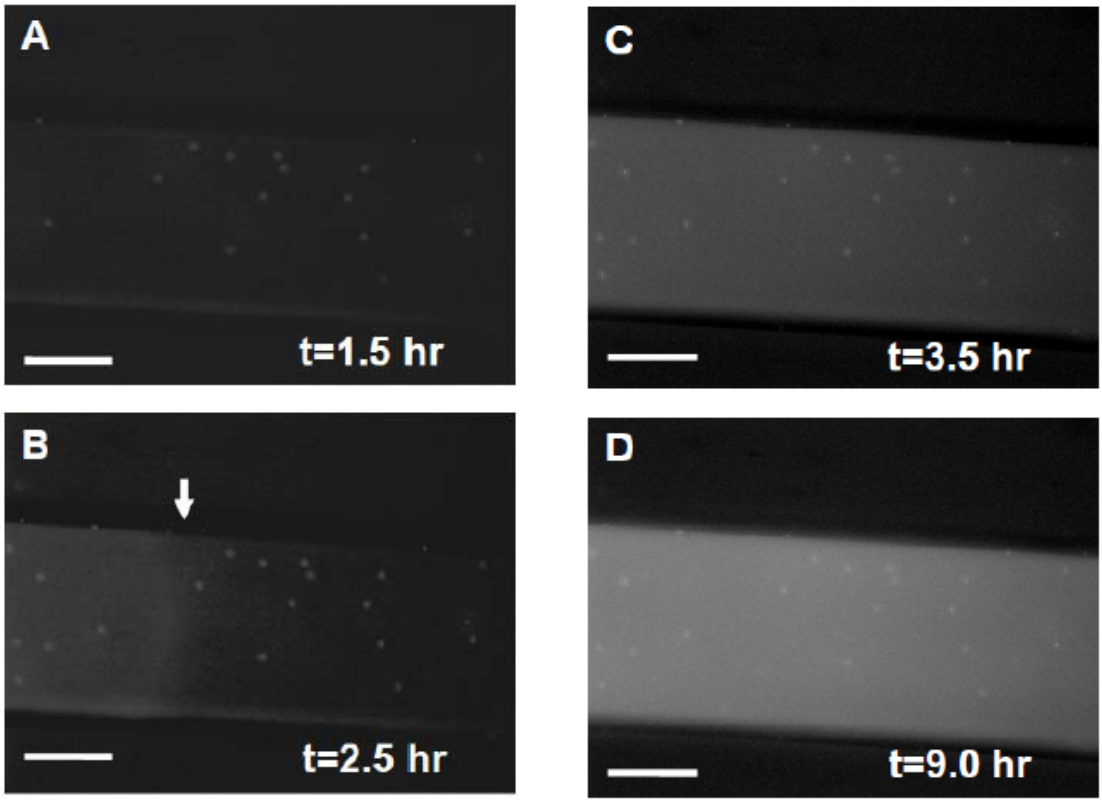

Figure 5.2: Images of Dextran transport within the microchannel over time. Arrow points to the leading edge of Dextran transport visibly observed in the microchannel after 2.5 hours (B). Dextran fluorescence was initially observed throughout the microchannel in 3.5 hours (C), with increasingly strong fluorescence after 9 hours (D), until reaching steady-state in 18 hours. The white dots seen in images represent fluorescent beads used inside of the bridged μLane system to measure bulk velocity (if present) during experiments. Scale bar: 50μm.

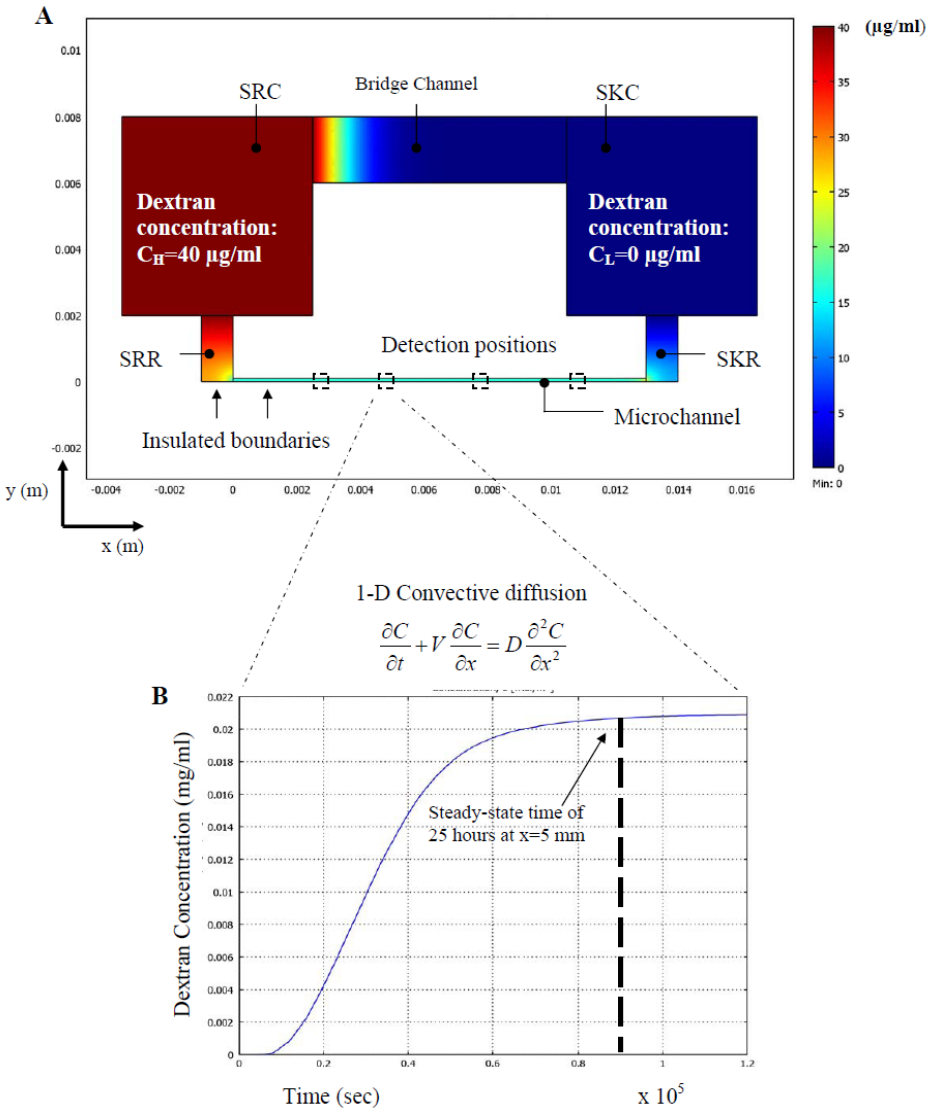

Figure 5.3: Simulation of Dextran transport within the bridged µLane system. The source chamber (SRC), source reservoir (SRR), microchannel, sink reservoir (SKR), sink chamber (SKC) and bridge channel were modeled using finite element software (A). The Dextran concentration in the SRC chamber was set to a maximum of C_H = 40 ng/ml, while the Dextran concentration in the SKC chamber was set to a minimum of C_L = 0 ng/ml. The bulk velocity within the microchannel was measured using fluorescent beads, and inputted into the Dextran transport model for numerical simulation. All of the boundaries of the bridged µLane system were modeled as insulated from mass transfer. Dextran transport at different positions within the microchannel, x=5mm, x=8mm and x=11mm, respectively, was examined over time. One-dimensional convective diffusion equation was used to model the transport of Dextran within the microchannel, where C represents concentration, V is bulk velocity and D is the diffusion coefficient. The simulation illustrates that the Dextran concentration at a representative microchannel position of x=5mm increases over time and reaches steady-state in 11 hours (B).

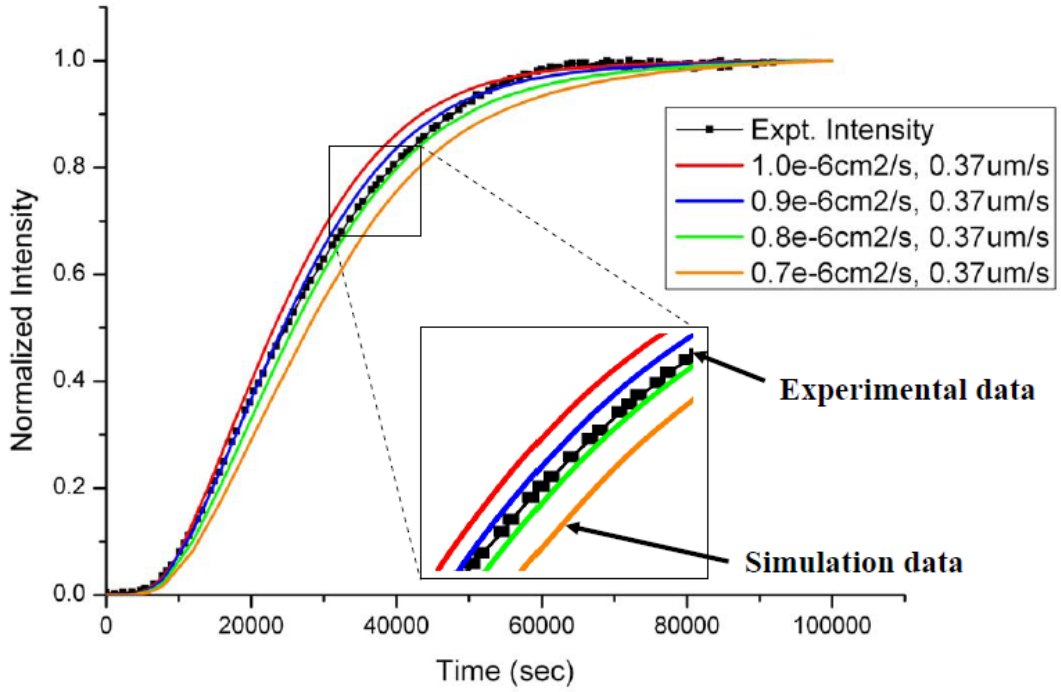

Figure 5.4: Graph of normalized experimental data obtained from Dextran transport experiments within the bridged μLane system, compared against normalized simulation data generated from the 1-D convective diffusion equation These normalized data were plotted as a function of time. A range of Dextran diffusion coefficients between 0.7 x 10^{-6} and 1.0 x 10^{-6} cm^2/s, and the experimentally measured mean bulk velocity for Dextran of V=0.37μm/s, were used in the numerical simulation to generate the Dextran concentration profiles shown at different detection positions over time.

The previous experiments demonstrated that the numerical modeling of Dextran transport within the μlane system was consistent with the experimental results. Therefore, we continued to use the numerical model to predict the transport of unlabeled EGF within the μlane system, and analyze EGF concentration and gradient as a function of position within the microchannel over time. Note that the value of EGF diffusivity used in our model was the average of values published in the literature and shown in **Table 5.1**. The EGF simulation model used was similar to the one used in Dextran transport experiments. The test additionally used fluorescent beads to optically measure bulk velocity within the

microchannel, which was 0.40±0.01 μm/s. The EGF concentration applied in the SRC chamber was denoted as C_0, while the EGF concentration within the microchannel was C(x, t). The ratio of C(x, t)/C_0 was defined as dimensionless concentration. When different C_0 were applied, the local EGF concentration within the microcahnnel varied. However, the dimensionless concentration barely changed (data not shown). Our computational models illustrated that the local EGF concentration and gradient, defined as $\partial C/\partial x$, reached steady-state in 18 hours at the entire microchannel. The EGF concentration and gradient were non-linearly distributed along the microchannel. as shown in **Figure 5.5**.

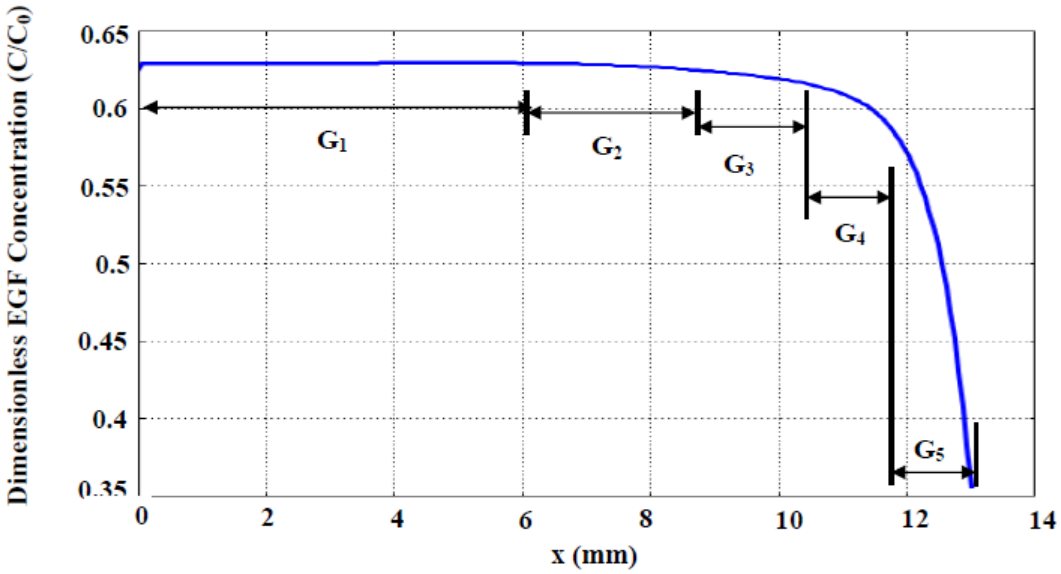

Figure 5.5: Graph of steady-state EGF concentration gradients distributed along the microchannel. EGF gradients were categorized into 5 ranges: $0<G_1<10^{-3}$ ng/(ml.mm), $10^{-3}<G_2<10^{-2}$ ng/(ml.mm), $10^{-2}<G_3<10^{-1}$ ng/(ml.mm), $10^{-1}<G_4<10^{0}$ ng/(ml.mm), and $10^{0}<G_5<10^{1}$ ng/(ml.mm). These gradients were unevenly distributed at different positions along the length of the microchannel.

The predicted spatial and temporal profiles of local EGF concentration and gradients within the μlane system were then used to analyze effects of different EGF gradients on cell morphology and cell motility in our experiments.

Effects of uniform EGF concentrations and EGF gradients on cell migration

In the control experiments where no EGF was applied, cells were observed to migrate without persistent direction, as shown in **Figure 5.6A**. The maximum displacement was measured to be 6.1±3.4 μm from the cell centroid and the cell motility was 2.4±2.1 μm/hr, as shown in **Table 5.2**. When uniform EGF concentrations of 40 ng/ml, 80 ng/ml and 400 ng/ml were applied, cells were also observed to migration in all directions. As seen in **Figure 5.6B**, cells stimulated at the uniform EGF concentration of 40 ng/ml were observed to migrate in the area where the maximum cell displacement was measured to be 10.5±4.4 μm. The cell motility exhibited 4.4±1.1 μm/hr. When EGF concentration was increased to 80 ng/ml and 400 ng/ml, cells were seen to migrate with the maximum cell displacement of 13.3±4.2 μm and 20.8±5.1 μm, respectively, as seen in **Figure 5.6C** and **Figure 5.6D**. The motility was also found to increase to 5.4±2.4 μm/hr for uniform EGF concentration of 80 ng/ml and 6.2±2.7 μm/hr for 400 ng/ml.

After EGF concentration gradients were established and reached steady-state within the microchannel, cells were observed to migrate toward higher concentration of EGF, i.e. toward the SRR reservoir, as seen in **Figure 5.6E**, **5.6F** and **5.6G**. When EGF of 40 ng/ml was used, maximum cell displacement measured 218.5±80.6 μm, while cell motility was 22.4±2.1 μm/hr. When EGF of 80 ng/ml and EGF of 400 ng/ml were used, maximum cell displacement measured 237.8±76.8 μm and 174.3±53.2 μm, respectively.

The cell motility was measured to be 25.4±3.4 µm/hr for 80-ng/ml EGF used and 7.4±2.9 µm/hr for 400-ng/ml EGF used.

Uniform Concentration (ng/ml)	Maximum Displacement (µm)	Motility (µm/hr)		Gradient-Concentration (ng/ml)	Maximum Displacement (µm)	Motility (µm/hr)
0 (n=49)	6.1±3.4	2.4±2.1		0 (n=49)	6.1±3.4	2.4±2.1
40 (n=44)	10.5±4.4	4.4±1.1		40 (n=62)	218.5±80.6	22.4±2.1
80 (n=52)	13.3±4.2	5.4±2.4		80 (n=60)	237.8±76.8	21.4±3.4
400 (n=40)	20.8±5.1	6.2±2.7		400 (n=64)	174.3±53.2	7.4±2.9

Table 5.2: Maximum cell displacement and motility measured in response to uniform EGF concentrations (no gradient) and EGF concentration gradients, generated by 40 ng/ml, 80 ng/ml and 400 ng/ml. The total number of cells per experiment is shown. Note that data illustrate values accumulated from all gradients.

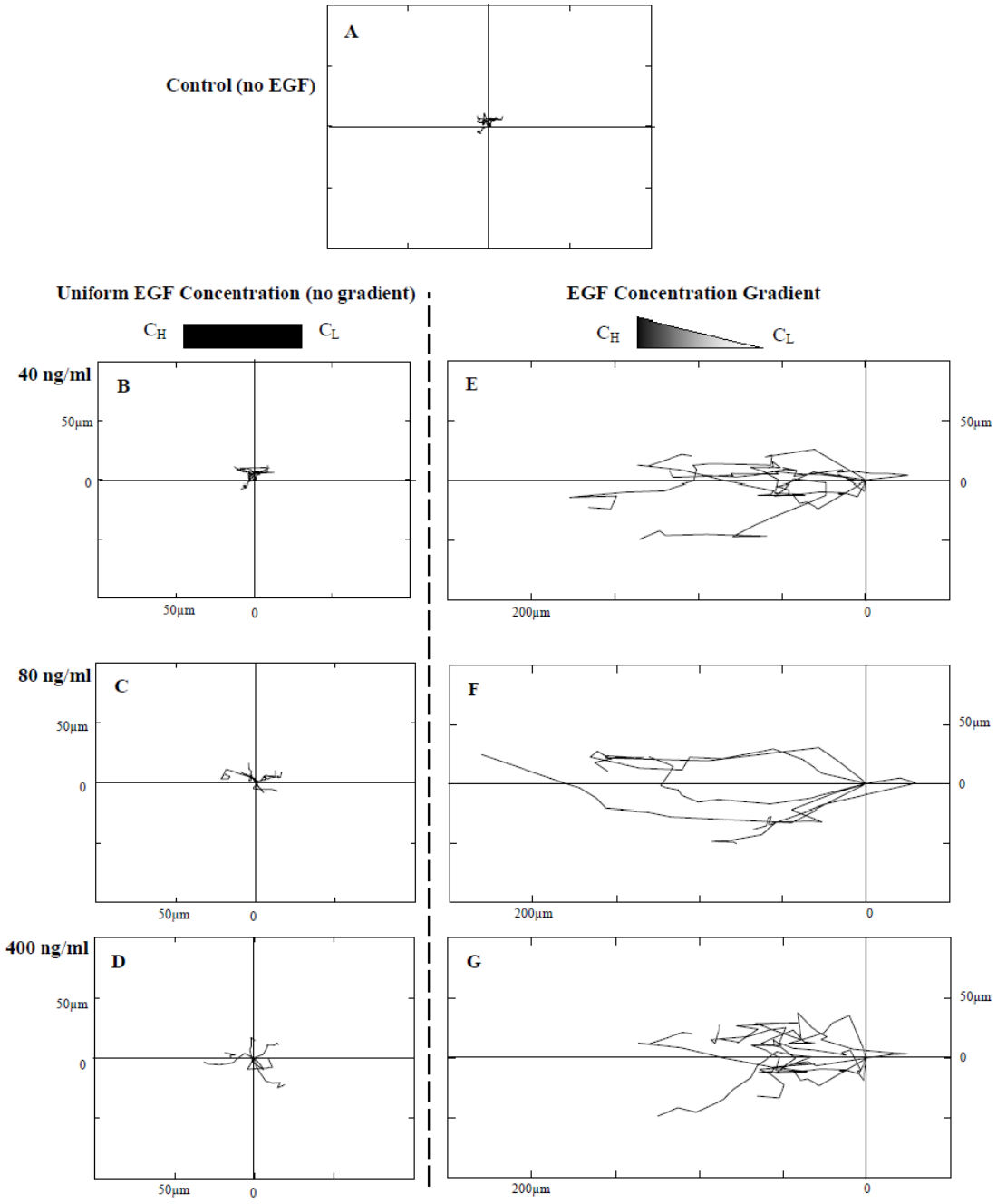

Figure 5.6: Wind-Rose plots of cell trajectory in response to EGF stimulation within the microchannel. Six representative cell paths are illustrated in each plot for different experimental conditions at 15 hours: control (no EGF applied) (A), uniform EGF concentration (no EGF gradient generated) of 40 ng/ml (B), 80 ng/ml (C) and 400 ng/ml (D), and EGF concentration gradient, generated using 40 ng/ml (E), 80 ng/ml (F) and 400 ng/ml (F) as initial stimulus. Distance between hatch marks on both axes in each plot is 50 µm. Note that the induced cell migration is seen from right to left.

Cell motility in response to EGF gradients

In order to further analyze how EGF gradients affect cell migration, all the EGF gradients that were generated by 3 different EGF concentrations (i.e. 40 ng/ml, 80 ng/ml and 400 ng/ml) were categorized into 5 ranges: $0<G_1<10^{-3}$ ng/(ml.mm), $10^{-3}<G_2<10^{-2}$ ng/(ml.mm), $10^{-2}<G_3<10^{-1}$ ng/(ml.mm), $10^{-1}<G_4<10^{0}$ ng/(ml.mm), and $10^{0}<G_5<10^{1}$ ng/(ml.mm). These gradients, G_1 to G_5, occupied different length of positions along the microchannel, and distributed non-linearly along the microchannel, as shown in **Figure 5.5**. The lowest gradient G_1 located near the SRR reservoir within the largest area of approximately 6 mm along the microchannel, while the highest gradient G_5 exhibited near the SKR reservoir within a smallest area of approximately 1 mm. The slope of EGF concentrations in the area near the SKR reservoir, i.e. the gradient G_5, was the steepest, while the slope near the SRR reservoir, i.e. G_1, appeared flat. As seen, gradients G_1, G_2 and G_3 displayed approximately linear profiles, while G_4 and G_5 exhibited highly non-linear. Note that the location of each EGF gradient slightly shifted along the microchannel when different EGF concentrations were used. However, the EGF gradient patterns appeared similar.

The motility of cells that located within different EGF gradient areas were measured, and found to vary per EGF gradient, as displayed in **Figure 5.7**,. In the control experiments where no EGF gradient was applied, i.e. G0, the cell motility was 4.4±1.1 μm/hr for uniform EGF concentration of 40 ng/ml, 5.4±2.4 μm/hr for 80 ng/ml, and 6.2±2.7 μm/hr for 400 ng/ml, as described previously in **Table 5.1**. In the experiments where EGF gradients were generated using 40-ng/ml of EGF, the cell motility was measured to be 25±1.3 μm/hr for G1, 26±1.3 μm/hr for G2, 31±1.6 μm/hr for G3, 16±1.1

μm/hr for G4, and 20±1.2 μm/hr for G5. While 80 ng/ml of EGF was used, the cell motility measured for G1 to G5 was 22±1.2 μm/hr, 23±1.5 μm/hr, 27±1.3 μm/hr, 15±0.8 μm/hr, and 18±1.1 μm/hr, respectively. The cell motility were also observed to be 6±0.5 μm/hr for G1, 7±0.6 μm/hr for G2, 9±0.7 μm/hr for G3, 6±0.5 μm/hr for G4, and 5±0.5 μm/hr for G5.

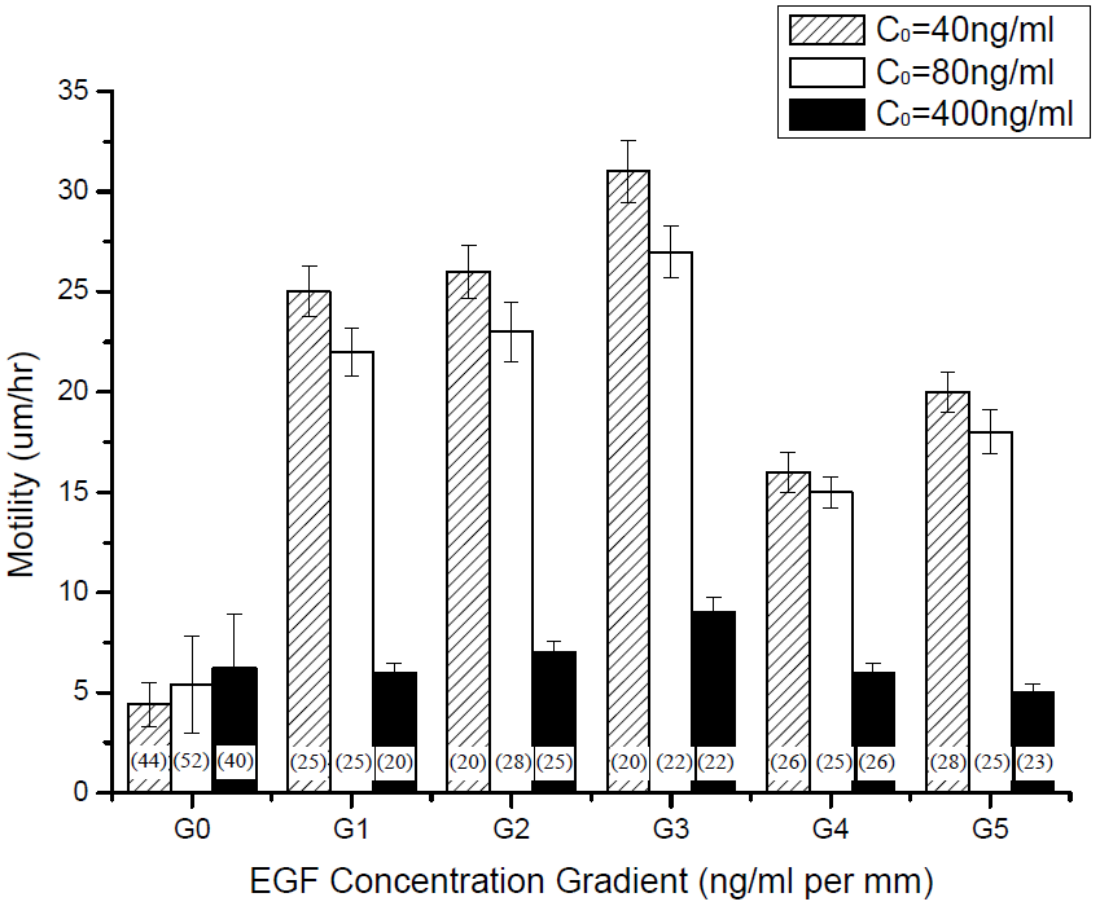

Figure 5.7: Cell motility measured as a function of EGF concentration gradients. EGF gradients, defined as EGF concentration difference over distance, were categorized into 6 ranges: $G_0=0$, $0<G_1<10^{-3}$ ng/ml per mm, $10^{-3}<G_2<10^{-2}$ ng/ml per mm, $10^{-2}<G_3<10^{-1}$ ng/ml per mm, $10^{-1}<G_4<10^{0}$ ng/ml per mm, and $10^{0}<G_5<10^{1}$ ng/ml per mm of the microchannel. Cell motility was defined as the distance traveled by each cell divided by time. The number of cells per experiment is shown in parentheses.

Effects of EGF gradient on numbers of migratory cells

In order to examine the number of cells that migrated in response to different EGF gradients, we first set a criterion that only the cells that migrated more than 80 μm measured from the cell centroids were counted. And the cells of such migration distance were denoted as motile cells. Note that this minimum migration distance was measured three times larger than the average cell diameter. Here, we also denoted the ratio of the number of motile cells to the number of total cells at a given EGF gradient range as chemotaxis index (CI).

As seen in **Figure 5.8**, CI was EGF gradient-dependent. In the control experiments (G0, i.e. no EGF gradient), no cells were found to migrate more than 80 μm. Therefore, the CI was measured to be 0 for the three uniform EGF concentrations used. In the experiments where EGF gradient was generated with 40-ng/ml EGF applied, 1.6±0.1% of total cells migrated as motile cells at gradient G1, i.e. CI=1.6±0.1%. CI were then measured to be 6.7±0.5 for G2, 38±3.3% for G3, 55.6±3.0% for G4, and 75±4.1% for G5. Similarly, when 80 ng/ml of EGF was used, CI became 4±0.2%, 18±0.8%, 36.4±1.8%, 66.7±3.3%, and 85±3.8% for the gradients from G1 to G5, respectively. As 400-ng/ml EGF was used, CI was 7.4±0.6% for G1, 9.5±0.8% for G2, 21.8±1.7% for G3, 17.6±1.4% for G4, and 34.8±2.8% for G5.

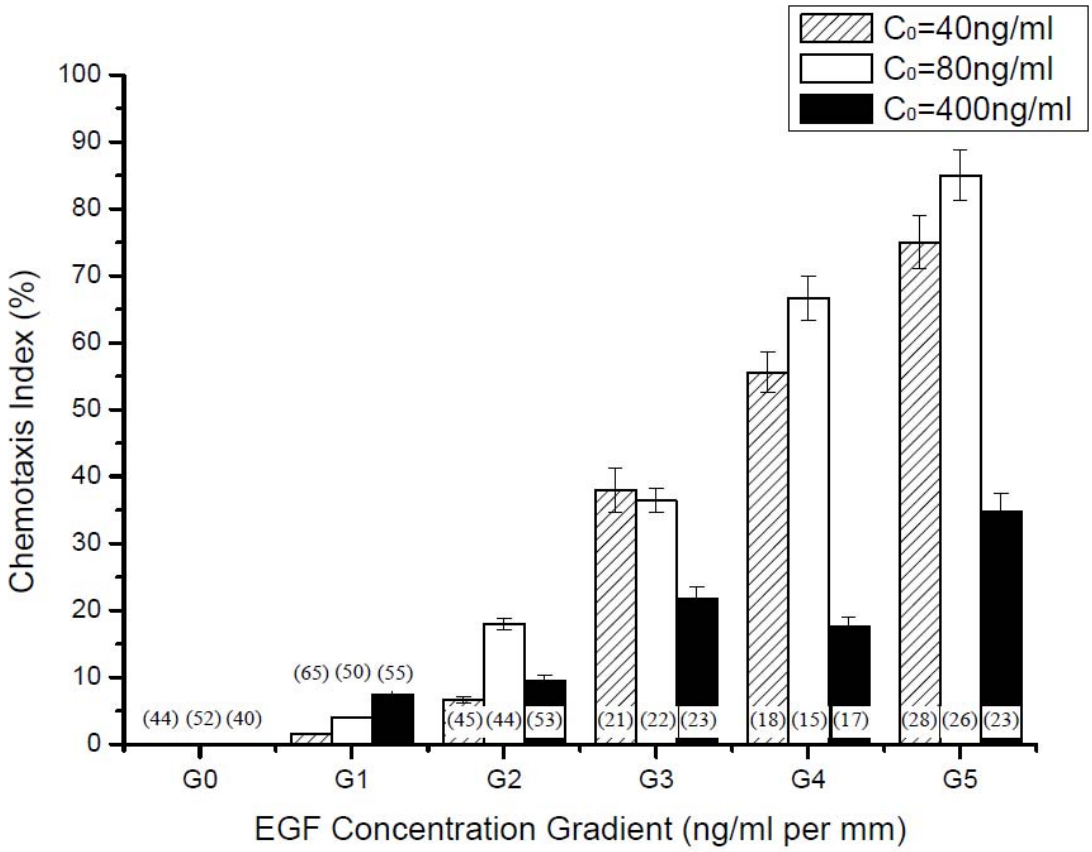

Figure 5.8: Percentage of motile cells observed in response to imposed EGF gradients, G_0 through G_5: $G_0=0$, $0<G_1<10^{-3}$ ng/ml per mm, $10^{-3}<G_2<10^{-2}$ ng/ml per mm, $10^{-2}<G_3<10^{-1}$ ng/ml per mm, $10^{-1}<G_4<10^{0}$ ng/ml per mm, and $10^{0}<G_5<10^{1}$ ng/ml per mm of the microchannel. The Chemotaxis Index (CI) is defined as the ratio of motile cells per total number of cells in the microchannel. The total number of cells is displayed in parentheses.

Phosphorylation of EGF receptor in response to uniform EGF concentrations

Cells that were cultured with uniform EGF concentrations were immunostained against EGF receptors and phosphorylated EGF receptors. The percentage of the phosphorylated EGF receptors to the total EGF receptors was observed to vary per EGF concentration applied, as shown in **Figure 5.9**. In the control experiment where no EGF was applied, 6.8±0.3% of total EGF receptors were observed to be phosphorylated. When 0.1-ng/ml EGF was used, 32.6±2.6% of total EGF receptors became phosphorylated.

When EGF concentration increased from 1.0 ng/ml, to 10 ng/ml, 40 ng/ml, 80 ng/ml and 400 ng/ml, the percentage of EGFR phosphorylation was 38.3±1.9%, 38.6±1.5%, 39.2±3.0%, 37.3±1.8%, and 38.7±2.6%, respectively.

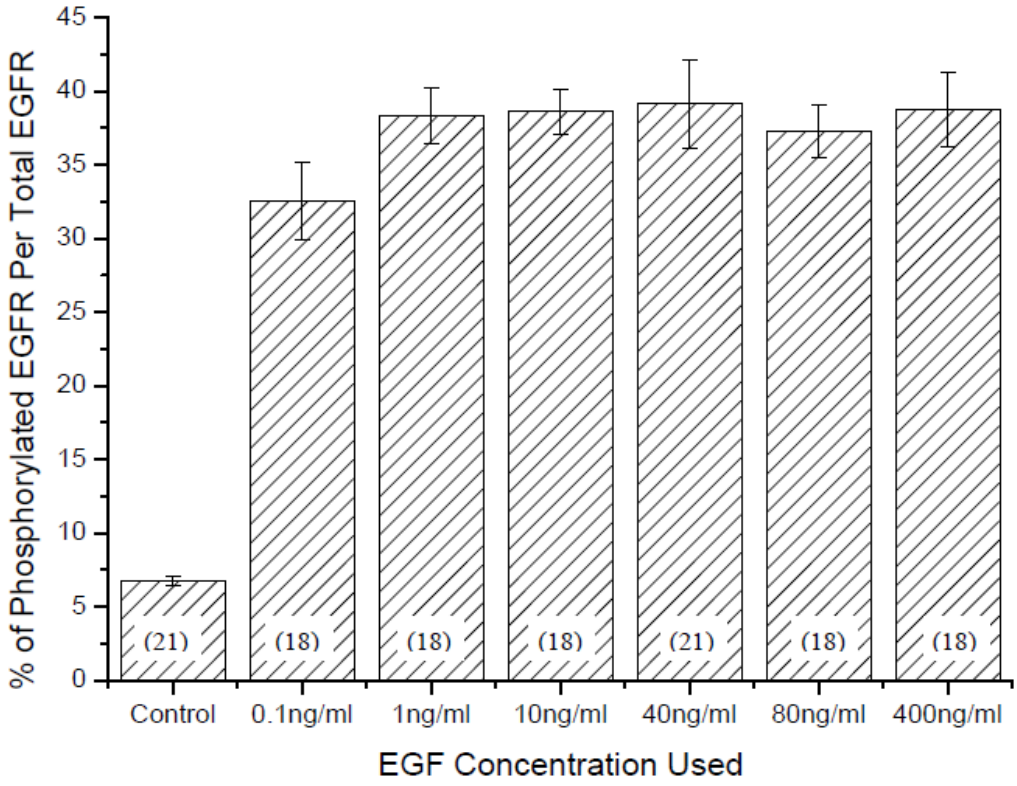

Figure 5.9: The percentage of phosphorylated EGF receptor to the total EGF receptor in response to 0.1-ng/ml, 1-ng/ml, 10-ng/ml, 40-ng/ml, 80-ng/ml and 400-ng/ml EGF concentration (no gradient). The number of samples tested is displayed in parentheses.

Cell proliferation in response to uniform EGF concentrations

EGF was seen to affect cell proliferation, as illustrated in **Figure 5.10**. Cells of control (no EGF applied), and cells that were treated with EGF concentrations of 0.1 ng/ml, 1 ng/ml, 10 ng/ml, 40 ng/ml, 80 ng/ml and 400 ng/ml proliferated over time and reached maximum proliferation in 72 hours. In 96 hours, cells of the control proliferated

3.5 fold. The cells treated with EGF of 0.1 ng/ml, 1 ng/ml, 10 ng/ml, 40 ng/ml, 80 ng/ml and 400 ng/ml proliferated 2.8, 3.1, 3.6, 4.9, 4.1 and 3.6 fold, respectively, in 96 hours.

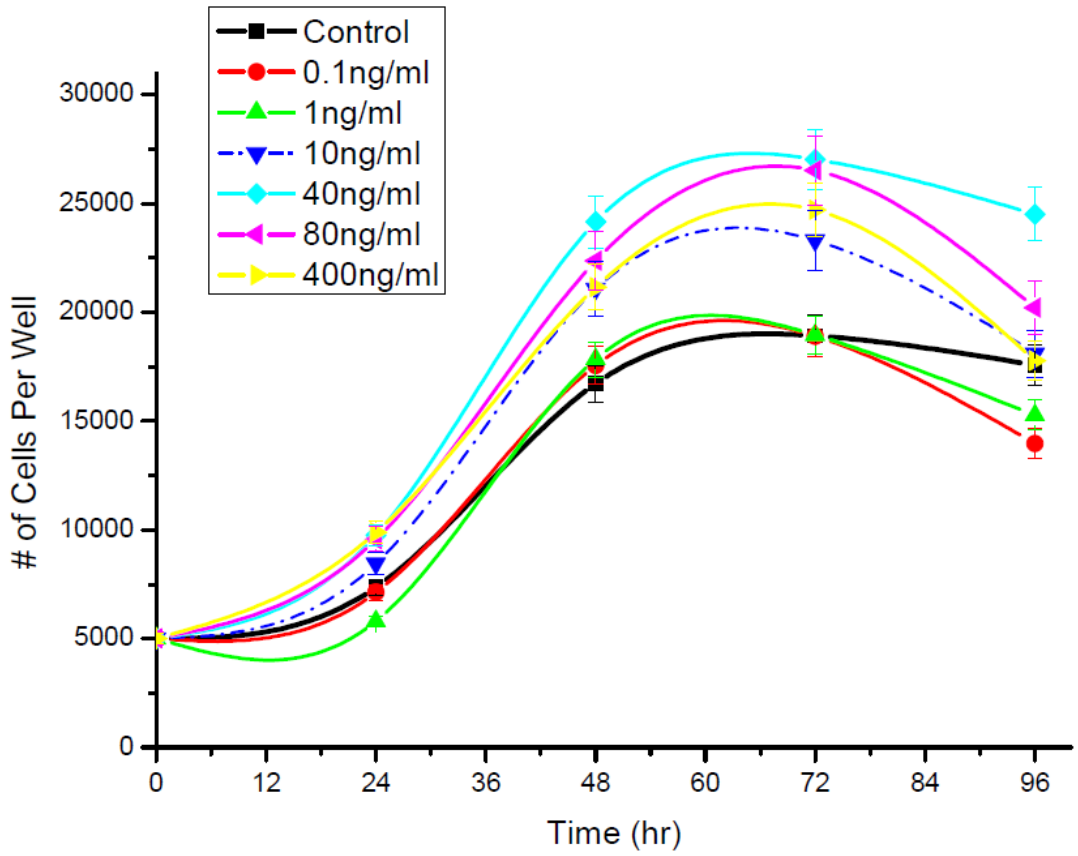

Figure 5.10: Cell proliferation measured in 96-well proliferation assays when cultured in absence of EGF (control), and with EGF at concentrations of 0.1 ng/ml, 1 ng/ml, 10 ng/ml, 40 ng/ml, 80 ng/ml and 400 ng/ml.

5.4 Discussion

Design rationale

Our microsystem was designed to reliably deliver ligands to cells and observe how these compounds stimulated cell behavior in real time [55-57]. The capability to produce specific ligand concentrations and concentration gradients in the microdevice over time, and mathematically validate these values, was essential for the study of ligand-dependent cell function. By using a straightforward design, our system delivered ligands to cells via mathematically-validated transport models and enabled optical measurement of primary migration parameters, such as motility, directionality, and distance traveled. Our microsystems is similar to some existing microdevices [24, 58], but is distinct in its efficient, convenient manufacturing, and user-friendly manipulation. While others have used machined parts and complex 3-D assembly, the μlane system accomplishes microfluidic transport using inexpensive PDMS layering. Further, cell seeding can be accomplished manually and yields reliable cell numbers within the microchannel without external pump, power supplies and sterilization concerns that accompany these peripheral accessories.

In the bridged μLane system, two volumetric reservoirs are used to gradually deliver ligands into the microchannel with minimal entrance effects, which facilitates stable ligand gradient formation within the system. Although ligand was indeed transported from the SRC chamber to the SKC chamber through the microchannel, the transport within the microchannel was treated 1-D due to the large ratio of microchannel length to its hydraulic diameter. Experiments of fluorescent Dextran transport (**Figure 5.2**) and 1-D Fick's law (**Figure 5.3**) were therefore used to verify ligand gradient

generation within the microchannel. The Dextran diffusivity measured using this methodology was in line with the published values (**Figure 5.4**), suggesting that 1-D Fickian modeling of ligand transport within the microchannel is reliable. Further, the 13-mm length of the microchannel enables optical measurement of cell migration over long, observable distances. A 2nd device layer contains two additional large volumetric chambers, and an open, so-called bridge channel that largely eliminates potential hydrostatic pressure differences in the chambers that can cause large pressure-driven flow in the microchannel during experimental loading. We note that minimal ligand transport in the bridged channel from the SRC chamber to the SKC chamber was present during the experiments (**Figure 5.5**). However, such transport in the bridge channel did not affect the ligand transport in the microchannel in this work, due to the facts that the ligand diffused slowly in the bridge channel without significant bulk flow and ligand concentration within the SKC chamber remained zero during the entire experiments (measured up to 96 hours).

As clearly shown in the experiments using fluorescent Dextran and micro-beads, the bridged μLane system relies upon convective transport, i.e. bulk flow, rather than molecular diffusion alone to generate ligand gradients during the desired experimental time. This study utilized the bulk flow as an advantage, as convective transport within the microchannel rapidly decreased the time required for ligand concentration to reach steady-state within the entire microchannel. As an example, EGF transport via diffusion alone (using the average of cited EGF diffusivities, $2.0 \times 10^{-6} cm^2/s$) would require over 230 hours to reach a linear, steady-state gradient within our 13-mm-long microchannel. However, as a consequence of convection, the bridged μLane system generated steady-

state EGF concentration profiles within approximately 18 hours (**Figure 5.5**). Additionally, such bulk flow did not significantly cause shear effects on cells, as the shear stress generated by the convection flow was measured to be less than 10^{-3} dyn/cm^2, which is far smaller than the value used to induce various cell function [59, 60]. Further, convection within the microchannel also changed the ligand gradient profile from linear, to highly non-linear along the microchannel length, which many biomedical studies have recently suggested plays an important role in the chemotaxis of live, biological systems [61-63].

Integrated effects of EGF concentration and gradients on cell migration

EGF ligand increased cell motility and migration distance (**Table 5.2**). However, cells were stimulated to migrate in a random manner (**Figure 5.6**). As a contrast, EGF gradient not only increased the cell motility and migration distance, but also directed cell migration. Ligand gradients generated a particular cellular microenvironment where asymmetric ligand concentration was allocated along the cell length [3, 64]. This asymmetric ligand distribution stimulated cells differently in the leading edge and trailing edge, and therefore directed cells to migrate toward the higher ligand concentration. The directionality hence caused cells to migrate with longer distance than the uniform concentration. Moreover, ligand gradients induced cells to be more sensitive to ligand stimulation than the uniform lignad concentration [2, 65]. It therefore could stimulate cells with higher motility than the uniform concentrations, as observed in our experiments.

The effects of EGF gradients on cell motility were gradient-dependent. EGF gradients that were almost linear with lower magnitudes (G_1, G_2 and G_3) induced higher cell motility than higher, steep and non-linear EGF gradients (G_4 and G_5) (**Figure 5.5**). Steepness may play a role in stimulating cell migration, as steeper gradients present more asymmetric ligand concentration distribution along the cell body to trigger higher cell migration. Additionally, profiles of non-linear gradients have been reported to stimulate higher cell motility than linear gradients [38, 66]. However, the magnitude of ligand gradients also regulates cell migration, as higher concentrations may affect ligand receptor affinity [67, 68] and increase intracellular inhibition [65, 69], which may therefore result in lower cell motility. These may suggest that magnitude, steepness and linearity of EGF gradients are coordinated to regulate cell motility, and that there is an optimal range of EGF gradients to induce the highest cell motility per cell type.

Local EGF concentrations also played an important role in regulating cell motility. When cells were exposed to EGF gradients, the highest local EGF concentrations that were generated by the initial application of C_0=400 ng/ml exhibited the lowest cell motility. The lowest local EGF concentration generated by C_0=40 ng/ml induced highest cell motility. This may be related to the down regulation of receptor activity at high growth factor concentrations [65, 67, 70], as such concentration could generate thresholds to inhibit cell migration [65, 69].

EGF concentration and gradient were also observed to synergistically stimulate the number of motile cells. The chemotaxis index (CI), i.e. percentage of motile cells, increased with increasing EGF gradients (**Figure 5.8**). However, local EGF concentrations significantly regulated the number of motile cells, as the CI varied at each

given range of EGF gradients. As the EGF gradients increased within the range of lower, flat EGF gradients from G_1 to G_3, higher local EGF concentrations alternatively induced fewer cells to migrate. Interestingly, intermediate local EGF concentrations caused highest number of motile cells at the higher, steep gradients (G_4 and G_5), while the highest local EGF concentrations significantly stimulated fewest cells to migrate. The thresholds caused by high growth factor concentrations to inhibit cell migration may be responsible for such migratory phenomena.

The EGF concentration may be integrated with EGF gradients to stimulate cell motility and the number of motile cells, and play as an essential role to regulate cell migration as EGF gradients.

Effects of uniform EGF concentrations on EGFR phosphorylation and cell proliferation

EGF-stimulated cell migration was initiated with EGF-EGFR binding and EGFR phosphorylation. The phosphorylation of growth factor receptors could largely affect cell function, such as cell migration and proliferation [71, 72]. However, our In-Cell Western experiments showed that the low, intermediate and high uniform EGF concentrations did not significantly affect EGFR phosphorylation, and suggested that the EGFR phosphorylation may be saturated at these EGF concentrations (**Figure 5.9**). However, how these pathways eventually lead to cell migration remains under investigation.

EGF is also well-known to stimulate fibroblast proliferation in a dose-dependent manner [36, 73]. In this work, EGF caused fibroblast proliferation at levels higher than seen in the controls (**Figure 5.10**). The highest EGF concentration (i.e. 400 ng/ml)

stimulated cells with lower proliferation rate than the intermediate (80 ng/ml) and low (40 ng/ml) EGF concentrations, and higher random cell motility than the other lower concentrations (**Table 5.2**). This may be related to the recent observation that cells either migrated or continued proliferation when cells experienced cell cycles for division [74]. However, more experiments need to perform for such investigation of coordination between proliferation and migration.

In summary, we have designed the bridged μLane system to investigate cell migration stimulated by steady-state EGF gradients. The bridged μLane can be utilized to deliver a variety of ligands toward cells, generate ligand concentration gradients, and observe consequent cell function known to play important roles in a multitude of biomedical-related studies [73, 75, 76]. Our results point to the importance of ligand gradients in cell migration rather than concentration alone, illustrate the effects of different gradient profiles on cell migration, and also suggest the integrative contributions of growth factor concentration and gradients to cell migration. The bridged μLane system is, therefore, a novel platform with which to study cell chemotaxis in a quantitative microenvironment.

Acknowledgements:

This work was supported by the National Institutes of Health (GM071702-01), the National Science Foundation (CBET0428573) and PSC-CUNY.

Reference:

1. Devreotes P and Janetopoulos C, *Eukaryotic Chemotaxis: Distinctions between Directional Sensing and Polarization.* J. Biological Chemistry, 2003. **278**(23): p. 20445-8.
2. Sahai E, *Mechanisms of Cancer Cell Invasion.* Current Opinion in Genetics and Development, 2005. **15**: p. 87-96.
3. Van Haastert, P. and Devreotes PN, *Chemotaxis: Signalling the Way Forward.* Nature, 2004. **5**: p. 626-34.
4. Ware MF, Wells A, and Lauffenburger DA, *Epidermal Growth Factor Alters Fibroblast Migration Speed and Directional Persistence Reciprocally and in a Matrix-Dependent Manner.* J. Cell Science, 1998. **111**: p. 2423-32.
5. McKean JM, Hsieh AH, and Sung KL, *Epidermal growth factor differentially affects integrin-mediated adhesion and proliferation of ACL and MCL.* Biorheology, 2004. **41**(2): p. 139-52.
6. Kayali A. G., Stotland A., Gunst K. V., Kritzik M., Liu G., Dabernat S., Zhang Y. Q., Wu W., and Sarvetnick N., *Growth factor-induced signaling of the pancreatic epithelium.* J Endocrinol, 2005. **185**(1): p. 45-56.
7. Nicholson C and Tao L, *Hindered Diffusion of High Molecular Weight Compounds in Brain Extracellular Microenvironment Measured with Integrative Optical Imaging.* Biophysical J., 1993. **65**: p. 2277-90.
8. Raghavan S., Nelson C. M., Sniadecki N. J., Lim E. A., and Chen C. S., *Engineered microenvironments to investigate cellular behavior.* Conf Proc IEEE Eng Med Biol Soc, 2006. **1**: p. 2357.
9. Saadi W, Rhee SW, Lin F, Vahidi B, Chung BG, and Jeon NL, *Generation of stable concentration gradients in 2D and 3D environments using a microfluidic ladder chamber.* Biomed Microdevices, 2007. **9**(5): p. 627-35.
10. Walker, G.M., J. Sai, A. Richmond, M. Stremler, C.Y. Chung, and J.P. Wikswo, *Effects of flow and diffusion on chemotaxis studies in a microfabricated gradient generator.* Lab Chip, 2005. **5**(6): p. 611-8.
11. Saadi, W., S.J. Wang, F. Lin, and N.L. Jeon, *A parallel-gradient microfluidic chamber for quantitative analysis of breast cancer cell chemotaxis.* Biomed Microdevices, 2006. **8**(2): p. 109-18.
12. Thorne RG, Hrabetova S, and Nicholson C, *Diffusion of Epidermal Growth Factor in Rat Brain Extracellular Space Measured by Integrative Optical Imaging.* J. Neurophysiol, 2004. **92**: p. 3471-81.
13. Whitesides GM, *The origins and the future of microfluidics.* Nature, 2006. **442**(7101): p. 368-73.
14. Folch A, *BioMEMS and cellular biology: perspectives and applications.* J Vis Exp, 2007(8): p. 300.
15. Keenan, T.M. and A. Folch, *Biomolecular gradients in cell culture systems.* Lab Chip, 2008. **8**(1): p. 34-57.
16. Paguirigan, A.L. and D.J. Beebe, *Microfluidics meet cell biology: bridging the gap by validation and application of microscale techniques for cell biological assays.* Bioessays, 2008. **30**(9): p. 811-21.

17. Weibel DB, Garstecki P, and Whitesides GM, *Combining microscience and neurobiology* Curr Opin Neurobiol. , 2005. **15**(5): p. 560-7.
18. Kane RS, Takayama S, Ostuni E, Ingber DE, and Whitesides GM, *Patterning proteins and cells using soft lithography.* Biomaterials, 1999. **20**(23-24): p. 2363-76.
19. Li N., Sip C., and Folch A., *Microfluidic chips controlled with elastomeric microvalve arrays.* J Vis Exp, 2007(8): p. 296.
20. Wu X and Dewey TG, *From microarray to biological networks: Analysis of gene expression profiles.* Methods Mol Biol., 2006. **316**: p. 35-48.
21. Folch, A. and M. Toner, *Microengineering of cellular interactions.* Annu Rev Biomed Eng, 2000. **2**: p. 227-56.
22. Dufva M, *Microchips for cell-based assays.* Methods Mol Biol., 2009. **509**: p. 135-44.
23. Di Carlo, D., Wu LY, and Lee LP, *Dynamic single cell culture array.* Lab Chip, 2006. **6**(11): p. 1445-9.
24. Kanegasaki S, Nomura Y, Nitta N, Akiyama S, Tamatani T, Goshoh Y, Yoshida T, Sato T, and Kikuchi Y, *A novel optical assay system for the quantitative measurement of chemotaxis.* J Immunol Methods., 2003. **282**(1-2): p. 1-11.
25. Lin, F., W. Saadi, S.W. Rhee, S.J. Wang, S. Mittal, and N.L. Jeon, *Generation of dynamic temporal and spatial concentration gradients using microfluidic devices.* Lab Chip, 2004. **4**(3): p. 164-7.
26. Motoo K, Toda N, Arai F, Fukuda T, Sekiyama K, and Nakajima M, *Generation of concentration gradient from a wave-like pattern by high frequency vibration of liquid-liquid interface.* Biomed Microdevices, 2008. **10**(3): p. 329-35.
27. Xia N, Hunt TP, Mayers BT, Alsberg E, Whitesides GM, Westervelt RM, and Ingber DE, *Combined microfluidic-micromagnetic separation of living cells in continuous flow.* biomed Microdevices, 2006. **8**(4): p. 299-308.
28. Oberti S, Neild A, Möller D, and Dual J, *Towards the automation of micron-sized particle handling by use of acoustic manipulation assisted by microfluidics.* Ultrasonics, 2008. **48**(6-7): p. 529-36.
29. Mosadegh B, Huang C, Park JW, Shin HS, Chung BG, Hwang SK, Lee KH, Kim HJ, Brody J, and Jeon NL, *Generation of stable complex gradients across two-dimensional surfaces and three-dimensional gels.* Langmuir, 2007. **23**(22): p. 10910-2.
30. Lin, F., C.M. Nguyen, S.J. Wang, W. Saadi, S.P. Gross, and N.L. Jeon, *Effective neutrophil chemotaxis is strongly influenced by mean IL-8 concentration.* Biochem Biophys Res Commun, 2004. **319**(2): p. 576-81.
31. Yang J, Yang J, Yin ZQ, Svir I, Xu J, Luo HY, Wang M, Cao Y, Hu N, Liao YJ, and Zheng XL, *Microfluidic pool structure for cell docking and rapid mixing.* Anal Chim Acta., 2009. **634**(1): p. 61-7.
32. Li, N., C.H. Hsu, and A. Folch, *Parallel mixing of photolithographically defined nanoliter volumes using elastomeric microvalve arrays.* Electrophoresis, 2005. **26**(19): p. 3758-64.
33. Tanaka Y, Morishima K, Shimizu T, Kikuchi A, Yamato M, Okano T, and Kitamori T, *Demonstration of a PDMS-based bio-microactuator using cultured cardiomyocytes to drive polymer micropillars.* Lab Chip, 2006. **6**(2): p. 230-5.

34. Balagaddé FK, You L, Hansen CL, Arnold FH, and Q. SR, *Long-term monitoring of bacteria undergoing programmed population control in a microchemostat.* Science, 2005. **309**(5731): p. 137-40.
35. Friedl P and Wolf K, *Tumour-Cell Invasion and Migration: Diversity and Escape Mechanisms.* Nature, 2003. **3**: p. 362-74.
36. Hung CT, Allen FD, Pollack SR, Attia ET, Hannafin JA, and Torzilli PA, *Intracellular calcium response of ACL and MCL ligament fibroblasts to fluid-induced shear stress.* Cell Signal, 1997. **9**(8): p. 587-94.
37. Iwabu A, Smith K, Allen FD, Lauffenburger DA, and Wells A, *Epidermal Growth Factor Induces Fibroblast Contractility and Motility via a Protein Kinase C Delta-Dependent Pathway.* J. Biological Chemistry, 2004. **279**(14551-60).
38. Wang SJ, Saadi W, Lin F, Nguyen CM, and Jeon NL, *Differential Effects of EGF Gradient Profiles on MDA-MB-231 Breast Cancer Cell Chemotaxis.* Experimental Cell Research, 2004. **300**: p. 180-9.
39. Arai H, Tsou CL, and Charo IF, *Chemotaxis in a lymphocyte cell line transfected with C-C chemokine receptor 2B: evidence that directed migration is mediated by betagamma dimers released by activation of Galphai-coupled receptors.* Proc. Natl. Acad. Sci., 1997. **94**(26): p. 14495-9.
40. Imshik Lee, Kwong-Yu Chan, and David Lee Phillips, *Growth of electrodeposited platinum nanocrystals studied by atomic force microscopy* Applied Surface Science, 1998. **136**(4): p. 321-30.
41. Timothy E. McKnight, A.V.M., Derek W. Austin, Tyler Sims, Michael A. Guillorn, and Michael L. Simpson, *Microarrays of Vertically-Aligned Carbon Nanofiber Electrodes in an Open Fluidic Channel.* J. Phys. Chem. B, 2004. **108**(22): p. 7115–7125.
42. Vazquez, M., Schmalzing D., D. Ehrlich, P. Matsudaira, and G. McKinley, *Shear Induced Degradation of Linear Polyacrylamide Solutions during Pre-electrophoretic Loading.* Anal Chem, 2001. **73**: p. 3035-44.
43. Vazquez, M., G. McKinley, L. Mitnik, S. Desmarais, P. Matsudaira, and Ehrlich D., *Electrophoretic Injection within Microdevices.* Anal Chem, 2002. **93**: p. 3088-98.
44. Crowe CT, Elger DF, and Roberson JA, *Engineering Fluid Mechanics*. 7th ed: John Wiley & Sons, Inc.
45. Holden MA, Kumar S, Beskok A, and Cremer PS, *Microfluidic diffusion diluter: bulging of PDMS microchannels under pressure-driven flow.* J. Micromech. Microeng., 2003. **13** p. 412-8.
46. Kong Q and Vazquez M, *Flow-induced shear stresses increase the number of cell-cell contacts within extracellular matrix.* Journal of Biomedical Materials Research Part A, 2008. **[In production, Epub ahead of print]**.
47. Bird RB, Stewart WE, and Lightfoot EN, *Transport Phenomena*. 2nd ed. 2002, New York: John Wiley & Sons, Inc.
48. Gennerich A and Schild D, *Anisotropic Diffusion in Mitral Cell Dendrites Revealed by Fluorescence Correction Spectroscopy.* Biophysical J., 2002. **83**: p. 510-22.

49. Das, M., T. Miyakawa, C.F. Fox, R.M. Pruss, A. Aharonov, and H.R. Herschman, *Specific radiolabeling of a cell surface receptor for epidermal growth factor.* Proc Natl Acad Sci U S A, 1977. **74**(7): p. 2790-4.
50. Haller MF and Saltzman WM, *Localized Delivery of Proteins in the Brain: Can Transport Be Customized? .* Pharmaceutical Research, 1998. **15**(3): p. 377-85.
51. Hiemenz PC and Rajagopalan R, *Principles of Colloid and Surface Chemistry* 3rd ed. 1997, New York: Marcel Dekker. 650.
52. Saltzman WM, Radomsky ML, Whaley KJ, and Cone RA, *Antibody Diffusion in Human Cervical Mucus.* Biophys J, 1994. **66**: p. 508-15.
53. Chen, H., J. Kovar, S. Sissons, K. Cox, B. Matter, F. Chadwell, P. Luan, C.J. Vlahos, A. Schutz-Geschwender, and D.M. Olive, *A Cell Based Immunocytochemical Assay for Monitoring Kinase Signaling Pathways and Drug Efficacy.* Anal. Biochem., 2005. **338**: p. 136-42.
54. Loan CE, Aberle T, and Burchard W, *Structure Properties of Dextran. 2. Dilute Solution.* Macromolecules, 2000. **33**(15): p. 5730 -5739.
55. Carpenter G and Cohen S, *Epidermal Growth Factor.* J. BIOLOGICAL CHEMISTRY, 1990. **265**(14): p. 7709-7712.
56. Haugh, J.M., *Deterministic model of dermal wound invasion incorporating receptor-mediated signal transduction and spatial gradient sensing.* Biophys J, 2006. **90**(7): p. 2297-308.
57. Sanabria, H., Y. Kubota, and M.N. Waxham, *Multiple diffusion mechanisms due to nanostructuring in crowded environments.* Biophys J, 2007. **92**(1): p. 313-22.
58. Abhyankar, V.V., M.A. Lokuta, A. Huttenlocher, and D.J. Beebe, *Characterization of a membrane-based gradient generator for use in cell-signaling studies.* Lab Chip, 2006. **6**(3): p. 389-93.
59. Kong Q and Vazquez M, *Flow-induced shear stresses increase the number of cell-cell contacts within extracellular matrix.* Journal of Biomedical Materials Research Part A, 2009. **89**(4): p. 968-79.
60. Kong, Q. and M. Vazquez, *Internal fluid flow increases cellular interconnects between Medial Collateral Ligament fibroblasts and cellular extensions within three-dimensional collagen matrixes.* Cell Commun Adhes, 2006. **13**(3): p. 139-49.
61. Abhyankar V. V., Toepke M. W., Cortesio C. L., Lokuta M. A., Huttenlocher A., and Beebe D. J., *A platform for assessing chemotactic migration within a spatiotemporally defined 3D microenvironment.* Lab Chip, 2008. **8**(9): p. 1507-15.
62. Naoki H, Sakumura Y, and Ishii S, *Stochastic control of spontaneous signal generation for gradient sensing in chemotaxis.* J Theor Biol., 2008. **255**(2): p. 259-66.
63. Wang, S.J., W. Saadi, F. Lin, C. Minh-Canh Nguyen, and N. Li Jeon, *Differential effects of EGF gradient profiles on MDA-MB-231 breast cancer cell chemotaxis.* Exp Cell Res, 2004. **300**(1): p. 180-9.
64. Vicente-Manzanares M, W.D., Horwitz AR, *Cell Migration at A Glance.* J. Cell Science, 2005. **118**: p. 4917-9.
65. Parent CA and Devreotes P, *A Cell's Sense of Direction.* Science, 1999. **284**: p. 765-70.

66. Saadi W, W.S., Lin F, Jeon NL, *A Parallel-Gradient Microfluidic Chamber for Quantitative Analysis of Breast Cancer Cell Chemotaxis.* Biomed. Microdevices, 2006. **8**: p. 109-18.
67. Rees AR, Gregoriou M, Johnson P, and Garland PB, *High Affinity Epidermal Growth Factor Receptors on the Surface of A431 Cells Have Restricted Lateral Diffusion.* EMBO Journal, 1984. **3**(8): p. 1843-7.
68. Bellot F, M.W., Kris R, Mirakhur B, Verlaan I, Ullrich A, Schlessinger J, Felder S,, *High-Affinity Epidermal Growth Factor Binding Is Specifically Reduced by a Monoclonal Antibody, and Appears Necessary for Early Responses.* J, Cell Biology, 1990. **110**: p. 491-502.
69. Woo SL, Debski RE, Zeminski J, Abramowitch SD, Saw SS, and Fenwick JA, *Injury and repair of ligaments and tendons.* Annu. Rev. Biomed. Eng., 2000. **02**(83-118).
70. Lauffenburger DA, H.A., *Cell Migration: A Physically Integrated Molecular Process.* Cell, 1996. **84**: p. 359-69.
71. Sogabe Y, Abe M, Yokoyama Y, and Ishikawa O, *Basic fibroblast growth factor stimulates human keratinocyte motility by Rac activation.* Wound Repair Regen, 2006. **14**(4): p. 457-62.
72. Kurten, R.C., P. Chowdhury, R.C. Sanders, Jr., L.M. Pittman, L.W. Sessions, T.C. Chambers, C.S. Lyle, B.J. Schnackenberg, and S.M. Jones, *Coordinating epidermal growth factor-induced motility promotes efficient wound closure.* Am J Physiol Cell Physiol, 2005. **288**(1): p. C109-21.
73. Pedowitz RA, O'connor JJ, and Akeson WH, *Daniel's Knee Injuries: Ligament and Cartilage Structure, Function, Injury, and Repair*. 2nd ed. 2003, Philadelphia: Lippincott Williams & Wilkins.
74. Boehm, M. and E.G. Nabel, *Cell cycle and cell migration: new pieces to the puzzle.* Circulation, 2001. **103**(24): p. 2879-81.
75. Corcoran, A. and R.F. Del Maestro, *Testing the "Go or Grow" hypothesis in human medulloblastoma cell lines in two and three dimensions.* Neurosurgery, 2003. **53**(1): p. 174-84; discussion 184-5.
76. Maheshwari G, Wiley HS, and Lauffenburger DA, *Autocrine epidermal growth factor signaling stimulates directionally persistent mammary epithelial cell migration.* J. Cell Biology, 2001. **155**(7): p. 1123-8.
77. Liu, Y., R. Sun, W. Wan, J. Wang, J.J. Oppenheim, L. Chen, and N. Zhang, *The involvement of lipid rafts in epidermal growth factor-induced chemotaxis of breast cancer cells.* Mol Membr Biol, 2007. **24**(2): p. 91-101.

CHAPTER 6

Cell Behavior in Response to Transient EGF Concentration Gradients

Qingjun Kong

Department of Mechanical Engineering

The City College of The City University of New York (CCNY)

140th Street and Convent Ave., T-402

New York, NY 10031

Qkong@gc.cuny.edu

Phone: 212.650.6766 Fax: 212.650.6727

and

*Maribel Vazquez, Sc.D.**

New York Center for Biomedical Engineering

Department of Biomedical Engineering

The City College of The City University of New York (CCNY)

140th Street and Convent Ave., T-403D

New York, NY 10031

Vazquez@ccny.cuny.edu

Phone: 212.650.5209 Fax: 212.650.6727

**Corresponding Author*

Keywords: microfluidic device, microfabrication, concentration gradient, fibroblast, EGF

Abstract: Cell response to ligand stimulation is well-known to regulate multiple biological functions, such as homeostasis and wound repair. However, precise in vitro establishment of biological gradients across individual cells, and observation of cell response to such molecular stimulation remain under development and investigation. We have utilized a microfluidic device, the so-called bridged μLane system, to generate non-linear concentration gradients of the studied ligand, Epidermal Growth Factor (EGF), and expose cells over time to image cell responses. Cells were cultured within the system and observed to migrate, change morphology, and proliferate in response to distinct EGF gradients and EGF concentrations. In addition to real-time experiments, finite element methods were utilized to predict time-dependent EGF distribution at any position within the bridged μLane system.

6.1 Introduction

Cell migration along a ligand concentration gradient, known as chemotaxis [1-3], has been found to play an essential role in a variety of biological processes, such as tissue healing, cancer metastasis, immune response and angiogenesis [3-8]. When ligands, such as growth factors and cytokines, bind to the extracellular portion of transmembrane receptors, they trigger intracellular signal transduction pathways that lead to numerous cell functions including proliferation, change in morphology and cell migration [3, 4, 9, 10].

Research has demonstrated that epidermal growth factor (EGF) can stimulate cell proliferation and morphology change [11-13]. EGF concentration can increase cell motility [14-16], while EGF gradient can direct cell migration via the front-to-rear asymmetry of ligand concentration [2, 17, 18]. However, little is known about how ligand concentration gradient quantitatively affects cell migration, morphology change and proliferation. Moreover, such study is often limited by the assays used. For example, the most commonly-used transwell assay, the Boyden chamber, measures cell motility by counting the number of cells that migrate through a membrane filter under the stimulation of ligands at given concentrations [19]. However, this endpoint measurement does not provide detailed information about the ligand concentrations and gradients located around individual cells. How cells migrate through the membranes is also unobservable using traditional assays, leaving many unresolved questions.

As microfabricated devices have been widely applied in biology, real-time observation of cell behavior at different ligand gradients has been documented during cell proliferation [20, 21], apoptosis [20, 22] and migration [16, 23]. Microfluidic devices can

also be designed to generate ligand gradients across the microchannel and precisely deliver ligands to cells at desired concentration, as well as enable visualization of cell function in response to different microenvironments in real time [24-26]. Recently, using the microfabricated devices, non-linear ligand gradients were generated and found to be more chemoattractive to cells than linear ligand gradients [16]. Using such microfabricated devices, researchers have examined cell response to steady-state ligand gradients [27] and found that cell motility was ligand gradient-dependent [28]. However, many of these groups have not investigated how cell function is affected by transient ligand gradients known to be physiologically meaningful in a variety of biomedical research areas such as tissue engineering and cancer metastasis [29-31].

In this work, we microfabricated a two-layer PDMS microsystem, named the bridged μlane system, to deliver EGF ligand to cells [32], and analyze how cells react in response to different EGF concentrations and gradients during migration. The ligand gradients were formed in a non-linear profile along the microchannel. We used the microsystem to generate time-evolving EGF gradients around individual cells for observation of cell migration and morphology change. We observed that both transient EGF gradients and steady-state gradients stimulated cell function, while transient EGF gradient exhibited fewer effects on cell migration and morphology change than the steady-state gradients.

6.2 Materials and Methods

Microfabrication of the bridged μLane system: The fabrication of the bridged μLane system has been previously described [32]. Briefly, after contact photolithography and elastomeric stamping, a piece of poly-dimethylsiloxane (PDMS) with a single μlane-pattern was bonded onto a glass to form a closed microchannel of 13.0±0.1-mm-length (mean ± SD), 100±1-μm-width, 90±1-μm-depth, and two 2-mm-diameter reservoirs in both ends. Then, another layer of PDMS was cast onto the previous layer to form a double-layered bridged μLane system, composed of two cylindrical chambers, 6-mm in diameter and 6-mm in height, and a bridge channel, 9-mm in length and 2-mm in depth (**Figure 6.1A**). The two reservoirs in the bottom layer were vertically, and fluidically, connected with the two chambers in the top layer (**Figure 6.1B**). One of the chambers that growth factor solution was applied was denoted as source chamber (SRC), while the other chamber was denoted as sink chamber (SKC). The reservoirs that fluidically connected with the source chamber and the sink chamber were then denoted as source reservoir (SRR) and sink reservoir (SKR), respectively.

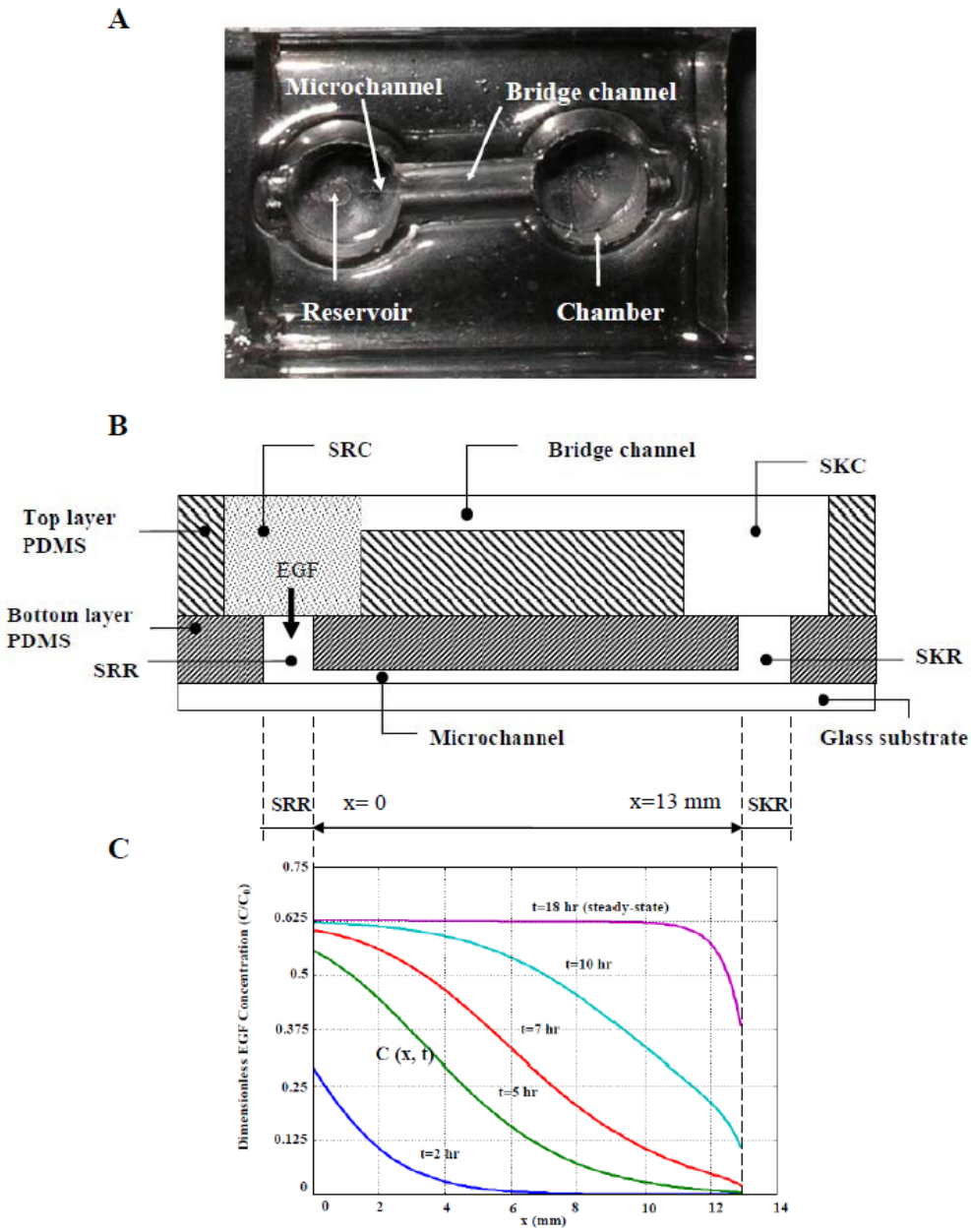

Figure 6.1: Image of the bridged μLane system (A), schematic of the bridged μLane system (not to scale), and the numerical profile of EGF concentration as a function of time and axial position within the microchannel. The two-layer PDMS system consists of a microchannel, two reservoirs, two vertically-fluidic chambers, and a larger so-called bridge channel, as shown (B). EGF solutions at concentration of C_0 are manually inserted into the source chamber (SRC) and allowed to transport toward the sink reservoir (SKR) through the 13-mm-long microchannel. EGF transport within the microchannel was modeled using mathematical equations of convective diffusion. The axial change in dimensionless EGF concentration, defined as $C(x,t)/C_0$, is graphically illustrated at 2, 5, 7, 10 and 18 hours (C).

Cell culture: Primary fibroblast cells were harvested from bovine Medial Collateral Ligament (MCL) explants received from the Soft Tissue laboratory of Dr. Peter Torzilli at the Hospital for Special Surgery (New York, NY) [33]. Primary cells were washed and cultured onto sterile polystyrene tissue culture flasks (Becton Dickinson Labware, Franklin Lakes, NJ) with sterile complete Essential Modified Eagle's Medium (EMEM) of pH 7.1-7.4, contained 10% fetal bovine serum (FBS) and 2% L-Glutamine (Mediatech Inc., Manassas, VA). Cells were then maintained at 37^{o}C in a 5% CO_2 humidified incubator. Serial passages were performed when cultures became ~ 90% confluent by detaching cells from flasks via a five-minute treatment with 0.05% trypsin-0.53mM EDTA (Mediatech Inc., Manassas, VA) at 37^{o}C. The cells were collected via centrifuge, suspended in growth medium, and subcultured for less than 5 passages prior to experimental use.

Transwell assays: A 24-well transwell assay (Becton Dickinson and Company, Franklin Lakes, NJ) was used to analyze cell migration. A 50 µl of 1-mg/ml collagen (BD Biosciences, Bedford, MA) that was diluted using 70% ethanol (EMD Chemicals Inc., Gibbstown, NJ) was pipetted into each insert and allowed to dry overnight at room temperature (25^{o}C). A 350 µl volume of fibroblast solution with a cell density of $5x10^4$ cells/ml was pipetted in each of the collagen-coated inserts, which were then placed in the 24-well transwell assays. In control experiments, 700 µl of EMEM complete media (10% FBS + 2% L-Glutamine) was added into each well of 4 wells while, in the experiments of EGF stimulation, 700 µl of EMEM complete media mixed with EGF (MW: 6 kDa, Molecular Probes, Eugene, OR) of concentrations between 0.1 ng/ml and 100 ng/ml was pipetted into wells in quadruplicates. After incubating the transwell assays

at 37^{o}C for 20 hours, inserts were removed from the plate and subsequently immersed in solutions of Triarylmethane dye (Fixative, Dade Behring Inc., Newark, DE), Xanthene dye (Solution I, Dade Behring Inc., Newark, DE) and Thiazine dye (Solution II, Dade Behring Inc., Newark, DE) to stain fibroblasts that migrated and adhered at the bottom of each insert. These migratory cells were then counted using a Nikon microscope. Relative Chemotaxis Factor (RCF), defined as the ratio between the number of cells that migrated at a given EGF concentration to the number of cells that migrated in the control experiments, (i.e. EMEM complete media), was used to analyze fibroblast migration in response to different EGF concentration. This transwell assay experiment was repeated 4 times, and 16 total samples for each EGF concentration used in this experiment were measured and analyzed.

Cell proliferation assays: To monitor cell proliferation stimulated by EGF within 96 hours, four 96-well culture plates (Corning Inc., Corning, NY) were used. In the control experiments, a 100 µl of fibroblast solution at a density of 5x10^{4} cells/ml in EMEM complete media was added into 8 wells of the culture plates. Fibroblast solutions mixed with EGF of 20 ng/ml concentration and 40 ng/ml concentration, respectively, were added into 8 additional wells for each concentration. Note that each well contained minimum of 5000 cells, as required by the manufacture of proliferation assays. The plates were then incubated at 37^{o}C. To measure cell proliferation, each well was then treated 15 µl of cell proliferation Dye Solution (Part # G4002, Promega Corp., Madison, WI), followed with a 2-hour incubation. Subsequently, 100 µl of cell proliferation Stop Solution (Part # G4001, Promega Corp., Madison, WI) was pipetted into each well and the plate was incubated for another 1 hour. To measure cell proliferation, a 96-well plate

reader (Synergy HT, BioTek Instruments Inc., Winooski, VT) was used to record the absorbance of the plate at a wavelength of 570 nm. The proliferation rates in cells were calculated based on the initial number of cells that were placed into plates on the first day. The cell proliferation experiments were repeated 4 times to ensure data reliability.

Cell loading and EGF application in the bridged μLane system: Three different procedures were applied when experimental conditions were changed. (1) In the control experiments where no EGF was applied, solutions of fibroblasts at a cell density of 5 x 10^4/ml in EMEM complete media were injected into the microchannel of the μlane system via the SKR reservoir using a 1-ml syringe. The SRC chamber, SKC chamber, and the bridged channel were subsequently filled with solutions of EMEM complete. Note that 4 to 6 cells were initially seeded within each microchannel. (2) In the experiments that used uniform EGF concentrations (no EGF gradient), fibroblasts at the density of 5 x 10^4/ml in EMEM complete were mixed with EGF to reach final EGF concentrations of 20 ng/ml and 40 ng/ml, respectively, which were then injected into the μlane systems to initially seed 6 to 8 cells within each microchannel. The SRC chamber, SKC chamber, and the bridged channel were subsequently filled with the EMEM complete solutions with the corresponding EGF concentration. The μlane systems were incubated at 37^{o}C. (3) In the experiments where different EGF gradients were formed, cell solutions, EGF solutions and media were loaded in different steps. After cells of 5 x 10^4/ml in EMEM complete were injected into the microchannel to seed 8 to 15 cells within each microchannel and incubated overnight, the SKC chamber and the bridged channel were replaced with fresh EMEM complete media, and EGF was only added into the SRC chamber and made contact with the complete media in the bridged channel. The

μlane systems were then placed in a micro-incubator (Warner Instruments LLC, Hamden, CT) mounted on a motorized stage of a microscope for real-time observation. The micro-incubator was maintained 37ºC. Note that all experiments of different experimental conditions were repeated 6 times to have enough cell samples for statistical analysis.

Cell morphology analysis: Fibroblast morphology was analyzed using a dimensionless Cell Shape Index (CSI) [34, 35], which was defined as $4\pi A/P^2$, where A is cell area on a substrate and P is cell perimeter on a substrate. Only fibroblasts adhered onto the substrate bottom of 96-well plates and μlane systems were imaged. The area and perimeter of cells were measured using a microscope and accompanying software. CSI has a value of 1 when cells display a completely round morphology, and equal to 0 when, in the limiting case, cells are infinitely elongated. A sample size between 16 and 25 cells was used for all experiments, as shown in accompanying data.

Microscopy and cell images: An inverted epi-microscope (Nikon TE2000) with a 20X microscope objective (Nikon Plant 20X, Morrell Instrument Company Inc., Melville, NY) was used to image cells that adhered in the culture plates and the μlane systems via a cooled CCD camera (CoolSNAP EZ, Photometrics, Tucson, AZ) with Nikon software (Nikon Instrument Element 2.30 with 6D module, Morrell Instrument Company Inc., Melville, NY). All images were in dimensions of 0.38-mm-length by 0.46-mm-width, and displayed the specific cell positions within the culture plates and the microchannels. A shutter (HF204, Prior Scientific Inc., Rockland, MA) mounted in the Nikon TE2000 was used to control the exposure time.

Simulation of ligand transport in the μlane system: The transport of EGF solution within the μlane system was simulated using a finite element molding software Comsol Multiphysics (Comsol Inc., Burlington, MA), as described previously [32]. A one-dimensional convective-diffusion equation was used to model the convective diffusion in the bridged μLane system [36, 37] due to the large volume ratio between the chambers and the microchannel:

$$\frac{\partial C}{\partial t} + V\frac{\partial C}{\partial x} = D\frac{\partial^2 C}{\partial x^2} \qquad (6.1)$$

where C (mg/ml) is ligand concentration, V (m/s) is the mean bulk velocity in the microchannel, and D (m^2/s) is the diffusion coefficient of ligand. The mean bulk velocity, V, measured in our experiments, and the EGF diffusivity, D, averaged from the published values were input into the model to generate EGF concentration profiles as a function of time and position, as reported before [32]. The simulated EGF concentration was illustrated in **Figure 6.1C**, when EGF of 40 ng/ml was used. The nodes of the mesh selected in the simulation were large enough to accurately predict EGF concentration and concentration gradient across cells.

6.3 Results

Effects of uniform EGF concentrations on fibroblast migration, proliferation and morphology

EGF solutions of different concentration between 0.1 ng/ml and 100 ng/ml were observed to stimulate fibroblast migration. As seen in **Figure 6.2**, EGF solutions of 0.1-100 ng/ml caused a greater number of fibroblasts to migrate within the transwell assays than in the control experiments (no EGF). However, EGF of 80 ng/ml caused the number of cells to decrease. As shown, EGF of 40 ng/ml stimulated the largest number of fibroblasts to migrate (3.6 times more than the control) among all the EGF concentrations tested in our study.

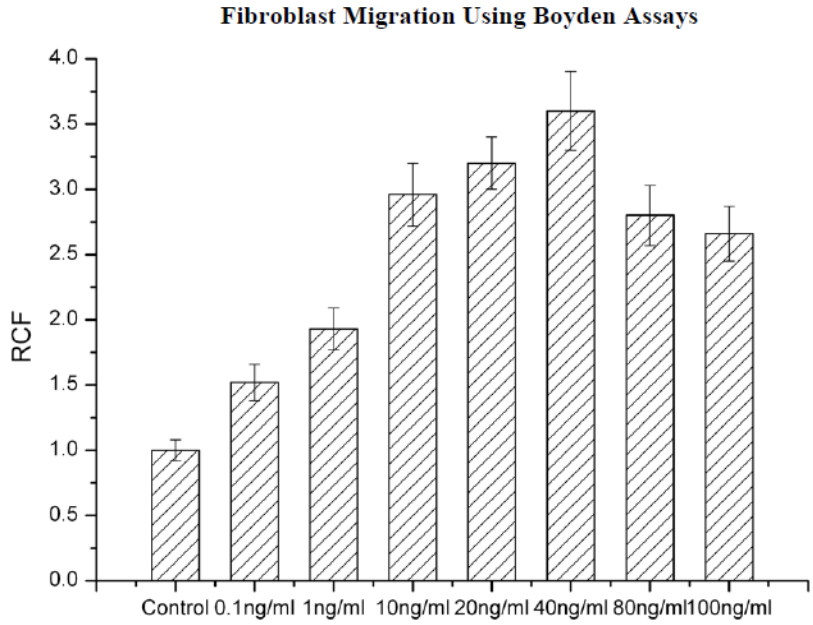

Figure 6.2: Effects of EGF on fibroblast migration. Boyden transwell assays were used to analyze cell migration in the absence of EGF, i.e. control, and the presence of EGF at concentrations between 0.1 ng/ml and 100 ng/ml. Relative Chemotaxis Factor (RCF) was defined as the ratio of motile cells in the presence of EGF at a given concentration to the number of migratory cells in control experiments. Note that the RCF of control experiments were normalized to a value of 1. Experiments have been repeated so that 16 total samples for each EGF concentration (n=16) used in this experiment were measured and analyzed.

Studies of fibroblast proliferation were performed in proliferation assays and μlane systems in order to investigate how fibroblasts proliferated in two different micro-environments. **Figure 6.3A** shows that fibroblasts of the control, and fibroblasts that were treated with EGF concentrations of 20 ng/ml and 40 ng/ml proliferated over time and reached their highest number in 72 hours. In 96 hours, cells of the control proliferated 3.7 fold, while fibroblasts treated with 20-ng/ml EGF and 40-ng/ml EGF proliferated 4.8 fold and 4.9 fold, respectively. Fibroblasts that were examined in μlane systems were also seen to proliferate in the 96-hour period, as displayed in **Figure 6.3B**. The number of cells in the control experiments increased by 4.4 times in 96 hours, while the cells treated with 20-ng/ml EGF and 40-ng/ml EGF proliferated by 6.4 times and 8.0 times in 96 hours, respectively.

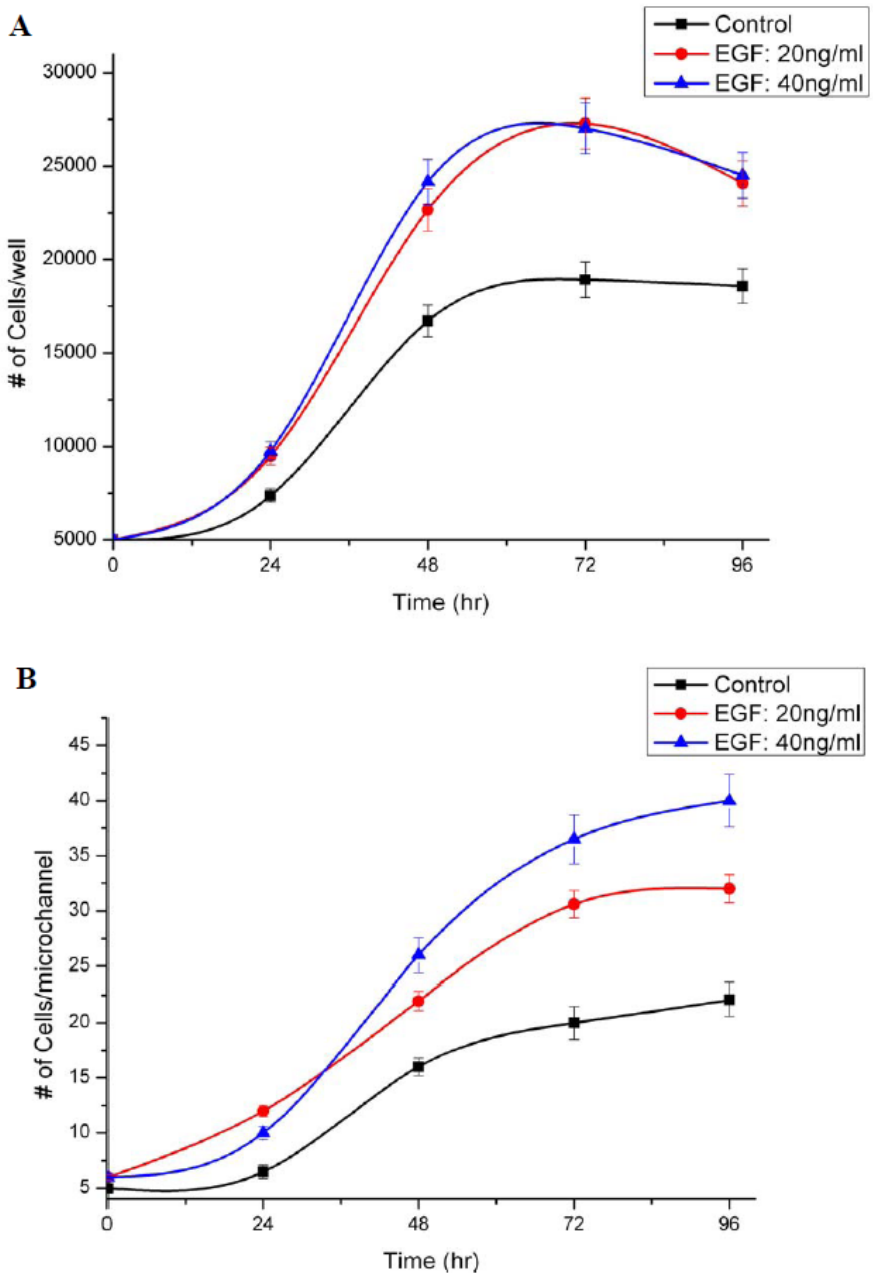

Figure 6.3: Fibroblast proliferation within 96-well proliferation assay and µlane system. Cells proliferated in 96-well proliferation assay for 96 hours (A). In the control experiments, no EGF was applied. EGF at the concentration of 20 ng/ml and 40 ng/ml was used to stimulate cell proliferation. Fibroblasts also proliferated in µlane systems without EGF application, i.e. control (B). When EGF at concentrations of 20 ng/ml and 40 ng/ml was applied, cells within the µlane system were observed to proliferate. In the proliferation experiments using 96-well proliferation assays, experiments were repeated 4 times with cell seeding in 8 wells per each EGF concentration used (n=32). When µlane systems were used, experiments with each EGF concentration were repeated 6 times.

Effects of EGF on fibroblast morphology within the 96-well plates and the µlane system were also analyzed after cells were incubated for 20 hours. As illustrated in **Table 6.1**, cells in the control experiments displayed a CSI of 0.36±0.11. The cells that were treated with EGF at the concentrations of 20 ng/ml and 40 ng/ml illustrated CSI of 0.26±0.05 and CSI of 0.27±0.05, respectively. Fibroblasts cultured in the µlane system displayed similar changes in morphology when EGF was applied. The cells of the control illustrated a morphology with CSI of 0.42±0.01, while cells in the presence of 20-ng/ml EGF and 40-ng/ml EGF exhibited CSI of 0.21±0.05 and CSI of 0.21±0.04, respectively.

Experimental conditions	96-well plate	µlane system
Control (no EGF)	0.41±0.02 (n=15)	0.42±0.01 (n=18)
EGF: 20ng/ml	0.26±0.05 (n=14)	0.21±0.05 (n=16)
EGF: 40ng/ml	0.27±0.05 (n=16)	0.21±0.04 (n=18)

Table 6.1: Cell Shape Index (CSI) of fibroblasts in 96-well plate and µlane system. After cell culture in 96-well plates and the µlane system for 20 hours, cell morphology was analyzed using CSI. The CSI was calculated for the experiments in the absence of EGF, i.e. controls, and in the presence of EGF at concentrations of 20 ng/ml and 40 ng/ml.

Generation of EGF gradients within the µlane system

The bridged µlane system was microfabricated to facilitate the formation of concentration gradients and observation of real-time chemotaxis. As seen in **Figure 6.1A** and **6.1B**, the system is composed of two poly-dimethylsiloxane (PDMS) layers that are fluidically connected via source (SRC) and sink (SKC) chambers in the top layer, and source (SRR) and sink (SRR) reservoirs in the bottom PDMS layer. As described previously [32], fluorescently-labeled Dextran was used to experimentally validate the

development of chemical concentration gradients within the microsystem. As a control, the diffusion coefficient of Dextran was measured in these experiments, as well as modeled using numerical simulations, to produce results that were within 5% of each other and in line with published values [32]. EGF was next applied into the system in order to generate EGF gradients within the microchannel. Numerical models were used to predict EGF transport within the microchannel as a function of position and time, as shown in **Figure 6.1C**. Here, the EGF concentration initially inserted into the source chamber (SRC) is denoted as C_0, while the EGF concentration within the microchannel is represented as C(x, t). The dimensionless concentration, $C(x, t)/C_0$, was then used to describe changes in local EGF concentration within the microchannel. As seen, the EGF gradient profile reached steady-state within the microchannel after 18 hours, generating a non-linear, time-invariant, axial distribution of EGF. Numerical data was then used to tabulate the local EGF concentration and gradient present surrounding each cell within the system.

The predicted spatial and temporal profiles of local EGF concentration and gradients within the μlane system were then used to analyze effects of different EGF gradients on cell morphology and cell motility in our experiments.

Cell responses to EGF concentration gradients in the bridged μLane system

After EGF gradients were generated, the cells that were exposed to transient EGF gradients, i.e. within 18 hours of EGF application, and steady-state EGF gradients, i.e. more than 18 hours of EGF application, exhibited changes in morphology and migrated toward EGF, as seen in **Figure 6.4**. The real-time local EGF concentrations and gradients

surrounding individual cells within the microchannel were numerically obtained from the transport simulation (**Figure 6.1C**), and used to analyze their effects on cell morphology change and motility. The EGF gradients were separated in 4 different ranges for this study: 0.2-2.0 ng/(ml.mm), 2.2-4.0 ng/(ml.mm), 4.1-6.0 ng/(ml.mm), and 6.1-8.0 ng/(ml.mm).

EGF gradients were seen to alter fibroblast morphology, as the measured Cell Shape Index (CSI) was dependent on EGF gradients, shown in **Figure 6.5**. The EGF gradients, including transient-state and steady-state gradients, all stimulated cells to exhibit a lower CSI than the control experiments (no EGF). Meanwhile, the CSI of cells stimulated by EGF gradients was less than that of those cells cultured in uniform EGF concentration (no EGF gradient). Additionally, cells of transient EGF gradients exhibited lower CSI than those of steady-state gradients at all the gradient ranges. CSI of cells subjected to transient gradients reached maximum, 0.41±0.04, at the EGF gradient range between 2.1 ng/(ml.mm) and 4.0 ng/(ml.mm). Furthermore, CSI of cells within steady-state EGF gradients decreased as gradient increased.

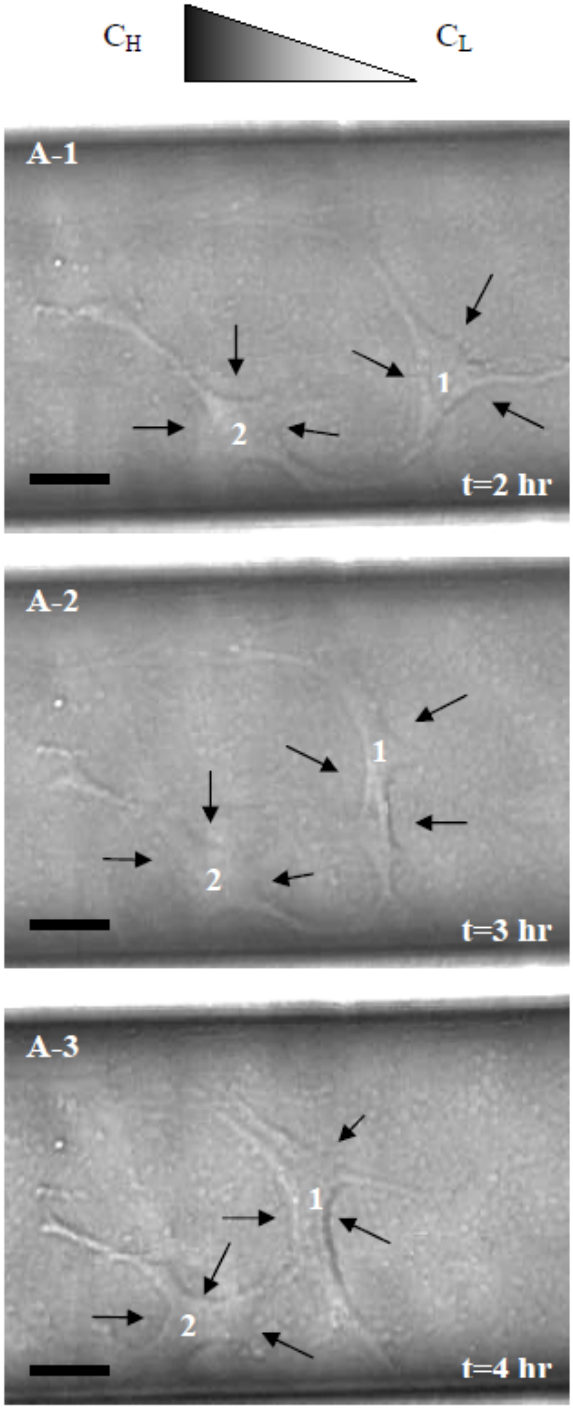

Figure 6.4: Images of cells treated with EGF within the microchannel. After 2 hours of EGF application, two representative cells at the position 8 mm away from the SRR reservoir migrated toward higher concentration of EGF (from right to left) with morphology change (A-1 to A-3). Arrows point to cell bodies. Scale bar: 20μm

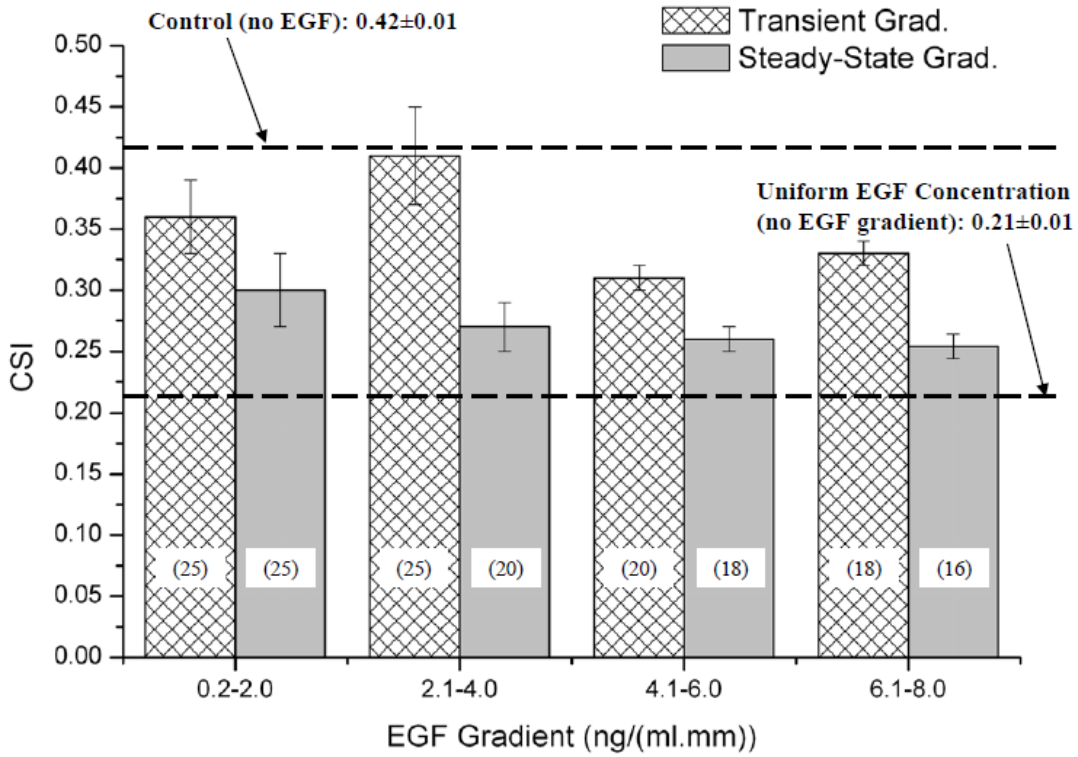

Figure 6.5: Effects of EGF gradients on fibroblast morphology. Cell Shape Index (CSI) was used to measure cell morphology. EGF gradients were separated into 4 different ranges: 0.2-2.0 ng/(ml.mm), 2.1-4.0 ng/(ml.mm), 4.1-6.0 ng/(ml.mm), and 6.1-8.0 ng/(ml.mm). CSI of cells in control experiments (no EGF applied) measured 0.42±0.01, while CSI of cells subjected to uniform EGF concentration (no EGF gradient) exhibited CSI values of 0.21±0.01. The CSI of cells that were stimulated with transient EGF gradients and steady-state EGF gradients at each EGF gradient range are shown. The number of cells examined is shown in parenthesis.

We then observed how cell motility was affected by different EGF gradients. As seen in **Figure 6.6**, both transient EGF gradients and steady-state EGF gradients were found to cause cells to migrate with higher motility than seen in control and experiments of uniform EGF concentration. As EGF gradient increased, cell motility stimulated by transient EGF gradients also increased from 10.0±1.0 μm/hr at gradients between 0.2-2.0 ng/(ml.mm) to 13.2±1.1 μm/hr at gradients between 6.1-8.0 ng/(ml.mm). Steady-state EGF gradients were also found to increase cell motility from a minimum of 16.0±1.8

μm/hr to 21.0±1.0 μm/hr as gradients increased. However, it was also observed that cell motility did not significantly increase after both the transient and steady-state EGF gradients reach the range of 4.1 ng/(ml.mm)and 6.0 ng/(ml.mm). Further more, steady-state EGF gradients was seen to cause cells to migrate with higher motility than when acted upon by transient EGF gradients for all values studied.

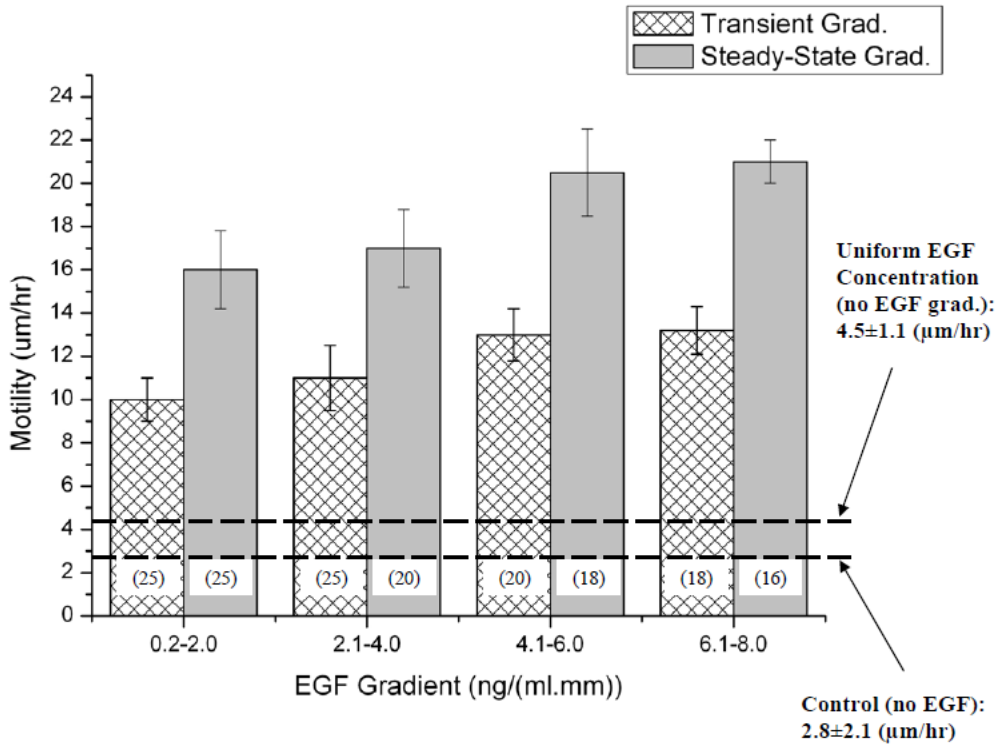

Figure 6.6: Effects of EGF gradients on fibroblast motility. Cell motility was measured at 4 different EGF gradient ranges: 0.2-2.0 ng/(ml.mm), 2.1-4.0 ng/(ml.mm), 4.1-6.0 ng/(ml.mm), and 6.1-8.0 ng/(ml.mm). Cell motility in control experiments (no EGF applied) and cell motility in the experiments where uniform EGF concentration (no EGF gradient) was applied exhibited motilities of 2.8±2.1 μm/hr and 4.5±1.1 μm/hr, respectively. Motility of cells that were stimulated via transient EGF gradients and steady-state EGF gradients at each gradient range are illustrated. The number of cells examined is shown in parenthesis.

6.4 Discussion

Transient ligand gradients generated in the bridged μlane system

As described previously [32], our microsystem was designed to deliver ligands to cells and quantitatively measure the ligand-induced cell migration in real time [7, 9, 38]. By using the convective diffusion models, spatiotemporal profiles of ligand concentration and gradients across individual cells were predicted. This was essential for the study of cell function in response to ligand stimulation. The bridged μLane system generated steady-state EGF concentration profiles within approximately 18 hours (**Figure 6.1**). The transient time (18 hours) provided us opportunities to observe cell responses to non-linear transient ligand gradients compared to the immediate steady-state ligand gradients [28, 39, 40], as effects of such transient gradient were little reported.

Effects of uniform EGF concentration on cell function

Numerous experiments using conventional assays have reported that EGF stimulates fibroblast migration in a dose-dependent manner [33], as increasing EGF concentration can trigger larger numbers of cells to migrate. Interestingly, this study illustrated that low to intermediate EGF concentration appeared to be most chemoattractant to the fibroblasts used, as high EGF concentrations did not stimulate larger numbers of cells to migrate (**Figure 6.2**). This finding may suggest that the EGF receptor most specifically related to chemotaxis was down-regulated at higher EGF concentrations for the fibroblast populations used [41, 42].

EGF is also well-known to stimulate fibroblast proliferation in a dose-dependent manner [33, 43]. In this work, EGF caused fibroblast proliferation at levels higher than

seen in the controls for both the conventional 96-well plate and the μLane system (**Figure 6.3**). We note that cells in our microdevice did not illustrate maximum proliferation during the time of experiments because cells were not confluent within the microchannel as a consequence of low cell seeding. However, low celll seeding was specifically selected to produce an initial number of 4-8 cells within the microchannnel in the proliferation experiments in order to investigate proliferation of individual cells without the effects of cell-cell interactions during testing. Hence, the averaged values measured for proliferation within multiple channels (n=6) appear meaningfully lower than in the assays because the desired cell seeding was achieved reliably using different microdevices. Additionally, we note that while different concentrations of EGF within the conventional assay increased fibroblast proliferation by 5 fold, EGF caused a larger increase of 6-8 fold within μLane systems when compared to the control (no EGF).

Cell Shape Index (CSI) was used to analyze changes in fibroblast morphology in response to EGF (**Table 6.1**). CSI was seen to decrease in the presence of EGF, indicating that cells become more elongated [15]. However, no significant difference in CSI was found in the experiments of EGF applied in the 96-well assay and those in the μLane system. This result importantly denotes that the microenvironment itself did not significantly affect fibroblast morphology and that EGF plays a significant role on fibroblast cell morphology.

Effects of EGF concentration gradients on cell morphology and motility

While the majority of studies have reported how EGF concentration can stimulate changes in cell behavior [11, 44, 45], data that examines how changes in cell behavior are

triggered in response to particular ligand concentration gradients is currently under investigation [46, 47]. Recently, it has been reported that non-linear concentration gradients could drive more cells to migrate than linear gradients [41], which might suggest that non-linear gradients are more chemoattractive. The current work developed the bridged μlane system to examine how fibroblasts responded to different non-linear EGF gradients in real-time. Meaningfully, our work also examined the effects of transient, non-linear EGF gradients versus steady-state, non-linear EGF gradients, as well as low EGF gradients versus high EGF gradients, as they may play important roles in regulating cell homeostasis and directing cell migration [29-31].

During both transient and steady-state EGF stimulation, cell morphology was observed to be more elongated than in the primary control (no EGF and no EGF gradient), as the CSI values decreased (**Figure 6.5**). It has been suggested that such EGF-stimulated changes in morphology are induced because of reorganization of the actin cytoskeleton and integrin-mediated cell/substratum adhesion sites [11]. Steady-state EGF gradients induced cells to migrate with more elongated morphology than seen during migration induced by transient EGF gradients. However, we also noticed that uniform EGF concentration (i.e. threshold EGF concentration but no EGF gradient) caused fibroblasts to be even more elongated than those subject to either transient or steady-state EGF gradients. These findings might suggest that the stability of EGF ligand distribution around the cell perimeter plays a role in cytoskeleton reorganization and integrin mediation. Moreover, we also found that the cell morphology was EGF gradient-dependent, as intermediate transient EGF gradients caused cells to be more round. However, cell morphology was consistently more elongated at increasing steady-state

EGF gradients. This may suggest that temporal gradient profiles affect ligand-receptor binding in ways that could weaken ligand stimulation [18, 42, 48]. However, further study is needed to properly investigate this finding.

Although uniform EGF concentrations are well-known to increase cell motility [15], our work illustrated that steady-state EGF gradients stimulated higher cell motility than uniform EGF concentrations (**Figure 6.6**). This result is in line with the biological literature, as ligand gradient was reported to alter cell sensitivity toward ligand concentration [17, 18], which may also work to increase cell motility. Our finding might then suggest that the intracellular polarization induced by EGF gradients may help cells become prone to migrate [8, 42, 49] and therefore increase cell motility.

Fibroblasts were also observed to have higher cell motility at increasing transient, non-linear EGF gradients. It has been reported that steady-state EGF gradients can trigger cell migration [33], but our experiments are among the first to illustrate that transient, non-linear EGF gradient can also induce cell migration: such transient microenvironment plays a meaningful role in various biological processes, such as wound healing, tissue repair and cancer studies [29, 40, 41]. Interestingly, we note that this effect appears to be gradient-dependent, as motility did not significantly change when both transient EGF gradients and steady-state gradients were increased to the intermediate to high range. Such a finding may be related to receptor saturation and requires further biological study [18, 42, 50, 51].

In summary, we have designed the bridged μLane system that allows investigation of cell function in response to transient ligand gradients, as they may be important to regulate homeostasis [52] and facilitate wound healing [53, 54]. Our results

show that both transient EGF gradients and steady-state gradients are important to stimulate cell function, and illustrate the differences in cell behavior when gradients are applied for different time periods. The bridged μLane system may provide a platform to examine the effects of both transient and steady-state ligand concentration gradients on cell populations to help gather different perspectives to the study of cell chemotaxis.

Acknowledgements:

This work was supported by the National Institutes of Health (GM071702-01), the National Science Foundation (CBET0428573) and PSC-CUNY.

Reference:

1. Vicente-Manzanares M, W.D., Horwitz AR, *Cell Migration at A Glance.* J. Cell Science, 2005. **118**: p. 4917-9.
2. Lauffenburger DA, H.A., *Cell Migration: A Physically Integrated Molecular Process.* Cell, 1996. **84**: p. 359-69.
3. Van Haastert PJ, D.P., *Chemotaxis: Signalling the Way Forward.* Nature, 2004. **5**: p. 626-34.
4. G Maheshwari, H.W., and DA Lauffenburger, *Autocrine epidermal growth factor signaling stimulates directionally persistent mammary epithelial cell migration.* J. Cell Biology, 2001. **155**(7): p. 1123-8.
5. RA Pedowitz, J.O.c., and WH Akeson, *Daniel's Knee Injuries: Ligament and Cartilage Structure, Function, Injury, and Repair*. 2nd ed. 2003, Philadelphia: Lippincott Williams & Wilkins.
6. McKean JM, Hsieh AH, and Sung KL, *Epidermal growth factor differentially affects integrin-mediated adhesion and proliferation of ACL and MCL.* Biorheology, 2004. **41**(2): p. 139-52.
7. Haugh, J.M., *Deterministic model of dermal wound invasion incorporating receptor-mediated signal transduction and spatial gradient sensing.* Biophys J, 2006. **90**(7): p. 2297-308.
8. Devreotes P and Janetopoulos C, *Eukaryotic Chemotaxis: Distinctions between Directional Sensing and Polarization.* J. Biological Chemistry, 2003. **278**(23): p. 20445-8.
9. Carpenter G and Cohen S, *Epidermal Growth Factor.* J. BIOLOGICAL CHEMISTRY, 1990. **265**(14): p. 7709-7712.
10. Keren K, P.Z., Allen GM, Barnhart EL, Marriott G, Mogilner A, Theriot JA, *Mechanism of Shape Determination in Motile Cells.* Nature, 2008. **453**: p. 475-81.
11. Wells A, Ware MF, Allen FD, and Lauffenburger DA, *Shaping Up for Shipping Out: PLCr Signaling of Morphology Changes in EGF-Stimulated Fibroblast Migration.* Cell Motility and the Cytoskeleton, 1999. **44**: p. 227-33.
12. Sahai E, *Mechanisms of Cancer Cell Invasion.* Current Opinion in Genetics and Development, 2005. **15**: p. 87-96.
13. Becker WM, K.L., Hardin J,, *The World of The Cell*. Sixth ed. 2005, San Francisco: Pearson Education, Inc.
14. Ware MF, Wells A, and Lauffenburger DA, *Epidermal Growth Factor Alters Fibroblast Migration Speed and Directional Persistence Reciprocally and in a Matrix-Dependent Manner.* J. Cell Science, 1998. **111**: p. 2423-32.
15. Iwabu A, Smith K, Allen FD, Lauffenburger DA, and Wells A, *Epidermal Growth Factor Induces Fibroblast Contractility and Motility via a Protein Kinase C Delta-Dependent Pathway.* J. Biological Chemistry, 2004. **279**(14551-60).
16. Wang SJ, Saadi W, Lin F, Nguyen CM, and J. NL, *Differential Effects of EGF Gradient Profiles on MDA-MB-231 Breast Cancer Cell Chemotaxis.* Experimental Cell Research, 2004. **300**: p. 180-9.
17. Ridley AJ, Schwartz MA, Burridge K, Firtel RA, Ginsberg MH, Borisy G, Parsons JT, and Horwitz AR, *Cell Migration: Integrating Signals from Front to Back.* Science, 2003. **302**: p. 1704-9.

18. Parent CA and Devreotes P, *A Cell's Sense of Direction.* Science, 1999. **284**: p. 765-70.
19. Saadi W, W.S., Lin F, Jeon NL, *A Parallel-Gradient Microfluidic Chamber for Quantitative Analysis of Breast Cancer Cell Chemotaxis.* Biomed. Microdevices, 2006. **8**: p. 109-18.
20. Ito Y, *Surface micropatterning to regulate cell functions.* Biomaterials, 1999. **20**(23-24): p. 2333-42.
21. Carlo DD, W.L., Lee LP, *Dynamic Single Cell Culture Arrary.* Lab on a Chip, 2006. **6**: p. 1445-9.
22. Chin VI, T.P., Sanga S, Scheel J, Gage FH, Bhatia SN,, *Microfabricated platform for studying stem cell fates.* Biotechnol. Bioeng., 2004. **88**(3): p. 399-415.
23. Nie FQ, Y.M., Kobayashi J, Yamato M, Kikuchi A, Okano T,, *On-Chip Cell Migration Assay Using Microfluidic Channels.* Biomaterials, 2007. **28**: p. 4017-22.
24. Irimia D, G.D., Toner M,, *Universal Microfluidic Gradient Generator.* Anal. Chem., 2006. **78**: p. 3472-7.
25. Sabounchi P, I.-Z.C., Chen R, Karandikar M, Seo J, Lee LP,, *Soft-State Biomicrofluidic Pulse Generator for Single Cell Analysis.* Applied Physics Letters, 2006. **88**: p. 183901(1)-(3).
26. Walker GM, S.J., Richmond A, Stremler M, Chung CY, Wikswo JP,, *Effects of Flow and Diffusion on Chemotaxis Studies in a Microfabricated Gradient Generator.* Lab on a Chip, 2005. **5**: p. 611-8.
27. Mosadegh B, Huang C, Park JW, Shin HS, Chung BG, Hwang SK, Lee KH, Kim HJ, Brody J, and Jeon NL, *Generation of stable complex gradients across two-dimensional surfaces and three-dimensional gels.* Langmuir, 2007. **23**(22): p. 10910-2.
28. Lin, F., C.M. Nguyen, S.J. Wang, W. Saadi, S.P. Gross, and N.L. Jeon, *Effective neutrophil chemotaxis is strongly influenced by mean IL-8 concentration.* Biochem Biophys Res Commun, 2004. **319**(2): p. 576-81.
29. Zigmond SH, *Polymorphonuclear leucocyte chemotaxis: detection of the gradient and development of cell polarity.* Ciba Found Symp., 1980. **71**: p. 299-311.
30. Abhyankar V. V., Toepke M. W., Cortesio C. L., Lokuta M. A., Huttenlocher A., and Beebe D. J., *A platform for assessing chemotactic migration within a spatiotemporally defined 3D microenvironment.* Lab Chip, 2008. **8**(9): p. 1507-15.
31. Naoki H, Sakumura Y, and Ishii S, *Stochastic control of spontaneous signal generation for gradient sensing in chemotaxis.* J Theor Biol., 2008. **255**(2): p. 259-66.
32. Kong Q, V.M., *A Bridged Microlane System for Diffusivity Measurement and Cell Response.* Biomed. Microdevices, 2008. **Submitted**.
33. Hung CT, Allen FD, Pollack SR, Attia ET, Hannafin JA, and Torzilli PA, *Intracellular calcium response of ACL and MCL ligament fibroblasts to fluid-induced shear stress.* Cell Signal, 1997. **9**(8): p. 587-94.
34. Malek AM and Izumo S, *Mechanism of endothelial cell shape change and cytoskeletal remodeling in response to fluid shear stress.* J. Cell Science, 1996. **109**: p. 713-26.

35. Thakara RG , Hoa F, Huanga NF, Liepmanna D, and Li S, *Regulation of vascular smooth muscle cells by micropatterning.* Biochemical and Biophysical Research Communications, 2003. **307**(4): p. 883-90.
36. CT Crowe, D.E., JA Roberson, *Engineering Fluid Mechanics*. 7th ed: John Wiley & Sons, Inc.
37. GA Truskey, F.Y., DF Katz, *Transport Phenomena in Biological Systems*. 2004, Upper Saddle River, New Jersey: Pearson Education, Inc.
38. Sanabria, H., Y. Kubota, and M.N. Waxham, *Multiple diffusion mechanisms due to nanostructuring in crowded environments.* Biophys J, 2007. **92**(1): p. 313-22.
39. Kanegasaki S, Nomura Y, Nitta N, Akiyama S, Tamatani T, Goshoh Y, Yoshida T, Sato T, and Kikuchi Y, *A novel optical assay system for the quantitative measurement of chemotaxis.* J Immunol Methods., 2003. **282**(1-2): p. 1-11.
40. Lin, F., W. Saadi, S.W. Rhee, S.J. Wang, S. Mittal, and N.L. Jeon, *Generation of dynamic temporal and spatial concentration gradients using microfluidic devices.* Lab Chip, 2004. **4**(3): p. 164-7.
41. Wang, S.J., W. Saadi, F. Lin, C. Minh-Canh Nguyen, and N. Li Jeon, *Differential effects of EGF gradient profiles on MDA-MB-231 breast cancer cell chemotaxis.* Exp Cell Res, 2004. **300**(1): p. 180-9.
42. Xiao Z, Z.N., Murphy DB, Devreotes PN,, *Dynamic Distribution of Chemoattractant Receptors in Living Cells During Chemotaxis and Persistent Stimulation.* J, Cell Biology, 1997. **139**(2): p. 365-74.
43. Pedowitz RA, O'connor JJ, and Akeson WH, *Daniel's Knee Injuries: Ligament and Cartilage Structure, Function, Injury, and Repair*. 2nd ed. 2003, Philadelphia: Lippincott Williams & Wilkins.
44. Maheshwari G, Wiley HS, and Lauffenburger DA, *Autocrine epidermal growth factor signaling stimulates directionally persistent mammary epithelial cell migration.* J. Cell Biology, 2001. **155**(7): p. 1123-8.
45. Baer, P.C. and H. Geiger, *Different effects of growth factors on human renal early distal tubular cells in vitro.* Kidney Blood Press Res, 2006. **29**(4): p. 225-30.
46. Saadi W, Rhee SW, Lin F, Vahidi B, Chung BG, and Jeon NL, *Generation of stable concentration gradients in 2D and 3D environments using a microfluidic ladder chamber.* Biomed Microdevices, 2007. **9**(5): p. 627-35.
47. Walker, G.M., J. Sai, A. Richmond, M. Stremler, C.Y. Chung, and J.P. Wikswo, *Effects of flow and diffusion on chemotaxis studies in a microfabricated gradient generator.* Lab Chip, 2005. **5**(6): p. 611-8.
48. Friedl P and Wolf K, *Tumour-Cell Invasion and Migration: Diversity and Escape Mechanisms.* Nature, 2003. **3**: p. 362-74.
49. Chung CY and Firtel RA, *Signaling Pathways at the Leading Edge of Chemotaxis Cells.* J. Muscle Research and Cell Motility, 2002. **23**: p. 773-9.
50. Van Haastert, P. and Devreotes PN, *Chemotaxis: Signalling the Way Forward.* Nature, 2004. **5**: p. 626-34.
51. Rees AR, Gregoriou M, Johnson P, and Garland PB, *High Affinity Epidermal Growth Factor Receptors on the Surface of A431 Cells Have Restricted Lateral Diffusion.* EMBO Journal, 1984. **3**(8): p. 1843-7.

52. H Naokia, Y.S., S Ishii, *Stochastic control of spontaneous signal generation for gradient sensing in chemotaxis.* Journal of Theoretical Biology, 2008. **255**(2): p. 259-66.
53. SAVIO L-Y. WOO, FENGYAN JIA, LI ZOU, and MARY T. GABRIEL, *Functional Tissue Engineering for Ligament Healing: Potential of Antisense Gene Therapy.* Annals of Biomedical Engineering, 2004. **32**(3): p. 342–351.
54. Woo SL, Debski RE, Zeminski J, Abramowitch SD, Saw SS, and Fenwick JA, *Injury and repair of ligaments and tendons.* Annu. Rev. Biomed. Eng., 2000. **02**(83-118).

7 Future work

7.1 Summary

In the research of cell migration described thus far, we have 1) Investigated how shear stress affected cell-cell communication, cell-ECM interaction and cell morphology in order to examine optimal methodology for cell seeding in microenvironment with minimum shear effects; 2) Developed a microfluidic system to deliver ligands to cells with quantitative spatiotemporal measurement of ligand concentration and gradients; 3) Studied how cells migrated in response to transient ligand gradients and steady-state gradients. Moreover, we have suggested that ligand concentration also played an important role in regulating cell migration when integrated with ligand gradients.

In this section, we will discuss the future experiments and methodologies used to further investigate cell migration. We propose three sets of examinations to be completed in the near future: 1) Development of microfluidic devices to facilitate cell migration study; 2) Combination of different growth factors to stimulate cell migration; and 3) Intracellular activities during cell migration.

7.2 Development of microfluidic devices

Microfluidic devices provide platforms for quantitative measurement of single-cell migration with feasibility to establish different ligand gradients. By controlling bulk flow within the microchannel, we will be able to design linear ligand gradient or non-linear ligand gradients.

7.2. A Porous membrane

We modify the bridge µlane system by adding two biopolymer-coated porous polymeric membranes into the microsystem, as shown in **Figure 7.1**. The membranes are vertically placed near both ends of the microchannel and penetrated through the microchannel. This design ensures pure ligand diffusion through the microchannel because bulk flow is eliminated between the two membranes. The pure diffusion leads to linear ligand gradient at steady-state, which can be precisely predicted using diffusion models. Further, cells migration through the coated membranes can be used to mimic the cell migration through transwell assays. Using this design, we will be able to observe how cells change their morphology while migrating through the pores. This may provide another way to investigate how cells adapt to microenvironment during migration.

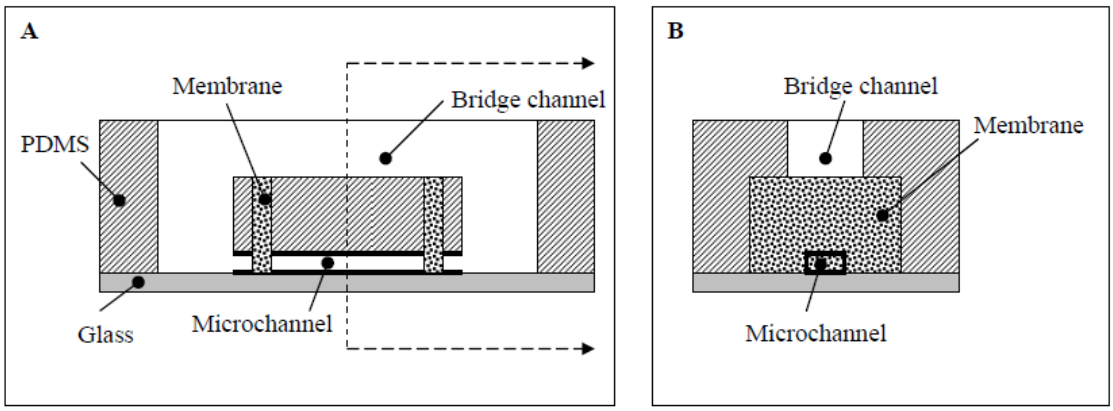

Figure 7.1: Schematics of side view (A) and cross-section (B) of the modified bridge µlane system using porous membranes. Two membranes were placed vertically into the microsystm and penetrated through the microchannel. The perimeter of the microcahnnel was highlighted.

7.2. B Multi-microchannel devices

We also design another microfluidic device, multi-microchannel device, as illustrated in **Figure 7.2**. Cells are cultured within hydrogels in each microchannel, which allows cell migration within 3-D matrices. Ligand solutions and PBS solutions are placed

in the reservoirs. **Figure 7.2A** illustrates the experiments where ligand is placed in the center Reservoir 0 and displaces outwards. This design can be used to examine the effects of hydrogel stiffness on cell migration, when hydrogels of different concentrations are used in the microchannels. We can also use this microdevice to test how different ligands or liangd of different concentrations affect cell migration. As shown in **Figure 7.2B**, cell migration toward different ligands or ligand concentrations can be observed simultaneously. Further, ligands displace within the hydrogels via pure diffusion as bulk flow is eliminated. As mentioned above, the stead-state linear ligand gradient generated by the pure diffusion within the microchannel can be predicted and precisely measured.

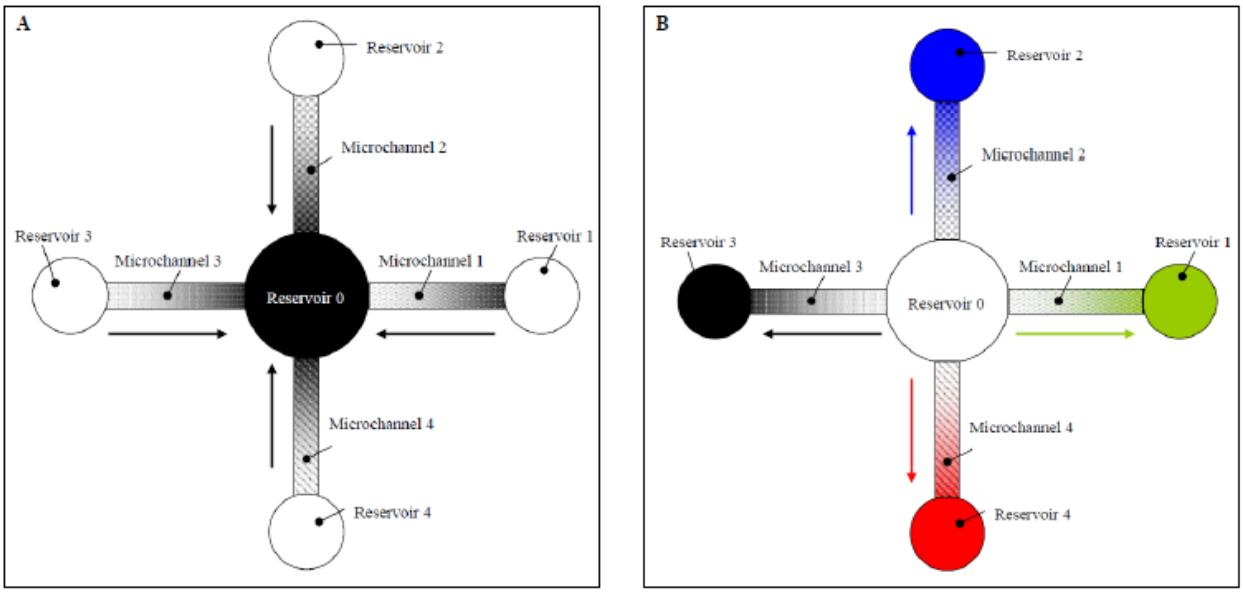

Figure 7.2: Schematic of multi-microchannel devices. Cell solutions mixed with hydrogels at different concentrations are injected into the microchannels while Reservoirs 0, 1, 2, 3 and 4 are filled with ligand solutions or PBS solution. In (A), Reservoir 0 is filled with ligand solution while Reservoir 1 to Reservoir 4 is filled with PBS. In (B), Reservoir 0 is placed with PBS while the other reservoirs are filled with different ligand solutions. Arrows point to cell migration directions.

7.3 Combination of different growth factors

In addition to EGF, other growth factors, such as PDGF and TGF-β, have been demonstrated to enhance ligament-derived fibroblast proliferation, trigger cell migration and stimulate ECM protein synthesis, which are largely helpful to facilitate tissue healing. Recent research has also conducted studies on the synergistic effects of growth factor combination on wound healing. PDGF alone has been reported to increase ligament mechanical properties during tissue healing [5]. Addition of TGF-β to PDGF could not improve structures of wound tissues [5]. However, some other tests have also shown that the combination of PDGF and TGF-β could significantly increase ligament fibroblast proliferation [84]. Different growth factors may trigger distinct signal pathways, which could be interacted to affect cell functions. The mechanism by which combination of growth factors affect cell migration is still under investigation.

Using our bridged μlane system, we will be interested in examining how the combination of EGF, PDGF and TGF-β affects cell migration, as these growth factors are widely studied in wound healing. Additionally, we can also investigate cell migration within ECM in response to growth factor combination via the multi-microchannel devices.

7.4 Intracellular activities during cell migration

In the course of growth factor-induced cell migration, multiple signal pathways are activated. In order to track intracellular activity during migration, fluorescent labeling with live cells is the methodology we will be interested in. Using the novel nanotechnology, fluorescently-labeled nanoparticles are delivered into cells and targeted

to specific organelles. Therefore, we will be able to observe intracellular activities during cell migration within our microfabricated devices. Additionally, we will utilize green fluorescent protein (GFP) actin to highlight the fibroblast cytoskeleton during migration in our microsystems. We will measure cell morphology change in overall cytoskeleton deformation in response to growth factors. We will also investigate cytoplasmic changes during cell migration within 3-D ECM to study dynamic interactions between cells and ECM microenvironment.

In summary, we will be able to design and develop microfabricated devices to meet different needs of biological research, and investigate cell migration with focus on synergistic effects of growth factors and intracellular activities. The novel methodologies used in recent experiments and future studies will not only facilitate investigation of cell migration in wound healing, immunological response and cancer metastasis, but also provide platforms to visualize protein activities in real time, such as ligand-receptor binding and signal transduction.

Acknowledgements

This research has been supported by the National Science Foundation (BES 0428573), the National Institutes of Health (1R21 GM071703), and the PSC-CUNY Foundation (64683-00-01). First of all, I would like to cordially thank my advisor, Maribel Vazquez, for instructing me with patience and encouragement these years. I would also like to thank my lab mates, friends and family who have supported me and given me valuable suggestions and advice.

Reference:

1. Cheung C, *The Future of Bone Healing.* Clin Podiatr Med Surg. , 2005. **22**(4): p. 631-41.
2. C. T. Laurencin, A. M. A. Ambrosio, M. D. Borden, and J. J. A. Cooper, *Tissue Engineering: Orthopedic Applications.* Annu. Rev. Biomed. Eng., 1999. **1**: p. 19-46.
3. Cole BJ, Frederick RW, Levy AS, and Zaslav KR, *Management of a 37-year-old man with recurrent knee pain.* J Clin Outcomes Manage, 1999. **6**(46-57).
4. McCormick F, Yanke A, Provencher MT, and Cole BJ, *Minced Articular Cartilage-Basic Science, Surgical Technique, and Clinical Application.* Sports Medicine and Arthroscopy Review, 2008. **16**(4): p. 217-20.
5. Woo SL, Debski RE, Zeminski J, Abramowitch SD, Saw SS, and Fenwick JA, *Injury and repair of ligaments and tendons.* Annu. Rev. Biomed. Eng., 2000. **02**(83-118).
6. Jung HJ, Fisher MB, and Woo SL, *Role of biomechanics in the understanding of normal, injured, and healing ligaments and tendons.* Sports Med Arthrosc Rehabil Ther Technol, 2009. **1**(1): p. 9.
7. RA Pedowitz, JJ O' Connor, and WH Akeson, *Daniel's Knee Injuries: Ligament and Cartilage Structure, Function, Injury, and Repair*. 2 ed. 2003, Philadelphia, PA: Lippincott Williams & Wilkins.
8. SAVIO L-Y. WOO, FENGYAN JIA, LI ZOU, and MARY T. GABRIEL, *Functional Tissue Engineering for Ligament Healing: Potential of Antisense Gene Therapy.* Annals of Biomedical Engineering, 2004. **32**(3): p. 342–351.
9. Lo IK, Ou Y, Rattner JP, Hart DA, Marchuk LL, Frank CB, and Rattner JB, *The cellular networks of normal ovine medial collateral and anterior cruciate ligaments are not accurately recapitulated in scar tissue.* J Anat, 2002. **200**(pt3): p. 283-96.
10. Konttinen YT, Li TF, Hukkanen M, Ma J, Xu JW, and Virtanen I, *Fibroblast biology. Signals targeting the synovial fibroblast in arthritis.* Arthritis Res, 2000. **2**(5): p. 348-55.
11. Chiquet M, Renedo AS, Huber F, and Flück M, *How do fibroblasts translate mechanical signals into changes in extracellular matrix production?* Matrix Biology, 2003. **22**(1): p. 73-80.
12. T Andriacchi, P Sabiston, and K DeHaven, *Ligament: injury and repair.*, in *Injury and repair of the musculoskeletal soft tissues*. 1988, American Academy of Orthopedic Surgeons: Chicago. p. 103-108.
13. SP Arnoczsky, ed. *Physiologic principles of ligament injuries and healing*. Ligament and extensor mechanism injuries of the knee: diagnosis and treatment. 1991, C V Mosby: St. Louis.
14. Hantash BM, Zhao L, Knowles JA, and Lorenz HP, *Adult and fetal wound healing.* Front Biosci. , 2008. **1**(13): p. 51-61.
15. Barrientos S, Stojadinovic O, Golinko MS, Brem H, and Tomic-Canic M, *Growth factors and cytokines in wound healing.* Wound Repair Regen, 2008. **16**(5): p. 585-601.

16. Hannafin JA, Attia ET, Warren RF, and Bhargava MM, *Characterization of chemotactic migration and growth kinetics of canine knee ligament fibroblasts.* J Orthop Res., 1999 **17**(3): p. 398-404.
17. Deuel TF, Senior RM, Huang JS, and Griffin GL, *Chemotaxis of monocytes and neutrophils to platelet-derived growth factor.* J Clin Invest., 1982. **69**(4): p. 1046-9.
18. Mustoe TA, Pierce GF, Thomason A, Gramates P, Sporn MB, and Deuel TF, *Accelerated healing of incisional wounds in rats induced by transforming growth factor-beta.* Science, 1987. **237**(4820): p. 1333-6.
19. Roberts AB, Anzano MA, Lamb LC, Smith JM, and Sporn MB, *New class of transforming growth factors potentiated by epidermal growth factor: isolation from non-neoplastic tissues.* PNAS, 1981. **78**(9): p. 5339-43.
20. Roberts AB, Sporn MB, Assoian RK, Smith JM, Roche NS, Wakefield LM, Heine UI, Liotta LA, Falanga V, and Kehrl JH, *Transforming growth factor type beta: rapid induction of fibrosis and angiogenesis in vivo and stimulation of collagen formation in vitro.* PNAS, 1986. **83**(12): p. 4167-71.
21. Seppä H, Grotendorst G, Seppä S, Schiffmann E, and Martin GR, *Platelet-derived growth factor in chemotactic for fibroblasts.* J Cell Biol, 1982. **92**(2): p. 584-8.
22. Becker, W.M., L.J. Kleinsmith, and J. Hardin, *The World of The Cell*. 2005, San Francisco: Benjamin Cummings.
23. Janetopoulos C and Firtel RA, *Directional sensing during chemotaxis.* FEBS Lett., 2008. **582**(14): p. 2075-85.
24. Lang K, H.H., Niggemann B, Zaenker KS, Entschladen F, *A novel function for chemokines: downregulation of neutrophil migration.* Scand J Immunol, 2003. **57**(4): p. 350-61.
25. Glading A, C.P., Lauffenburger DA, Wells A, *Epidermal growth factor receptor activation of calpain is required for fibroblast motility and occurs via an ERK/MAP kinase signaling pathway.* J Biol Chem, 2000. **275**(4): p. 2390-8.
26. Chung CY and Firtel RA, *Signaling pathways at the leading edge of chemotaxing cells.* J Muscle Res Cell Motil, 2002. **23**(7-8): p. 773-9.
27. Ware MF, W.A., Lauffenburger DA, *Epidermal growth factor alters fibroblast migration speed and directional persistence reciprocally and in a matrix-dependent manner.* J Cell Sci, 1998. **111**(16): p. 2423-32.
28. Corkidi G, Taboada B, Wood CD, Guerrero A, and Darszon A, *Tracking sperm in three-dimensions.* Biochem Biophys Res Commun, 2008. **373**(1): p. 125-9.
29. Eisenbach M, *Chemotaxis*. 2004, Danvers, MA: Imperial College Press.
30. Wolgemuth CW, *Lamellipodial contractions during crawling and spreading.* Biophys J., 2005. **89**(3): p. 1643-9.
31. Chao PH, Lu HH, Hung CT, Nicoll SB, and Bulinski JC, *Effects of applied DC electric field on ligament fibroblast migration and wound healing.* Connect Tissue Res, 2007. **48**(4): p. 188-97.
32. Paul R, Heil P, Spatz JP, and Schwarz US, *Propagation of mechanical stress through the actin cytoskeleton toward focal adhesions: model and experiment.* Biophys J., 2008. **94**(4): p. 1470-82.

33. PJ Schreck, D Amiel , and VL Wood Jr, *The role of integrin adhesion receptors in anterior cruciate ligament physiology*, in *The anterior cruciate ligament: current and future concepts*, D. Jackson, Editor. 1993, Raven Press: New York.
34. Hadjipanayi E, Brown RA, and Mudera V, *Interface integration of layered collagen scaffolds with defined matrix stiffness: implications for sheet-based tissue engineering.* J Tissue Eng Regen Med, 2009. **3**(3): p. 230-41.
35. Rosner MR, *Regulation of the epidermal growth factor receptor by growth-modulating agents.* Biotechnol Appl Biochem, 1990. **12**(5): p. 473-7.
36. Ozcan F, Klein P, Lemmon MA, Lax I, and Schlessinger J, *On the nature of low- and high-affinity EGF receptors on living cells.* PNAS, 2006. **103**(15): p. 5735-40.
37. Parent CA and Devreotes P, *A Cell's Sense of Direction.* Science, 1999. **284**: p. 765-70.
38. Ridley AJ, Schwartz MA, Burridge K, Firtel RA, Ginsberg MH, Borisy G, Parsons JT, and Horwitz AR, *Cell Migration: Integrating Signals from Front to Back.* Science, 2003. **302**: p. 1704-9.
39. Van Haastert, P. and Devreotes PN, *Chemotaxis: Signalling the Way Forward.* Nature, 2004. **5**: p. 626-34.
40. Lauffenburger DA and Linderman JJ, *Receptors: Models for binding, trafficking and signaling*. 1996, New York: Oxford University Press, Inc.
41. Lin, F., C.M. Nguyen, S.J. Wang, W. Saadi, S.P. Gross, and N.L. Jeon, *Effective neutrophil chemotaxis is strongly influenced by mean IL-8 concentration.* Biochem Biophys Res Commun, 2004. **319**(2): p. 576-81.
42. Li CW, Chen R, and Yang M, *Generation of linear and non-linear concentration gradients along microfluidic channel by microtunnel controlled stepwise addition of sample solution.* Lab Chip, 2007. **7**(10): p. 1371-3.
43. Abhyankar VV, Toepke MW, Cortesio CL, Lokuta MA, Huttenlocher A, and Beebe DJ, *A platform for assessing chemotactic migration within a spatiotemporally defined 3D microenvironment.* Lab Chip, 2008. **8**(9): p. 1507-15.
44. Janetopoulos C, Ma L, Devreotes PN, and Iglesias PA, *Chemoattractant-induced phosphatidylinositol 3,4,5-trisphosphate accumulation is spatially amplified and adapts, independent of the actin cytoskeleton.* PNAS, 2004. **101**(24): p. 8951-6.
45. Zigmond SH, *Polymorphonuclear leucocyte chemotaxis: detection of the gradient and development of cell polarity.* Ciba Found Symp., 1980. **71**: p. 299-311.
46. Naoki H, Sakumura Y, and Ishii S, *Stochastic control of spontaneous signal generation for gradient sensing in chemotaxis.* J Theor Biol., 2008. **255**(2): p. 259-66.
47. Friedl P and Wolf K, *Tumour-Cell Invasion and Migration: Diversity and Escape Mechanisms.* Nature, 2003. **3**: p. 362-74.
48. Lauffenburger DA, H.A., *Cell Migration: A Physically Integrated Molecular Process.* Cell, 1996. **84**: p. 359-69.
49. Boyden S, *The chemotactic effect of mixtures of antibody and antigen on polymorphonuclear leucocytes.* J. Exp. Med., 1962. **115**: p. 453-66.
50. Sogabe Y, Abe M, Yokoyama Y, and Ishikawa O, *Basic fibroblast growth factor stimulates human keratinocyte motility by Rac activation.* Wound Repair Regen, 2006. **14**(4): p. 457-62.

51. Entschladen F, Drell TL 4th, Lang K, Masur K, Palm D, Bastian P, Niggemann B, and Zaenker KS, *Analysis methods of human cell migration.* Exp Cell Res, 2005. **307**(2): p. 418-26.
52. Kurten, R.C., P. Chowdhury, R.C. Sanders, Jr., L.M. Pittman, L.W. Sessions, T.C. Chambers, C.S. Lyle, B.J. Schnackenberg, and S.M. Jones, *Coordinating epidermal growth factor-induced motility promotes efficient wound closure.* Am J Physiol Cell Physiol, 2005. **288**(1): p. C109-21.
53. P. Bastian, K. Lang, B. Niggemann, K.S. Zaenker, and F. Entschladen, *Myosin regulation in the migration of tumor cells and leukocytes within a three-dimensional collagen matrix.* Cell. Mol. Life Sci., 2005. **62**: p. 65-76.
54. D. Ilic, B. Kovacic, K. Johkura, D.D. Schlaepfer, N. Tomasevic, Q. Han, J.B. Kim, K. Howerton, C. Baumbusch, N. Ogiwara, D.N. Streblow, J.A. Nelson, P. Dazin, Y. Shino, K. Sasaki, and H. Damsky, *FAK promotes organization of fibronectin matrix and fibrillar adhesions.* J. Cell Sci., 2004. **117**: p. 177-87.
55. Sarvestani, A.S. and E. Jabbari, *Analysis of cell locomotion on ligand gradient substrates.* Biotechnol Bioeng, 2009. **103**(2): p. 424-9.
56. Bornfeldt, K.E., E.W. Raines, T. Nakano, L.M. Graves, E.G. Krebs, and R. Ross, *Insulin-like growth factor-I and platelet-derived growth factor-BB induce directed migration of human arterial smooth muscle cells via signaling pathways that are distinct from those of proliferation.* J Clin Invest, 1994. **93**(3): p. 1266-74.
57. Kim, W.J., R.R. Mohan, R.R. Mohan, and S.E. Wilson, *Effect of PDGF, IL-1alpha, and BMP2/4 on corneal fibroblast chemotaxis: expression of the platelet-derived growth factor system in the cornea.* Invest Ophthalmol Vis Sci, 1999. **40**(7): p. 1364-72.
58. Zigmond, S.H., *Ability of polymorphonuclear leukocytes to orient in gradients of chemotactic factors.* J Cell Biol, 1977. **75**(2 Pt 1): p. 606-16.
59. Zicha, D., G.A. Dunn, and A.F. Brown, *A new direct-viewing chemotaxis chamber.* J Cell Sci, 1991. **99 (Pt 4)**: p. 769-75.
60. Zicha, D., G. Dunn, and G. Jones, *Analyzing chemotaxis using the Dunn direct-viewing chamber.* Methods Mol Biol, 1997. **75**: p. 449-57.
61. Gundersen, R.W. and J.N. Barrett, *Neuronal chemotaxis: chick dorsal-root axons turn toward high concentrations of nerve growth factor.* Science, 1979. **206**(4422): p. 1079-80.
62. Yarrow, J.C., Z.E. Perlman, N.J. Westwood, and T.J. Mitchison, *A high-throughput cell migration assay using scratch wound healing, a comparison of image-based readout methods.* BMC Biotechnol, 2004. **4**: p. 21.
63. Soderholm, J. and R. Heald, *Scratch n' screen for inhibitors of cell migration.* Chem Biol, 2005. **12**(3): p. 263-5.
64. Gunawan, R.C., J. Silvestre, H.R. Gaskins, P.J. Kenis, and D.E. Leckband, *Cell migration and polarity on microfabricated gradients of extracellular matrix proteins.* Langmuir, 2006. **22**(9): p. 4250-8.
65. Paguirigan, A.L. and D.J. Beebe, *Microfluidics meet cell biology: bridging the gap by validation and application of microscale techniques for cell biological assays.* Bioessays, 2008. **30**(9): p. 811-21.
66. Keenan, T.M. and A. Folch, *Biomolecular gradients in cell culture systems.* Lab Chip, 2008. **8**(1): p. 34-57.

67. Breslauer, D.N., P.J. Lee, and L.P. Lee, *Microfluidics-based systems biology.* Mol Biosyst, 2006. **2**(2): p. 97-112.
68. von Philipsborn, A.C., S. Lang, A. Bernard, J. Loeschinger, C. David, D. Lehnert, M. Bastmeyer, and F. Bonhoeffer, *Microcontact printing of axon guidance molecules for generation of graded patterns.* Nat Protoc, 2006. **1**(3): p. 1322-8.
69. Quist, A.P., E. Pavlovic, and S. Oscarsson, *Recent advances in microcontact printing.* Anal Bioanal Chem, 2005. **381**(3): p. 591-600.
70. von Philipsborn, A.C., S. Lang, J. Loeschinger, A. Bernard, C. David, D. Lehnert, F. Bonhoeffer, and M. Bastmeyer, *Growth cone navigation in substrate-bound ephrin gradients.* Development, 2006. **133**(13): p. 2487-95.
71. Hattersley, S.M., C.E. Dyer, J. Greenman, and S.J. Haswell, *Development of a microfluidic device for the maintenance and interrogation of viable tissue biopsies.* Lab Chip, 2008. **8**(11): p. 1842-6.
72. Gutierrez, E. and A. Groisman, *Quantitative measurements of the strength of adhesion of human neutrophils to a substratum in a microfluidic device.* Anal Chem, 2007. **79**(6): p. 2249-58.
73. Nie, F.Q., M. Yamada, J. Kobayashi, M. Yamato, A. Kikuchi, and T. Okano, *On-chip cell migration assay using microfluidic channels.* Biomaterials, 2007. **28**(27): p. 4017-22.
74. Chaw, K.C., M. Manimaran, E.H. Tay, and S. Swaminathan, *Multi-step microfluidic device for studying cancer metastasis.* Lab Chip, 2007. **7**(8): p. 1041-7.
75. Abhyankar, V.V., M.A. Lokuta, A. Huttenlocher, and D.J. Beebe, *Characterization of a membrane-based gradient generator for use in cell-signaling studies.* Lab Chip, 2006. **6**(3): p. 389-93.
76. Frevert, C.W., G. Boggy, T.M. Keenan, and A. Folch, *Measurement of cell migration in response to an evolving radial chemokine gradient triggered by a microvalve.* Lab Chip, 2006. **6**(7): p. 849-56.
77. Kanegasaki S, Nomura Y, Nitta N, Akiyama S, Tamatani T, Goshoh Y, Yoshida T, Sato T, and Kikuchi Y, *A novel optical assay system for the quantitative measurement of chemotaxis.* J Immunol Methods., 2003. **282**(1-2): p. 1-11.
78. Chung, B.G., F. Lin, and N.L. Jeon, *A microfluidic multi-injector for gradient generation.* Lab Chip, 2006. **6**(6): p. 764-8.
79. Lin, F., W. Saadi, S.W. Rhee, S.J. Wang, S. Mittal, and N.L. Jeon, *Generation of dynamic temporal and spatial concentration gradients using microfluidic devices.* Lab Chip, 2004. **4**(3): p. 164-7.
80. Kamholz, A.E., B.H. Weigl, B.A. Finlayson, and P. Yager, *Quantitative analysis of molecular interaction in a microfluidic channel: the T-sensor.* Anal Chem, 1999. **71**(23): p. 5340-7.
81. Wu, H., B. Huang, and R.N. Zare, *Generation of complex, static solution gradients in microfluidic channels.* J Am Chem Soc, 2006. **128**(13): p. 4194-5.
82. Keenan, T.M., C.H. Hsu, and A. Folch, *Microfluidic "jets" for generating steady-state gradients of soluble molecules on open surfaces.* Applied Physics Letters, 2006. **89**(11).
83. Capon, A. and S. Mordon, *Can thermal lasers promote skin wound healing?* Am J Clin Dermatol, 2003. **4**(1): p. 1-12.

84. Khatod M, Akeson WH, and Amiel D, *Ligament Injury and Repair*, in *Daniel's Knee Injuries: Ligament and Cartilage Structure, Function, Injury, and Repair*, Pedowitz RA, O' Connor JJ, and Akeson WH, Editors. 2003, Lippincott Williams & Wilkins: Philadelphia, PA.